A Multi-Physics Model for Wet Clutch Dynamics

by

Jungdon Cho

A dissertation submitted in partial fulfillment
of the requirements for the degree of
Doctor of Philosophy
(Mechanical Engineering)
in The University of Michigan
2012

Doctoral Committee:

Professor Nikolaos D. Katopodes, Co-Chair
Professor Anna G. Stefanopoulou, Co-Chair
Associate Professor Aline J. Cotel
Associate Professor Hong G. Im

Dedicated to my wife and to my mother

ACKNOWLEDGEMENTS

My doctoral studies would not have been possible without the support of many individuals whose advice and support have culminated in this thesis, and will undoubtedly shape my future career. I am especially grateful to several people who, at very timely moments, provided me with encouragement that gave direction to my graduate studies.

I wish to express my sincere appreciation to my advisor, Professor Nikolaos Katopodes for his confidence in me, for his foresight of such an interesting research subject, for his academic advisement, and for sharing his insight into the physical and mathematical nature of fluid mechanics. I am also grateful to my co-advisor, Professor Anna Stefanopoulou for helping me put this work into the realm of automotive research. I am also thankful for the valuable comments and suggestions of my dissertation committee members, Professors Aline Cotel and Hong G. Im.

This work would not have been possible without the continuous guidance and collaboration of Dr. Yuji Fujii and Dr. Nimrod Kapas of the Ford Motor Company. They selflessly made available their past experiences, insightful advice, technical specifications and experimental facilities to my dissertation research. I am also grateful to Jeffrey Kutrukis, Carl Waldrop, and Dr. Dengfu Zhang from the Ford Motor Company for sharing with me the results of their research. I would also like to acknowledge the help and support of Dr. Ibrahim Yavuz of Ansys, Inc. for his cooperation and advice throughout the duration of this project.

Finally, I am thankful for the support of my family, particularly to my mother for

her unlimited love and sacrifice throughout my life; my wife for her constant support and understanding and her encouragement during my studies; my wonderful children Hanna and Daniel; my parents in law; and my sisters.

This research has been funded by the Ford Motor Company under the Ford-University of Michigan Innovation Alliance program.

TABLE OF CONTENTS

LIST OF FIGURES

Figure

LIST OF TABLES

Table

LIST OF APPENDICES

Appendix

LIST OF ABBREVIATIONS

CFD Computational Fluid Dynamics

TGC Tested Grooved Clutch

VOF Volume of Fluid

FEM Finite Element Method

UDF User Defined Functions

PDF Probability Density Function

ABSTRACT

A Multi-Physics Model for Wet Clutch Dynamics

by

Jungdon Cho

Co-Chairs: Nikolaos D. Katopodes and Anna G. Stefanopoulou

A multi-physics model is developed for predicting the dynamic behavior of wet clutch engagement under realistic driving conditions. The primary function of an automatic transmission system is to transfer torque according to driving demands. The transmission clutch plays a significant role in determining drivability and fuel economy. The present work overcomes previous limitations by constructing a detailed computational fluid dynamics model for wet clutch engagement.

An open clutch model for single and multi-phase flow is developed using the Volume of Fluid method. This model is used to provide the initial conditions for the dynamic engagement model. New extended boundary formulations are examined in order to reduce numerical errors at inlet and outlet boundaries. A new approach for squeeze-film flow is developed based on an iterative method. Given the external force responsible for plate movement, the squeeze velocity is computed by trial until the internal fluid stresses balance the external force. The results are validated using analytical solutions of the Reynolds equation in cylindrical coordinates in terms of film thickness and squeeze velocity under the influence of various boundary conditions. The latter are shown to have a major effect on squeeze-film flow and clutch engage-

ment in general. The squeeze-flow model includes the compression of porous material during engagement. The model also captures the flow in the micro-channels created by the grooves on the friction material surface. Furthermore, the flow through the porous friction material is simulated using Darcy's law.

The influence of a rough surface on lubrication flow is simulated by using the concept of flow factor. Mechanical contact is simulated based on the real contact area. Subsequently, these models are combined with the squeeze-film flow model to create an integrated clutch engagement model. Finally, the heat flux at the interface between the friction and separator plates is computed using a virtual volume having a very small thickness.

A series of squeeze flow experiments were performed at the Ford Motor Company testing facility. Using typical test conditions in terms of lubricating oil flow rates, oil temperatures and applied pressures, clutch plate movement was directly measured using a position sensor. The experimental data are noisy due to friction and deflection of the piston module. The data are de-noised using standard statistical filters and then are used to validate the numerical results.

Based on the comparison with the experimental data, the performance of the proposed model is found satisfactory. The wet clutch model developed in this research can become a baseline model for the prediction of the engagement behavior of a real wet clutch. When various material properties and further detailed geometric features are included, the present model may become an efficient alternative to laboratory testing and lead to designs that cannot be envisioned by other approaches.

CHAPTER I

Introduction

1.1 Motivation and Background

An automatic transmission system utilizes wet friction to change gear configurations for automatic shifting. The system employs a torque converter and planetary gear set to achieve a range of torque multiplication. In order to alter the planetary gear configurations, a wet clutch system has been successfully used in most automatic transmissions for several decades. The clutch plates of a wet clutch system play an important role in transferring torque smoothly.

Prior to the development of the automatic transmission, the driver had to shift gears manually, so it was difficult to alter the gear ratio smoothly, i.e. without a gear shift shock. Although manual transmissions are still used in many vehicles, the convenience offered by an automatic transmission is now considered a standard automotive feature. However, automatic transmissions are generally associated with lower fuel efficiency compared to manual transmissions, so the automobile industry has recently made significant investments in research for new types of automatic transmission in order to improve fuel economy. These new automatic transmission systems involve a more complicated control system that requires new design parameters. Specifically, since the required torque conditions of the new systems differ from those of conventional gear shifting transmissions, it is difficult to find optimal control conditions and

design parameters that result in a satisfying experience for the driver, a high power transmission performance and high fuel efficiency. To achieve all of these objectives, a good understanding of the physical phenomena taking place inside an engaging wet clutch is necessary, especially as the clutch undergoes the transition from an open to an engaged position.

Over the last several decades, many experimental and theoretical studies have been conducted on wet clutches. However there is no generally accepted model that can make accurate and reliable predictions of the dynamic behavior of wet clutch engagement, especially for the automatic transmission systems, because of the complexity of the clutch mechanism. The recent development of high performance computers and computational methods offers an opportunity for constructing a detailed Computational Fluid Dynamics (CFD) model of the flow and heat transfer during clutch engagement. The Finite Element Method (FEM) and the Finite Volume Method (FVM) have been recently employed in various transient, three-dimensional flow problems and made great advancements towards the solution of complicated physical phenomena encountered in the automobile industry. Although the generality of these numerical methods introduces additional complexities and uncertainties, it is believed that as more detail is introduced to the model the simulation results will converge towards the true physical behavior of the prototype clutch. The increased computational effort is justified since a complete dynamic computational model can ultimately lead to optimal control conditions and design features without the need for manufacturing test products and tedious experimentation.

Therefore, the development of a reliable CFD model for a wet clutch is highly desirable, as it has the potential to become a powerful tool for the prediction of the engagement and disengagement behavior of a wet clutch. The inclusion of detailed material properties and geometric features may make such a model an efficient alternative to laboratory testing and lead to designs that cannot be envisioned by other

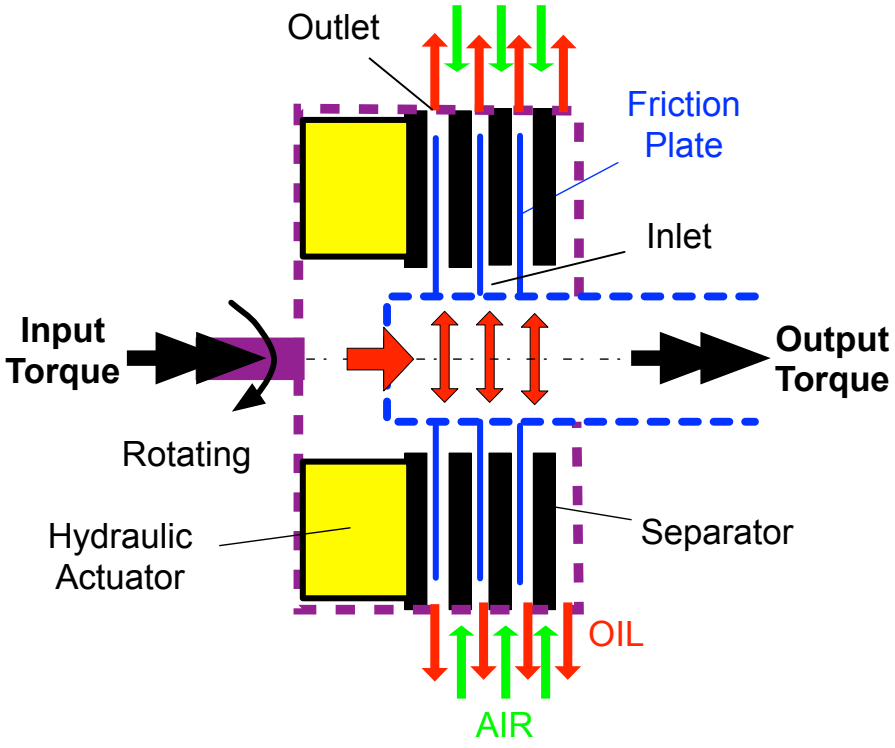

Figure 1.1: Schematic of automatic transmission clutch

approaches. Finally, once validated, a CFD model will enable engineers to fully understand the details of the flow and heat transfer within a wet clutch that could lead to increased fuel efficiency and durability.

1.2 Problem Definition and Objectives

A wet clutch system consists of a multi-layer assembly of steel and friction plates, as shown in Figure 1.1. The wet clutch plates are submerged in transmission oil that lubricates the space between the friction and separator steel plates.

The friction material is bonded on the surface of the steel core plate and may be grooved, as shown in Figure 1.2. The groove dimensions and pattern play a significant role in shift quality and fuel economy, as oil flows through the micro-channels of the friction material during the squeeze phase of clutch engagement.

The physics of open clutch operation, squeeze-film flow, flow through the porous

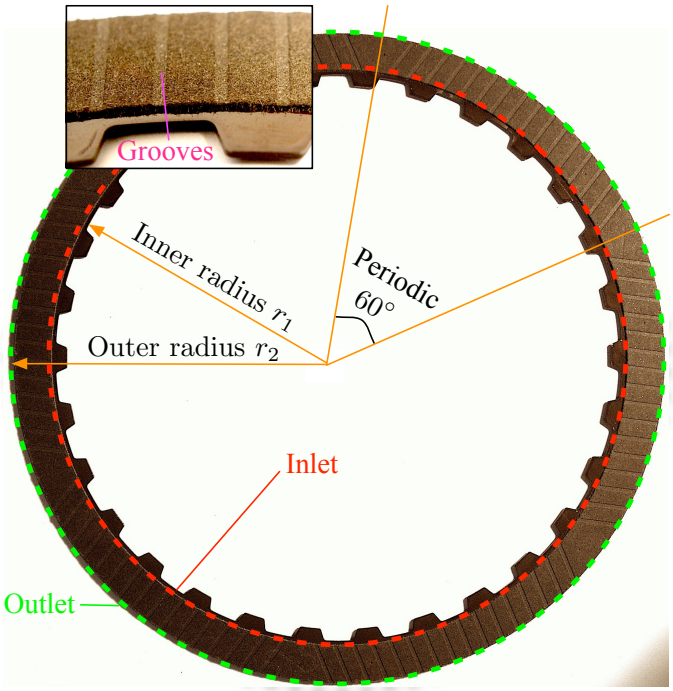

Figure 1.2: Grooved friction plate

friction material, engagement and heat transfer can be studied easier if only a single pair of of disk plates is considered, as shown in Figure 1.3.

The clutch system has two main operating modes: open clutch mode and engagement mode. When the clutch is open, the friction and steel plates rotate at different speeds (rpm) as shown in Figure 1.4. A hydrodynamic torque develops due to the shear stresses in the oil. The drag torque depends on the viscosity of the oil and is also affected by the presence of air bubbles that may be trapped between the rotating plates, as the pressure drops due to the centrifugal force. This creates a multi-phase flow problem that is not very well understood, as it is difficult to determine the direction of flow and the associated boundary conditions.

In the engagement mode, the plates are pushed together and the oil is squeezed out of the gap and the porous friction material, as shown in Figure 1.5. Therefore, the oil flow during engagement is significantly different than that occurring in the gap of an open clutch. Any trapped air bubbles are quickly squeezed out of the gap,

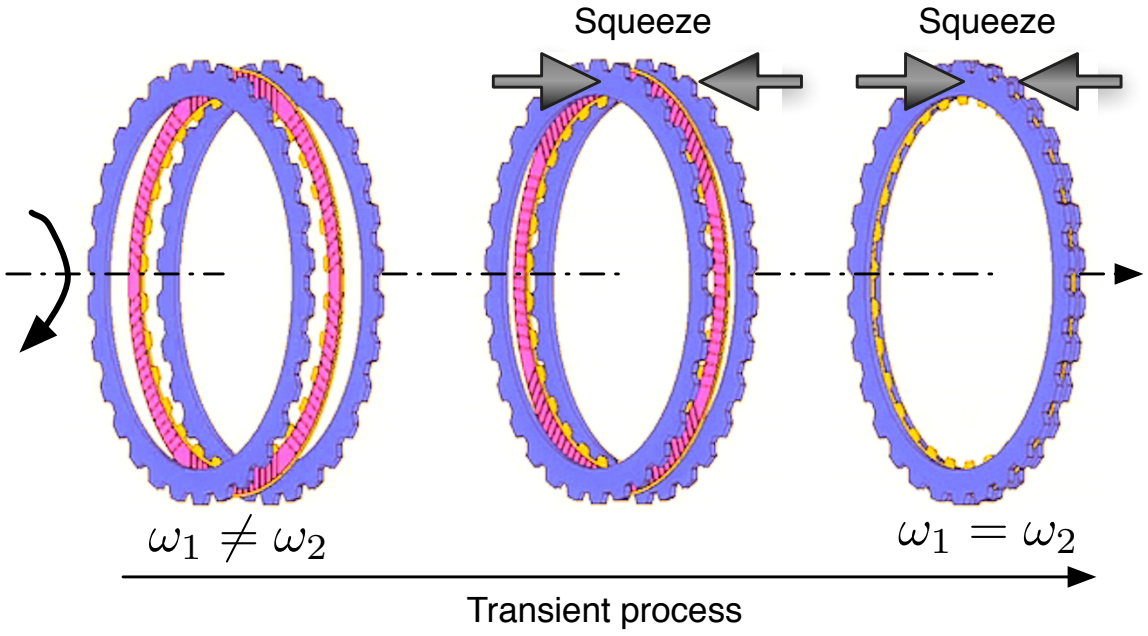

Figure 1.3: Engaging clutch plates

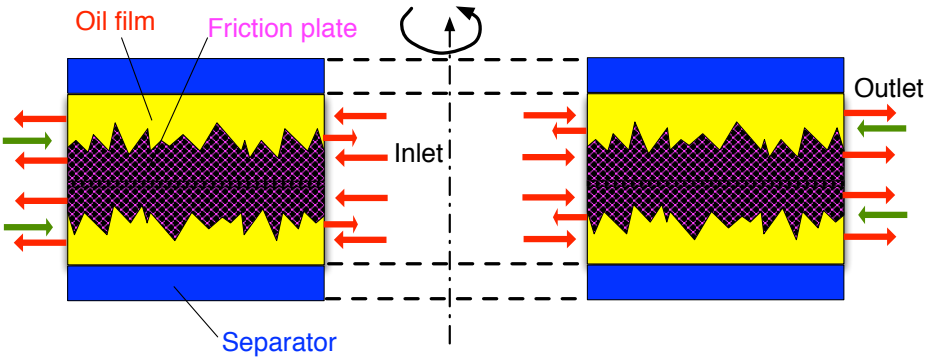

Figure 1.4: Open clutch flow between steel and friction plates

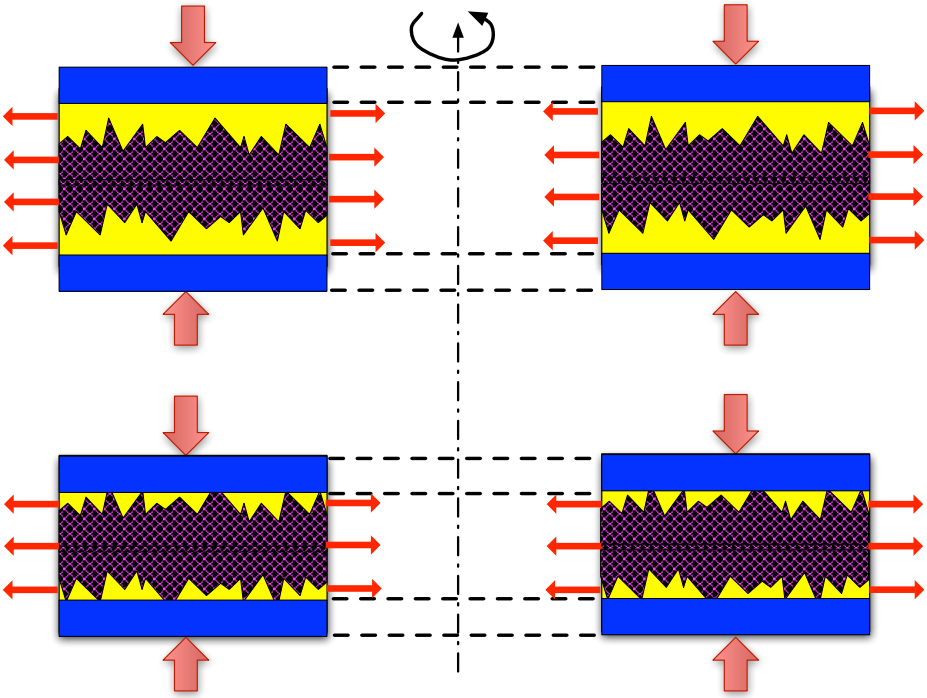

Figure 1.5: Squeeze-film flow during engagement

which is now dynamically changing in size. The friction material is also deformed, squeezing additional oil out of the gap. Finally, solid contact is made with the friction material, and the plates become completely engaged.

The general behavior of hydrodynamic torque as a function of rotation speed is shown in Figure 1.6. In general, the torque increases with speed in the low rpm range. After reaching a peak value, the torque begins to decrease until a constant level is established in the high speed range.

The operating conditions of an open clutch correspond to a low pressure between the rotating plates when compared to the pressure in the clutch engagement stage. A typical clutch engagement behavior is shown in Figure 1.7. As an open clutch enters the engagement stage, the clearance between the friction and steel plates decreases and hydrodynamic torque is transferred until the plates come in contact with each other. As the oil film between the plates becomes thinner, the hydrodynamic torque decreases and a friction torque begins to develop. Finally, the steel and friction

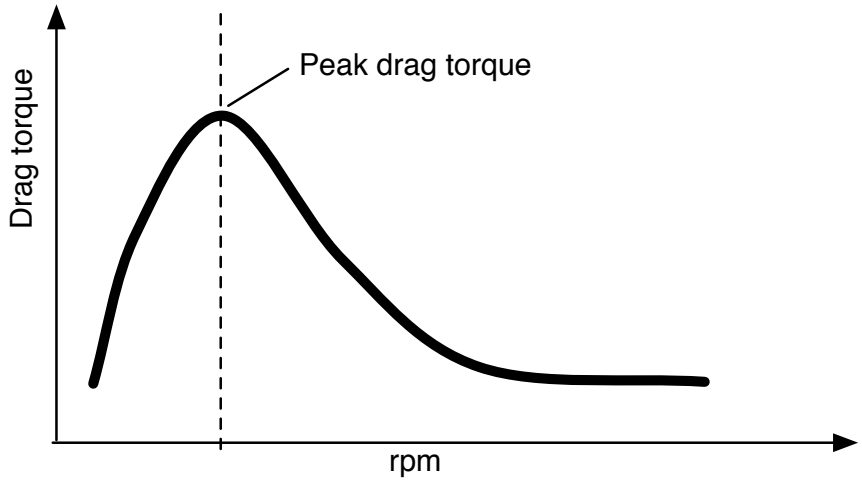

Figure 1.6: General relationship between rotating speed and drag torque

plates become completely engaged and begin to rotate with the same speed. During the engagement mode, air bubbles that may have been trapped between the plates are removed by squeeze oil flow. At the same time, the oil viscosity changes as a result of changes in oil temperature. The latter increases due to both fluid and solid friction. In addition, the permeability of the friction material may also affect the squeeze velocity, so the properties of the porous friction plate play a major role on the torque profile. Finally, any groove patterns on the friction alter the flow conditions for the oil between the clutch plates, so the presence and form of groves also has a major influence on oil flow, torque, and heat transfer in an automatic transmission.

The objective of this study is to develop a CFD model capable of predicting the flow and thermal characteristics of a wet plate clutch and to provide further insight of wet clutch design. Because of the multi-physics aspects of clutch engagement, e.g. multi-phase flow, flow through porous media, groove boundary geometry, solid contact mechanics and heat transfer, four secondary objectives are also considered. These are

- Construct an open clutch model including multi-phase flow for oil and air. The results of this model may be used as the initial condition for dynamic clutch

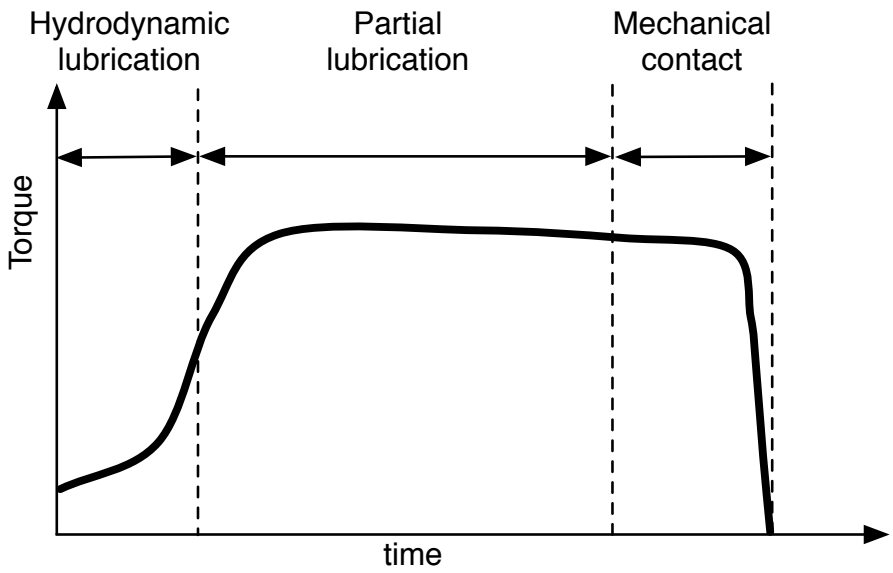

Figure 1.7: Torque vs Time: typical engagement

engagement.

- Construct a squeeze-film flow model. During engagement, squeeze-film flow is caused by the translational motion of the clutch plates. This represents the core component of the integrated clutch model.

- Construct asperity contact and heat transfer models. These models are also significant components of an integrated clutch model and must be addressed individually.

- Conduct clutch engagement experiments and use the laboratory data to validate the integrated CFD model. Document the accuracy and reliability of the CFD model.

- Study each component of the validated model are used to analyze the effect of grooves and permeability of the friction material, oil flow rate and oil temperature and viscosity.

CHAPTER II

Literature Review

The construction of a multi-physics model for wet clutch dynamics requires the integration of several physical processes. Specifically, multi-phase flow between rotating annular disks, mechanics of squeeze film, flow through deforming porous media, asperity and consolidating contact and heat transfer. There exists a vast literature for each of these subjects, so the following review is by no means exhaustive. Emphasis was placed on recent developments in clutch dynamics and on the key components of the physical processes that are captured by the present model.

2.1 Flow Between Disks

One of the earliest attempts to analyze the engagement of two annular disks was made by *Ting* (1975). In his study, one of the disks was made of porous material, so both the roughness and deformation of the friction material were considered. The engagement behavior consisted of three phases, i.e. squeeze film flow, mixed asperity contact and consolidating contact. Ting developed analytical solutions for squeeze film flow and consolidating contact. The analysis showed that the permeability of the friction material reduces film pressure. Furthermore, as the variance of the surface roughness distribution increases, film pressure decreases further. Ting studied the effects of skewness in surface roughness distribution. He found that positive skewness

decreases film pressure while negative skewness increases the pressure. Therefore, increasing permeability and roughness reduces the squeeze time when compared to squeeze flow in disks with a smooth surface and without porous media. However, the influence of surface roughness was found to be less important than the permeability of the friction material, as far as squeeze time in of the film is concerned. In the consolidating contact phase, the decay time of the contact surface deformation increases as the real contact area and oil viscosity increase and the permeability decreases.

Gorin and Shilyaev (1976) studied the analytical solutions between two rotating annular disks having small gaps. Since the analytical solutions were derived from the Navier-Stokes equations using an integral approach, i.e. the Slezkin-Targ method, the inertial terms were not considered. The study was limited to laminar flow between a rotating and a stationary disk, and computed exactly the radial, axial and tangential velocity components.

Matveev and Pustovalov (1982) conducted a numerical simulation for flow between annular disks by using an explicit conservative scheme for the Navier-Stokes equations. The model corresponded to two disks rotating with the same speed. The radial velocity and pressure profiles were computed for turbulent and laminar flow regimes. The radial velocity profiles showed a strong dependence of the flow regime.

A. Z. Szeri and Kaufman (1983) made measurements of the velocity components and developed a numerical model for flow between rotating disks in four different cases with respect to the rotating speeds of the two disks. These corresponded to $\omega_1 = \omega_2 = 0; \omega_2/\omega_1 = -1; \omega_2/\omega_1 = 0; \omega_2/\omega_1 = 1;$. Szeri and Kaufman found that at mid-radius, the velocity profiles exhibit only minimal effects of the boundary conditions. Furthermore, they noticed that while the centrifugal force field causes the fluid to increase its outward radial velocity near the rotating disk, back flow is developed near the stationary disk to compensate the centrifugal flow effect. The results showed that when one disk is rotating and the other is stationary, the back flow that develops

depends on the ratio of the through-flow Reynolds number, $R_Q = Q/2\pi\nu h$, to the rotational Reynolds number, $Re = r_2^2\omega/\nu$. Typically, R_Q/R_e has a small value in the back flow. Finally, it is worth mentioning that the numerical solution Szeri and Kaufman had a poor rate of convergence for small R_Q/R_e.

Li and Tao (1994) compared three types of outflow boundary conditions for recirculating flows with experiment data for convective heat transfer of a two-dimensional jet impinging on a rectangular cavity. They tried a local mass conservation method, a local one-way method and a fully-developed flow assumption. They concluded that, if possible, the area of the outflow boundary should be located far enough from the recirculating area in order to obtain a realistic numerical solution and avoid significant errors. Of the three methods that Li and Tao studied, the mass conservation method for the outflow boundary model having a recirculating flow at the boundaries had the best agreement with the experimental data .

Yuan et al. (2007) proposed an improved hydrodynamic model for open, wet-clutch behavior. This theoretical model includes not only the effects of trapped air bubbles, but also surface tension and wall adhesion. The surface tension between fluid and air at outer interface is assumed and the relation between the surface tension and the pressure jump is formulated. With the formulation, an equivalent radius assumption was made. The drag torque for the equivalent radius was validated with experiment results and the computed drag torque from this model was proven to be more accurate than previous models at high rpm. The analytical solution of Yan et al. agreed well with the experimental results, however the need for adjustment of the oil viscosity was rather problematic. Also, since the model corresponded to a non-grooved open wet clutch, there were limitations to any potential applications to a realistic wet clutch having a grooved friction plate and undergoing dynamic engagement.

2.2 Engagement process

To analyze a wet clutch system, squeeze-film flow needs to be understood because it represents the main physical process of wet clutch engagement. The study of squeeze-film flow has a long history and has been recognized as an important and complex fluid mechanics problem since it appears in many practical applications such as printing, thrust bearing, band braking, wet clutch engagement, etc. Squeeze-film flows have different characteristics depending on the geometrical shapes, material properties and roughness of the squeezing plates, squeezing liquid properties, and dynamic motion that include rotational and translational movement. Because of the complexity of squeeze-film flow, studies of its characteristics have a long history.

In the automobile industry, the study of squeeze-film flow has been of interest to automatic transmissions developers because wet clutch automatic transmissions are used in many vehicles. There have been numerous contributions to approximate clutch modeling over the last three decades; however, there is no complete CFD model available in the open literature. In the following review of clutch modeling, previous studies of squeeze-film flow are surveyed and the various physical characteristics of plate properties, plate motion, and fluid properties are discussed. Finally, some recent applications of wet clutch models are evaluated.

Hays (1963) conducted a theoretical analysis of squeeze-film flow between curved rectangular plates. The analysis used the two-dimensional Reynolds equation, neglecting inertial forces, and investigated the effect of surface curvature on squeeze-film flow. Hays found that when the surface of a plate has concave or convex curvature of a sinusoidal form, the squeeze film load capacity is reduced. Furthermore, it was observed that a convex surface is more sensitive to this effect than a concave surface.

Jackson (1964) studied the dynamics of squeeze flow between two parallel circular plates. He derived analytical solutions for the velocity profile and pressure distribution using an iterative method that included the inertial terms in the momentum equation.

Jackson assumed initially a uniform velocity profile along the rotating axis, and then substituted this profile in the momentum equation. Next, a modified velocity profile from the momentum equation was introduced to the continuity equation. The solution assumed that the squeeze flow is axisymmetric in order to simplify the momentum equation, so the flow velocity is a function of the radius, r and time t. Also, the pressure is a function of r, t and the film thickness y. The resulting solutions for dp/dr include a viscous effect term and two inertial effect terms. The study concluded that if the Reynolds number of the squeeze-flow model is larger than unity, the inertia term becomes dominant.

Moore (1965) summarized the history of studying squeeze-film flow in terms of the effects of inertia, variable viscosity, non-Newtonian fluid behavior, surface tension, dynamic loading, surface roughness and magneto-hydrodynamic effects. Depending on the shape of the flat plate, e.g. round, elliptical or rectangular, the squeeze-flow velocities and load capacity were expressed in terms of the applied force and geometric parameters. Moore found that the velocity corresponding to a round plate has a parabolic profile at any radius r while its mean value increases linearly with increasing r. The maximum pressure for a static load is independent of the squeeze flow clearance h. Furthermore, it was found that at a specified time placing the plate at an angle to the surface or replacing a smooth surface by a rough one decreased the film thickness, as compared to the film thickness corresponding to a parallel plate and the one with a smooth surface. To predict the behavior of rough surfaces, a superposition approach, i.e. a combination of viscous channel flow and bulk flow, and a dimensionless number approach were used.

Many squeeze film problems include asperity contact between two nominally flat surfaces. *Greenwood and Williamson* (1966) studied several contact relations, such as the real area of contact, the number of micro contacts, and the load and the conductance between two flat surfaces associated with the separation of their mean planes.

Greenwood and Williamson also developed a criterion for deformation modes, i.e. plastic or elastic, using a plasticity index. They found that many engineering applications satisfied the assumption for plastic deformation experimentally. In addition, the total area of contact and the number of micro contacts depend on the load only while the separation between two plates depends on the nominal pressure, i.e. the load divided by the nominal contact area.

Wu (1971) developed an analytical model for porous annular disks. For the squeeze film between two rotating disks, the analytical model includes the effects of porosity and inertia due to the centrifugal force using the modified Reynolds and Poisson equations. Wu assumed zero pressure boundary conditions at both the inner and outer radii. The load capacity and pressure distribution we represented in series form. The film thickness and the squeeze time were expressed in integral form. The load capacity and the film pressure between the rotating disks were found to decrease faster than those of non-rotating disks. The relative significance of inertial effects increases as the permeability parameter increases. The criterion for determining whether the inertial effects can be neglected for disks with the same rotating speed was determined. It was found that inertial effects can be considered negligible when the centrifugal force is much smaller than the applied load. Furthermore, increasing the permeability of a rotating porous disk decreases the required time to arrive at a specific film thickness. The effect of the porous media becomes important when the product of the permeability parameter and the inverse cube of the film thickness is greater than 0.001.

Wu (1978) conducted a thorough review of results for squeeze films in the presence of porous boundaries. He compared the load carrying capacities according to the shape of plates for non-rotating disks. The effects of velocity slip, inertia, and magneto-hydrodynamics were discussed. Since the no-slip condition on the porous surface allows velocity discontinuities, the existence of a slip velocity was consid-

ered. It was concluded that because the slip velocity increases the flow rate, the load capacity of the squeeze film is reduced under these conditions.

Patir and Cheng (1978) developed a model based on the averaged Reynolds equation that included the effects of surface roughness. The averaged Reynolds equation uses pressure and flow factors that represent the ratio of the average pressure flow over a rough surface to that over a smooth surface. In addition, a shear flow factor is defined to account for flow transport due to sliding in a rough bearing. This method provided the means for determine the effects of surface roughness on hydrodynamic bearings by introducing flow factors to the averaged Reynolds equation corresponding to the various types of contact area, e.g. longitudinally or transversely oriented surfaces.

Vora and Bhat (1980) studied the load capacity of curved, rotating porous circular plates. They found that the effects of the rotating fluid inertia decrease the load capacity. They also concluded that an increase in permeability increases the load capacity. *Gupta et al.* (1982) analyzed the process in which a rotating curved upper plate with uniform permeability approaches the impermeable flat lower plate. They found that an increase in the rotating speed of the upper plate decreased the load capacity up to a critical curvature value, but at larger curvature values (concave shape) the load capacity increased.

Singh et al. (1990) derived an analytical solution for flow between two parallel circular plates using the approximate Navier-Stokes equations and a similarity transformation. They assumed that the plates move symmetrically with respect to the central axis of the channel. This analytical solution included the effects of inertia. It was found that the load supporting capacity of the fluid film increases as the magnitude of the Reynolds number increases. The authors concluded that the assumption of quasi-steady flow may introduce large errors.

Natsumeda and Miyoshi (1994) developed a numerical solution for the clutch

engagement process including the permeability of the friction plate, the compressive strain and the asperity contact of the friction material. In addition, they solved the equations of heat conduction to model the heat generated by the asperity contact. Furthermore, the conducted experiments with multi-friction plates to measure the torque and temperature variation in the system. They found that during engagement the temperature at the centerline of the separator plates begins to rise from its initial state. Also, it was observed that during the engagement process the temperature at the end of clutch pack was much lower than that between the friction plates although the temperature at the both locations was almost identical prior to engagement. Since the friction material insulates the separator area surrounded by the friction plates, it achieves a higher temperature than that of the separator area, whose one side is in contact with the piston.

Sanda et al. (1995) studied the oil film behavior during an engagement process. They measured directly the flow characteristics near the surface of the friction material of a wet clutch in in an automatic transmission. Small bubbles were observed at the end of the engagement process. Based on these observations, they developed an analytical model for mixed boundary lubrication, which represents the oil film on a contact unit. This theoretical model simplified the complex paper-facing surface to one-dimensional contact units. Using this model, the authors concluded that the friction coefficient decreases as the sliding velocity increases under $5m/s$.

Gnoevoi et al. (1996) solved the Reynolds equations for the flow of a visco-plastic medium assuming that the magnitude of the interpolated distance to the plate was very small, so the inertia terms could be neglected. The reciprocal of the local Saint-Venant number was shown to be sufficient to define all the flow characteristics, i.e. the velocity, pressure and shear stress.

Berger et al. (1996) developed a Finite-Element Model (FEM) model to simultate the engagement of rough, grooved, paper-based permeable wet clutches. A modified

Reynolds equation was adopted from the Patir and Cheng flow model using average flow factors to include surface roughness effects. The Reynolds equation and force balance equations were discretized using the Galerkin approach. The simulation results indicate that increasing the applied force increases the torque peak and decreases the engagement time. Furthermore, the permeability of the friction material affects the magnitude of the increase in torque peak and the corresponding decrease in engagement time. The FEM model radial grooves on the friction material and the computational results showed that an increase in groove width results in a decrease of the torque peak while groove depth only slightly affects the torque. Furthermore, the film thickness decay was shown to be related to increasing the torque peak. However, no comparison between the simulation and available experimental measurements were made. In 1997, to obtain a more efficient solution to the problem, the modified Reynolds equation of *Berger et al.* (1997) was simplified assuming axisymmetric flow, and neglecting the compressive strain of the friction material. The system of Reynolds and force balance equations was reduced to a single, first-order differential equation that resulted in a fast executing model.

Sanni (1997) studied the unsteady squeeze-film flow between rectangular plates and validated the quasi-steady approach for the unsteady solution. He solved the Navier-Stokes equations including the acceleration terms using the Laplace transform. As a result, a modified Reynolds equation was obtained. The effects of unsteadiness on the pressure distribution, load-carrying capacity and velocity fields were studied. According to the interval of Reynolds number, the load capacity for the unsteady squeeze film can be approximated by the corresponding value under steady state conditions for various degrees of accuracy. Furthermore, using sufficient small time steps, the variation of the Reynolds number is small, so the numerical solution based on a force balance can be treated as a quasi-steady state problem. This quasi-steady approach has formed the basis of the present proposed iterative method to achieve

a force balance between the applied force on a moving plate and the internal fluid stresses.

Holgerson (1997) conducted experimental and theoretical studies for wet clutch engagement. The experiments consisted of a single friction plate and a single separator, and the clutch surface temperature was measured using an infrared thermometer. The experimental data indicate that the temperature begins rising during clutch engagement from its initial state very slowly. Furthermore, the maximum temperature occurs at the end of the engagement process in contrast to the maximum derived power, which occurs at about the mid-point of the engagement period.

Bujurke and Naduvinamani (1998) studied the effects of both surface roughness and anisotropic permeability in squeeze flow between rough, porous rectangular plates. They performed an analytical study which found that the maximum load capacity is more sensitive to anisotropic permeability of the friction material than its roughness.

Gethin et al. (1998) developed a numerical model for the squeeze film for circular plates including porous media. They also made extensive comparisons between the numerical results and experimental data. An analytical solution for a simplified version of the problem was derived based on the Reynolds equation and Darcy's law. For the porous media, slip velocity at the was adopted at the surface. The numerical results were achieved by using FEM. Constant loads were applied during the squeeze film experiments, and measurements were made for the pressure at the center of a rigid circular plate and the film gap. The presence of porous media in the squeeze-film flow causes the gap and the pressure to decay rapidly. In particular, the effects of permeability are significant when the fluid film is extremely thin. Furthermore, the pressure in the porous medium decreased to zero while the pressure corresponding to rigid surface was sustained at the lubricant pressure level. The author justified this observation by claiming that it was impossible to achieve complete contact between

parallel smooth surfaces and that viscosity increases at very small values of film thickness. The film gap decay rates of the numerical results were slightly more rapid than the those of the experimental results because the analytical solution of the Gethin at. al study neglected the inertial terms in Goverinig equations.

Olsson et al. (1998) showed the advantages of dynamic friction models with the improvement of controller performance, as compared to static friction models. Actually, dynamic friction models show a certain simplicity compared to static friction models although they include the dynamic aspects of friction. Furthermore, the authors investigated the effect of friction on the clutch engagement process, using the Dahl and Static friction models.

The thermal effects of wet clutch engagement were investigated by *Davis et al.* (2000). Their model used the modified Reynolds equation from *Berger et al.* (1997) and, in addition, included the fluid thermal effects. The variable temperature model showed a longer engagement time and a smaller peak torque than the isothermal model. Comparison of analytical and experimental results showed that inclusion of heat transfer in the model produced results that are closer to the experimental measurements compared to the isothermal model.

For highly viscous incompressible liquid, *Hoffner and Verlag* (2001) showed that pattern of a squeeze flow can be affected by the inclination of the translating plates. The study, based on analytical and experiment results confirmed that the forces generated by a constant displacement velocity using inclined plates are smaller than those obtained with parallel plates.

Fujii et al. (2001a,b) studied the engagement behavior of a wet band brake model. The model included the characteristics of squeeze-film flow, asperity deformation, flow in the porous media, heat transfer and loading pressure distribution caused by a self-energizing mechanism. The results of model showed good agreement with experimental data over a wide range of operating conditions. The effects of temperature,

rotating speed and permeability were almost identical with those reported by *Berger et al.* (1996).

Mansouri et al. (2001) performed simulations of wet clutch engagement including drive torque. In previous studies, the influence of drive torque had not been included although drive torque can affect the temperature pattern of the engagement. Drive torque is continuously transferred from the engine to the wheels during a gear-shift. The temperature of an engagement without drive torque can be higher than an engagement with drive torque. In this study, a dynamic model for frictional brake torque was developed and the friction coefficient was obtained experimentally.

Tatara and Payvar (2002) carried out numerical simulations of a wet clutch during multiple engagements. They employed a zero-flux boundary conditions for heat transfer at the separator mid-plane, where both sides of the separator are covered by friction plates. The temperature of the friction lining face is much higher than the temperatures of either the core-friction interface of the oil outlet. The study concluded that during engagement the temperature of the friction lining face rises more rapidly than that of the core-friction interface.

Hamrock et al. (2004), derived an analytical solution for squeeze flow between parallel plates using the one-dimensional Reynolds equation and assuming the pressure variation along the z-axis and the inertia terms are negligible. This analytical solution is adopted in the present study of a squeeze model and extended with the application of various boundary conditions.

Deur et al. (2005) derived an expression for the pressure distribution and the squeeze flow velocity for a clutch without grooves using the modified Reynolds equation of *Berger et al.* (1996). Also, for a grooved clutch, an ad hoc modeling approach was employed, as the effective fluid film thickness depends on the groove geometry and a direct analytical solution of the squeeze velocity is nearly impossible. A model of the hydrodynamic actuator was developed to explain the initial delay of torque.

Therefore, the friction between the piston and cylinder wall and the resistance of the return spring were included in the dynamic model. An empirical scaling factor for the squeeze velocity equation was applied to obtain an accurate prediction of initial torque delay. The scaling factor is a function of pressure rate of change and the initial rotating speed. Without this empirical scaling factor, the predictive ability of the grooved clutch model was unsatisfactory.

Jang and Khonsari (2011) studied the effects of grooves in a comprehensive transient thermo-hydrodynamic analysis of a wet clutch during the engagement process. Their model included fluid compressibility, surface roughness and permeability of the friction material. The solution procedure of *Jang and Khonsari* (2011) is similar to that of *Jang and Khonsari* (1999). Grooves of radial and waffle shape were additionally investigated. The flow in the grooves was modeled by computational mesh adjustments that reflected the depth of the grooves. The engagement time of grooved models is in general longer than that of non-grooved models because the hydrodynamic pressure in the grooves generates an additional load-carrying capacity. Furthermore, the final film thickness of grooved models is slightly smaller that that of non-grooved models because the contact area is smaller. As the groove depth increases, the engagement time also increases. However, after a critical value, while the groove depth continues to increase, the engagement time decreases. Additionally, increases in the grooved area fraction, lead to increased engagement times. During the engagement process, the effect of the grooves on temperature rise is small because heat is basically generated by asperity contact friction. In general, the temperature rise is proportional to the kinetic energy produced. However, back flow or recirculation flow may take place at the inlet or outlet boundary of the clutch. Since the Jang and Khonsari model uses a modified Reynold's equation that is valid only for very thin oil films, the possibility of using extended boundaries to avoid these improper boundary conditions is limited.

2.3 Multiphase flow

To develop a wet clutch model, several CFD techniques were considered that can capture the physical features of oil flow in a wet clutch, i.e. muti-phase flow, squeeze-film flow, the rotation of the clutch plates, the permeability of the friction plate, heat transfer, the groove geometry of the friction plates, etc. In addition, the Volume of Fluid method (Volume of Fluid (VOF)) for of multi-phase flow was evaluated for use in the open clutch model.

Hirt and Nichols (1981) introduced the VOF method to track free fluid surfaces. Since Lagrangian methods were not appropriate for large surface deformation problems, the VOF was focused on an Eulerian formulation. In the VOF, a single set of momentum equations is shared by both fluids. The fraction of fluid volume in each computational cell is computed and the movement of the free surface is tracked. The fluid in partially filled cells is transported using a conservative form of the advection-diffusion equation. The VOF method has been used to model stratified flows, free-surface flows, filling, sloshing, the motion of large bubbles in a liquid, the motion of water after a dam break, the prediction of jet breakup, and the steady or transient tracking of any liquid-gas interface. The commercial codes FLUENT and Star-CD have used a modified VOF that simulates both oil and air while the original VOF method simulates the free surface between oil and a void. Since the original VOF method simulates one fluid, the free surface interface is sharp and well defined. However, the modified VOF method of FLUENT does not allow for a void region, so each computational cell is assigned a certain volume fraction for each phase and a simple advection scheme is used to track the interface. According to *FLUENT* (2009), the method is very robust, but the interface sharpness tends to deteriorate with time, as numerical diffusion smears the initially sharp front. To maintain a sharp interface for the interface, a fine grid size is required. However, using reconstruction techniques, it is possible to maintain reasonable accuracy provided while keeping the grid resolution

at relatively coarse levels.

Benson (2002) reviewed several volume of fluid interface reconstruction methods for for their differences and strengths. There have been three basic methods to track or reconstruct material interfaces. These are Lagrangian particle methods, level set methods and volume of fluid methods. Lagrangian particle methods may encounter several problems in practice. They do not permit the generation of a new free surface without additional algorithmic development because of limitations in a Lagrangian calculation; Interpolating the particle velocity from the mesh can cause large errors in the boundary motion; Errors from the particle motions can force the boundaries to become tangled; Since the resolution of the boundary can change as the material expands or compresses , an algorithm to add or delete particles is necessary. Level set methods are relatively new. They are similar to contouring algorithms used in computer graphics. A function having a zero contour level set is updated every time step from the velocity field. The method is globally conservative, but not locally. VOF methods reconstruct the material interface based on the volume fractions of the materials, so in general, VOF methods are conservative both locally and globally.

Brennen (2009) evaluated two types of models in disperse flows: trajectory models and two-fluid models. The trajectory models are based on the Euler-Lagrange approach while the two-fluid models are use an Euler-Euler approach. Brennen remarked that two-fluid models require an averaging process since they neglect the discrete nature of the disperse phase and approximate its effect as in a continuous phase. This averaging process involves some difficulties. For example, each averaging volume is assumed to have an infinitesimal volume with dimensions that are much smaller than the distance over which the flow properties vary significantly. At the same time, the averaging volume must be larger then the size of the individual phase elements, so it is very difficult to satisfy these two conditions together. Many efforts have been made to resolve these issues, but there remain significant challenges in

any real multi-phase flow modeling approach. Based on comparisons between SLIC, Hirt-Nichols, Rudman's FCT-VOF and Young's, VOF algorithm, the latter yielded the best overall results.

To construct a multi-phase flow model for the oil-air interface, there are two approaches presented in *FLUENT* (2009). These are the Euler-Lagrange and and the Euler-Euler approach. In *Suzzi et al.* (2009) and *FLUENT* (2009), the Euler-Lagrange approach is used to solve the Navier-Stokes equations for the continuous phase on an Eulerian frame of reference. The disperse phase is tracked explicitly within a Lagrangian frame of reference and Newton's equation of motion is solved for each individual particle. The dispersed phase can exchange momentum, mass and energy with the continuous phase. In the Euler-Euler approach both the continuous (liquid) and dispersed phase (gas bubbles) are solved on a Eulerian frame of reference. The different phases are treated as inter-penetrating continua. The concept of phase volume fraction is defined because the volume of each phase cannot be occupied the other. The Euler-Lagrange approach has a limitation on the volume fraction of the discrete phase. The latter should be sufficiently low ($< 10\%$) because the method was formulated under the assumption that the dispersed phase occupies only a low volume fraction. However, the air volume in a wet open clutch may represent a significant volume fractions as the rotating speed increases. This is due to the fact that the drag torque of a wet clutch decreases rapidly after a critical rotation speed is exceeded. The Euler-Lagrange approach was not considered because the approach has limitations depending on the rotating speed. The Euler-Euler approach of FLUENT makes available three different models: VOF, the mixture model and the Eulerian model. In these models, VOF is a surface tracking technique for immiscible fluids. Since the air volume of a wet clutch is not mixed with oil and the position of the interface between air and oil is important to the design a wet clutch, the VOF model was adopted for multi-phase flow in the present wet clutch model.

CFD models, including multi-phase flow in a wet clutch system have rarely appeared in the literature. A CFD simulation of an open clutch along with experimental validation was conducted by *Aphale et al.* (2006) without, however, considering the effect of air bubbles in the transmission oil. Air bubbles are formed as the relative angular velocity of the friction plate increases, so another CFD model of open clutch characteristics was developed by *Yuan et al.* (2003). This model considers the air bubble effect using the VOF method for multi-phase flow, but is not capable of providing an accurate prediction of dynamic clutch behavior because it only addresses open clutch behavior. Furthermore, the *Yuan et al.* (2003) model made no attempt of imposing realistic boundary conditions or studying their effect on the flow characteristics.

CHAPTER III

Flow Between Rotating Disks

A description of the basic fluid mechanics problem behind clutch engagement is presented in this chapter. Some basic analytical solutions for open clutch and squeeze-film flow are obtained and extended to include alternative boundary conditions. These solutions are used in later chapters to validate the numerical model and establish its accuracy and consistency characteristics before validation with experimental measurements. Furthermore, the analytical solutions for squeeze-film are used to investigate the sensitivity of the results to various boundary conditions.

The analytical solutions in this chapter correspond to simple rotating disk configurations. The associated fluid mechanics problem is formulated after simplifying the Navier-Stokes equations for the simple, axisymmetric geometry encountered in the clutch engagement problem. Under laminar flow conditions, equilibrium is achieved between the dominant forces in the gap between the two disks, and use of cylindrical coordinates leads to a linear problem, whose exact solution is not difficult to find, provided that the boundary conditions are carefully selected.

3.1 Laminar Flow Between a Rotating and a Stationary Disk

Consider the following model for oil flow in an open clutch. As shown in Figure 3.1, the two identical annular discs with inner radius r_1 and outer radius r_2 are separated

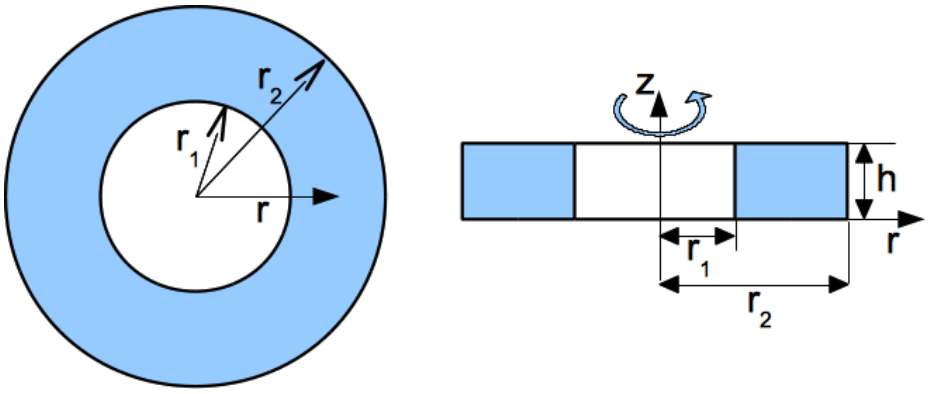

Figure 3.1: Diagram of circular plate model with inlet boundary

by a distance h in the direction of the rotation axis z. The bottom disk is stationary with its plane perpendicular to the rotation axis $z = 0$. The upper disk is parallel to the bottom disk and rotating with a constant speed, ω. The gap h is constant along the radial distance r, which is measured from the center of the annuli, and is assumed to be completely filled with an incompressible viscous fluid.

The rotation of the upper disk sets the fluid in the gap in motion due to the no-slip condition at the the surface of the disks. Typically, the gap h is very small for clutch disks, so the boundary layer is fully developed and, under steady-state, axisymmetric flow conditions, the Navier-Stokes equations are considerably simplified. *Hori* (2006) derived the simplified momentum equations using cylindrical coordinates, as follows

$$\mu \frac{\partial^2 v_r}{\partial z^2} = \frac{p}{r} - \frac{\rho v_\theta^2}{r} \tag{3.1a}$$

$$\mu \frac{\partial^2 v_\theta}{\partial z^2} = \frac{1}{r} \frac{\partial p}{\partial \theta} \tag{3.1b}$$

where ρ is fluid density, μ is fluid viscosity, p is pressure, v_r is the velocity component in the radial direction r and v_θ is the velocity component in the tangential direction θ. Equations (3.1a) and (3.1b) show that as the upper disk rotates, the pressure gradient in fluid is balanced by viscous stresses resulting in a steady radial flow.

Conservation of mass for an incompressible fluid can be written in cylindrical coordinates as follows

$$\frac{1}{r}\frac{\partial}{\partial r}\left(rv_r\right) + r\frac{\partial v_r}{\partial z} = \frac{1}{r}v_r + \frac{\partial v_r}{\partial r} + r\frac{\partial v_r}{\partial z} = 0 \tag{3.2}$$

Due to the no-slip condition, the boundary conditions for the flow between the two disks considered in the present case are as follows

$$\begin{aligned} v_\theta &= r\omega \text{ at } z = h \\ v_\theta &= 0 \text{ at } z = 0 \\ v_r &= 0 \text{ at } z = 0 \text{ and } z = h \end{aligned} \tag{3.3}$$

Since the present simplified model corresponds to axisymmetric flow of a thin oil film, several assumptions can be made regarding the variation of the pressure and film thickness, as follows,

$$\frac{\partial p}{\partial \theta} = 0 \qquad \frac{\partial p}{\partial z} = 0 \qquad \frac{\partial h}{\partial \theta} = 0 \tag{3.4}$$

The pressure varies only in the radial direction. The associated inlet and outlet boundaries are assumed to be at atmospheric conditions, so

$$p(r_1) = p(r_2) = 0 \tag{3.5}$$

Substitution of Eq. (3.4) in Eq. (3.1) leads to the following simplification

$$\mu\frac{\partial^2 v_\theta}{\partial z^2} = \frac{1}{r}\frac{\partial p}{\partial \theta} = 0 \tag{3.6}$$

Integration of Eq. (3.6) using the boundary conditions (3.3) leads to the following

expression for the tangential velocity

$$v_\theta = \frac{\omega}{h} r z \tag{3.7}$$

Substituting Eq. (3.7) into Eq. (3.1) yields the following differential equation for the radial velocity

$$\mu \frac{\partial^2 v_r}{\partial z^2} = \frac{\partial p}{\partial r} - \frac{\rho r \omega^2}{h^2} z^2 \tag{3.8}$$

Integrating Eq. (3.8) under the boundary conditions (3.3) yields the following expression for the radial velocity

$$v_r = \frac{z^2}{2\mu}\frac{dp}{dr} - \frac{\rho r \omega^2}{12\mu h^2} z^4 + \frac{z}{\mu}\left(\frac{\rho r \omega^2 h}{12} - \frac{h}{2}\frac{dp}{dr}\right) = \left(\frac{z^2 - zh}{2\mu}\right)\frac{dp}{dr} - \frac{\rho r \omega^2}{12\mu}\left(\frac{z^4}{h^2} - zh\right) \tag{3.9}$$

Next, substituting Eq. (3.9) into Eq. (3.2) we obtain

$$\left(\frac{z^2 - zh}{2\mu r}\right)\frac{1}{r}\frac{d}{dr}\left(r\frac{dp}{dr}\right) - \frac{\rho\omega^2}{6\mu}\left(\frac{z^4}{h^2} - zh\right) + \frac{\partial v_z}{\partial z} = 0 \tag{3.10}$$

Integrating Eq. (3.10) over z and enforcing the boundary conditions $v_z = 0$ at $z = 0$ and $z = h$ yields the axial velocity, as follows

$$v_z = \left(\frac{-2z^3 + 3z^2 h}{12\mu}\right)\frac{1}{r}\frac{d}{dr}\left(r\frac{dp}{dr}\right) + \frac{\rho\omega^2}{6\mu}\left(\frac{z^5}{5h^2} - \frac{z^2 h}{2}\right) \tag{3.11}$$

However, since $v_z = 0$ at both $z = 0$ and $z = h$, Eq. (3.11) becomes an ordinary differential equation for the pressure, i.e

$$\frac{1}{r}\frac{d}{dr}\left(r\frac{dp}{dr}\right) = \frac{3}{5}\rho\omega^2 \tag{3.12}$$

Now under the boundary condition (3.5), integrating Eq. (3.12) yields the pressure

variation in the gap, i.e.

$$p = \frac{3}{20}\rho\omega^2 r^2 - \frac{3}{20}\rho\omega^2 \frac{{r_1}^2 - {r_2}^2}{\ln(r_1) - \ln(r_2)} \ln(r) + \frac{3}{20}\rho\omega^2 \frac{{r_1}^2 \ln(r_2) - {r_2}^2 \ln(r_1)}{\ln(r_1) - \ln(r_2)} \tag{3.13}$$

In Eqs. (3.9) and (3.11), the derivative of the pressure is needed, so Eq. (3.13) is differentiated with respect to r to yield

$$\frac{dp}{dr} = \frac{3}{10}\rho\omega^2 r - \frac{3}{20}\rho\omega^2 \frac{{r_1}^2 - {r_2}^2}{\ln(r_1) - \ln(r_2)} \frac{1}{r} \tag{3.14}$$

Finally, the volume flow rate Q is obtained by integrating the radial velocity over the gap thickness, as follows

$$Q = 2\pi r \int_{z=0}^{z=h} v_r dz = \frac{\pi h^3 \rho\omega^2}{4\mu} \frac{r_1^2 - r_2^2}{\ln(r_1) - \ln(r_2)} \tag{3.15}$$

It is clear from Eq. (3.15) that when atmospheric (zero gauge) pressure conditions are specified at the inlet and outlet boundaries, Q is determined solely by the radial fluid motion driven by the centrifugal force.

The results of the analytical solution are shown in Figure 3.2 for $h = 0.19\ mm$, $r_1 =$ from 5 mm to 88 mm, $r_2 = 94\ mm$ and $\omega = 100\ rad/s$. As shown in Figure 3.2(a), the magnitude of the axial velocities v_a varies along the axial direction and the velocity profiles are almost similar at different radial distances r. The radial velocities v_r on the other hand depend strongly on r. At the inlet, v_r achieves its peak value while it becomes negative near the outlet. This means that with a small inner radius, back flow can develop at the outlet area. Figure 3.2(b) shows the pressure profiles in an open clutch as a function of dimensionless radial distance $\tilde{r} = (r - r_1)/(r_2 - r_1)$. The pressure assumes a negative value under open clutch flow conditions, which indicates that the two disks are forced closer to each other. Notice that the peak pressure location moves towards the inner radius r_1 and the pressure profiles become skewed

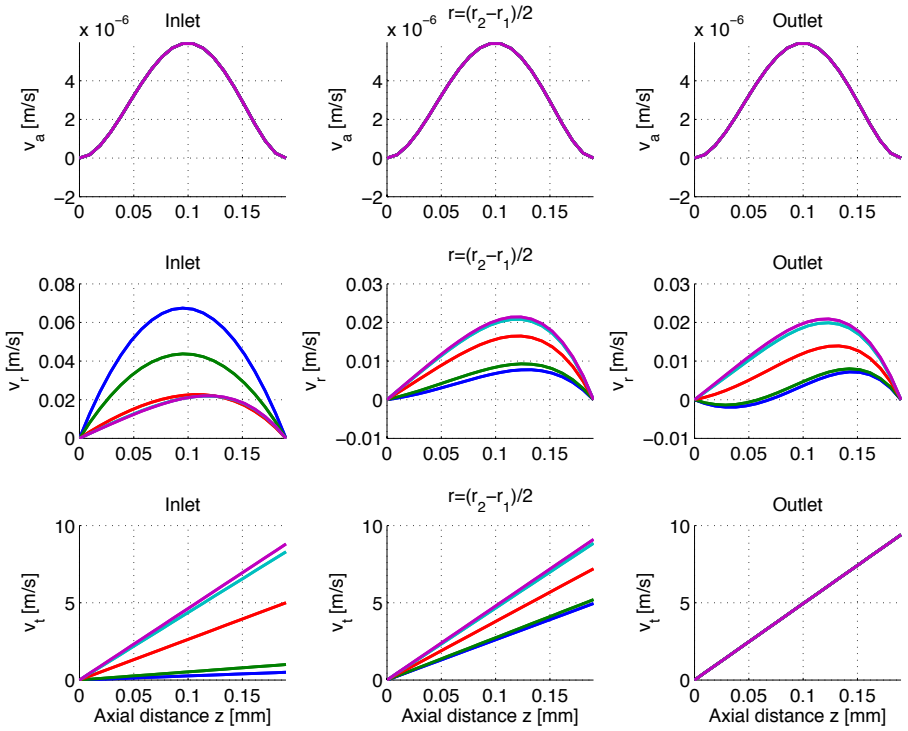

(a) Velocity profiles

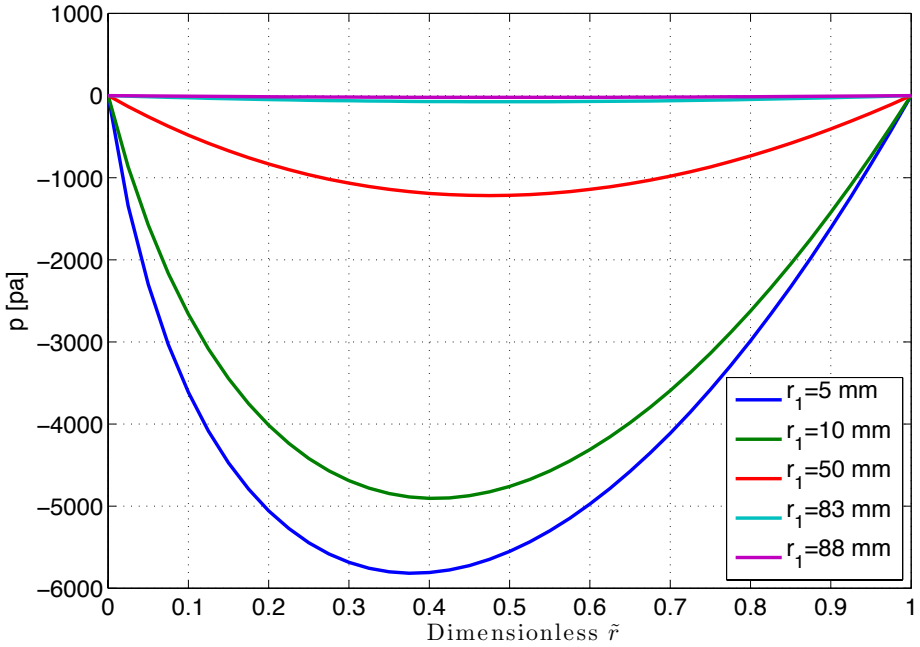

(b) Pressure profiles for dimensionless $\tilde{r}$

Figure 3.2: Velocity and pressure profiles for open clutch at $\omega = 100\ rad/s$

as r_1 decreases.

3.1.1 Forced Flow rate

In the case that the volume flow rate Q is externally specified, the relationship between the internal fluid force F_{fluid}, Q and h is analytically established. This relationship is used in Chapter VI for validation of the numerical solution using experimental data.

From Eq. (3.8), the volume flow rate Q can be expressed as follows

$$\begin{aligned} Q &= 2\pi r \int_{z=0}^{z=h} v_r dz \\ &= 2\pi r \int_{z=0}^{z=h} \left[\left(\frac{z^2 - zh}{2\mu} \right) \frac{dp}{dr} - \frac{\rho r \omega^2}{12\mu} \left(\frac{z^4}{h^2} - zh \right) \right] dz \\ &= 2\pi r \left(-\frac{h^3}{12\mu} \frac{dp}{dr} + \frac{\rho r \omega^2}{40\mu} h^3 \right) \end{aligned} \tag{3.16}$$

Equation (3.16) can be rearranged to yield the pressure gradient, i.e.

$$\frac{dp}{dr} = -\frac{6\mu Q}{\pi h^3} \frac{1}{r} + \frac{3\rho r \omega^2}{10} \tag{3.17}$$

Using the atmospheric pressure boundary conditions, this is easily integrated to yield an expression for the internal fluid pressure, as follows

$$p = \frac{6\mu Q}{\pi h^3} \ln(\frac{r_2}{r}) + \frac{3\rho \omega^2}{20} (r^2 - r_2^2) \tag{3.18}$$

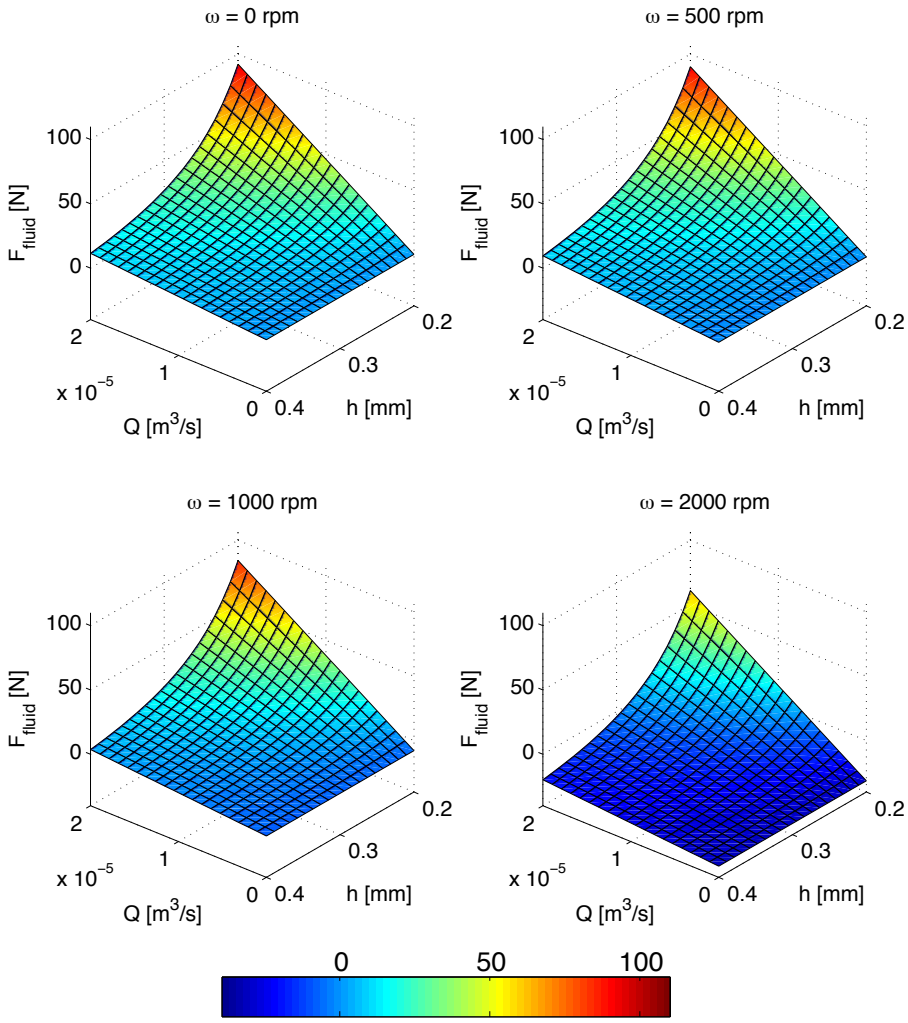

Figure 3.3: 3D surface plot for F_{fluid}, Q and h

Finally, the fluid force, F_{fluid}, can be expressed in the terms of Q and h as follows

$$\begin{aligned} F_{fluid} &= 2\pi \int_{r_1}^{r_2} prdr \\ &= \frac{12\mu Q}{h^3}\left[\frac{1}{2}\ln(r_2)({r_2}^2 - {r_1}^2) - \left\{\frac{1}{2}({r_2}^2\ln(r_2) - {r_1}^2\ln(r_1)) - \frac{1}{4}({r_2}^2 - {r_1}^2)\right\}\right] \\ &+ \frac{3\pi\rho\omega^2}{40}(2r_1^2r_2^2 - r_1^4 - r_2^4) \end{aligned} \tag{3.19}$$

Figure 3.3 shows the relationship between F_{fluid}, Q and h based on Eq. (3.19) for $\mu = 0.055266\ [kg/m \cdot s]$ and $\rho = 842\ [kg/m^3]$. F_{fluid} is proportional to Q while an

increase in h reduces F_{fluid}. Also, for high rotating speeds, ω, F_{fluid} assumes negative values when $h >> 0$. This indicates that the initial fluid force may have either negative or positive values, if the the flowrate is maintained constant throughout the engagement mode. Therefore, if a constant Q is specified, when the squeeze motion of the engagement process begins, the required applied force, F_{app}, can be varied according to the rotating speed ω.

Notice that in Eq. (3.19), when $F_{fluid} = 0$, the relationship between h, Q and ω can be expressed as follows

$$\frac{Q}{h^3\omega^2}\frac{\mu}{\rho} = \Omega \tag{3.20}$$

where

$$\Omega = -\frac{\pi}{160}\frac{2r_1^2r_2^2 - r_1^4 - r_2^4}{\left[\frac{1}{2}\ln(r_2)({r_2}^2 - {r_1}^2) - \left\{\frac{1}{2}({r_2}^2\ln(r_2) - {r_1}^2\ln(r_1)) - \frac{1}{4}({r_2}^2 - {r_1}^2)\right\}\right]}$$

If $\frac{Q}{h^3\omega^2}\frac{\mu}{\rho} > \Omega$, F_{fluid} remains positive. Otherwise, F_{fluid} becomes negative. Figure 3.4 shows the relationship between Q and ω varying h as a parameter from 0.2 mm to 0.4 mm. Notice that the upper part of each curve corresponds to negative F_{fluid} values while the lower part of the curve indicates a positive fluid force.

3.2 Laminar Flow Between a Stationary Disk and an Axially Moving Disk

We consider now the case in which the upper disk motion is restricted to the axial direction, i.e. squeeze motion only. The problem now corresponds to thin film lubrication at low Reynolds numbers, and a well-known simplified equation can be used to describe the flow *Hamrock et al.* (2004)

$$\frac{\partial}{\partial x}(\frac{\rho h^3}{12\mu}\frac{\partial p}{\partial x}) + \frac{\partial}{\partial y}(\frac{\rho h^3}{12\mu}\frac{\partial p}{\partial y}) = \frac{\partial(\rho h)}{\partial t} \tag{3.21}$$

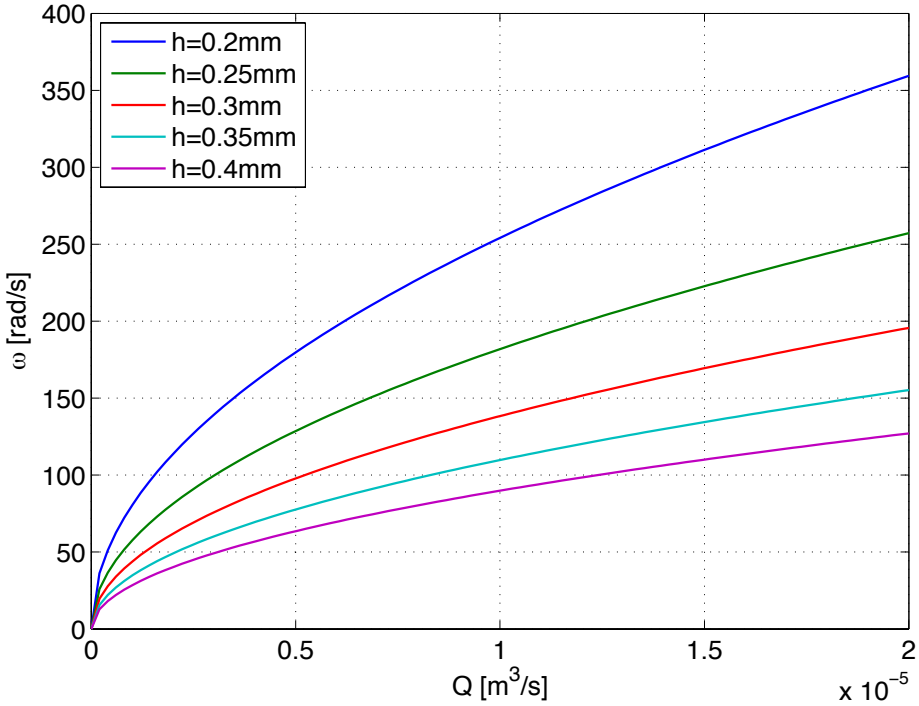

Figure 3.4: Q VS ω plot for $h = 0.2\ mm$ to $0.4\ mm$

where h is fluid film thickness, x, y are the Cartesian coordinates and t is time.

This is known as the Reynolds equation. It is derived from the Navier-Stokes and continuity equations, and describes the pressure and flow behavior in fluid film lubrication assuming incompressible flow with negligible acceleration. The squeeze motion is the result of an externally applied force, which may be a function of time. As a result, the analytical solution for squeeze-flow films are now time dependent, in contrast to the stationary flow solution of Section 3.1.

3.2.1 Annular Plate Model with Inlet Boundary

In the following sections, the disk geometry of Figure 3.1 is used; however, the translational motion of the upper disk is added as one of the boundary conditions. The motivation is once again to derive analytical solutions for validation of the CFD model. Whether the solution is numerical or exact, it is very difficult to specify

physically realistic boundary conditions in an actual wet clutch system that can be used to support the development of a high fidelity, multi-physics CFD model. In general, the true boundary conditions are either unknown or very poorly defined. To this purpose, various analytical solutions for annular plate squeeze-film flow are examined. These correspond to three types of boundary conditions at the inlet and outlet surfaces, i.e. Dirichlet, mixed and specified pressure profile conditions.

3.2.1.1 Dirichlet boundary condition

In cylindrical coordinates, the Reynolds Equation, i.e. (3.21), can be written as follows

$$\frac{\partial}{\partial r}(rh^3\frac{\partial p}{\partial r}) = 12\mu r\frac{\partial h}{\partial t} \tag{3.22}$$

Typically, the analytical solutions for squeeze-film flows given by *Hays* (1963); *Moore* (1965); *Wu* (1971, 1978); *Berger et al.* (1996); *Deur et al.* (2005); *Hamrock et al.* (2004) assume zero pressure at the inlet and outlet boundaries, which is considered a Dirichlet boundary condition for the pressure. Although this is acceptable for idealized flow between annular plates immersed in oil, an automotive wet clutch may require more general specifications at the boundaries, including non-zero pressure levels. In the following, we impose non-zero, constant pressure boundary conditions at the inlet boundary and outlet boundaries to obtain several new analytical solutions. Specifically, we set

$$p(r_1) = p_1 \qquad p(r_2) = p_2 \tag{3.23}$$

Additionally, we assume for simplicity that the applied force profile increases linearly with time, i.e.

$$F_{app} = at + b \tag{3.24}$$

Under these conditions, the Reynolds equation can be integrated twice with respect to r. Then, under the boundary conditions (3.23), the pressure variation is

given by

$$p = \frac{3\mu}{h^3}\frac{\partial h}{\partial t}(r^2 + \beta_1 \ln r + \beta_2) + \eta_1 \ln r + \eta_2 \tag{3.25}$$

where

$$\begin{aligned}
\beta_1 &= -\frac{r_1^2 - r_2^2}{\ln r_1 - \ln r_2} \\
\beta_2 &= \frac{r_1^2 \ln r_2 - r_2^2 \ln r_1}{\ln r_1 - \ln r_2} \\
\eta_1 &= \frac{p_1 - p_2}{\ln r_1 - \ln r_2} \\
\eta_2 &= \frac{p_1 \ln r_2 - p_2 \ln r_1}{\ln r_2 - \ln r_1}
\end{aligned}$$

The externally applied force F_{app} and the internal fluid force F_{fluid}, which is calculated by integrating the fluid pressure between the plates, must be balanced. Hence the applied force can be expressed by the integration of fluid pressure as follows

$$F_{app} = F_{fluid} = \int_{r_1}^{r_2} 2\pi p r \, dr = 2\pi \int_{r_1}^{r_2} [\frac{3\mu}{h^3}\frac{\partial h}{\partial t}(r^3 + \beta_1 r \ln r + \beta_2 r) + \eta_1 r \ln r + \eta_2 r] \, dr \tag{3.26}$$

After rearranging Eq. (3.26) for $\partial h/\partial t$, the squeeze velocity of a circular plate with an inlet boundary can be written as follows

$$\frac{\partial h}{\partial t} = \frac{h^3 F_{app}}{6\pi\mu}\frac{1}{M} \; - \frac{h^3 A}{6\pi\mu}\frac{1}{M} \tag{3.27}$$

where

$$\begin{aligned}
M &= \frac{1}{4}(r_2^4 - r_1^4) + \beta_1[\frac{1}{2}(r_2^2 \ln r_2 - r_1^2 \ln r_2) - \frac{1}{4}(r_2^2 - r_1^2)] + \frac{1}{2}\beta_2(r_2^2 - r_1^2) \\
A &= 2\pi\{\eta_1[0.5(r_2^2 \ln r_2 - r_1^2 \ln r_1) - 0.25(r_2^1 - r_1^2)] + 0.5\eta_2(r_2^2 - r_1^2)\}
\end{aligned}$$

Then, integrating Eq. (3.27) by separation of variables yields

$$\int_0^t \left(\frac{F_{app}}{6\pi\mu M} - \frac{A}{6\pi\mu M}\right) dt = \int_0^t \left(\frac{F_{app}(at+b)}{6\pi\mu M} - \frac{A}{6\pi\mu M}\right) dt = \int_{h_0}^{h} \frac{1}{h^3}\, dh \tag{3.28}$$

After rearranging the solution of Eq. (3.28), the film thickness h can be expressed as follows

$$h = \left[-\frac{at^2}{6\pi\mu M} + \frac{1}{h_0^2} + \frac{At}{3\pi\mu M} - \frac{bt}{3\pi\mu M}\right]^{-1/2} \tag{3.29}$$

where h_0 is the initial film thickness.

Since in the present case the volume flow rate Q at the inlet and outlet boundaries is equal to the volume change by the moving wall, Q must given by

$$Q = -\pi(r_2^2 - r_1^2)\frac{\partial h}{\partial t} \tag{3.30}$$

In Figures 3.5, 3.6, and 3.7, the analytical solution is shown for various Dirichlet boundary conditions. The newly derived solutions are also compared with the analytical solution from *Berger et al.* (1996), where zero-pressure boundary conditions were assumed. The solution at $p_1 = 0$ and $p_2 = 0$ agrees well with Berger's solution. From Figure 3.5, in the case of $p_1 \geq p_2$ and $p_2 = 0$, the reduction in h is slowed down, as p_1 increases. If p_1 is given large values, the solutions for h and dh/dt become erratic. At the other end, as shown in Figure 3.6, when $p_1 \leq p_2$ and $p_1 = 0$, the increase in p_2 causes h to decrease more rapidly. Finally, as shown in Figure 3.7, specifying the same non-zero values for p_1 and p_2 results in unrealistic solutions.

3.2.1.2 Mixed boundary condition

To investigate another possibility for boundary condition of squeeze-film flow, a mixed boundary condition is considered. The mixed boundary condition consists of a Neumann boundary condition at the inlet and a Dirichlet boundary condition at

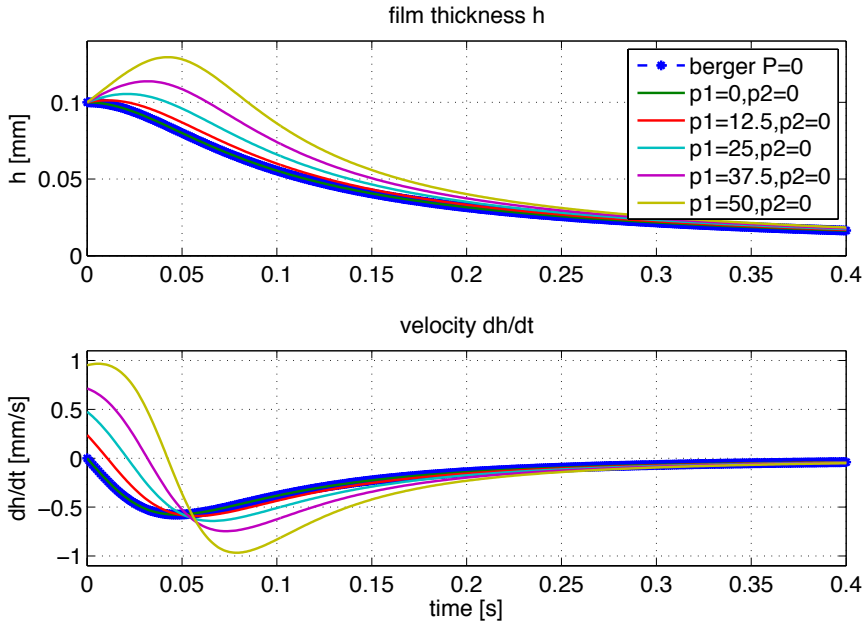

Figure 3.5: Oil film thickness and squeeze velocity when $p_1 \geq p_2 = 0$

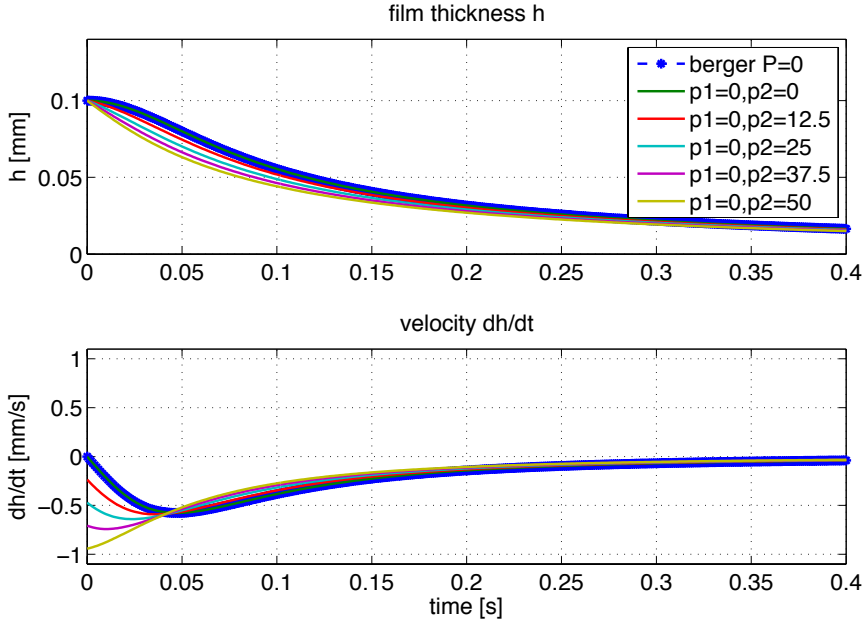

Figure 3.6: Oil film thickness and squeeze velocity when $p_1 \leq p_2 = 0$

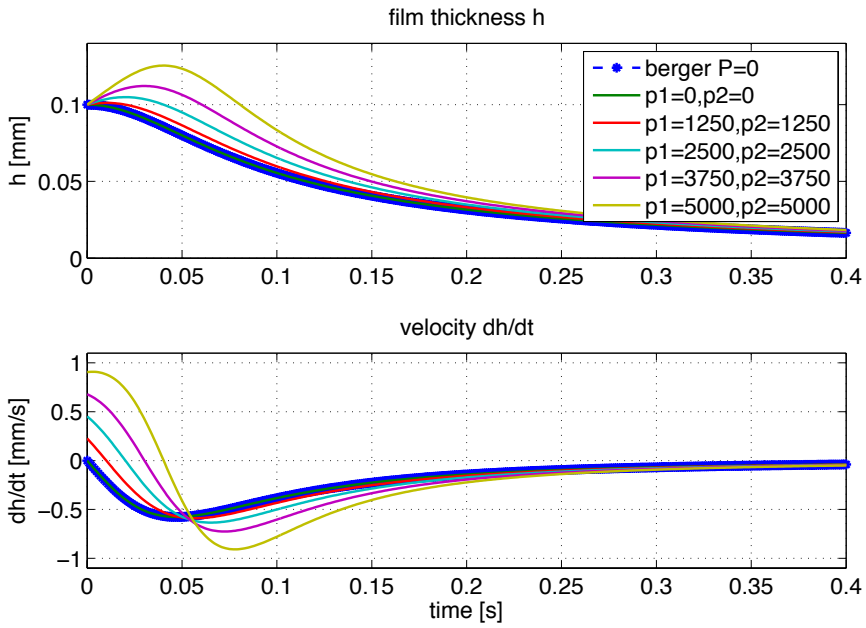

Figure 3.7: Oil film thickness and squeeze velocity when $p_1 = p_2 = 0$

the outlet, as follows

$$\frac{\partial p}{\partial r}|_{r=r_1} = k \qquad \text{and} \qquad p(r_2) = p_2 \tag{3.31}$$

where k is a constant. Following the same procedure as in 3.23, the pressure distribution can be obtained after integrating Eq. (3.22) using Eq. (3.24) and the mixed boundary condition (3.31), as follows

$$p = \frac{3\mu}{h^3}\frac{\partial h}{\partial t}(r^2 - r_2^2 - 2r_1^2 \log r + 2r_1^2 \log r_2) + (kr_1 \log r - kr_1 \log r_1 + p_2) \tag{3.32}$$

Then, since the force balance between the applied force F_{app} and the fluid force F_{fluid} is satisfied, after integrating Eq. (3.32), the squeeze velocity can be written as follows

$$\frac{\partial h}{\partial t} = (\frac{F_{app}}{2\pi} - g_5)\frac{h^3}{g_4} \tag{3.33}$$

Then, following integration of Eq. (3.33) by separation of variables, the film

thickness is given by

$$h = 1/\sqrt{2g_5 t/g4 - (0.5at^2 + bt)/(\pi g_4) + 1/h_0^2} \tag{3.34}$$

where

$$\begin{aligned}
F_{app} &= at + b \\
g_1 &= 0.25(r_2^4 - r_1^4) \\
g_2 &= 0.5(r_2^2 \log r_2 - r_1^2 \log r_1) - 0.25(r_2^2 - r_1^2) \\
g_3 &= 0.5(r_2^2 - r_1^2) \\
g_4 &= 3\mu(g_1 - 2r_1^2 * g_2 - r_2^2 g_3 + 2r_1^2 \log r_2 g_3) \\
g_5 &= -(-kr_1 g_2 - p_2 g_3 + kr_1 \log r_2 g_3)
\end{aligned}$$

Furthermore, consider the case in which $k = 0$ and $p_2 = 0$ The expression for pressure at the inlet boundary can be written as follows

$$p(r = r_1) = \frac{3\mu}{h^3}\frac{\partial h}{\partial t}(r_1^2 - r_2^2 - 2r_1^2 \log r_1 + 2r_1^2 \log r_2) \tag{3.35}$$

In Figure 3.8, the solution results between Dirichlet ($p_1 = 0$, $p_2 = 0$) and Mixed ($dp_1/dr = 0$, $p_2 = 0$) boundary conditions are compared. The decrease in h for the Mixed boundary condition is clearly slower than that corresponding to the Dirichlet boundary condition. This is due to the fact that the inlet pressure p_1 under the Mixed boundary condition increases with time. When the boundary values change with time, the impact on h is more pronounced when compared to the case of a constant Dirichlet boundary condition.

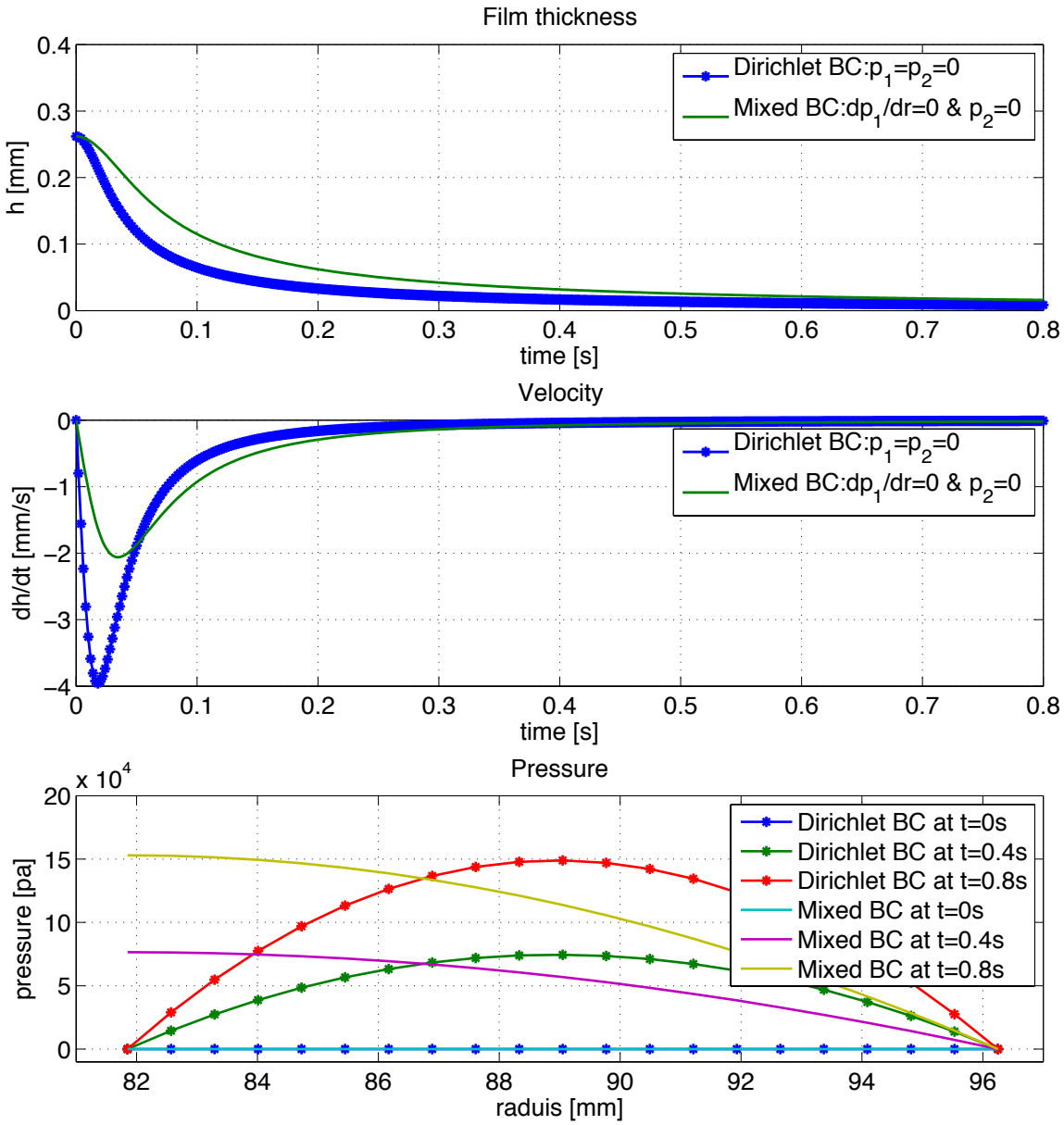

Figure 3.8: h, dh/dt and p comparison: Dirichlet BC VS Mixed BC

3.2.1.3 Pressure profile boundary from Neumann boundary

When boundary conditions are specified in connection to a CFD model for wet clutch engagement, a specified pressure boundary condition at the inlet or outlet boundary produces more stable results than Neumann boundary conditions. Therefore, an equivalent pressure profile corresponding to the Neumann condition at the boundary needs to be derived using the analytical solution of the previous section that was based on the mixed boundary condition.

At the inlet area, the pressure relationship for a mixed boundary condition, i.e. Eq. (3.35) can be rewritten as follows

$$p(r_1) = \frac{3\mu}{h^3}\frac{\partial h}{\partial t}(r_1^2 - r_2^2 - 2r_1^2 \log r_1 + 2r_1^2 \log r_2) = \frac{3\mu}{h^3}\frac{\partial h}{\partial t} J_1 \tag{3.36}$$

where

$$J_1 = r_1^2 - r_2^2 - 2r_1^2 \log r_1 + 2r_1^2 \log r_2$$

The inlet pressure, $p(r_1)$ can then be modified by using a gain factor, e.g. α. The outlet pressure $p(r_2)$ remains always zero, so the boundary conditions are written as follows

$$p_1 = \alpha \frac{3\mu}{h^3}\frac{\partial h}{\partial t} J_1, \qquad p_2 = 0 \tag{3.37}$$

Substituting the inlet and outlet pressures (3.37) into Eq. (3.25) as Dirichlet boundary conditions at the inflow and outflow sections, the solution for pressure becomes

$$p = \frac{3\mu}{h^3}\frac{\partial h}{\partial t}(r^2 + \beta_1 \log r + \beta_2 + \gamma_1 \ln r + \gamma_2) \tag{3.38}$$

where

$$\beta_1 = -\frac{r_1^2 - r_2^2}{\ln r_1 - \ln r_2}$$
$$\beta_2 = \frac{r_1^2 \ln r_2 - r_2^2 \ln r_1}{\ln r_1 - \ln r_2}$$
$$\gamma_1 = \frac{3\mu}{h^3}\frac{\partial h}{\partial t}\frac{J_1}{\ln r_1 - \ln r_2}$$
$$\gamma_2 = \frac{3\mu}{h^3}\frac{\partial h}{\partial t}\frac{J_1 \ln r_2}{\ln r_2 - \ln r_1}$$

Following integration of Eq. (3.38) with respect to r and rearranging, the squeeze velocity can now be written as follows

$$\frac{\partial h}{\partial t} = \frac{h^3 F_{app}}{6\pi\mu}\frac{1}{N} \tag{3.39}$$

where

$$N = \frac{1}{4}(r_2^4 - r_1^4) + \beta_3[\frac{1}{2}(r_2^2 \ln r_2 - r_1^2 \ln r_2) - \frac{1}{4}(r_2^2 - r_1^2)] + \frac{1}{2}\beta_4(r_2^2 - r_1^2)$$
$$\beta_3 = \beta_1 + \frac{J_1}{\ln r_1 - \ln r_2}$$
$$\beta_4 = \beta_2 + \frac{J_1 \ln r_2}{\ln r_2 - \ln r_1}$$

Finally, when $F_{app} = at + b$, integration of Eq. (3.39) yields the film thickness as follows

$$h = \left[-\frac{at^2}{6\pi\mu N} + \frac{1}{h_0^2} - \frac{bt}{3\pi\mu N}\right]^{-1/2} \tag{3.40}$$

3.2.2 Annular Plate Model without Inlet Boundary

To validate the CFD model for squeeze-film flow, we simplify the geometric configuration further. In this set-up we consider squeeze-film flow between two disks without a center inlet.

As shown in Figure 3.9, two parallel circular plates are separated by a gap h similar

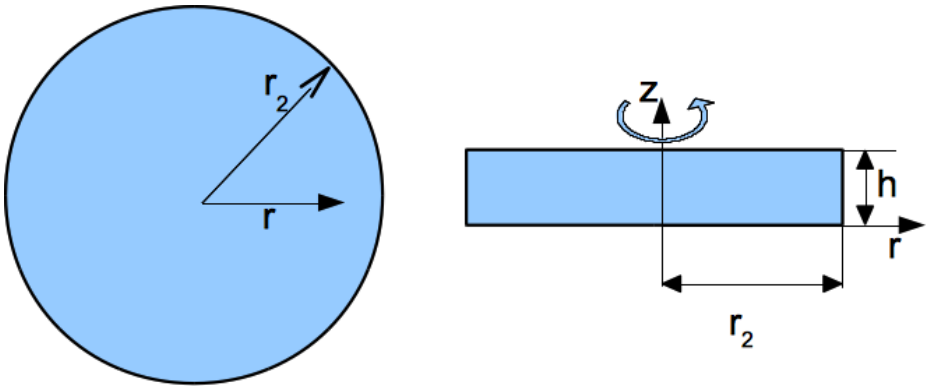

Figure 3.9: Diagram of circular plate model without inlet boundary

to the problem of Figure 3.1, but with no center inlet. In cylindrical coordinates, the Reynolds equation has the same form with Eq. (3.22). However, since there is no inlet boundary and the flow is symmetric along the center line of the disk, the boundary conditions are defined as follows

$$p = 0 \; at \; r = r_2 \qquad \frac{\partial p}{\partial r} = 0 \; at \; r = 0 \tag{3.41}$$

Then, integration of Eq. (3.22) leads to following solution for the pressure profile

$$p = \frac{3\mu}{h^3}\frac{\partial h}{\partial t}(r^2 - r_2^2) \tag{3.42}$$

Furthermore, if the applied force increases linearly with time, i.e. $F_{app} = at$, the squeeze velocity $\frac{\partial h}{\partial t}$ can be calculated using the force balance, as follows

$$\frac{\partial h}{\partial t} = -\frac{2F_{app}h^3}{3\pi\mu r_2^4} \tag{3.43}$$

Integration of Eq. (3.43) leads to the film thickness h as a function of time, i.e.

$$\therefore h = \left[\sqrt{\frac{2a}{3\pi\mu r_2^4}t^2 + \frac{1}{h_0^2}}\right]^{-1/2} \tag{3.44}$$

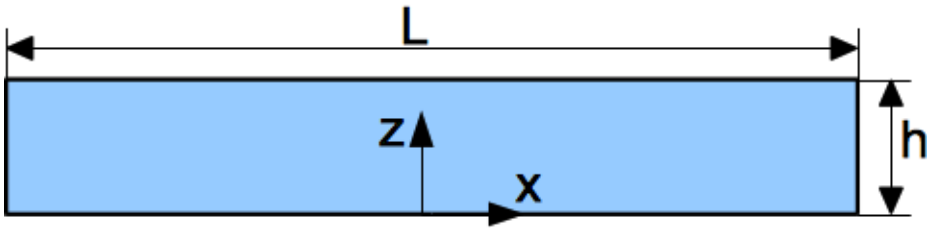

Figure 3.10: Diagram of 2-D rectangular model

Finally, the volume flow rate Q is found to be equal to the volume change due to the squeeze velocity, so Q becomes

$$Q = -\pi r_2^2 \frac{\partial h}{\partial t} \tag{3.45}$$

3.2.3 2-D Rectangular Plate Model

The final analytical solution considered in this work is actually the simplest. When validating numerical models, it is often desirable to establish the algorithmic characteristics of a model by the purest of applications. In particular, to avoid masking of errors due to using a radially symmetric computational grid, it is wise to validate the model using a simple rectangular plate and a Cartesian grid. The geometric configuration is shown in Figure 3.10. Two identical rectangular plates are initially separated by film with thickness h. Then, the gap is reduced by application of an external force. The fluid moves in the x direction only, as the boundaries in the transverse direction are impermeable. In this case, the Reynolds equation (3.22) is reduced to the following

$$\frac{\partial}{\partial x}\left(\frac{\rho h^3}{12\mu}\frac{\partial p}{\partial x}\right) = \frac{\partial(\rho h)}{\partial t} \tag{3.46}$$

Since there is no inlet boundary and the flow is symmetric with respect to the z

axis, the boundary conditions can be defined as follows

$$p = 0 \; at \; x = \pm\frac{L}{2} \qquad \frac{\partial p}{\partial x} = 0 \; at \; x = 0 \tag{3.47}$$

After the Reynolds equation is integrated twice with respect to x, the pressure distribution is found to be as follows

$$p = \frac{3\mu}{2h^3}(L^2 - 4x^2)(-\frac{\partial h}{\partial t}) \tag{3.48}$$

The squeeze velocity can be computed as before by balancing the external and internal forces. Integration of Eq. (3.48) leads to

$$F_{app} = at = \int_0^L bp \, dx = \int_0^L -b(\frac{\partial h}{\partial t})\frac{3\mu}{2h^3}(L^2 - 4x^2) \, dx$$

where b is the with of the plates. Then, the squeeze velocity $\frac{\partial h}{\partial t}$ can be obtained, as follows

$$\frac{\partial h}{\partial t} = -\frac{Fh^3}{b\mu L^3} \tag{3.49}$$

Integrating Eq. (3.49) by separation of variables leads to

$$\int_0^t F_{app} \, dt = -\int_{h_0}^h \frac{h^3}{b\mu L^3} \, dh \tag{3.50}$$

Also, since the volume flow rate Q is proportional to the squeeze velocity, Q can be expressed as follows

$$\therefore Q = -b\frac{\partial h}{\partial t}L \tag{3.51}$$

Thus, if the applied force is $F_{app} = at$, the film thickness is given as a function of

time by the following expression

$$h = \left[\sqrt{\frac{a}{b\mu L^3} t^2 + \frac{1}{h_0^2}} \right]^{-1/2} \tag{3.52}$$

CHAPTER IV

Computational Model Setup

The goal of the present research is to develop a multi-physics model that can form the basis for analysis and design of advanced automatic transmission systems. The proposed model involves multi-dimensional, multi-phase flow and heat transfer in a rotating computational frame. In addition, a deforming grid is necessary to capture the translational disk movement and changing oil film thickness during clutch engagement. The grid resolution needs to be sufficiently high to model accurately the flow in the grooves of the friction material. The latter is also undergoing deformation during engagement resulting in additional flow of oil through the porous media. Finally, solid contact between the disks must be included, if a realistic model of clutch engagement is desired.

All of the aforementioned processes have previously been successfully addressed individually by various investigators and do not represent topics of original research. It is therefore their combination in a single model that poses a new challenge rather than the reproduction of the distinct modules of the model. Furthermore, for the present model to become a tool that is easy to adopt in industrial design, a widely accepted platform needs to be available for training and support of future users. For this reason, it was decided to base the model on a commercial CFD code, specifically ANSYS *FLUENT* (2009). This has allowed the present research effort, to adapt

available model capabilities such as computational grid construction and solution of the viscous flow equations, so the research could focus on the physics of clutch engagement.

It is widely accepted that the typical range of oil viscosity and gap dimensions in a wet clutch lead to flow conditions that are laminar. Wall effects suppress turbulent in the oil film over the entire range of rotational speeds that are used in practice (*Yuan et al.*, 2003). Therefore, the fluid flow in the clutch system is considered to be laminar and incompressible, and turbulence phenomena are not considered in the modeling process of this research. To capture the effects of air bubbles trapped in the flow of a wet clutch, the Volume of Fluid (VOF) module of ANSYS CFD was adopted. New add-on modules were developed for capturing contact friction and asperity torque. More importantly an novel iterative scheme was developed in order to determine dynamically the oil film thickness during clutch engagement.

4.1 Laminar Flow Model

Since the Reynolds number is low in the case of wet clutch, laminar flow is assumed. For the laminar flow, conservation equation and momentum equation are solved by ANSYS CFD. The mass conservation equation can be written as follows

$$\frac{\partial \rho}{\partial t} + \nabla \cdot (\rho \vec{v}) = 0 \tag{4.1}$$

Also, when the gravitational body force is ignored, conservation of momentum in an inertial reference frame is given by

$$\frac{\partial}{\partial t}(\rho \vec{v}) + \nabla \cdot (\rho \vec{v} \vec{v}) = -\nabla p + \nabla \cdot (\bar{\bar{\tau}}) + \vec{F} \tag{4.2}$$

where p is the static pressure, $\bar{\bar{\tau}}$ is the stress tensor and $\vec{F}$ is the external body

forces. Since the friction material is porous media, the source term of porous media is included in $\vec{F}$. The pressure drop in porous media is described in Section 4.7.

4.2 Multi-phase Flow Model

Multi-phase flow occurs in any fluid flow consisting of more than one phase or component such as gas-liquid flows, liquid-liquid flows, liquid-solid flows, gas-solid flows, dust-gas flows, etc. In this study, two-phase flow of oil and air becomes important when back flow may allow entrainment of air bubbles during the open clutch stage. In the present study, the VOF model has been employed because it is capable of tracking the transient liquid-gas interface, which plays a crucial role in the overall wet clutch model.

4.2.1 Volume of Fluid (VOF) Scheme

The VOF model is a surface-tracking technique applied to a fixed Eulerian mesh. It is designed for two or more immiscible fluids where the position of the interface between the fluids is of interest. In the VOF model, a single set of momentum equations is shared by the fluids, and the volume fraction of each fluid in every computational cell is tracked throughout the domain.

The continuity equation for multi-phase flow can be written as follows (*FLUENT* (2009))

$$\frac{1}{\rho_q}\left[\frac{\partial}{\partial t}(\alpha_q\rho_q) + \nabla\cdot(\alpha_q\rho_q\vec{v}_q) = S_{\alpha_q} + \sum_{p=1}^{n}(\dot{m}_{pq} - \dot{m}_{qp})\right] \tag{4.3}$$

where

ρ_q : density of phase q

S_{α_q} : mass source for phase q

α_q : volume fraction of phase q

$\vec{v}_q$: velocity of phase q

$\dot{m}_{qp}$: mass transfer from phase q to phase p

$\dot{m}_{pq}$: mass transfer from phase p to phase q

In this study, the mass source and transfer terms on the right-hand side on Eq. (4.3) are zero because no chemical reaction or mass sources are present.

The volume fraction equation for the primary phase has the following constraint:

$$\sum_{q=1}^{n} \alpha_q = 1 \tag{4.4}$$

As shown in Figure 4.1, each computational cell is assigned a certain volume fraction for each phase, and a simple advection scheme is used to track the interface. The method is very robust, but the interface sharpness tends to deteriorate with time, as numerical diffusion smears the initially sharp front. However, using reconstruction techniques, it is possible to maintain satisfactory accuracy provided that the grid resolution is sufficiently high. It is possible to construct a smooth surface, delineating the fluid interface and conserve mass accurately. Since both a steady state solution for the open clutch and a transient solution for clutch engagement are necessary in this study, an implicit scheme that can be used for both time-dependent and steady state calculations has been selected. Then, in this research, the continuity equation

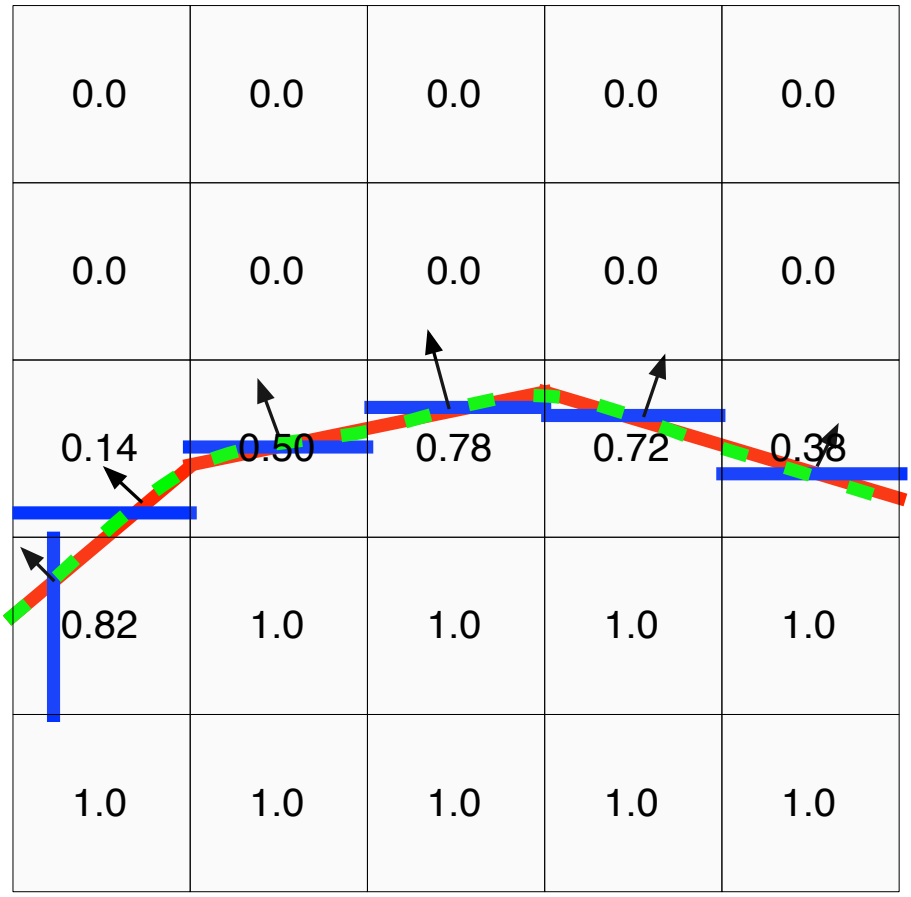

Figure 4.1: Volume of Fluid interface tracking

can be approximated as follows (*FLUENT* (2009))

$$\frac{{\alpha_q}^{n+1}{\rho_q}^{n+1} - {\alpha_q}^{n}{\rho_q}^{n}}{\Delta t} V + \sum_f ({\rho_q}^{n+1}{U_f}^{n+1}{\alpha_{q,f}}^{f}) = 0 \tag{4.5}$$

where

$n+1:$ index for new(current) time step

$n:$ index for previous time step

$\alpha_{q,f}:$ cell face value of the q^{th} volume fraction

$U_f:$ volume flux through the cell face, based on normal velocity

4.3 Dynamic Mesh Adaptation

For simulating clutch engagement and other dynamic behavior during squeeze flow, the clearance between the two clutch plates should be narrowed. In order to model these phenomena, a dynamic mesh adaptation needs to be employed in the CFD model. In the dynamic mesh scheme, internal node positions are automatically computed from externally specified boundaries or movement of objects in the flow domain.

In the present study, the CFD clutch model employs hexahedral elements, so a spring based-smoothing method combined with local dynamic layering is considered. These two dynamic mesh methods have the following features. First, as shown in Figure 4.2, for the spring based-smoothing method, the mesh nodes are connected and move as a network of interconnected springs. Hence, the node-element connectivity remains unchanged. This method is efficient in cases where the boundary of the cell zones moves in one direction and the motion is normal to the cell zones, as shown in

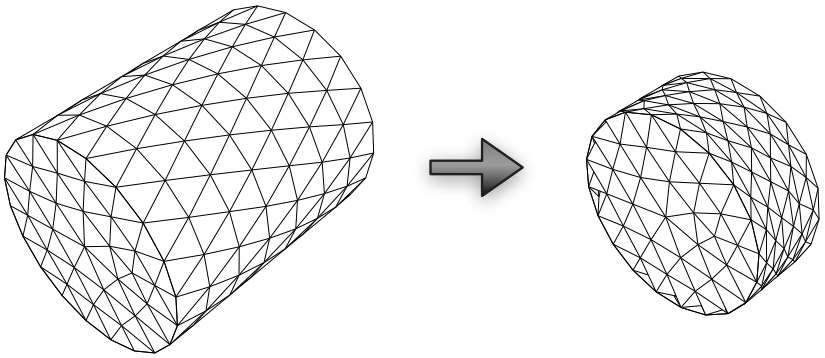

Figure 4.2: Spring based-smoothing on interior nodes (*FLUENT*, 2009)

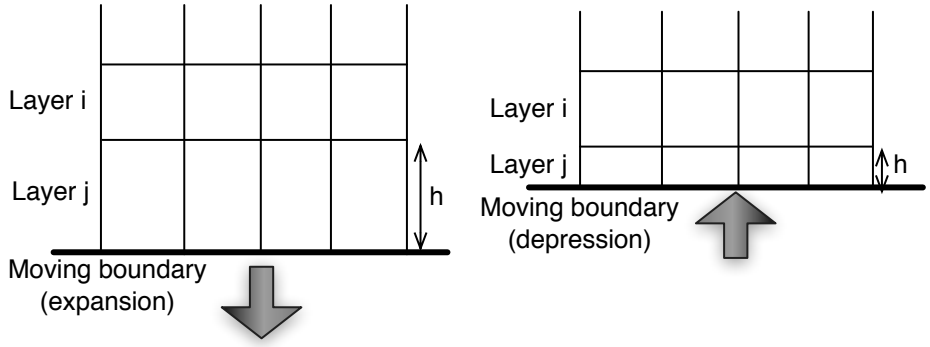

Figure 4.3: Dynamic layering: Expansion and depression of boundary

Figure 4.2.

Second, in the dynamic layering method new layers of cells adjacent to a moving boundary are added or deleted, as the zone grows or shrinks. As shown in Figure 4.3, if the cells of layer j undergo expansion, the cells are split provided that their dimensions satisfy the following criteria

$$h_{\min} > (1 + \alpha_s) h_{ideal} \tag{4.6}$$

where h_{min} is the minimum cell height of a cell layer, h_{ideal} is the ideal cell height, and α_s is a layer split factor.

If the cells of the j layer undergo compression, the cells are merged, provided their

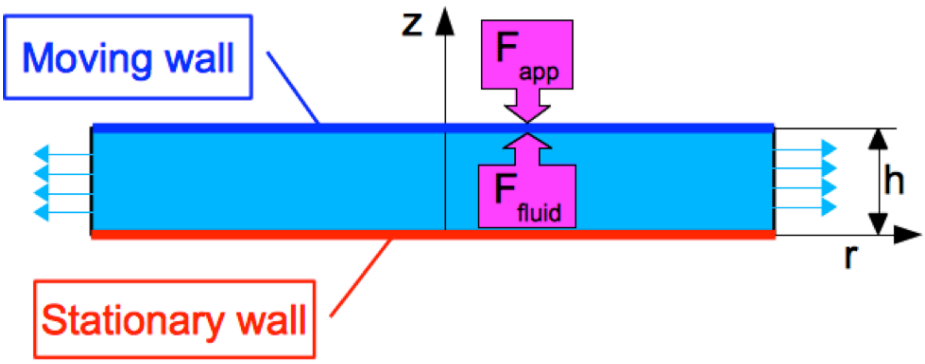

Figure 4.4: Force balance schematic between F_{app} and F_{fluid}

dimensions satisfy the following expression

$$h_{\min} < \alpha_c h_{ideal} \tag{4.7}$$

where α_c is the layer collapse factor.

4.4 Time Advancing Scheme for Clutch Plate Movement

The main physical process that takes place during clutch engagement is squeeze-film flow. To construct a squeeze-flow model, an iterative scheme was presented in *Cho et al.* (2011) and the resulting numerical solutions were compared with the corresponding analytical solutions. The proposed iterative method determines the squeeze velocity at each time by balancing the applied the external force F_{app} and the internal fluid force F_{fluid}, as shown in Figure 4.4. Prior to developing the aforementioned iterative method, the rigid body module of FLUENT was tried to simulate the squeeze motion. However, the solver required very small time steps to prevent solution divergence. Step sizes 100 times smaller than those corresponding to the proposed iterative method were needed to initiate the solution, and even with such small time steps, the solution failed to converge as the oil film thickness decreased.

Also, some non-iterative methods were considered such as a force balance method

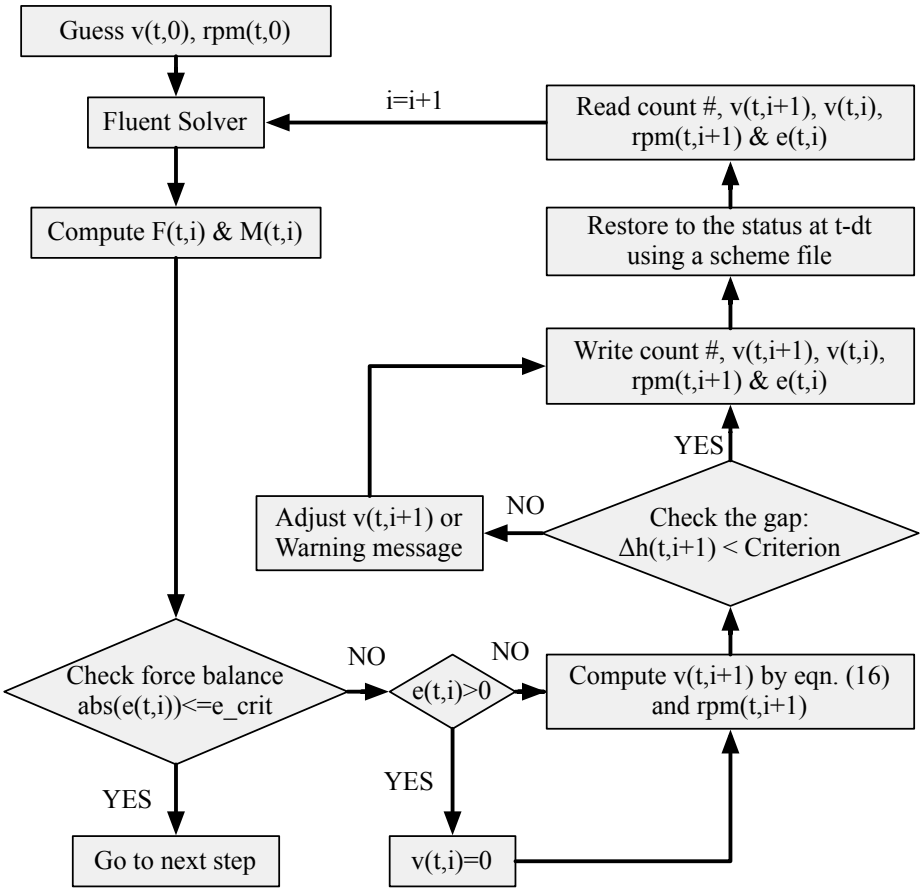

Figure 4.5: Iterative method flow chart

and a sigmoid transform method (*Yun*, 2008). However, the force balance method produced very unstable results regardless of time step size, and a sigmoid transform method failed to converge. Therefore, an iterative scheme is considered, which leads to accurate and stable predictions of the squeeze-flow film thickness.

According to *Sanni* (1997), for small *Re* numbers, unsteady flows can be approximated by a quasi-steady model. Therefore, during each time step the transient behavior of the squeeze velocity may be computed using an iterative scheme.

First, at time t and iteration i, a relative error function needs to be defined to ensure a force balance. The relative error function given by Eq. (4.8) is defined using

F_{app} and F_{fluid} as follows

$$e(t,i) = \frac{\vec{F}_{app} - \vec{F}_{fluid}}{\vec{F}_{app}} \tag{4.8}$$

where $e(t,i)$ is the relative error at time t and iteration i.

If the magnitude of F_{app} is larger than that of F_{fluid}, $e(t,i)$ will assume a positive value. This means that the current squeeze velocity needs to increase. In turn this will reduce the film thickness, increase the internal force and satisfy the force balance in Eq. (4.8).

As shown in Figure 4.5, if the force error function, Eq. (4.8), is larger than the minimum error criterion e_{crit}, all variables return to the status of the previous time level, $t - \delta t$, using a script code and User Defined Functions (UDF). This is done to prevent losing the current variable values necessary for computing a new squeeze velocity. Critical information at the current time step is stored in an external file and is then reloaded for use in computing the new squeeze velocity $v(t, i+2)$. At each time step, the desired squeeze velocity can be obtained using the Newton-Raphson Method. New velocity at time t and iteration $i+2$ can be computed using information from the previous iterations i and $i+1$.

Then, the new squeeze velocity $v(t, i+2)$ is given by the following expression

$$v(t,i+2) = -\frac{v(t,i+1) - v(t,i)}{e(t,i+1) - e(t,i)} e(t,i+1) + v(t,i+1) \tag{4.9}$$

The squeeze velocity $v(t)$ at each time step is an input parameter for a moving wall boundary condition. The internal force F_{fluid} caused by $v(t)$ has to balance F_{app} during each time step by satisfying the force error criterion e_{crit}. In other words, $v(t, i+2)$ is provided to the flow solver as an input. The iteration is repeated until the force balance criterion is satisfied. At simulation time $t = 0$, initial values of squeeze velocity are guessed using Newton's 2^{nd} law of motion. Then, at simulation time t, values of $v(t)$ and the rotation speed $rpm(t)$ are estimated by $v(t - \delta t)$ and

$rpm(t - \delta t)$, i.e. values available at the previous time step. At the beginning of each new time step, the flow solver carries out the simulation based on these estimated values.

In general, the squeeze velocity has a zero or negative value, i.e. one that reduces the film thickness, because in a typical clutch engagement process the applied force increases monotonically. If during the iterations, the squeeze velocity is assigned to a positive value, the pressure in the film is reduced and the internal fluid force decreases. This contradicts the assumed monotonicity of the applied force profile, so positive squeeze velocity values are not allowed. In addition, values of the squeeze velocity magnitude larger than a critical value may cause a large volume error in the dynamic mesh routine, as the grid fails to compress accordingly during a single time step. To prevent such errors, the gap displacement Δh is compared to a critical value Δh_{crit}. If Δh exceeds Δh_{crit}, the computed squeeze velocity is adjusted to a value that corresponds to the maximum allowable gap displacement. Δh_{crit} is determined by the dynamic grid routine which requires that the maximum displacement during each time step does not exceed the dimension of the associated cell layer.

4.5 Heat Transfer Model

As mentioned in Chapter 1, the key physical process associated with a wet clutch operation involves the change from hydrodynamic resistance to mechanical contact during engagement. Due to viscous shear and friction, kinetic energy is dissipated into heat. The temperature and oil viscosity change, which then affects the viscous torque and engagement time. The rise in temperature is also very important for the durability of the friction plate. Therefore it is crucial to model heat transfer in the clutch system during the engagement process.

The conservation of energy equation for the fluid can be written as follows (*FLU-*

ENT (2009))

$$\frac{\partial}{\partial t}(\rho E) + \nabla \cdot (\vec{v}(\rho E + p)) = \nabla \cdot (k\nabla T - \sum_j h_{s_j}\vec{J_j} + (\bar{\bar{\tau}} \cdot \vec{v})) + S \tag{4.10}$$

where E is the fluid energy, k is the thermal conductivity, $\bar{\bar{\tau}}$ is the viscous stress tensor, $\vec{J_j}$ is the diffusive flux of species j, h_{s_j} is the sensible enthalpy, and S is a generalized source term.

In Eq. (4.10), the fluid energy is defined by

$$E = h - \frac{p}{\rho} + \frac{v^2}{2} \tag{4.11}$$

Similarly, the enthalpy is computed as

$$h_s = \sum_j Y_j h_{s_j} + \frac{p}{\rho} \qquad h_{s_j} = \int_{T_{ref}}^{T} c_{p,j} dt \tag{4.12}$$

where Y_j is the mass fraction of species j and T_{ref} is 298.5 K.

According to *Davis et al.* (2000), frictional heat is generated during engagement in the contact interface of the steel and friction plates. The boundary condition at the interface is defined as follows

$$\frac{\partial}{\partial z}T(t, r, h_{int}) = \mu u \frac{\partial u}{\partial z} + \mu_{fric} p \omega r = q'' \tag{4.13}$$

where

μ_{fric} : friction coefficient

ω : angular velocity

h_{int} : film thickness at the contact interface between steel plate and friction plate

In Eq. (4.13), the first term on the right corresponds to heat flux due to viscous shear. The second terms accounts for the friction between the steel and friction plates during solid contact. Viscous heating becomes important when the Brinkman number $\mathbf{B_r}$ exceeds unity.

$$\mathbf{B_r} = \frac{\mu U^2}{k(T_w - T_b)} \tag{4.14}$$

where T_w is the wall temperature, T_b is the fluid bulk temperature and U is a representative fluid velocity. In the wet clutch model, $\mathbf{B_r}$ is relatively small under typical operating conditions. However, as soon as mechanical contact is made, $T_w - T_b$ increases rapidly as a result of frictional heating. Therefore, modeling frictional heating is important during engagement process. FLUENT is not capable of simulating thermal effects in connection with solid contact friction, so a volumetric heat generation scheme is used by introducing the concept of virtual thickness.

Suppose that the contact interface can be represented by a very thin volume having an axial virtual thickness t_{vir}. Then, the volumetric heat generation rate $\dot{q}$ can be defined as follows

$$\dot{q} = \frac{q}{A_{fric} t_{vir}} = \frac{q''}{t_{vir}} = \frac{\mu_{fric} p \omega r}{t_{vir}} \tag{4.15}$$

where

q : heat energy $[W]$

$\dot{q}$: volumetric heat generation rate $[W/m^3]$

q'' : heat flux $[W/m^2]$

t_{vir} : virtual ineterface thickness between friction plate and steel plate $[m]$

A_{fric} : friction plate area $[m^2]$

To test the sensitivity of the virtual thickness concept to heat transfer, a three-

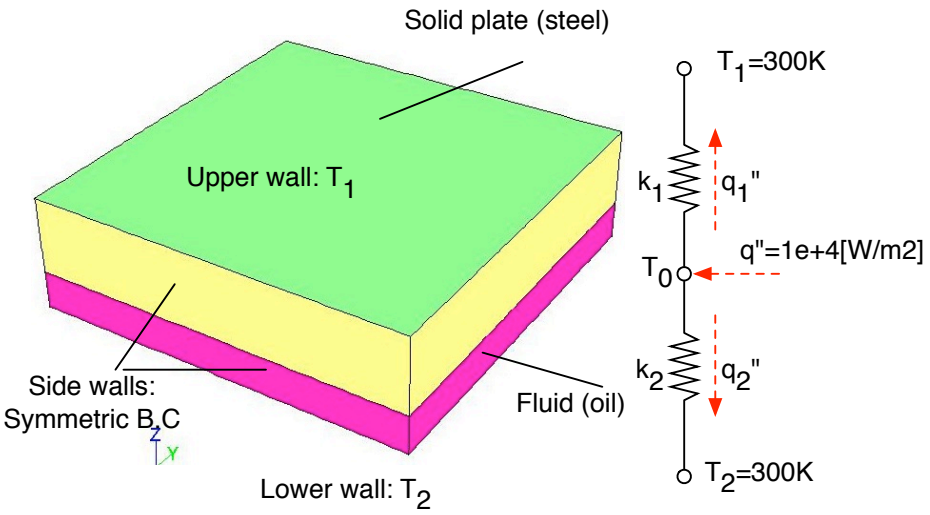

Figure 4.6: A transfer model of rectangular plates to check t_{vir} sensitivity

dimensional rectangular plate was modeled, as shown in Figure 4.6. The model consists of a rectangular steel plate and an adjacent fluid zone. The temperature at the upper and lower walls (T_1, T_2) is kept at 300 K while a constant heat flux $(q'' = 10^4\ W/m^2)$ is applied to the interface between the steel plate and the fluid zone. Periodic boundary conditions are used at the side walls.

When only heat conduction is considered, the interface temperature T_0 can be calculated as follows

$$T_0 = \frac{q'' + (k_2/l_2)T_2 + (k_1/l_1)T_1}{k_2/l_2 + k_1/l_1} \tag{4.16}$$

where l_1 and l_2 are the thickness of the two zones, respectively. Figure 4.7 shows the exact and computed temperature profiles in the z directions for $l_1 = 2\ mm$ and $l_2 = 1\ mm$. The numerical solutions agrees perfectly with the analytical solution regardless of the virtual interface thickness, provided that the latter is small. Therefore, the heat flux obtained using a virtual interface thickness can be used as the input to the model to include the frictional heat generation due to solid contact.

Figure 4.8 shows the overall heat transfer model for a wet clutch. The steel and friction plate have symmetrical geometries with respect to each horizontal centerline.

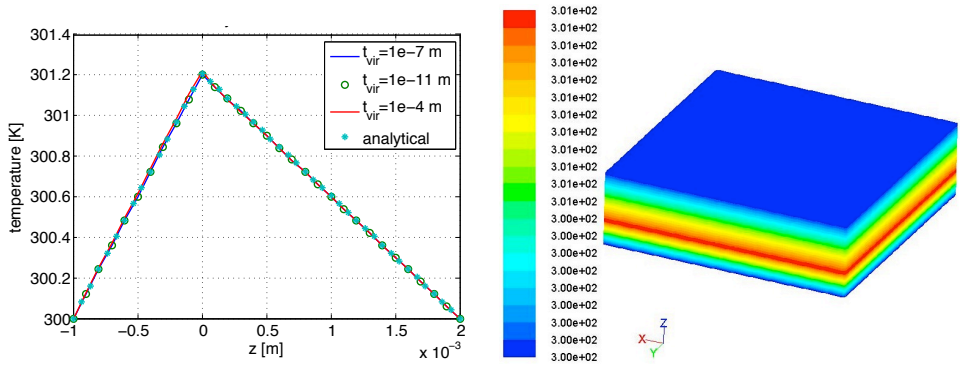

(a) Temperature plot to z-direction (b) Temperature contour

Figure 4.7: Heat transfer sol. of rectangular plate model when $q'' = 1e + 4\ W/m^2$

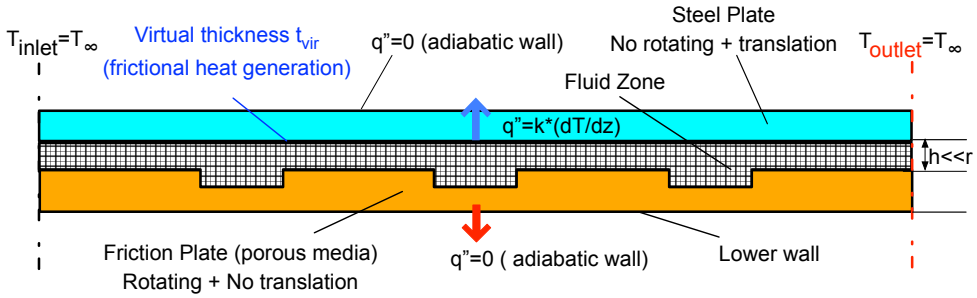

Figure 4.8: Heat transfer model with boundary conditions

Therefore The upper wall of the steel and the lower wall of friction plate can be treated as adiabatic walls. The temperature at the inlet and outlet is assumed to be equal to the initial oil temperature. The heat conduction within the steel plate is then computed based on frictional heat generation due to solid contact.

Since both oil viscosity μ and density ρ are functions of temperature, fitted curves for μ and ρ of TGC oil were used in the heat transfer model of the wet clutch simulations, as shown in Figure 4.9.

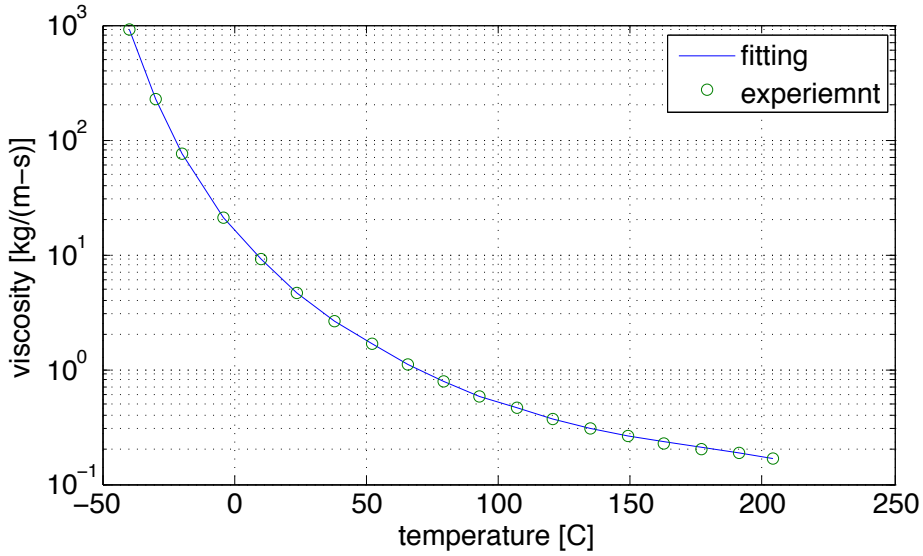

(a) Oil viscosity

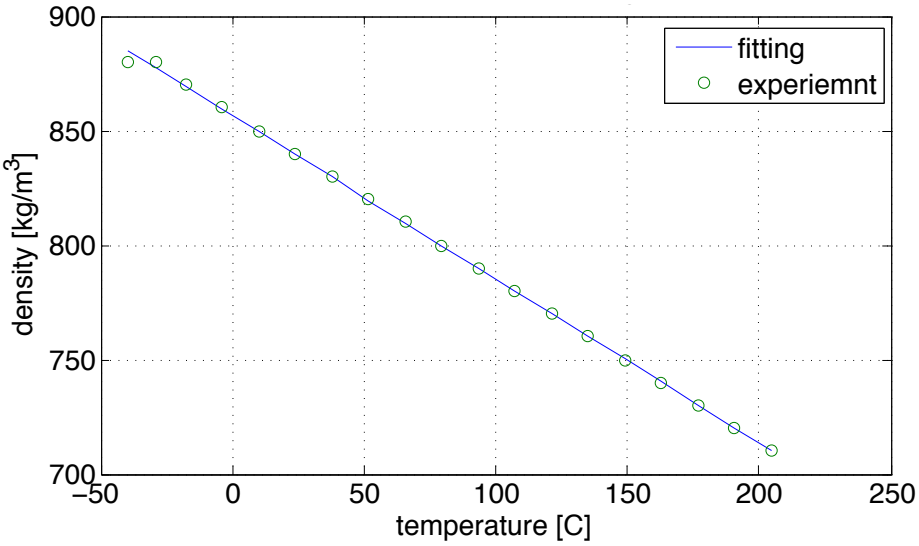

(b) Oil density

Figure 4.9: Fitted curves of oil viscosity and density used in TGC experiment

The equation for oil viscosity in the range $-40 \leq T\ [^{\circ}C] \leq 66$ is given by

$$\begin{aligned}\mu = &- 1.1165e-013 * T^9 + 2.5274e-011 * T^8 - 1.9758e-0.009 * T^7 \\ &+ 5.2999e-0.008 * T^6 + 3.237e-007 * T^5 - 1.1744e-005 * T^4 \\ &- 0.0014853 * T^3 + 0.058135 * T^2 - 0.1 * T + 15.829 \end{aligned} \tag{4.17}$$

when $T\ [^{\circ}C] \geq 66$;

$$\mu = 0.107 * e^{(e^{(22.0109-3.6314003*\log(T+273))}-0.02)} - 0.038 \tag{4.18}$$

Similarly, the oil density in the range $-40 \leq T\ [^{\circ}C] \leq 204$ is given by

$$\rho = -0.39742(\frac{9}{5}T + 32) + 869.34 \tag{4.19}$$

4.6 Surface Roughness

As the film thickness of a wet clutch decreases during the engagement process, the effect of rough surface becomes important in the determination of the film thickness, torque and heat generation between plates. Following *Patir and Cheng* (1978), the ratio of nominal film thickness h to roughness σ becomes an important parameter for the film flow when $h/\sigma < 3$. As h/σ decreases further, asperity contacts takes place, so the problem becomes one of boundary lubrication in which the effect of roughness can be critical. To include surface roughness in the simulation of film thickness of a grooved, wet clutch during engagement, an analytical "asperity contact torque" and a "real contact load" are added to the CFD model. In addition, the roughness effect on the oil film itself is captured using the "flow factor" of *Patir and Cheng* (1978, 1979).

4.6.1 Asperity Contact

As the film thickness is reduced during clutch engagement, asperity contact is made between the two disks. Furthermore, the asperity contact torque and force become begin to dominate the viscous torque and hydrodynamic force. The asperity contact force and real contact torque can be written as follows

$$F_{con} = \iint r p_{con} dr d\theta \tag{4.20}$$

$$T_{con} = \iint r^2 \mu_{fric} p_{con} dr d\theta \tag{4.21}$$

where p_{con} is the asperity contact pressure.

The friction coefficient μ_{fric} is defined by a curve fitted function from *Berger et al.* (1996):

$$\mu_{fric} = 0.15 - 0.011 \log \left(\frac{r_1 + r_2}{2} \omega \right) \tag{4.22}$$

While the viscous torque T_{fluid} due to viscous shear is computed by the CFD model, the asperity contact torque needs to be computed using Eq. (4.21). Thus, the total torque T is composed of two components: Viscous torque T_{fluid} due to viscous shear and asperity contact torque, as given by Eq. (4.21), i.e.

$$T = T_{con} + T_{fluid} \tag{4.23}$$

The speed of the rotating disk is given by

$$\omega = \omega_0 - \frac{1}{I} \int_{t_0}^{t} T dt \tag{4.24}$$

where I is the disk's moment of inertia.

Also, p_{con} can be written as (*Natsumeda and Miyoshi*, 1994)

$$p_{con} = E\varepsilon = E_R \frac{A_R}{A_N} \tag{4.25}$$

where E is Young's modulus for the friction material, ε is the strain, E_R is Young's modulus for the real contact area, A_R is the real contact area and A_N is the nominal area.

The nominal area is determined by the geometry of the disks, i.e. inner radius, outer radius and grooved area. However, the real contact area is related to the surface roughness. *Greenwood and Williamson* (1966) assumed that the peak of the asperities has a uniform spherical shape to compute the real contact area. Then, the relation between surface roughness and contact area per unit nominal area can be written as follows

$$A_r(h) = \pi\eta\beta \int_h^\infty (z-h) f(z) dz \tag{4.26}$$

where

A_r: real contact area per unit area

β: the mean radius of asperity peak

η: surface asperity density

$f(z)$: probability density function

The mean radius of asperity β and the number of asperities N are defined by

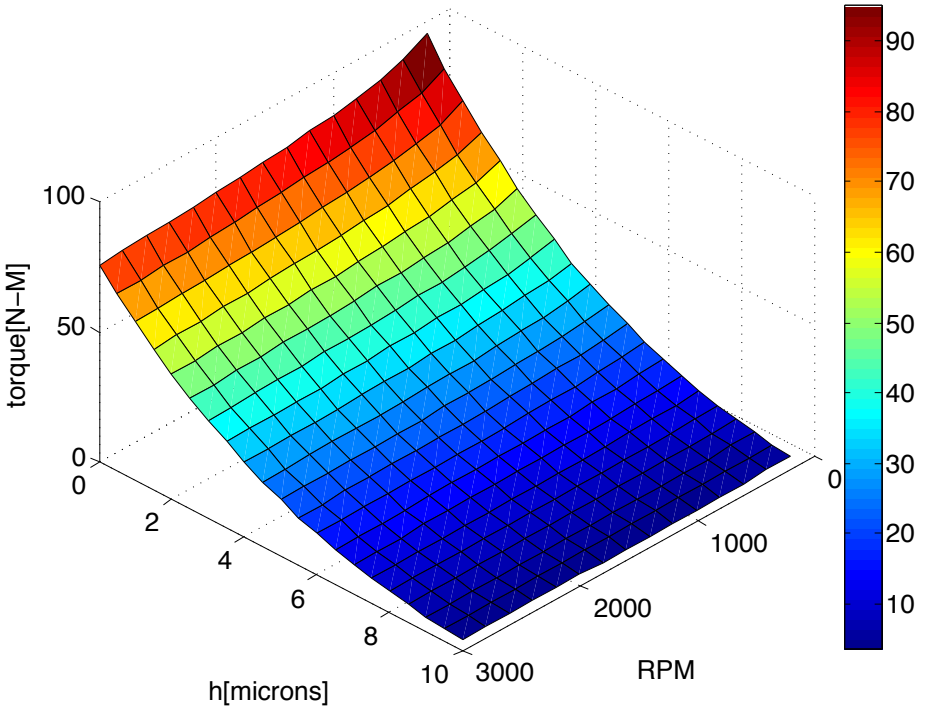

Figure 4.10: Contact torque T_{con} for rpm and h

Robbe-Valloire (2001)

$$\beta = \frac{1}{16}\frac{AR^2 + SAR^2}{R} \tag{4.27}$$

$$\eta = \frac{1.2}{AR^2} \tag{4.28}$$

where AR is the average of horizontal distance between two neighboring peaks, SAR is the root mean square of horizontal distance values between two neighboring peaks and R is the average of the mean height values between two neighboring peaks.

Using Eqs. (4.21) - (4.26), Figure 4.10 shows the relationship between T_{con}, h and rpm when $E_R = 27\ MPa$, $\eta = 3.0e+07\ m^{-2}$ and $\beta = 5.0e-04\ m$ for a Gaussian height distribution having a roughness $\sigma = 6.0e-06\ m$. As h decreases, T_{con} increases due to the increase in A_R. Since the friction coefficient μ_{fric} decreases as rpm increases, T_{con} is inversely proportional to rpm.

To compute Eq. (4.26), the PDF of surface roughness needs to be known. In gen-

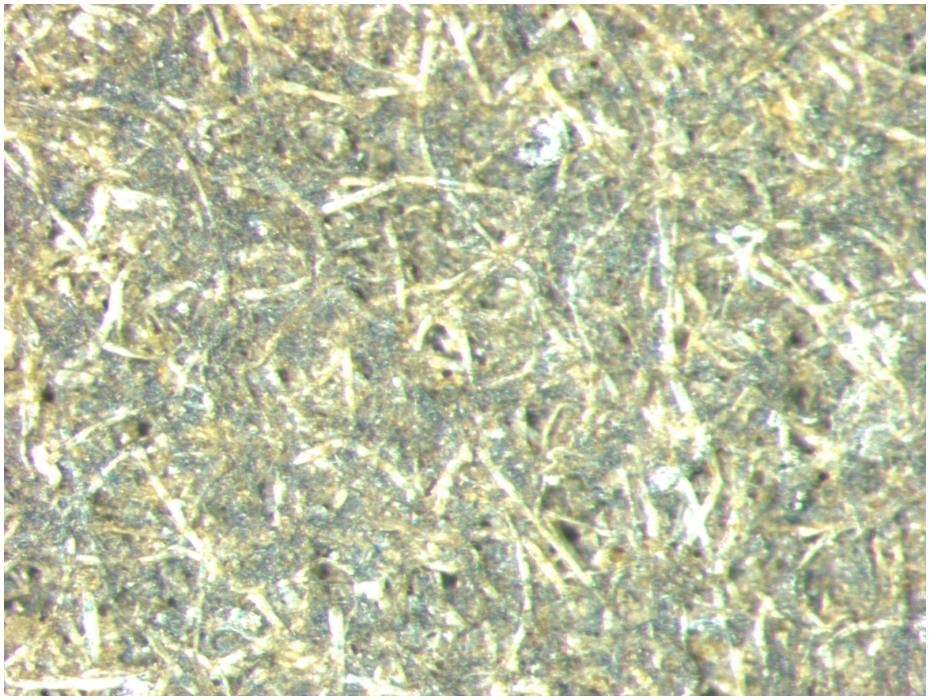

(a) TGC surface image

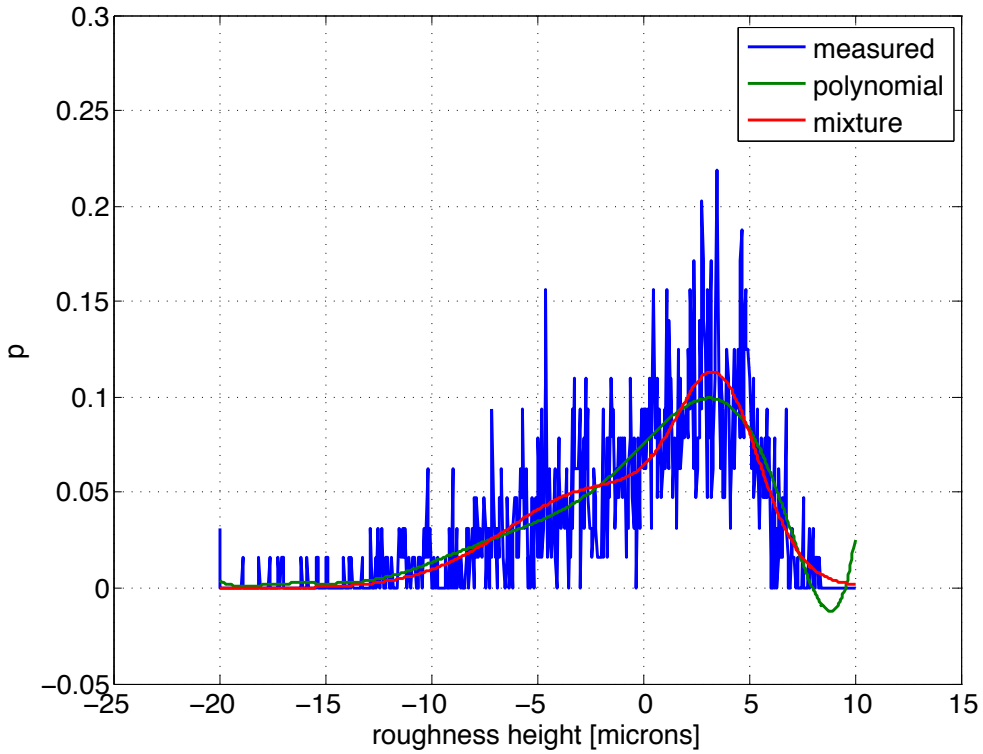

(b) TGC PDF for surface roughness and the fitting curves

Figure 4.11: TGC surface image and the probability density function

eral, the PDF is supposed to follow isotropic roughness conditions having a Gaussian distribution for height (*Natsumeda and Miyoshi*, 1994; *Berger et al.*, 1996; *Jang and Khonsari*, 1999, 2002, 2011). However, the PDF of TGC has a non-Gaussian distribution of height, as shown in Figure 4.11. Therefore, in this research two cases of surface roughness are considered to improve the solution accuracy of an engagement model. These are the Gaussian density function and the actual density function of TGC. The roughness of the friction material of TGC (Figure 4.11(a)) was measured by a profilometer using a contact stylus. Figure 4.11(b) shows the negatively skewed probability density function of TGC friction material. To fit the PDF of TGC, two approaches were used: 1) polynomial curve fitting and 2) the Gaussian mixture model.

The Gaussian probability density function is written as follows,

$$f_g(\mu_g, \sigma_g, z) = \frac{1}{\sqrt{2\pi}\sigma_g} e^{-\frac{(z-\mu_g)^2}{2{\sigma_g}^2}} \tag{4.29}$$

where μ_g is the mean value and σ_g is the standard deviation value of the roughness. When the roughness PDF is a Gaussian PDF, the real contact area A_r is given by

$$A_r(H = h/\sigma_g) = \pi\eta\beta\sigma_g \left[\frac{1}{\sqrt{2\pi}} e^{-(1/2)H^2} + \frac{1}{2} H \left(erf(\frac{H}{\sqrt{2}}) - 1 \right) \right] \tag{4.30}$$

Now, the polynomial fitting form can be written as follows

$$f_p(z) = \sum_{i=1}^{n+1} a_i z^{n+1-i} \tag{4.31}$$

where a_i are coefficients to be determined by the least-squares method based on the measured data for TGC roughness. For the polynomial curve, substitution of Eq.

(4.31) into Eq. (4.26) yields the real contact area, as follows

$$\begin{aligned} A_r(h) &= \pi\eta\beta \int_h^\infty (z-h) f_p(z) dz \\ &= \pi\eta\beta \int_d^\infty (z-h) \sum_{i=1}^{n+1} a_i z^{n+1-i} dz \\ &\approx \pi\eta\beta \sum_{i=1}^{n+1} a_i \left(\frac{1}{n+3-i} {z_{\max}}^{n+3-i} - \frac{h}{n+2-i} {z_{\max}}^{n+2-i} \right) \\ &- \pi\eta\beta \sum_{i=1}^{n+1} a_i \left(\frac{1}{n+3-i} h^{n+3-i} - \frac{h}{n+2-i} h^{n+2-i} \right) \end{aligned} \tag{4.32}$$

where z_{max} is an approximated maximum of roughness height in the range $z_{min} \leq z \leq z_{max}$. When $z \geq z_{max}$, it is assumed that the roughness height is statistically negligible.

As another approach to fit the PDF of TGC, the mixture PDF model with Gaussian PDF is considered. The mixture PDF model can express a non-Gaussian PDF as the linear combination of Gaussian PDF's. Through the comparison between the measured non-Gaussian PDF and the mixture PDF based on the computed values of Skewness and Kurtosis, it was confirmed that the combination of two Gaussian PDF's is sufficient to express the non-Gaussian PDF of TGC. Hence, the mixture model with Eq. (4.29) is defined as follows

$$\begin{aligned} & f_m(\mu_g, \sigma_g, z) \\ &= b_1 f_{g1}(\mu_{g1}, \sigma_{g1}, z) + b_2 f_{g2}(\mu_{g2}, \sigma_{g2}, z) \ \because b_1 + b_2 = 1 \\ &= b_1 \frac{1}{\sqrt{2\pi}\sigma_{g1}} e^{-\frac{(z-\mu_{g1})^2}{2{\sigma_{g1}}^2}} + (1-b_1) \frac{1}{\sqrt{2\pi}\sigma_{g2}} e^{-\frac{(z-\mu_{g2})^2}{2{\sigma_{g2}}^2}} \end{aligned} \tag{4.33}$$

where b_1, b_2, μ_{g1},σ_{g1}, μ_{g2} and σ_{g2} are determined by using the least-squares method for the measured PDF.

Finally, substituting Eq. (4.33) into Eq. (4.26) yields the real contact area as

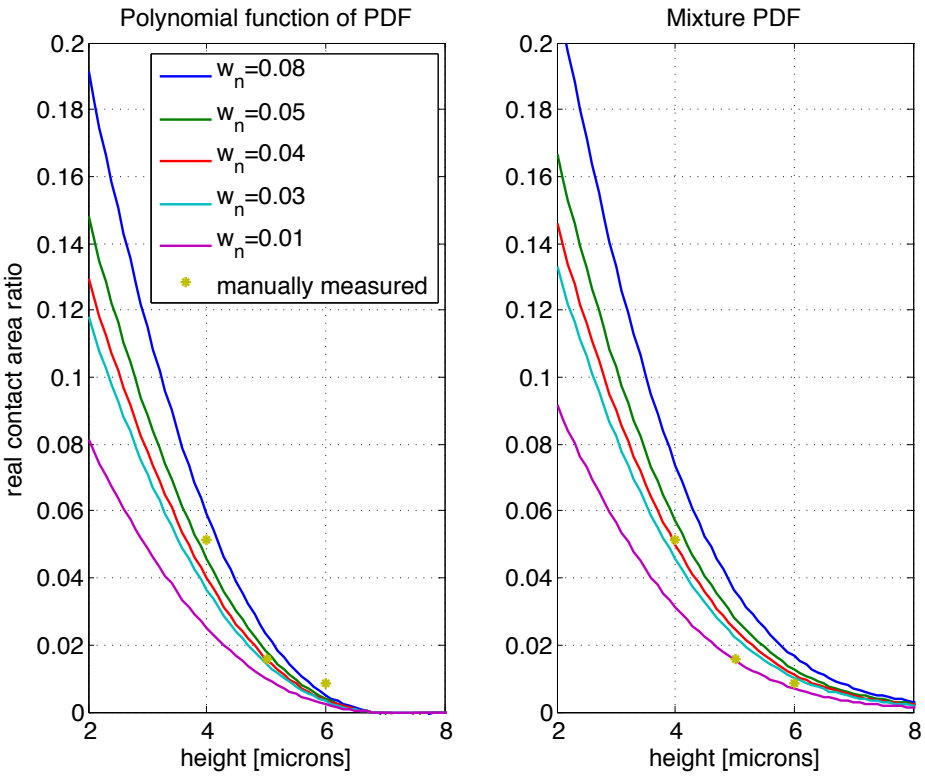

Figure 4.12: Real contact areas: Polynomial VS Mixture PDF for $\omega_n = 0.01 \sim 0.08$

follows

$$
\begin{aligned}
A_r(H = h/\sigma_g) &= \pi\eta\beta \int_h^\infty (\delta - h) f_m(\delta) d\delta \\
&= \pi\eta\beta \left[b_1 \int_h^\infty (\delta - h) f_{g1}(\delta) d\delta + b_2 \int_h^\infty (\delta - h) f_{g2}(\delta) d\delta \right] \\
&= \pi\eta\beta \left[\sum_{i=1}^{2} b_i \sigma_{gi} \left\{ \frac{1}{\sqrt{2\pi}} e^{-(1/2){H_i}^2} + \frac{1}{2} H_i \left(erf(\frac{H_i}{\sqrt{2}}) - 1 \right) \right\} \right]
\end{aligned} \tag{4.34}
$$

where $H_i = (h - \mu_i) / \sigma_{gi}$.

In Figure 4.12, the real contact area variation is shown, as a function of height, for a polynomial curve and a mixture using ω_n as the cutoff frequency that was used to filter the measured rough height profile. $\omega_n = 1$ corresponds to half of the sample rate. The real contact area of the polynomial curve fitting is closer to the manually

measured data than that of the mixture PDF at $h = 4$ and $h = 5$. However, for $h \geq 6$, A_r of the mixture PDF is smoother and closer to the measured data. Notice also that A_r of the polynomial fitting contains some negative values. From the comparison, it is found that the real contact area profile for the filtered data and the manually measured real contact area show a better match when $\omega_n = 0.04$. For the TGC filtered roughness data with $\omega_n = 0.04$, the asperity tip radius β is $3.3368e-05$ $[m]$ and the asperity density η is $1.3569e+09$ $[1/m^2]$.

Equations (4.20) - Eq. (4.34) can be used to compute T_{con}, F_{con} and ω including the real contact area when constructing a wet clutch model including the engagement process. However, since the rough surface can affect not only the solid contact but also the hydrodynamics of a wet clutch, the flow factor concept is also included to capture the effects of roughness on hydrodynamic pressure.

4.6.2 Fluid Flow Between Asperities

In *Patir and Cheng* (1978, 1979), an average flow model was studied that can compute the average pressure of the fluid without solving for the local pressure. In the average Reynolds equation, (4.35), a pressure flow factor (ϕ_x and ϕ_y) and a shear flow factor ϕ_s are defined to include the effects of roughness on the fluid flow. The modified Reynolds equation reads

$$\frac{\partial}{\partial x}(\phi_x \frac{h^3}{12\mu}\frac{\partial p}{\partial x}) + \frac{\partial}{\partial y}(\phi_y \frac{h^3}{12\mu}\frac{\partial p}{\partial y}) = \frac{U_1 + U_2}{2}\frac{\partial \bar{h}_T}{\partial x} + \frac{U_1 - U_2}{2}\sigma\frac{\partial \phi_s}{\partial x} + \frac{\partial \bar{h}_T}{\partial t} \qquad (4.35)$$

where h is nominal film thickness, $h_T = h + z$ is the local film thickness, z is the random roughness amplitude, $\bar{h}_T$ is the average gap height, and U_1 and U_2 are the velocities at the surface (see Figure 4.13)

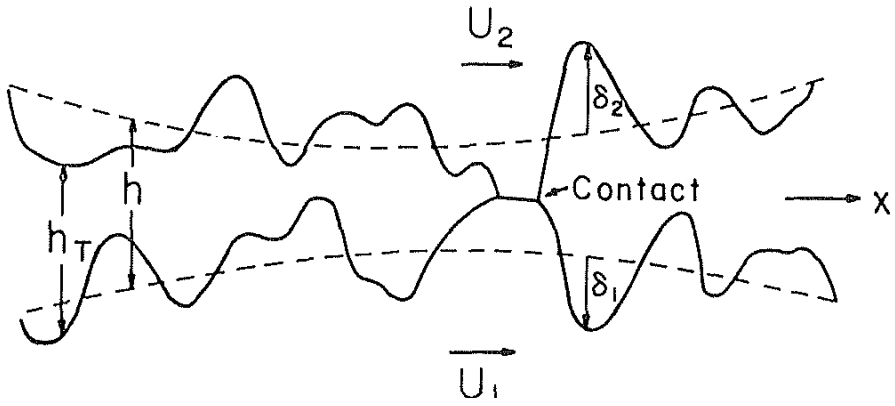

Figure 4.13: Film thickness function (*Patir and Cheng*, 1978)

As $\bar{h}_T$ becomes zero at contact points, the average gap is defined by

$$\bar{h}_T = \int_{-h}^{\infty} (h+z) f(z)\, dz \tag{4.36}$$

In cases of isotropic, transverse and longitudinal surface roughness, the flow factors for a Gaussian PDF of height were computed by (Patir and Cheng, 1978) who used a numerical model based on the finite differential method(FDM) to repeatedly solve the Reynolds equation. Since the surface roughness of TGC is assumed to be homogeneous and isotropic, the derivative of ϕ_s in Eq. (4.35) becomes zero. Hence, in this study the pressure flow factor is the only one considered with $\phi_x = \phi_y$. Then, the pressure flow factor ϕ_x is defined as follows

$$\phi_x = \frac{\frac{1}{L_y} \int_0^{L_y} \left(\frac{{h_T}^3}{12\mu} \frac{\partial p}{\partial x} \right) dy}{\frac{h^3}{12\mu} \frac{\partial \bar{p}}{\partial x}} \tag{4.37}$$

where

$$\frac{\partial \bar{p}}{\partial x} = \frac{p_B - p_A}{L_x}$$

p_A : inlet boundary pressure

p_B : outlet boundary pressure

In general, an isotropic surface is assumed for the wet clutch model having a Gaussian PDF of height and the pressure flow factor ϕ_x for isotropic roughness is approximated by a fitted equation as follows

$$\phi_x(H) = 1 - 0.90e^{-.56H} \tag{4.38}$$

where

$H = h/\sigma$

$\sigma : \sqrt{\sigma_1^2 + \sigma_2^2}$, standard devitations of combined roughness

However, since the TGC friction plate used in the wet clutch tests has a non-Gaussian PDF of height, the pressure flow factor needs to be determined. Following the procedure of *Patir and Cheng* (1978), the flow factors for the TGC friction plate were computed. The overall procedure from generating the roughness surface to computing the flow factor is summarized in Appendix A.1 and A.2.

To validate the simulation model for the flow factor, the computed results for a Gaussian roughness distribution are compared with Eq. (4.38) in Figure (4.14). Although the computed values do not agree perfectly with Eq. (4.38), the small differences observed are acceptable because the numerical solution contains randomly generated rough surfaces that are used in the simulation and Eq. (4.38) is an averaged profile of simulation results repeated several times.

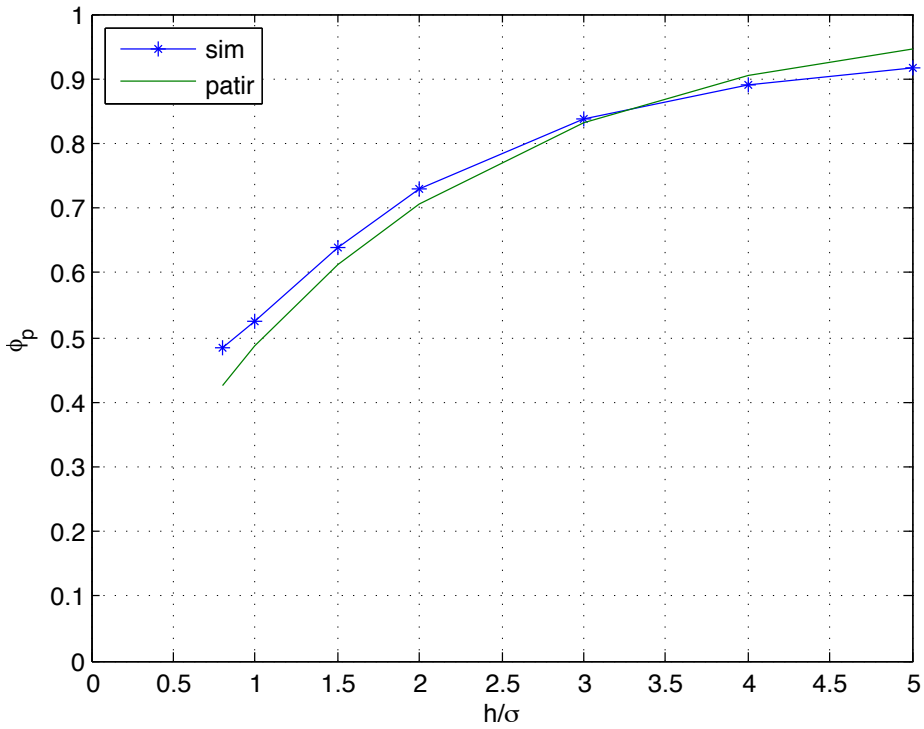

Figure 4.14: Simulation vs Eq. (4.38): pressure flow factor ϕ for isotropic surface

In addition to the procedure for the computation of the pressure flow factor of TGC as shown in Figure 4.14, an analytical method was used to compute the flow factor for a general clutch plate. The analytical method can readily extend the flow factor results for Gaussian roughness distribution to those for non-Gaussian roughness distributions without performing repetitive tasks, such as surface generation and FDM analysis. This analytical method is derived in the following.

First, from *Patir and Cheng* (1978), the unit flow q_x and the expected unit flow $\bar{q_x}$ are defined as follows

$$q_x = -\frac{{h_T}^3}{12\mu}\frac{\partial p}{\partial x} + \left(\frac{U_1 + U_2}{2}\right) h_T \tag{4.39}$$

$$\bar{q}_x = -\phi_x \frac{h^3}{12\mu}\frac{\partial \bar{p}}{\partial x} + \left(\frac{U_1 + U_2}{2}\right) \bar{h}_T + \frac{U_1 - U_2}{2}\sigma\phi_s \tag{4.40}$$

where $\bar{h}_T$ is avaverage gap.

The net mean flow of Eq. (4.39) is calculated using the expectancy operator as follows

$$\begin{aligned}\bar{q}_x &= E\left(-\frac{{h_T}^3}{12\mu}\frac{\partial p}{\partial x}\right) + E\left(\left(\frac{U_1+U_2}{2}\right)h_T\right) \\ &= E\left(-\frac{{h_T}^3}{12\mu}\frac{\partial p}{\partial x}\right) + \left(\frac{U_1+U_2}{2}\right)E(h_T)\end{aligned} \tag{4.41}$$

Since $E(h_T)$ in Eq. (4.41) is identical to Eq. (4.36) when contact points exist, Eq. (4.41) can be recast as follows

$$\bar{q}_x = E\left(-\frac{{h_T}^3}{12\mu}\frac{\partial p}{\partial x}\right) + \left(\frac{U_1+U_2}{2}\right)\bar{h}_T \tag{4.42}$$

For a pure rolling case ($U_1 = U_2$), ϕ_x can be solved by combining Eqs. (4.40) and (4.42). Therefore, Eq. (4.37) can be written as follows

$$\phi_x = \frac{E(\frac{h_T^3}{12\mu}\frac{\partial p}{\partial x})}{\frac{h^3}{12\mu}\frac{\partial \bar{p}}{\partial x}} = \frac{E(h_T^3\frac{\partial p}{\partial x})}{h^3\frac{\partial \bar{p}}{\partial x}} \tag{4.43}$$

Second, as shown in Appendix A.1, all terms of the matrix form of the discrete Reynolds equation contain h_T. Since the solution for pressure becomes a function of h_T, $\frac{\partial p}{\partial x}$ can be written as follows

$$\frac{\partial p}{\partial x} = \frac{\partial p}{\partial h_T}\frac{\partial h_T}{\partial x} \tag{4.44}$$

Therefore, $\frac{\partial p}{\partial h_T}$ becomes a function of h_T since p is a function of h_T. If the generated random number set does not allow any repeated numbers, the relation between the position variable x and h_T for the generated random number becomes an one to one function, which can have an inverse function. Since x can be expressed by h_T, $\frac{\partial h_T}{\partial x}$ also becomes a function of h_T. Therefore $\frac{\partial p}{\partial x}$ can be a function of h_T under the above mentioned assumptions. Notice that at contact points, $h_T = 0$ and that

several contact points can exist simultaneously. However, since p also becomes zero at contact points, $\frac{\partial p}{\partial x}$ at contact points is assumed to be negligible.

In general, if a random variable X is discrete, then the expectation of an general function $g(X)$ is defined as

$$E[g(X)] = \sum_{x \in \chi} g(X) f(X) \tag{4.45}$$

where f is the probability mass function of X and χ is the support of X.

Since h_T is a function of z, $\frac{\partial p}{\partial x}$ finally becomes a function of z. Therefore, the Gaussian mixture model Eq. (4.33) and the definition of Eq. (4.45) can be used in $E(h_T^3 \frac{\partial p}{\partial x})$ as follows

$$\begin{aligned}
&E(h_T^3 \frac{\partial p}{\partial x}) \\
&= \sum_{x \in \chi} h_T^3 \frac{\partial p}{\partial x} f_m(\mu_g, \sigma_g, z) \\
&= \sum_{x \in \chi} h_T^3 \frac{\partial p}{\partial x} [b_1 f_{g1}(\mu_{g1}, \sigma_{g1}, z) + b_2 f_{g2}(\mu_{g2}, \sigma_{g2}, z)] \text{ when } b_1 + b_2 = 1 \\
&= b_1 E_1(h_T^3 \frac{\partial p}{\partial x}) + b_2 E_2(h_T^3 \frac{\partial p}{\partial x})
\end{aligned} \tag{4.46}$$

Substituting Eq. (4.46) into Eq. (4.43) yields a superposed equation consisting of two Gaussian mixture PDF models as follows

$$\phi_x = b_1 \frac{E_1(\frac{h_T^3}{12\mu} \frac{\partial p}{\partial x})}{\frac{h_T^3}{12\mu} \frac{\partial \bar{p}}{\partial x}} + b_2 \frac{E_2(\frac{h^3}{12\mu} \frac{\partial p}{\partial x})}{\frac{h^3}{12\mu} \frac{\partial \bar{p}}{\partial x}} \tag{4.47}$$

Finally, by virtue of Eq. (4.47) and Eq. (4.38), as using a mixture PDF model,

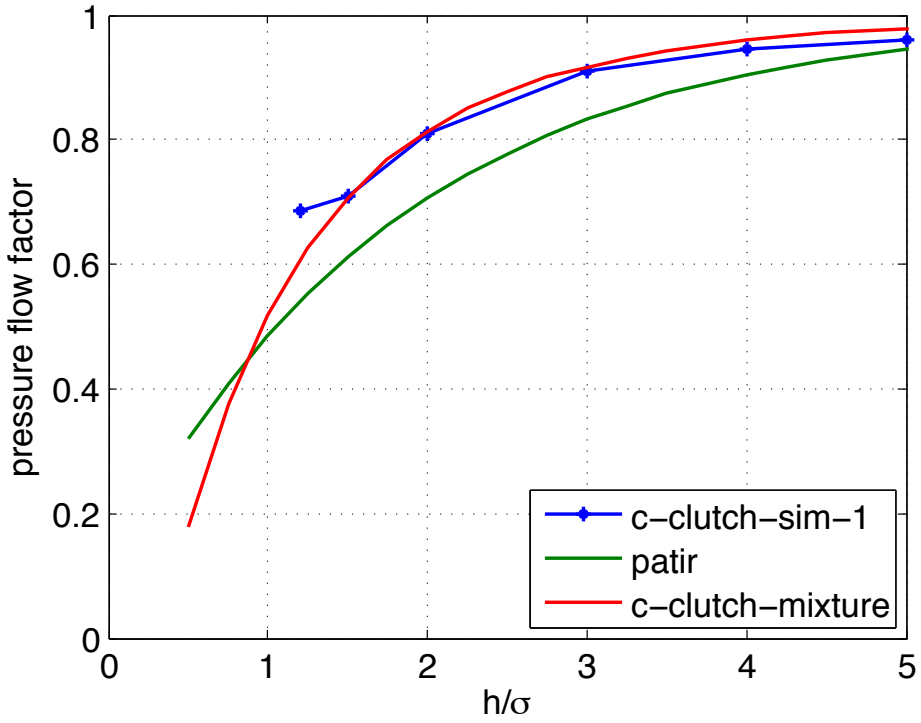

Figure 4.15: Simulation VS Eq. (4.48): pressure flow factor ϕ for TGC friction surface

the pressure flow factor for a non-Gaussian height distribution can be written as

$$\begin{aligned}\phi_x(H) &= b_1\phi_{x,ga}(H_1) + b_2\phi_{x,ga}(H_2) \\ &= b_1(1-0.90e^{-.56H_1}) + b_2(1-0.90e^{-.56H_2}) \\ &= b_1(1-0.90e^{-.56(\frac{h-\mu g1}{\sigma g1})}) + b_2(1-0.90e^{-.56(\frac{h-\mu g2}{\sigma g2})})\end{aligned} \tag{4.48}$$

As shown in Figure 4.15, the simulation results and the stochastic model for TGC friction surface have a good agreement. The ϕ_x for an isotropic surface is smaller than that of the TGC rough surface when $h/\sigma \geq 1$. However, when $h/\sigma \leq 1$, ϕ_x of the isotropic surface is smaller than that of the TGC rough surface. This is because the roughness PDF of the TGC has a negative skewness. For an isotropic rough surface, if the PDF of roughness is known, the PDF can be fitted with a Gaussian mixture model and then the pressure flow factor can be computed by Eq. (4.48).

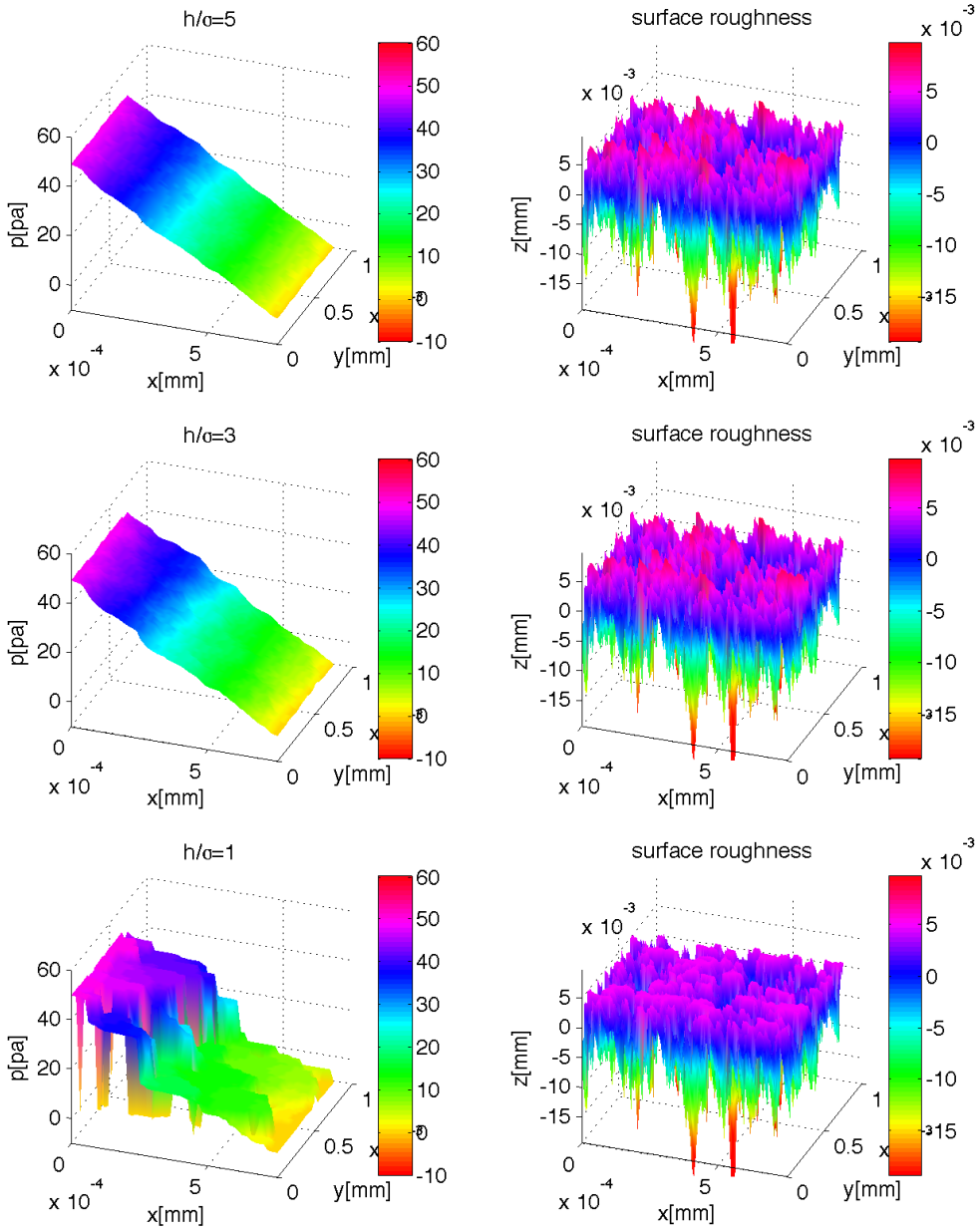

Figure 4.16: Pressure contour and height distribution of TGC: $h/\sigma = 5, 3, 1$

Figure 4.16 shows pressure contours and rough surface height distributions of the TGC based on the numerical results of the FDM model. With large h/σ, smooth pressure profiles are created that are similar to the pressure profile of a smooth surfaces. Since the pressure flow factor is the ratio of the pressure between rough and smooth surfaces, the flow factor is close to 1 for large h/σ. As h/σ decreases, the pressure profile is distributed and the pressure flow factor becomes smaller than 1.

To include the effect of surface roughness in terms of the computed pressure flow factors in the CFD model, the oil viscosity is adjusted instead of directly employing the pressure flow factor. Suppose that $\phi = \phi_x = \phi_y$ for a homogeneous flat surface, and that the adjusted viscosity is $\mu' = \mu/\phi$. Eq. (4.35) can be written in term of μ/ϕ while $\frac{\partial \phi_s}{\partial x} = 0$ as follows

$$\frac{\partial}{\partial x}(\frac{h^3}{12\mu'}\frac{\partial p}{\partial x}) + \frac{\partial}{\partial y}(\frac{h^3}{12\mu'}\frac{\partial p}{\partial y}) = \frac{U_1 + U_2}{2}\frac{\partial h}{\partial x} + \frac{\partial h}{\partial t} \tag{4.49}$$

As shown in Eq. (4.49), if the adjusted viscosity μ' is used in the CFD model, the numerical solution reflects accurately the effect of a rough surface.

4.7 Porous Media of Friction Plate

Since the grooved friction plate consists of a porous material, the permeability of the plate plays a significant role in the computation of the squeeze velocity. For very small oil film thickness, a porous media flow module needs to be included in the engagement process of the wet clutch model. In the ANSYS CFD model, porous media is handled as a source term to be added in the momentum conservation equations. The source term S_i consists of a viscous loss term and inertial loss term, as follows

$$S_i = -\left(\sum_{j=1}^{3} D_{ij}\mu v_j + \sum_{j=1}^{3} C_{ij}\frac{1}{2}\rho|v|v_j\right) \tag{4.50}$$

where S_i is the source term for the ith momentum equation, $|v|$ is the absolute value of the velocity and D and C are prescribed matrices. This equation is related to the pressure gradient in the porous cell and creates a pressure drop in the cell.

In the special case of homogeneous porous media, Eq. (4.50) becomes

$$S_i = -\left(\frac{\mu}{\alpha}v_i + C_2\frac{1}{2}\rho|v|v_i\right) \tag{4.51}$$

where α is the permeability and C_2 is the inertial resistance factor. α and C_2 become the diagonal elements of matrices D and C where all other elements are zero.

In laminar flows such as the thin oil film of a wet clutch, the pressure drop is proportional to the velocity and C_2 is considered to be zero. If the convective acceleration and diffusion are also negligible, Eq. (4.51) becomes Darcy's Law.

$$\bigtriangledown p = -\frac{\mu}{\alpha}\vec{v} \tag{4.52}$$

4.8 Overall computational model

Figure 4.17 shows the flow chart of the overall model that is used to simulate wet clutch engagement based on the ANSYS framework and using the new subroutines developed in this research. First, the steady state solution for an open clutch is obtained by using a multi-phase or single phase flow process. Then the unsteady flow solution is computed with the open clutch solution previously obtained used as the initial condition. It is necessary to establish a realistic starting point for the engagement computation, as the air and the oil are squeezed out of the gap between the clutch plates. For example, at high rpm, since the air volume fraction corresponds to large fraction of the total volume, an initial condition from the multi-phase flow model is necessary. However, at low rpm, since the air volume fraction represents a small fraction of total volume, an initial solution from a single phase flow model may

be sufficient for a transient simulation of the engagement process.

During clutch engagement, the film thickness between the friction and steel plates decreases, so its size is determined using the proposed iterative method. While the iterative method is run, asperity contact pressure is combined with the hydrodynamic pressure and then the total pressure is used to check the force balance against the applied force. Also, by means of the viscous shear torque and the asperity contact torque, the angular velocity is computed. When the angular velocity becomes zero, the engagement process is completed. Finally, the model includes the effects of heat transfer and flow through the porous friction material.

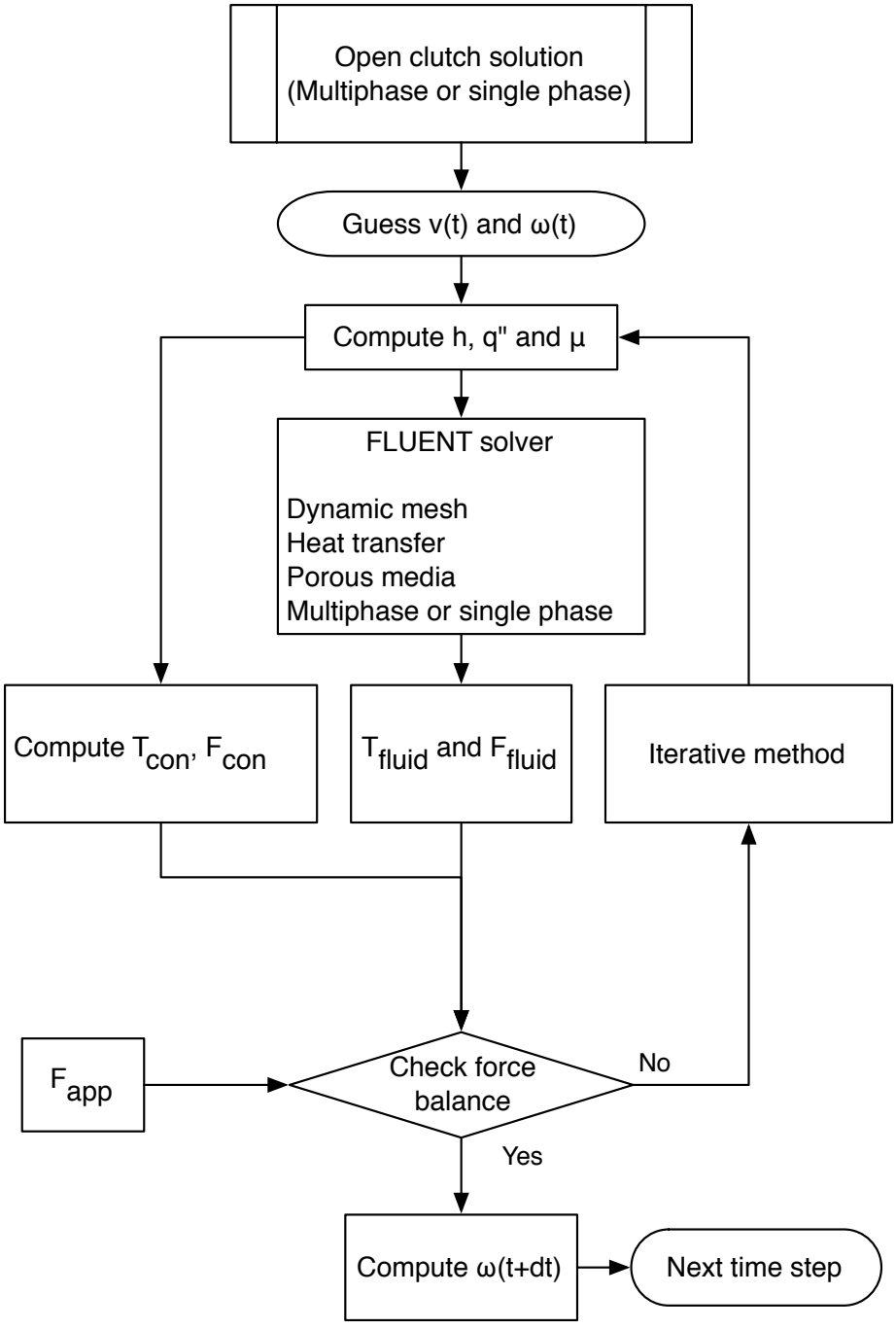

Figure 4.17: Overall flow chart of a computational wet clutch model

CHAPTER V

Computational Results

The multi-physics model presented in the previous chapter is tested here under a variety of initial and boundary conditions. The simulation of wet clutch engagement is complicated by several complex computational constructs, but also by the uncertainty of the location and nature of the boundary conditions. Furthermore, there exist several fluid and solid media parameters that introduce uncertainty in the simulations. The computational tests in this chapter aim at establishing the accuracy and consistency of the model. The simulations are performed sequentially to establish the self-consistency of the computational approach and to investigate various mesh structures, boundary conditions and parameter settings.

5.1 Multiple Reference Frame Scheme

As shown in Figure 1.1, a typical wet clutch system consists of multiple friction plates and steel plates. Oil flows between the separator and friction plates. To reduce the run time of the model, a single pair of friction and separator plates is considered in this study. Since this research represents the first attempt to employ a CFD model for wet clutch engagement, it is more important to understand the physical processes and produce a correct formulation than to capture the exact geometric details of the clutch housing, etc. Although the latter may be of importance for a variety of reasons,

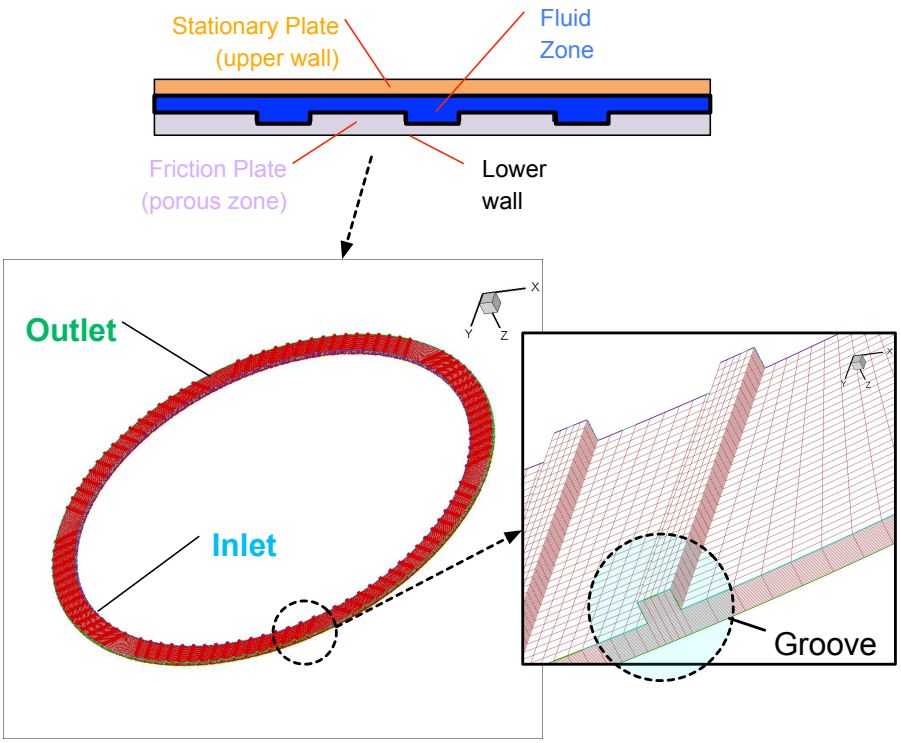

Figure 5.1: Single wet clutch model: Grooved friction plate

it was decided to postpone a complete model of a clutch system to future research.

The first computational test corresponds to an open clutch set up. The goal is to compute the hydrodynamic drag torque that develops in the oil film and obtain a steady state solution that can also be used as the initial condition of engaged wet clutch model. A single wet clutch model is constructed, as shown in Figure 5.1. The steel plate that undergoes a translational motion during the engagement process is now assumed to be stationary. The friction plate is rotating, but also maintains its position normal to the disk pair. Fluid is introduced through a central conduit and directed radially from the inner to the outer radii of the annular disks. The outflow boundary is specified as a pressure outlet. The inflow boundary is given by two alternative boundary conditions: either as a specified pressure inlet or as a mass flow rate inlet in which the velocity is prescribed normal to the inflow boundary. A hexahedral mesh is used to create the disk geometry due to the large aspect ratio of

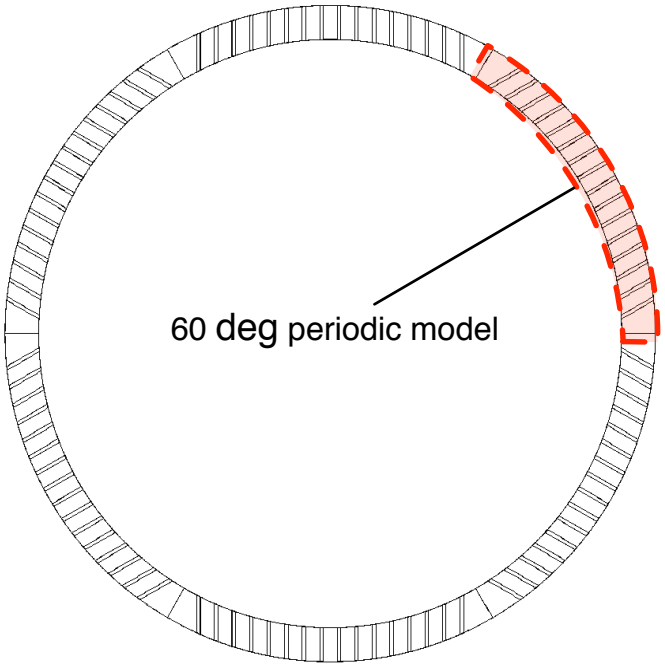

Figure 5.2: TGC model geometry for experiment and simulation

the cells.

Figure 5.2 shows the TGC model that was used in the clutch experiments in order to collect data for validation of the numerical model and to measure flow parameters. The dimensions of the clutch and the properties of the friction material are shown in Table. 5.1. The clearance between the friction and separator plates is 0.19 $\sim$ 0.25 mm. To reduce the grid size and improve computational efficiency, only a 60-degree section of the plates is considered. Periodic boundary conditions are specified at both ends of the repeated groove pattern, which contains 16 grooves.

In the experimental tests conducted in this study, the upper wall, i.e. the non-grooved plate, undergoes a translational motion during engagement while the friction plate is rotating. Furthermore, to construct a model that is valid for both open clutch simulation and the engagement process, the squeeze flow requires a dynamic mesh as discussed in 4.3. The combination of an axially moving boundary and a rotating wall boundary in the clutch system represents a challenge that can result in numerical

Table 5.1: Friction plate geometry dimension and properties

Inner radius $[mm]$	82.75
Outer radius $[mm]$	93.51
Thickness $[mm]$	0.66
Groove width $[mm]$	1.0
Groove depth $[mm]$	0.17
Axial permeability $[darcy]$	0.072
Radial permeability $[darcy]$	7.2
Young's modulus, E $[MPa]$	41.3

errors and loss of computational efficiency.

Several boundary and relative coordinate techniques were used in order to determine the best overall approach. These included the Multiple Reference Frame (MRF) scheme available in the ANSYS CFD framework and rotating fluid frames. As shown in Figure 5.3, the results of a rotating upper wall, i.e. the non-grooved disk, produced the same results with the MRF. When the lower wall, i.e. the grooved plate, is rotating, the results differ because the CFD model neglects the normal component of the wall motion. It was concluded that either a rotating upper wall (non-grooved surface) or using the MRF is appropriate for simulating rotating grooved clutch models. However, the MRF scheme is simpler and more efficient when considering the translational motion of upper wall, so it was adopted in the present model. Since the grooves are on rotating plate, a UDF routine was constructed to adapt the MRF for a time dependent rotating speed that is needed in dynamic clutch modeling.

5.1.1 Grid resolution

Computational efficiency is of paramount importance in dynamic clutch simulation. The transient process, in combination with the iterative scheme proposed in Chapter 4, places significant demands on the CPU. Therefore, the coarsest acceptable grid needs to be determined to eliminate unnecessary computations. To determine the optimal grid size for the clutch model, solution convergence tests were performed,

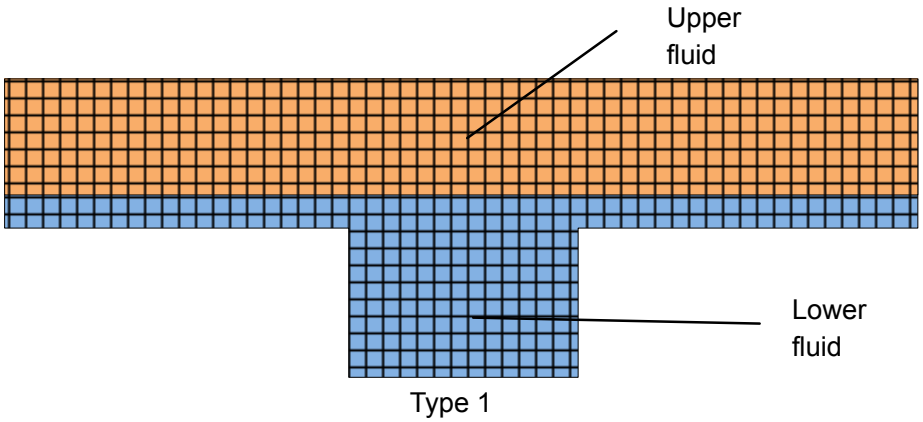

(a) Type 1

Type	Original	Original	Type 1	Type 1
Rotating wall	Upper wall	Lower wall	Upper wall	Lower wall
Moving reference frame	No	No	Upper fluid zone	Lower fluid zone
Pressure contour	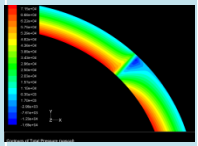	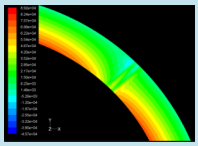	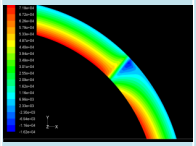	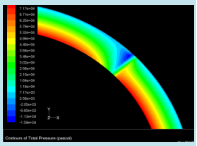

(b) MRF setup test

Figure 5.3: MRF model test for grooved plates

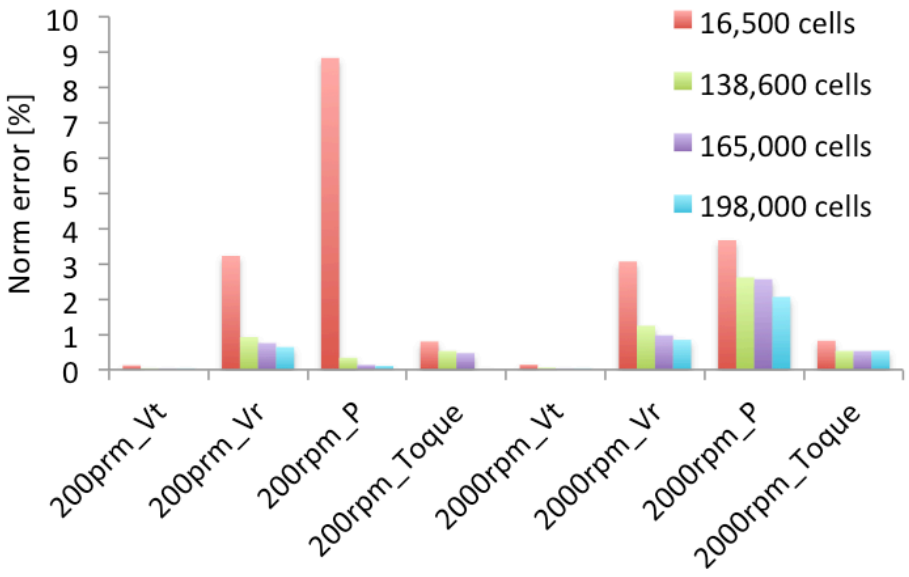

Figure 5.4: $L2$ error norm for pressure, velocity, torque and pressure

as shown in Figure 5.4. A high-resolution grid employing 1,056,600 cells was used as the reference model. Then, using the L2 norm, the differences between the finer-grid model and other resolutions were computed. The results show that a periodic clutch model with 198,000 cells (30 radial, 235 tangential and 40 axial cells) is satisfactory, so it was chosen for the present computational effort.

In addition to the grid convergence tests, numerical experiments were also performed to determine the accuracy of the periodic boundary conditions used to reduce the computational effort. Complete disk simulations were made and compared to the 60-degree sector results.

A typical comparison between the two model results is shown in Figure 5.5. The pressure distribution of the periodic boundary model agrees well with the full disk model; however, there are some minor discrepancies. The conditions prescribed in the periodic model correspond to enforcing purely normal flow across the periodic boundary along with a zero pressure gradient. These conditions are of course only partially correct. As a result, the periodic model does not produce results that are a perfect replica of the full disk model. However, the discrepancy between the two

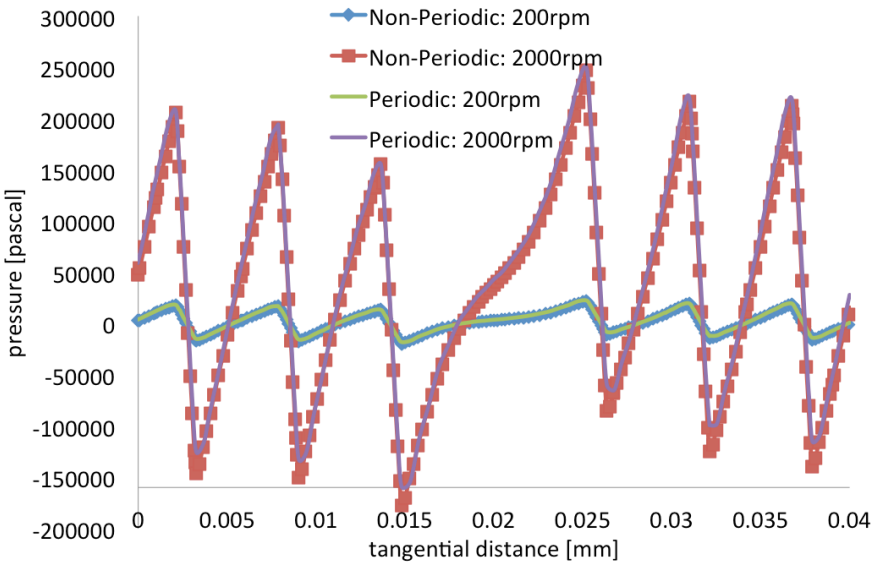

Figure 5.5: Pressure along the tangential direction of periodic boundary

models is deemed small for practical purposes. Thus, all work in the following was based on the periodic model in order to reduce execution times.

5.2 Open Clutch Simulation

5.2.1 Single-Phase, Wet-Clutch Model

As a first test, a single-phase open-clutch model was constructed to simulate the pressure distribution and velocity field in the oil film between the two disks.

5.2.1.1 A simplified wet clutch model with four grooves

As shown in Figure 5.6, a simplified clutch model having only four grooves was modeled. A mass flow inlet boundary condition was imposed. The simulation was used to identify the relationship between angular velocity, mass flow rate and the pressure pattern. Furthermore, the test aimed at shedding some light on the reason bubbles are formed in the gap between the clutch plates as the angular velocity increases.

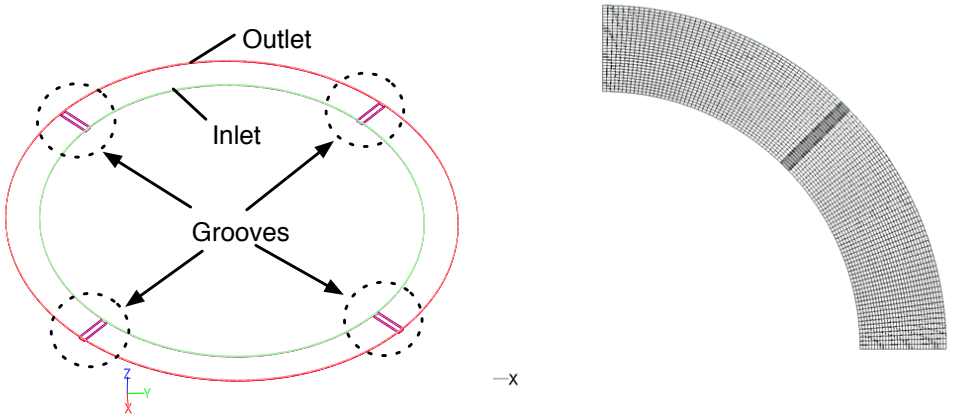

(a) 4 grooved clutch (b) Periodic model

Figure 5.6: Clutch model geometry having 4 grooves

The relationship between angular velocity, mass flow rate and pressure distribution is shown in Figure 5.7. When a mass flow rate inlet boundary condition is applied, as angular velocity increases, the pressure decreases at the upstream side of the groove. At the same time, the low pressure area moves from outside to the inside of the disk. As oil flows in from the upstream side of the groove, air bubbles can be formed on one side of the groove, as the disk keeps rotating. With a fixed rotational speed, any increase of mass flow rate pushes the low pressure area towards the outside of the disk. In turn, this justifies the increased rpm of drag torque peak with increasing mass flow rate.

In Figure 5.8, a zero-pressure boundary condition at both the inlet and outlet was used for the geometry of Figure 5.6. The velocity field corresponding to the test is shown in Figure 5.9. The results show a flow pattern consistent with the basic hypothesis and justification given in the previous paragraph. However, the pressure pattern between the clutch plates differs from that of Figure 5.7. It is clear that the computed pressure distribution depends on the inlet boundary conditions, as shown in Figure 5.10.

To check the sensitivity of the solution on the boundary conditions, the average

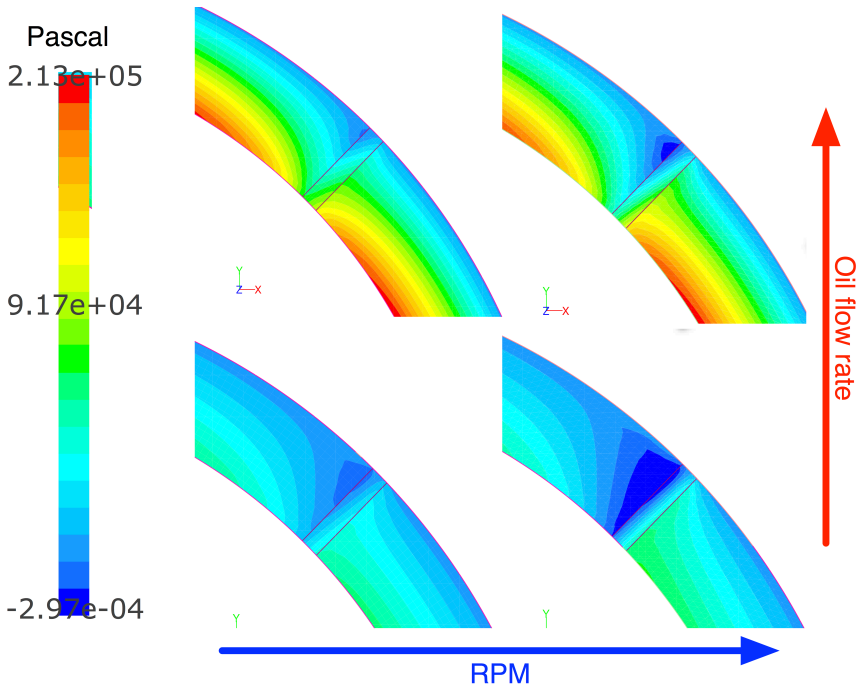

Figure 5.7: Pressure contour with mass flow inlet

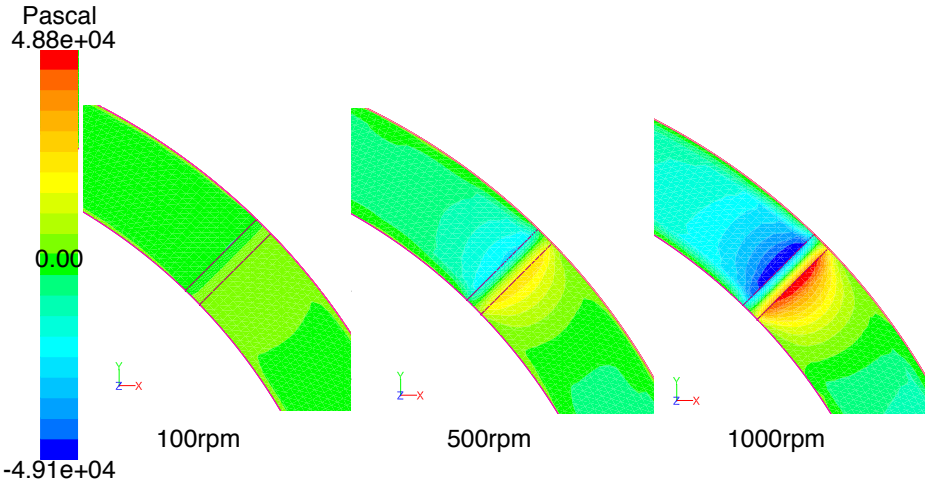

Figure 5.8: Pressure contour with zero pressure inlet

Table 5.2: Average pressure at inlet boundary of mass flow inlet model

Mass flow rate [kg/s]	100 rpm	500 rpm	1000 rpm
0.02	65,645 Pa	64,445 Pa	60,508 Pa
0.04	131,372 Pa	130,272 Pa	126,667 Pa
0.06	197,093 Pa	196,022 Pa	192,547 Pa

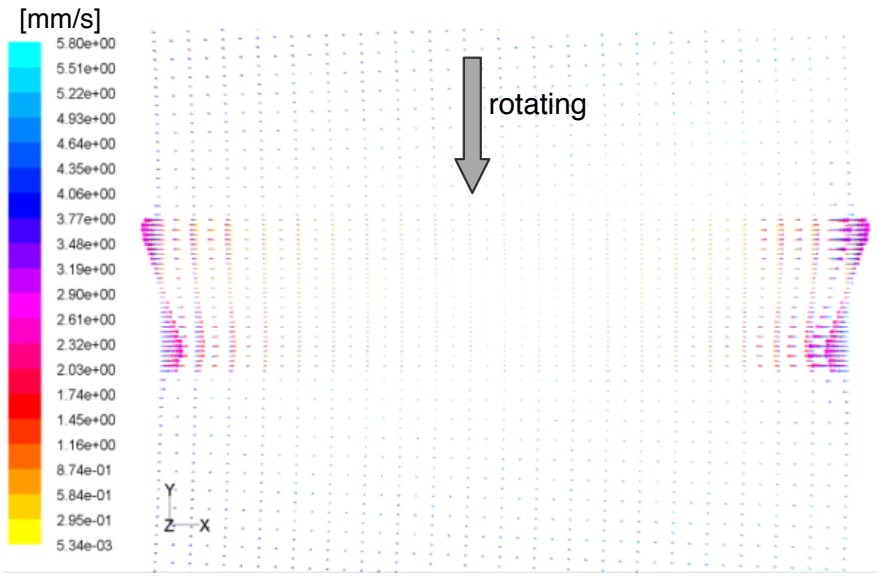

Figure 5.9: Velocity profile of a periodic clutch model

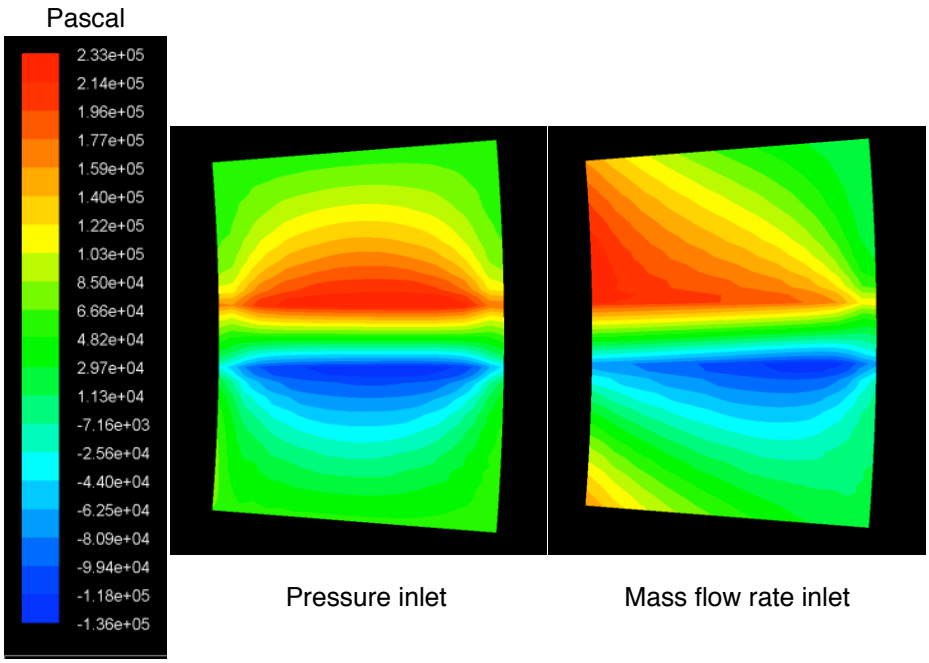

Figure 5.10: Pressure distribution of periodic clutch models

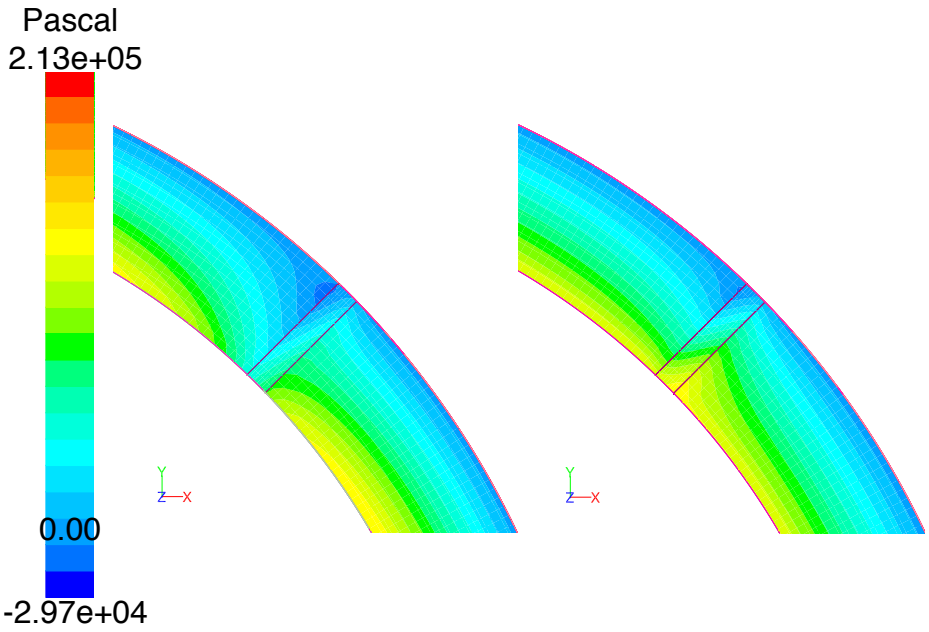

Figure 5.11: Pressure comparison of periodic clutch models: L) Mass flow rate inlet: 0.04 kg/s, R) Pressure inlet: 130, 272 Pa

pressure was calculated for the mass flow inlet, as shown in Table 5.2. As the rotating speed increases, the average pressure at the inlet decreases. The inlet pressure is also proportional to the increase in mass flow rate. This is a consequence of the centrifugal force of a rotating disk that drives the oil flow from the inlet to the outlet. Of course, the centrifugal force is proportional to the rotating speed, which explains the trend shown in the table.

To test this hypothesis for the case of $\dot{m} = 0.04\ kg/s$ and 500 rpm, the computed average pressure (130, 272 Pa) was used in a pressure inlet boundary simulation, and the results are compared in Figure 5.11. The pressure contours in Figure 5.11 show an improved agreement as compared to those in Figure 5.10. The computed mass flow rate of the pressure inlet model is almost identical to the fixed value of 0.04 kg/s, but there still exists some differences between the two simulations. Therefore, it is necessary to construct an appropriate inlet boundary pressure profile or some other boundary condition by comparison of the simulation results with experimental data.

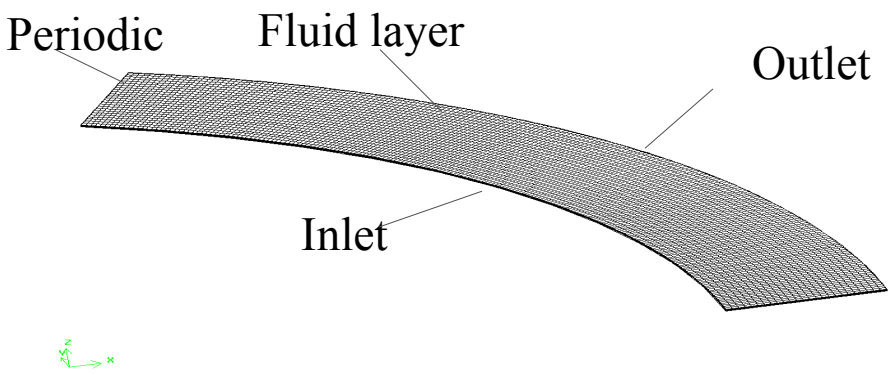

Figure 5.12: 3D non-grooved clutch model

In summary, the development and use of a simple, single phase clutch has provided important information on the appropriate boundary conditions, general pressure patterns and a reasonable explanation for air bubble formation.

5.2.1.2 Non-grooved clutch model

To investigate the effect of the boundary conditions on the flow pattern, it was decided to further simplify the modeling configuration. A non-grooved clutch model was constructed in both two and three space dimensions using periodic boundary conditions, as shown Figure 5.12.

When applying a pressure outlet boundary condition, one needs to additionally specify the direction of any potential backflow through the boundary. Backflow can be restricted to be always normal to the boundary or the flow direction can be left free and computed internally by considering the flow conditions in the cell adjacent to the boundary. Neither approach is perfect and the resulting flow patterns are substantially different. As shown in Figure 5.13, the computations revealed certain numerical errors near the outlet boundary. Since the flow in the model is axisymmetric, the velocity components in the circumference direction should theoretically be identical. However, the simulations show significant discrepancies.

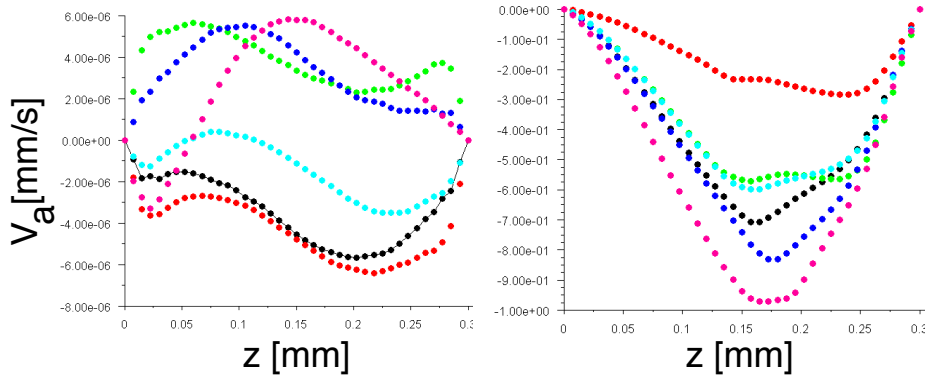

(a) v_a: L) Neighboring cell, R) Normal to boundary

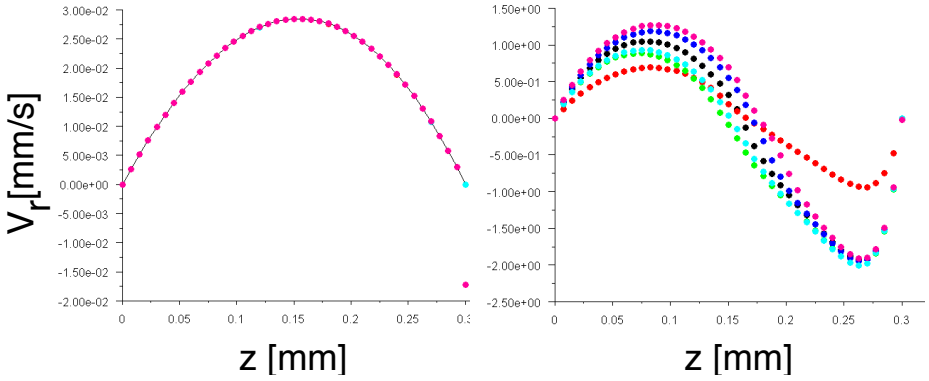

(b) v_r: L) Neighboring cell, R) Normal to boundary

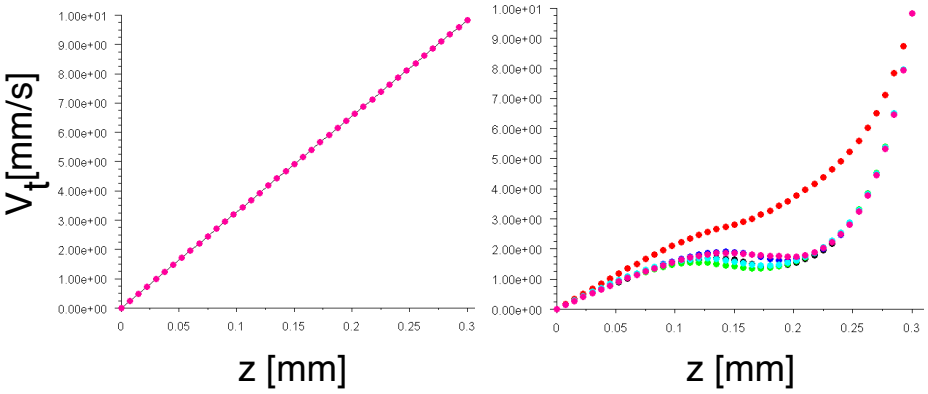

(c) v_t: L) Neighboring cell, R) Normal to boundary

Figure 5.13: Velocity components at outlet for 3D non-grooved periodic model when $\omega = 1000\ rpm$

To simplify the problem even more and to make comparisons with the analytical solution, a two-dimensional, full disks model was tested as shown in Figure 5.14. The comparison between the analytical solution and the numerical solutions shows that away from the outlet boundary, the numerical solution agrees well with the analytical solution. The numerical solution also agrees with the results obtained by *A. Z. Szeri and Kaufman* (1983). It is obvious that at mid-radius, the effect of the incorrect outlet boundary condition diminishes, so the velocity profile is no longer affected.

5.2.2 Extended Domain Models

The reliability of the results of the present model depends strongly on an accurate simulation of the backflow, as the latter is important for the onset of multi-phase flow. Outflow boundary conditions in computational fluid dynamics present a well-known challenge, so it is no surprise that the aforementioned schemes lead to unsatisfactory results. The truncation of the computational domain at a location where complex fluid mechanics occur is not wise. Therefore, an attempt is made next to improve the numerical solution by avoiding to specify boundary conditions at the edge of the disk plates. Instead, extended computational domains are considered that allow the computation of backflow without relying on artificial restrictions.

In Figure 5.15(a), type-1 corresponds to the conventional model without extended boundaries and the models from type-2 to type-4 include extended boundaries for the inlet and outlet, as shown in Figure 5.15(a). In addition, the real hardware configuration is shown in Figure 5.15(b). It is clear that in the true clutch system the flow is not terminated at the outer radius of the clutch disk. There is a significant amount of fluid in the surrounding enclosure, so it is evident that our decision to model only a pair of disks for simplicity leads to a model that cannot capture the true backflow. Of course, the computational restrictions remain and a complete, multi-disk model that includes the clutch enclosure is beyond the scope of this study. Thus,

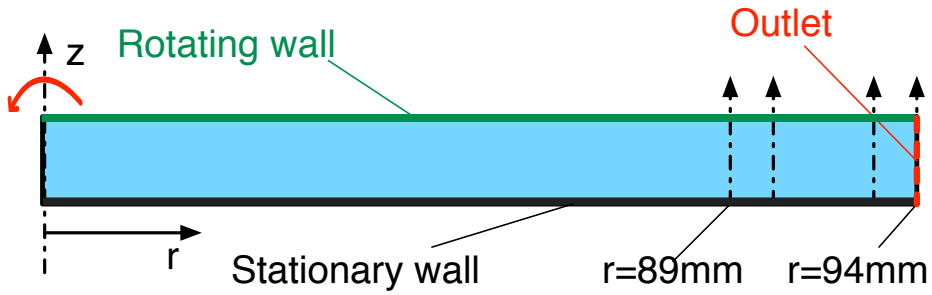

(a) 2D full disks without inlet boundary

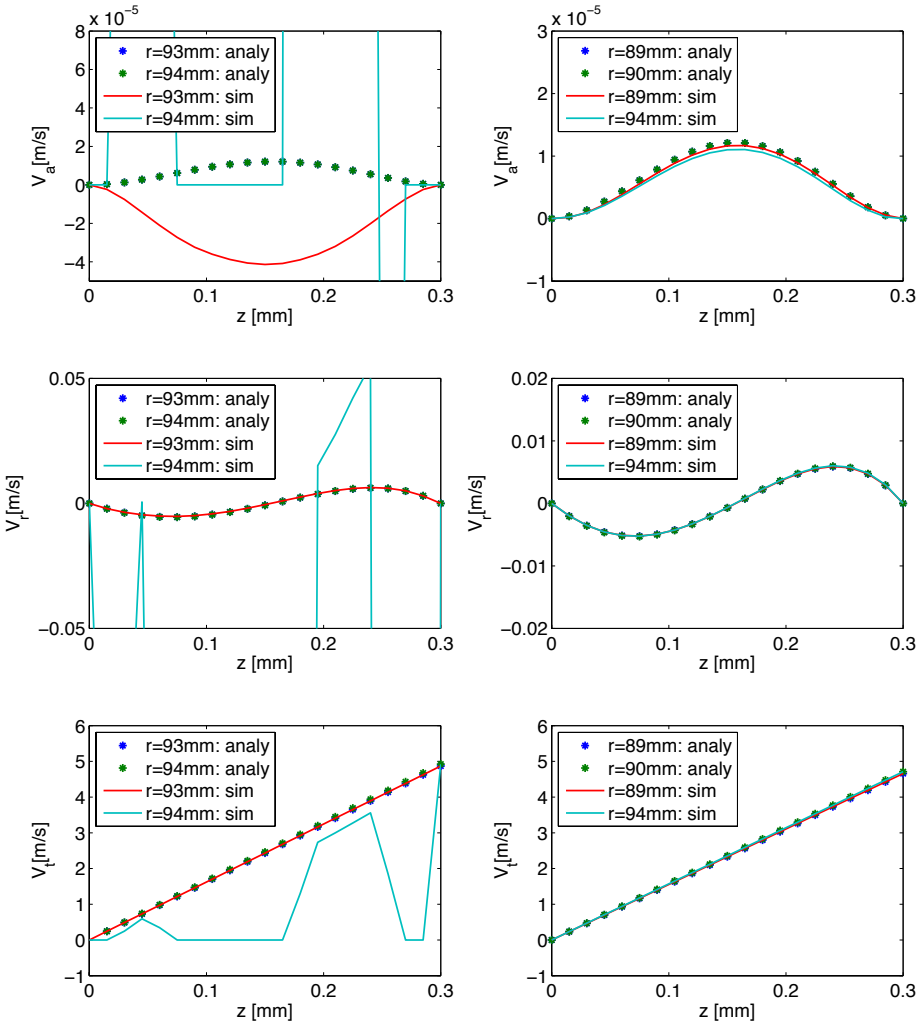

(b) Analytical Sol. vs CFD results

Figure 5.14: v_a, v_r, v_t for 2D non-grooved model without inlet boundary: 500 rpm

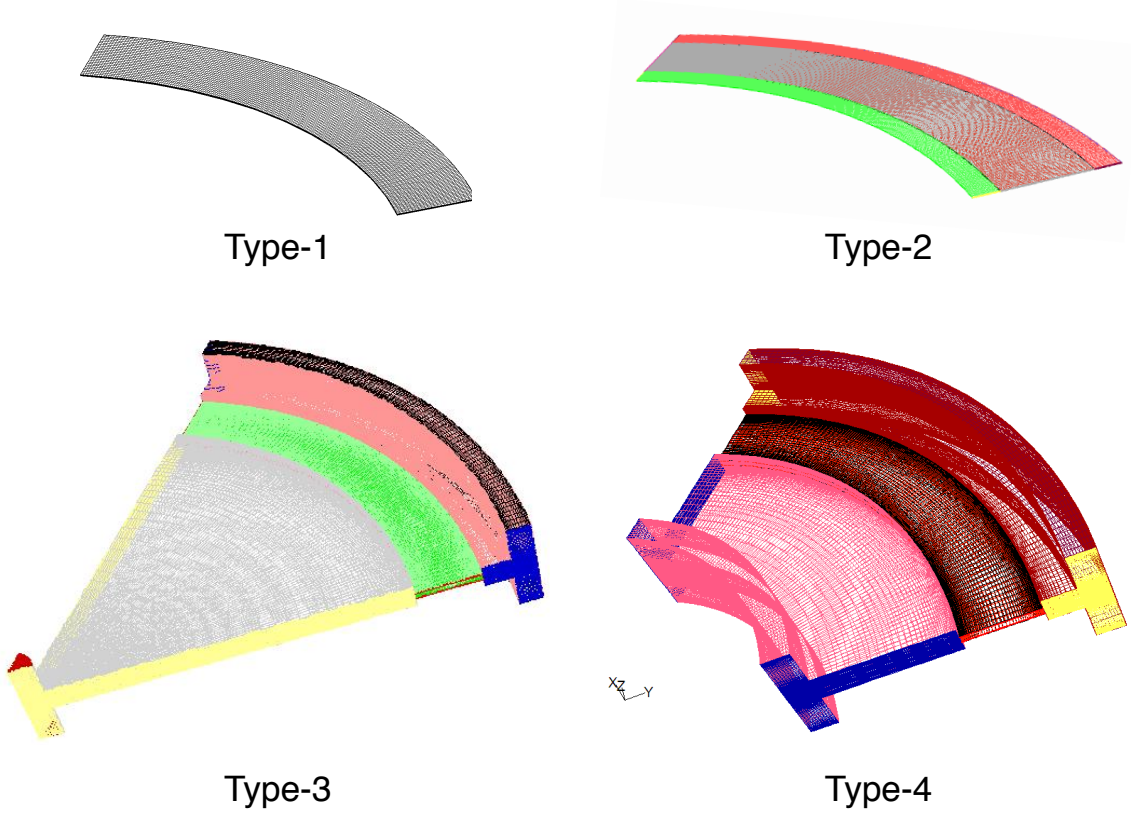

(a) Extended wall models

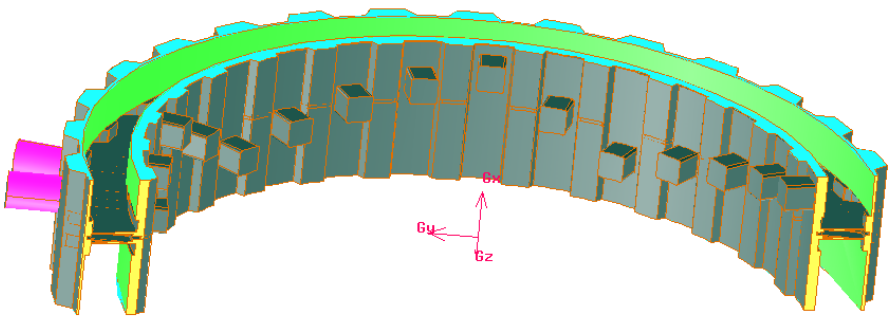

(b) Real test hardware

Figure 5.15: Extended wall model types to reduce numerical errors

the extended computational domains shown in Figure 5.15(a) offer a compromise in order to overcome the truncation of the computational domain.

Exhaustive computational tests were performed in order of increasing complexity and computational time. The open clutch simulation results for the extended-boundary models show convincingly that the Type-4 model performed best overall. Notice that the Type-4 model does not correspond to the largest domain. The results of Type-3, however, show larger errors in connection to the axisymmetric flow assumption that is made in the present formulation.

Figure 5.16 shows the velocity profiles corresponding to the Type-4 model when $\omega = 500\ rpm$. Due to the extended boundaries, the velocity profiles differ from the analytical solution under a zero-pressure boundary conditions. However, the errors due to the periodic boundary conditions are minimal. Figure 5.17 show the velocity field under the same flow conditions. Notice that due to the centrifugal force induced by the rotating friction plate, v_a has opposite signs at the inlet and outlet, but v_r and v_t do not change direction. Overall, the computational results are satisfactory despite the imperfect agreement with the analytical solution. However, it is anticipated that the velocity distribution in the real hardware will be more similar to that of Type-4 model rather than that of the analytical solution with a zero-pressure boundary conditions.

For many of the computational results of this study, the Type-1 model is still used even though the Type-4 model provides more accurate numerical solutions. Since engagement process is focused on this study, the squeeze flow becomes a main flow and the direction of the squeeze flow is outward. Therefore, the numerical errors at inlet and outlet is smaller than those of open clutch where the backflow may occur. Also, the numerical error at inlet and outlet dosz not affect at the inside of clutch as the numerical error are limited near inlet and outlet. Moreover, the use of Type-1 is done exclusively for economy in computational time. As additional com-

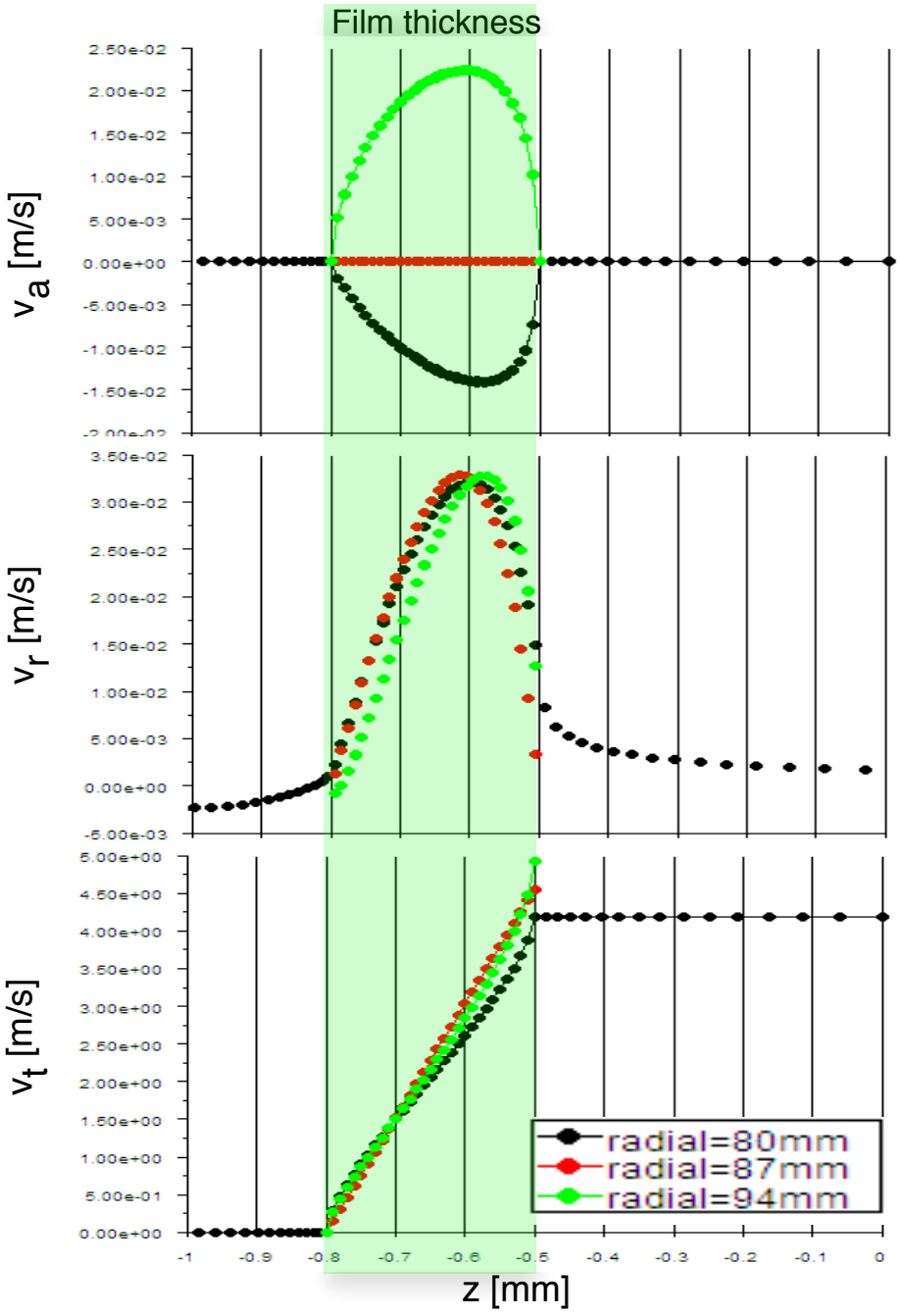

Figure 5.16: Velocity profiles of Type-4 at $r = 80$ (inlet), $87, 94$ mm (outlet) when $\omega = 500$ rpm

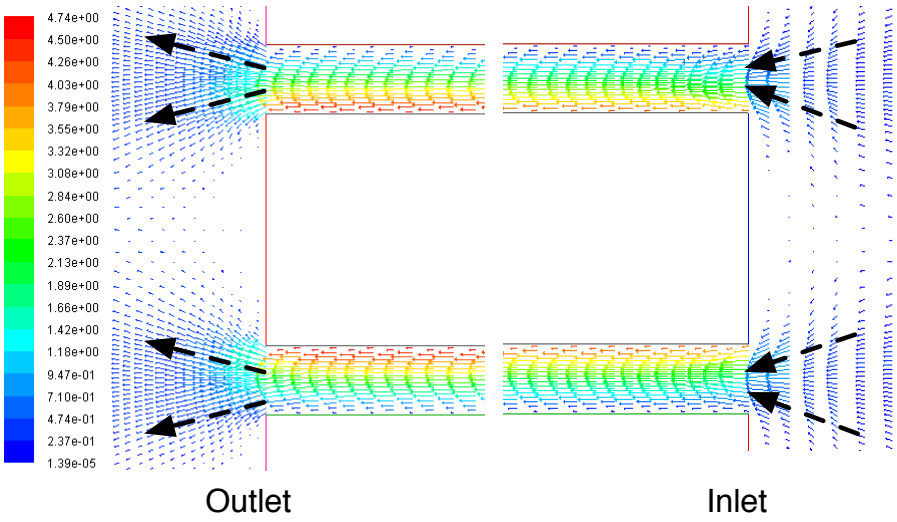

Figure 5.17: Velocity vector of Type-4 at inlet and outlet when $\omega = 500\ rpm$

ponents of the proposed multi-physics model are added, the CPU demands increase dramatically. Therefore, the Type-1 model offers a compromise between accuracy and computational efficiency. It is understood that the Type-4 model represent the correct modeling approach, however, so its use is reserved for future applications of the proposed methodology.

5.2.2.1 Three-dimensional grooved clutch model

The conventional and extended boundary models were modified to incorporated grooves in the friction material and the computational tests were repeated. Figure 5.18 shows periodic-boundary models for flow in the TGC. The oil temperature is 90 F. The flow has a single phase with $\rho = 834\ kg/m^3$, $\mu = 0.0344\ kg/ms$. The film thickness is $h = 0.25\ mm$. Figure 5.18(a) shows the computational mesh of the conventional of Type-0 model. Figure 5.18(b) shows an extended model of Type-4. For both models, zero pressure boundary conditions are specified at the inlet and outlet.

Figure 5.19 shows a comparison of computational results between the two models.

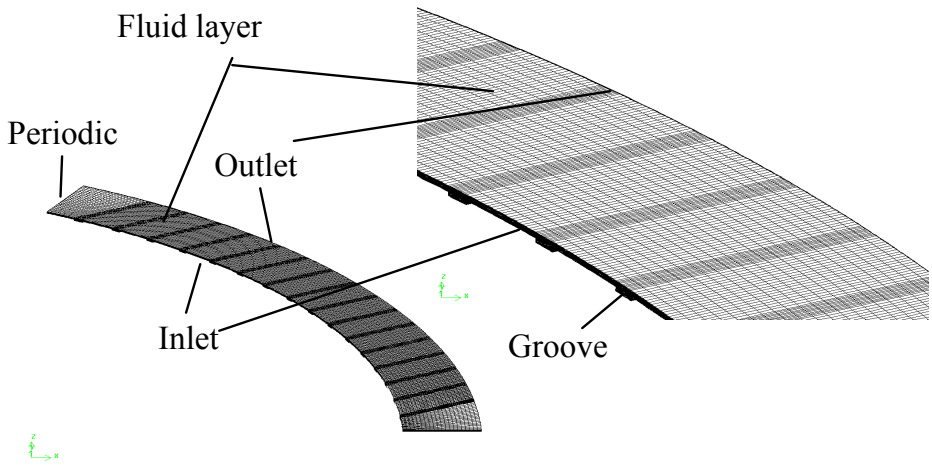

(a) Conventional model

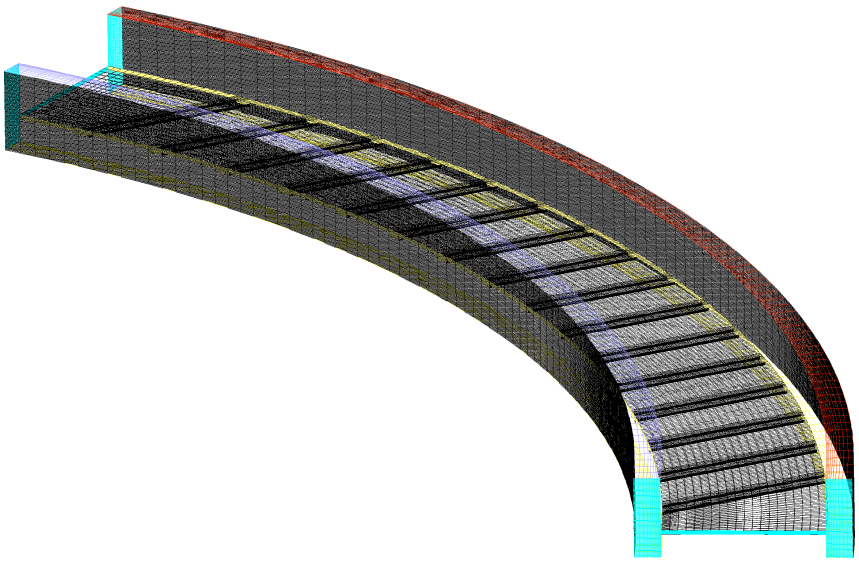

(b) Extended model

Figure 5.18: TGC periodic models for open clutch

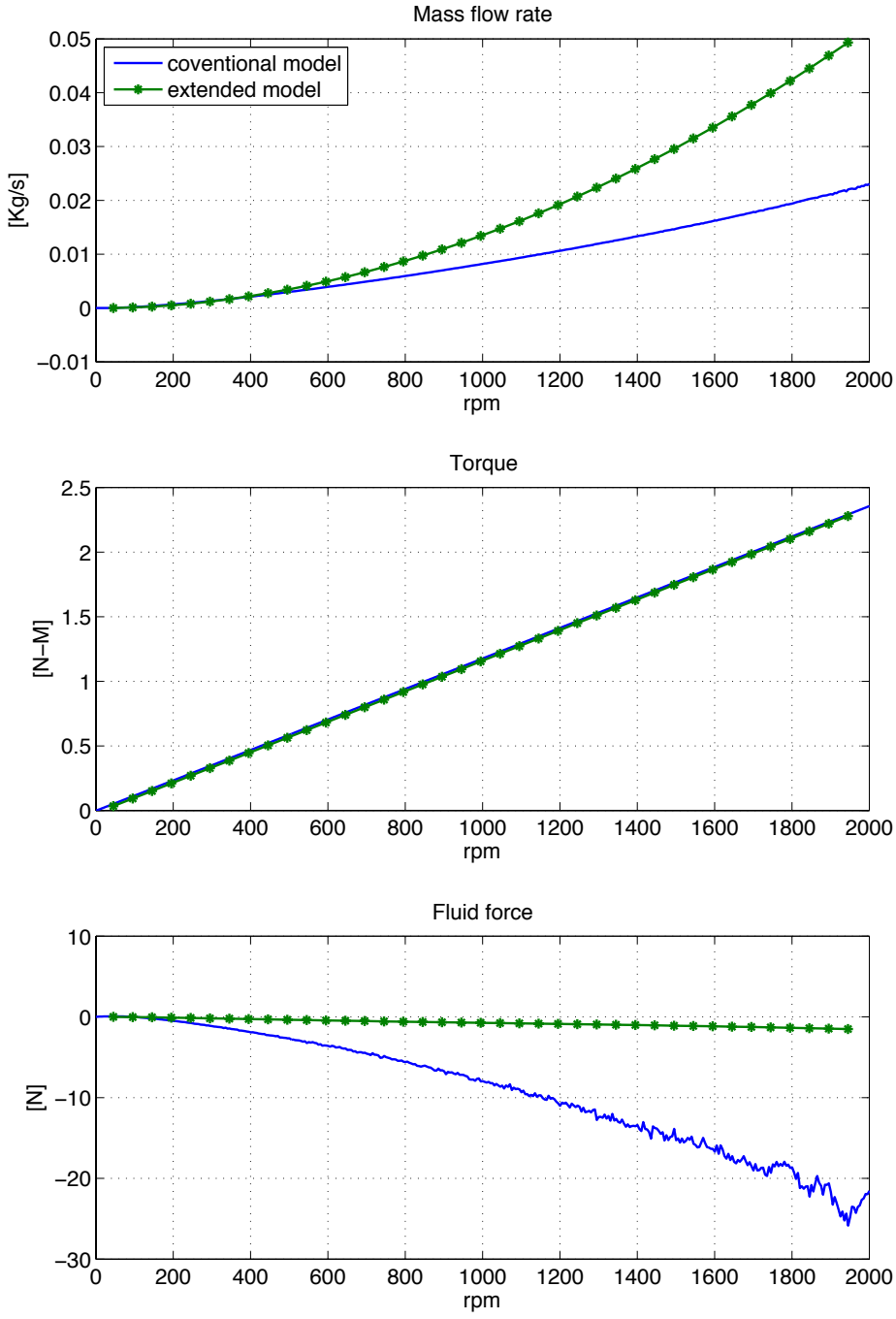

Figure 5.19: $\dot{m}$, torque and F_{fluid} for TGC single phase model

At low rotating speeds, the flow rates are low because the oil flow is driven by the centrifugal force. As rotation speed increases, the oil flow rate also increases and the applied force F_{fluid} decreases. The mass flow rate of the extended model is larger than that of the conventional model because the fixed pressure boundary condition of the conventional model restricts the oil flow depending on the rotation speed. In turn, this causes a difference in F_{fluid}. As mentioned in Section 3.1, an increase in flow rate results in an increase of F_{fluid}. The drag torque is proportional to rpm because single phase flow was assumed. It should be mentioned that at low angular velocities, the measured drag torque in wet clutch tests is proportional to the corresponding rotational speed because the presence of air bubbles effect is minimal.

5.2.3 Multiphase Wet Clutch Model

Two dimensional simulations for disks without grooves were performed to find the general characteristics of multi-phase flow in an open wet clutch.

Figure 5.20 compares the viscous torque between the multi-phase model and the single-phase model at a constant mass flow rate $\dot{m}_{in} = 0.02\ kg/s$. Both backflow options, i.e. normal flow to the boundary and neighboring cell direction were examined. As expected, in Figure 5.20(a), the torque in the single-phase model is proportional to the rotating speed. However, in the multi-phase flow model the drag torque begins to decrease at approximately 3000 rpm. Furthermore, the drag torque of normal to boundary backflow is larger than that of the neighboring cell option. The associated volume fraction contours are shown in Figure 5.20(b). Obviously, the air entrainment corresponding to the neighboring cell option is much larger than that of the normal to boundary option.

Computed torque profiles are compared under zero pressure or mass flow inlet boundary conditions in Figure 5.21. For mass flow inlet boundary conditions, $\dot{m}_{in} = 0.02\ kg/s$ is specified at the boundary. The comparison between the two

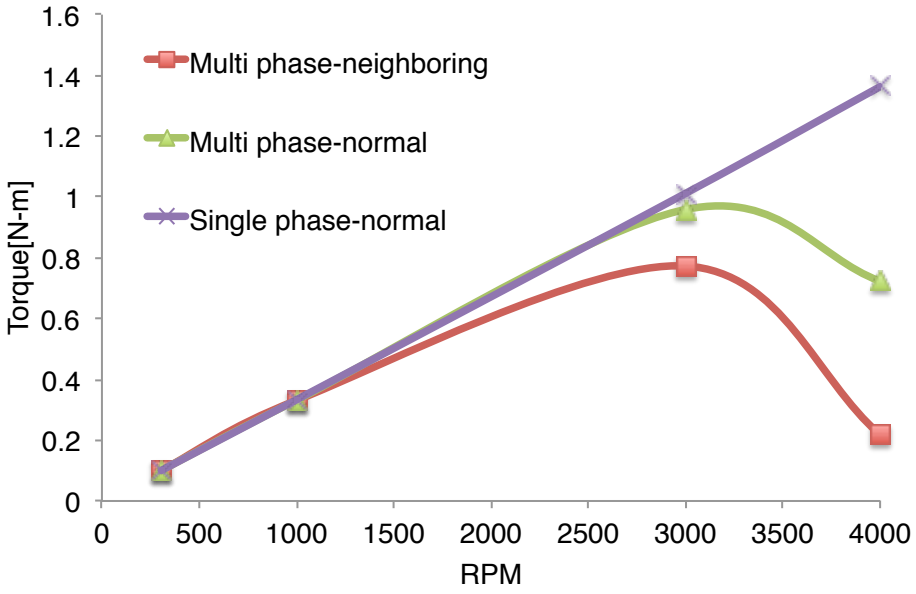

(a) Drag torque curves depending on *rpm*

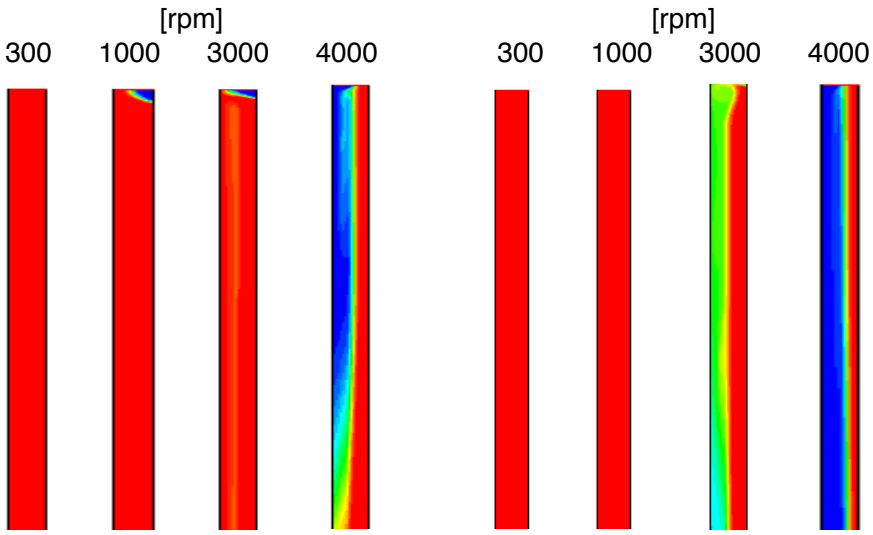

(b) Volume fraction contour: L) Normal to boundary, R) From neighboring cell

Figure 5.20: 2D non-grooved model with $\dot{m}_{in}$: $h = 0.3\ mm$, $\mu = 0.02\ kg/ms$, $\dot{m}_{in} = 0.02\ kg/s$

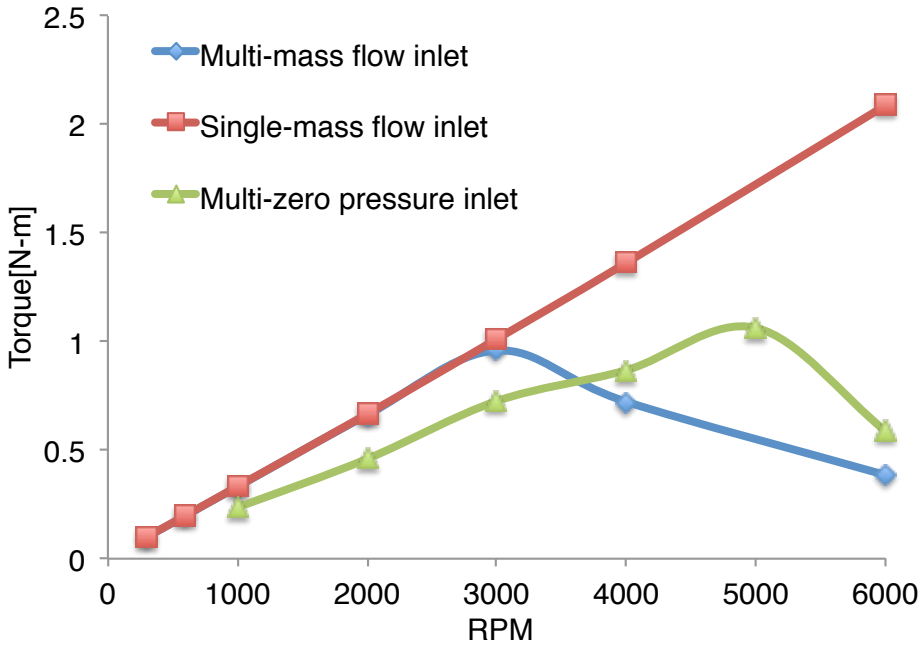

(a) Volume fraction contour depending on rpm

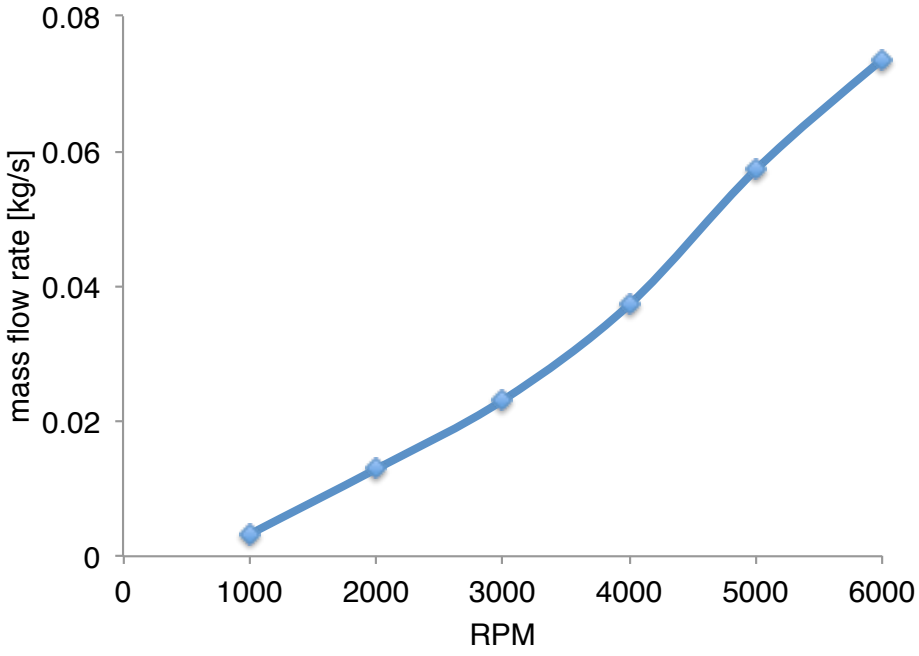

(b) Mass flow rate for multi-phase model with $p_{in} = 0$

Figure 5.21: Torque curves of 2D non-grooved models: $p_{in} = 0$ vs $\dot{m}_{in} = 0.02\ kg/s$

inlet boundary conditions shows that the peak torque with a zero-pressure inlet occurs at a higher rotation speed than that of a mass-flow inlet. Based on a constant $\dot{m}_{in} = 0.02\ kg/s$, the torque with a mass-flow inlet begins to decrease after 3000 rpm, but one with a zero-pressure inlet boundary, continues to increase as shown in Figure 5.21(b). When $\dot{m} = 0.02\ kg/s$ for the zero-pressure boundary model, the resulting rotation speed is approximately 2700 rpm. This may indicate that the drag torque can be reduced if $\dot{m} \leq 0.02\ kg/s$ beyond 2700 rpm.

Figure 5.22(a) shows the oil volume fraction as a function of rotational speed after reaching steady state. The oil volume fraction contours shown correspond to normal-to-boundary conditions with $p_{in} = 0$. The curve A-A corresponds to the boundary line between the fully filled with oil area and the partially filled area of the plate. The results show that after passing the peak drag torque, the volume fraction of oil volume increases. However, the pattern does not show a monotonic increase of volume fraction with increasing rpm. This could be attributed to numerical error, but also to the imperfect boundary conditions. Contrary to the results of the mass-flow inlet model in Figure 5.20(b), the air volume at 1000 rpm occupies a large part of the clutch volume. Figure 5.22(b) shows the oil film and velocity field for a rotating speed equal to 2000 rpm. The oil flows out along the rotating wall and air comes in from the outlet along the stationary wall. As the angular velocity of the rotating wall increases, air fills the clutch gap volume more.

5.2.4 Three-Dimensional Models

Following the study of non-grooved 2D models, 3D grooved TGC model tests were performed. Table 5.3 shows the oil properties and geometric configuration for the TGC model used in the tests.

In Figures 5.23 - 5.30, oil volume contours for mass-flow inlet and zero-pressure inlet are shown for the 3D TGC model. It was assumed that air can only flow into

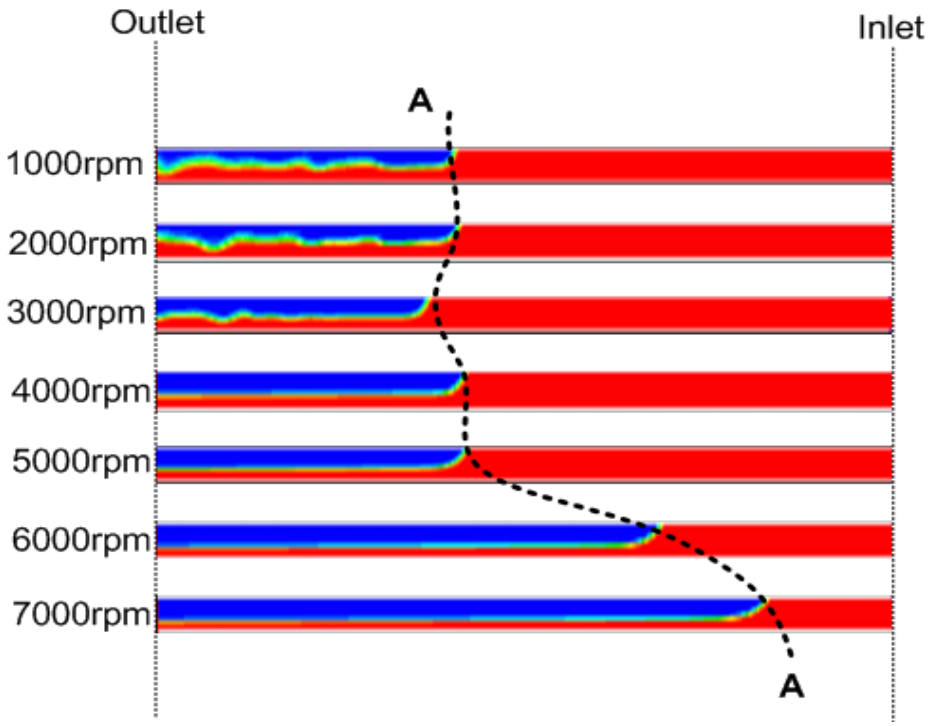

(a) Volume fraction contour depending on *rpm*

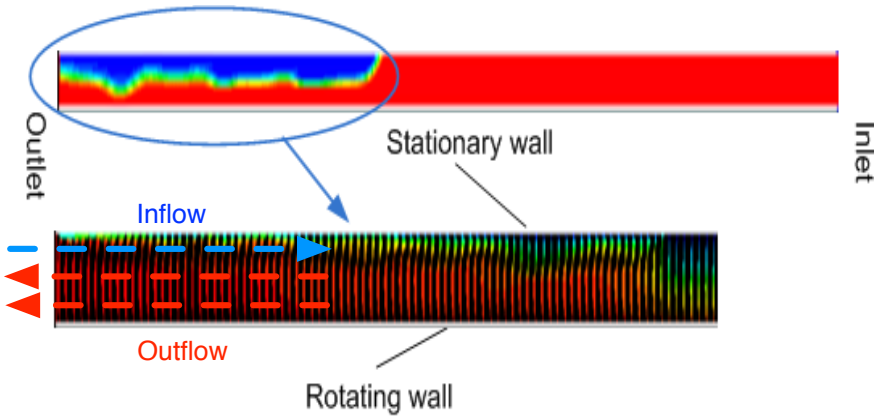

(b) Volume fraction contour and velocity vector at 2000 *rpm*

Figure 5.22: Volume faction contour of 2D non-grooved model with $p_{in} = 0$

Table 5.3: Properties for multiphase model of open clutch

	$\rho\ [kg/m^3]$	$\mu\ [kg/m \cdot s]$	$r_1\ [mm]$	$r_2\ [mm]$	$h\ [mm]$	initial air
2D	834	0.02	82.8	92.65	0.3	0
3D	834	0.0344	82.8	92.65	0.25	0

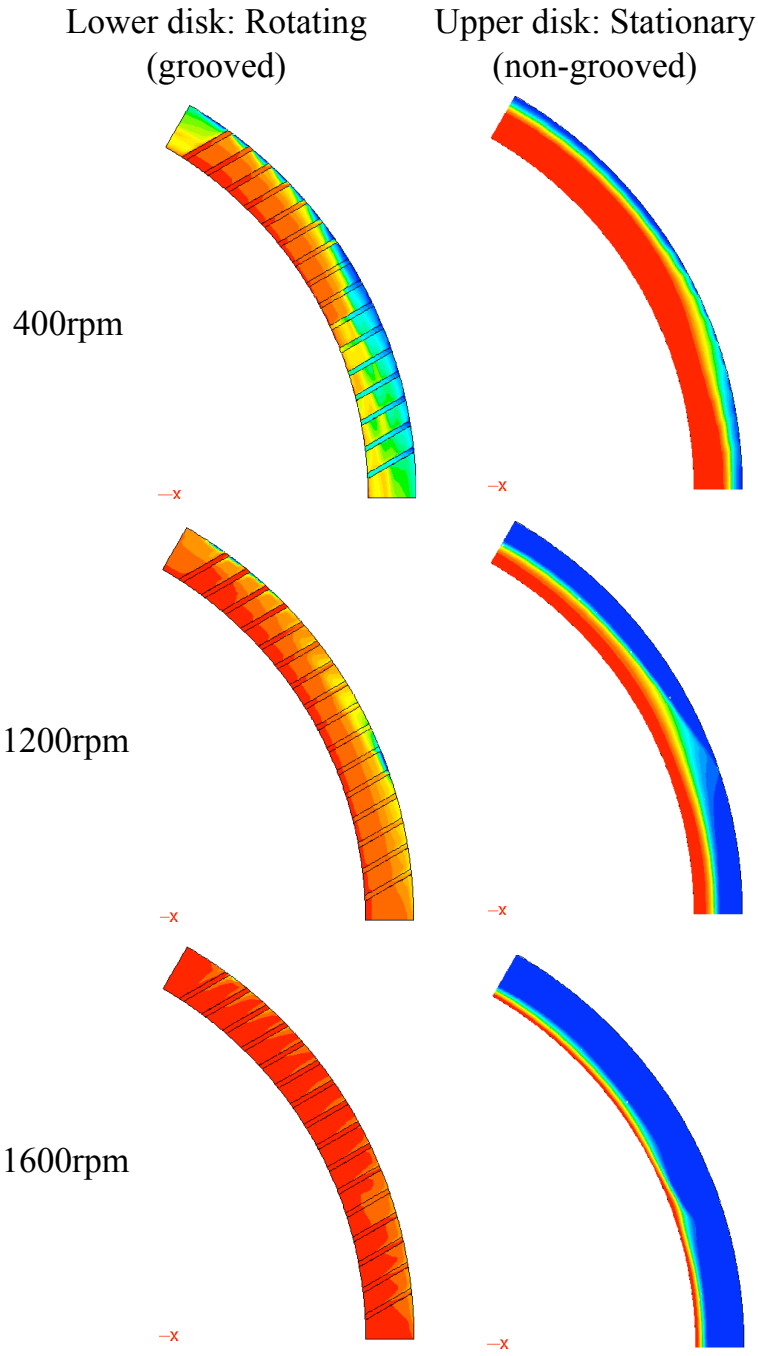

Figure 5.23: TGC oil volume contour: $p_{in} = 0, \theta = 0°, \sigma = 0\ N/m$

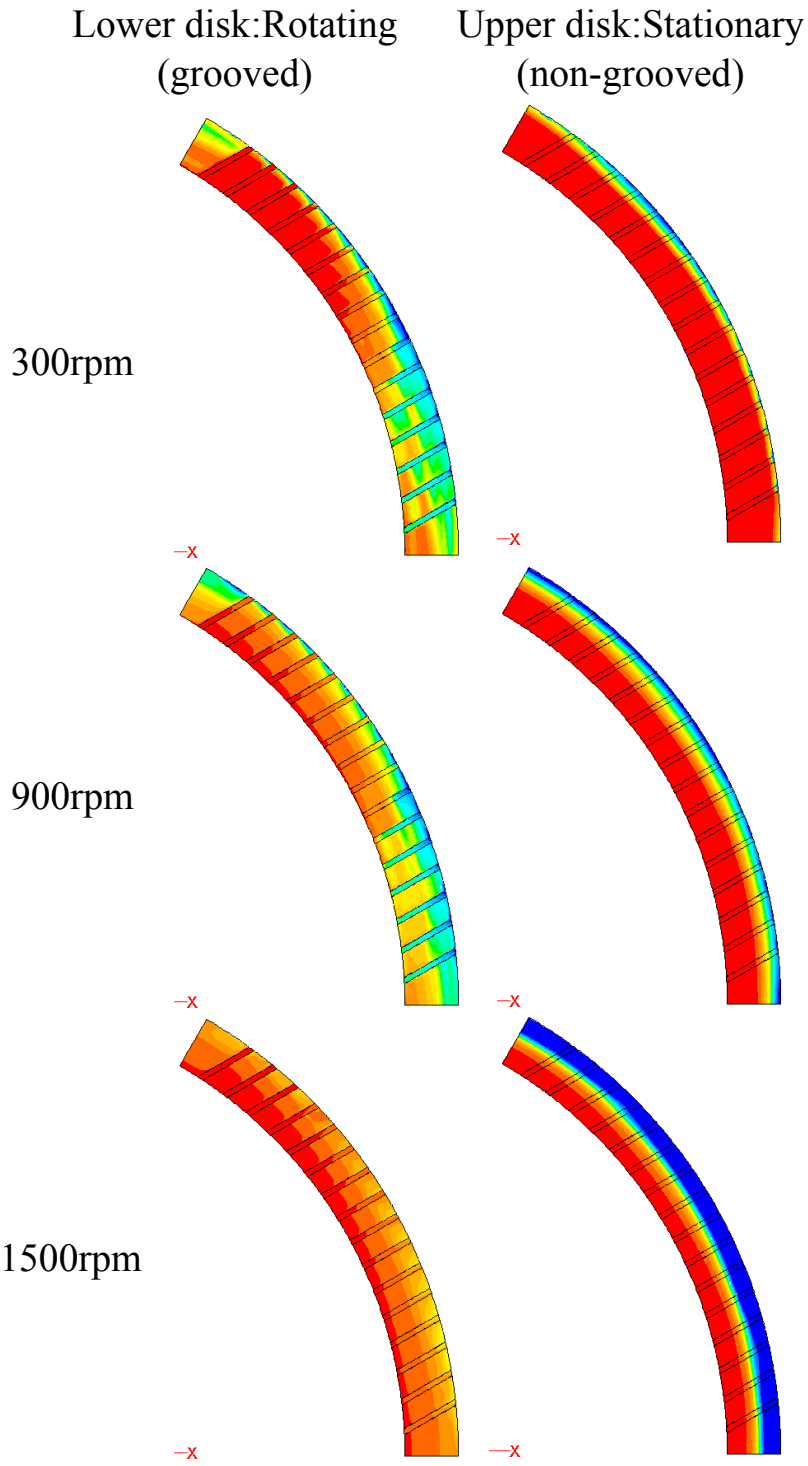

Figure 5.24: TGC oil volume contour: $p_{in} = 0, \theta = 170°, \sigma : 0.03\ N/m$

the clutch through outlet because air is filtered from the oil in the clutch test system. Examination of the oil volume fraction results of the mass-flow inlet model, reveals that the zero-pressure inlet model of Figure 5.23 contains a higher air volume fraction. Therefore, the peak torque of the zero-pressure inlet model is formed at lower rpm than that of the mass-flow inlet model. Increasing the rpm causes the oil to flow out along the surface of the rotating disk while air flows in along the stationary disk. Finally, Figures 5.23 and 5.24, shown that changing the oil surface tension and contact angle can prevent the entrainment of air in the clutch.

This is further confirmed by the results of Figures 5.25 and 5.26. Increasing the surface tension σ, the formation of air volume is obviously restricted. According to *Yuan et al.* (2007), the centrifugal force and oil surface tension are balanced at an effective outer radius. Therefore, a higher surface tension makes the oil at the outer radius difficult to penetrate because that requires a larger centrifugal force than that provided by the rotating disk. Also, notice that oil flows out downstream of the grooves because of the pressure difference across the sides of the groove as shown in Figures 5.27 and 5.28.

Figures 5.29 and 5.30 compare the oil volume fraction for mass flow rate $\dot{m} = 0.0058\ kg/s$ and $\dot{m} = 0.0116\ kg/s$. It is clear that a high inlet mass flow rate delays the increase in air volume, as the rotating speed increases.

Finally, Figure 5.31, shows a comparison of drag torque curves for the open clutch model of TGC under various conditions. Since the single phase simulations did not consider the effect of air bubbles in the wet clutch, the viscous torque increases monotonically as the rpm is increasing. On the other hand, for the multi-phase model, the drag torque increases until a peak drag torque is reached. After its peak, the drag torque decreases until it approaches a steady value because the air volume fraction is directly related to the viscous torque T. The air volume fraction shows a large variation after reaching the peak torque. In addition, the peak torque value is

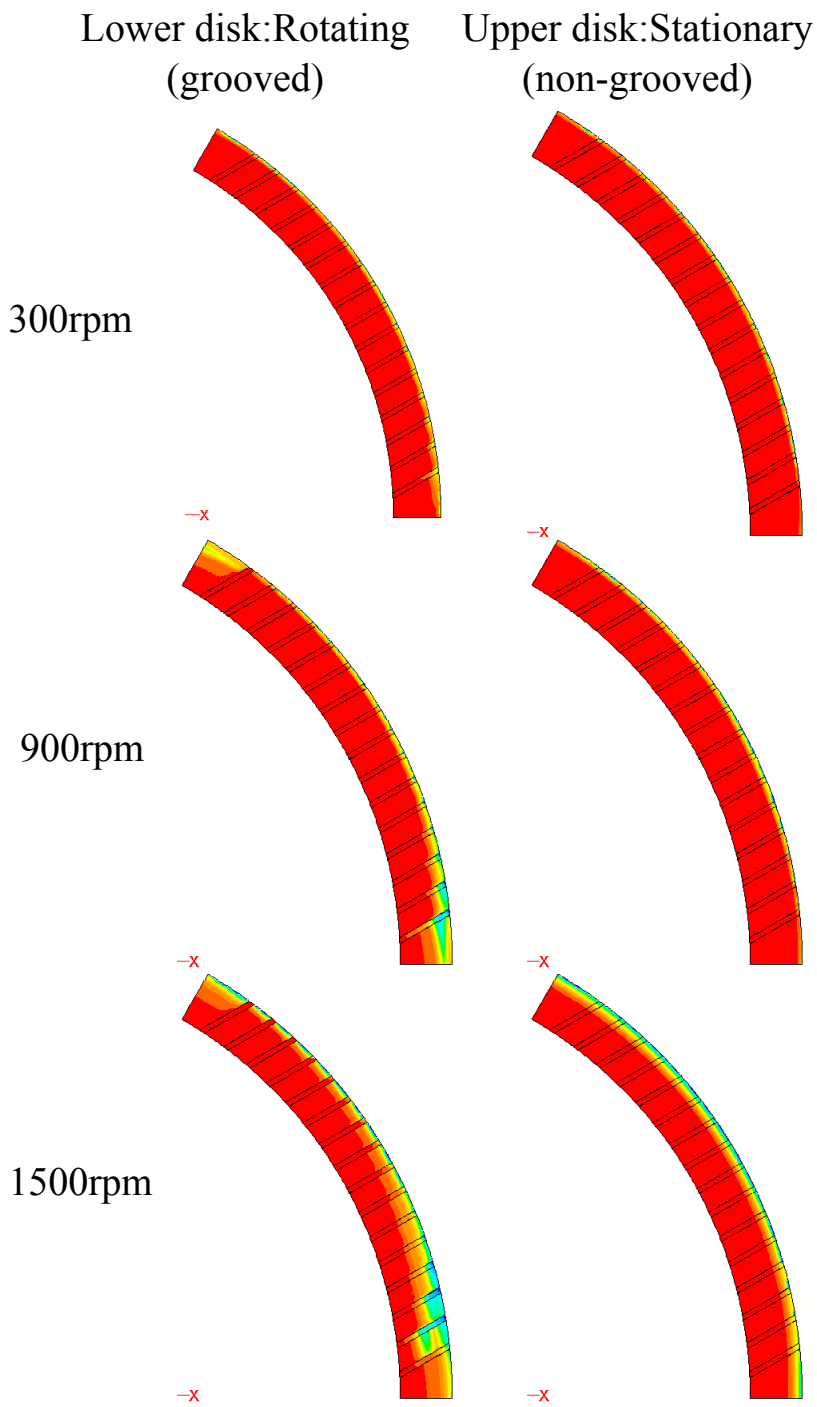

Figure 5.25: TGC oil volume contour: $\dot{m} = 0.0058\ kg/s, \sigma = 0.3\ N/m, \theta = 170°$

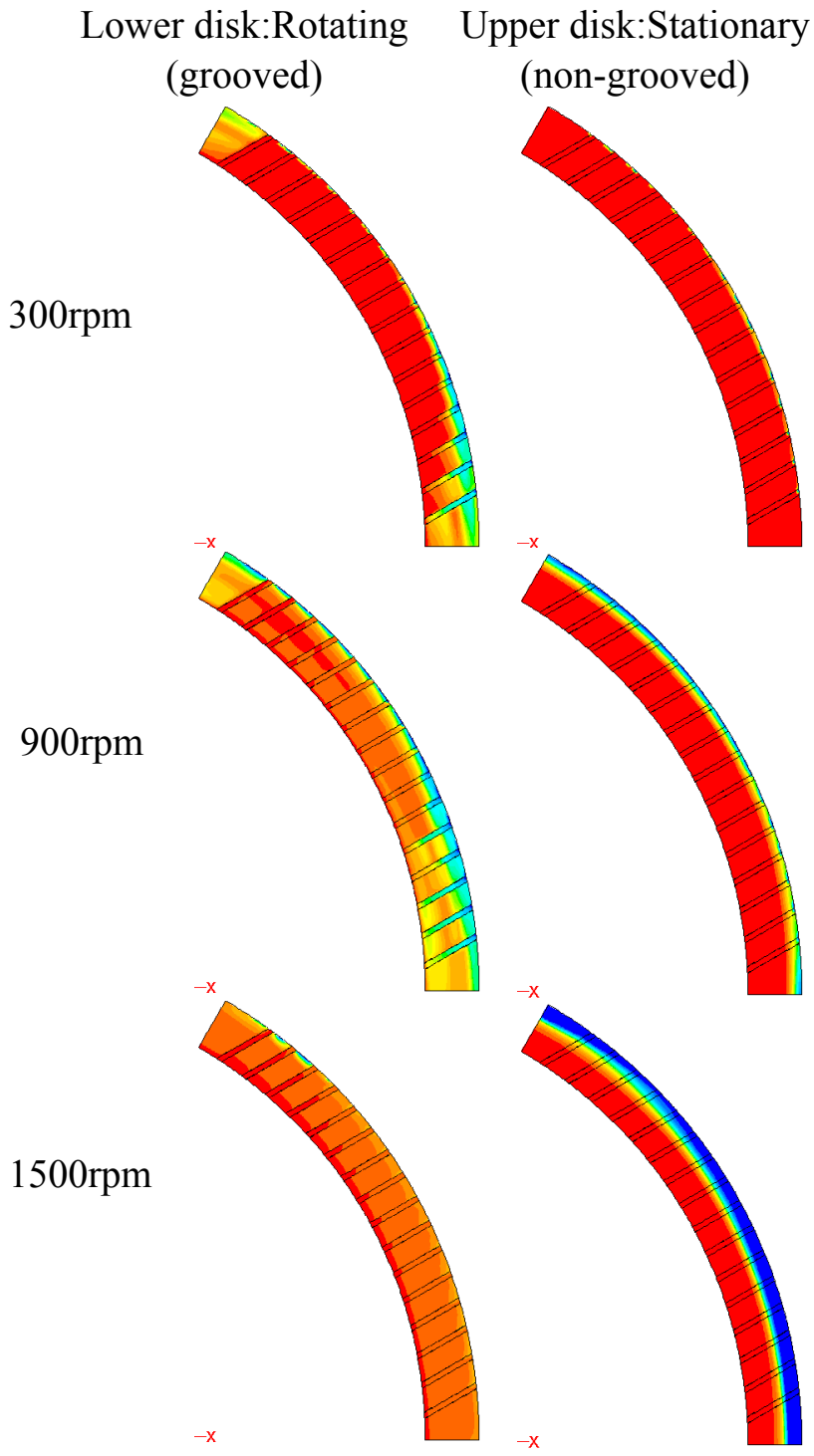

Figure 5.26: TGC oil volume contour: $\dot{m} = 0.0058\ kg/s, \sigma = 0.03\ N/m, \theta = 170°$

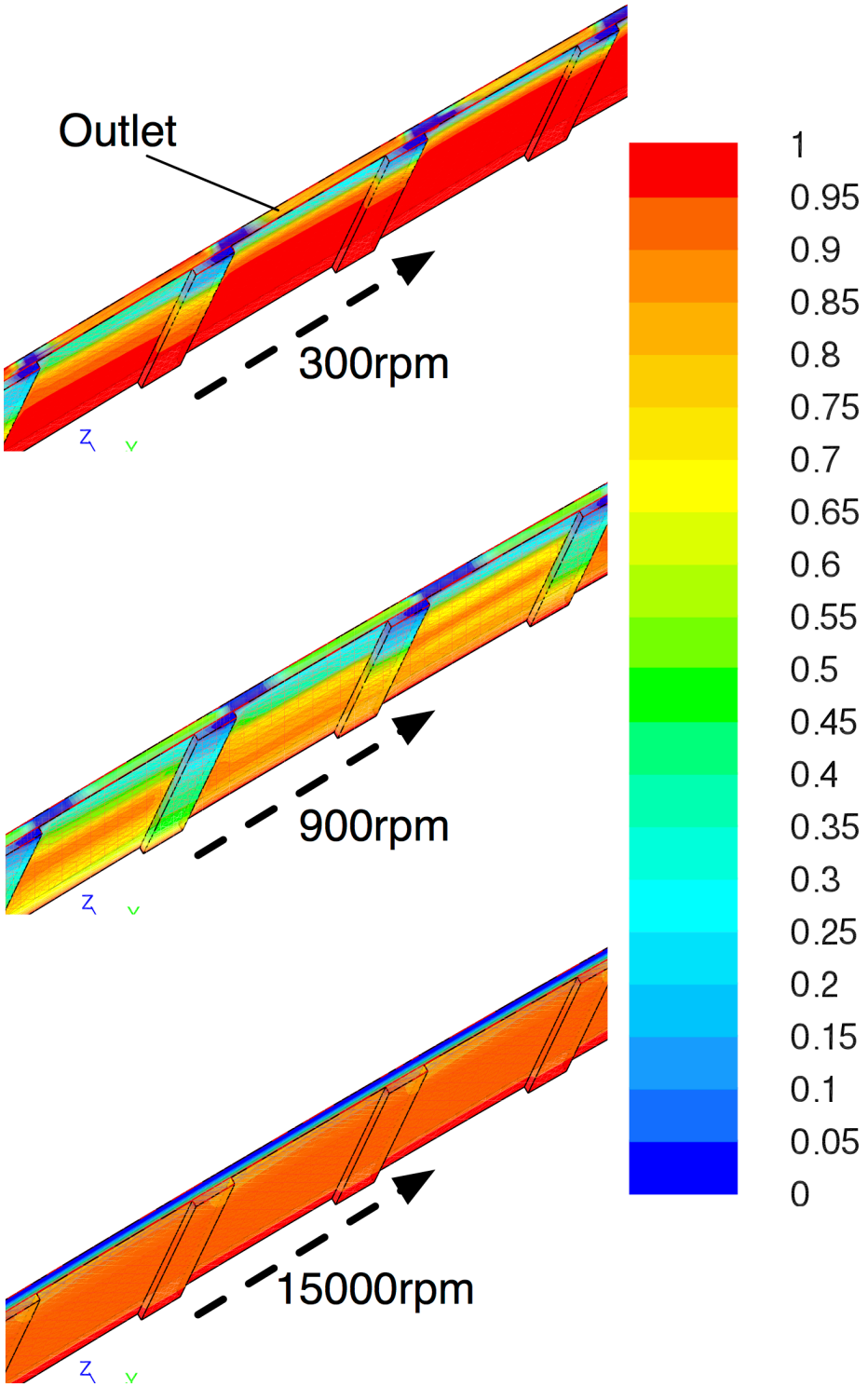

Figure 5.27: TGC oil volume contour at outlet: $\dot{m} = 0.0058\ kg/s, \sigma = 0.03\ N/m, \theta = 170°$

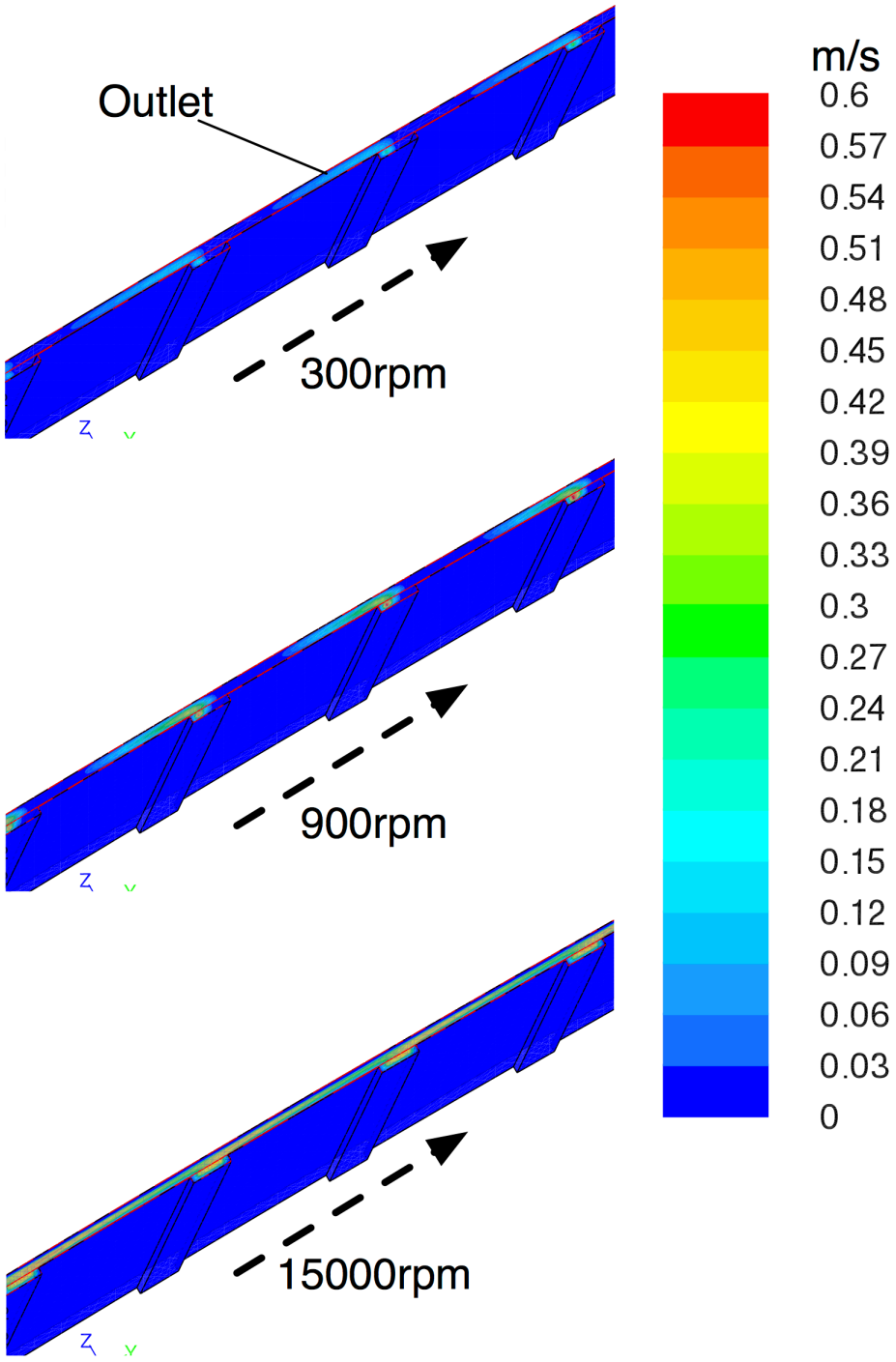

Figure 5.28: TGC radial velocity contour at outlet: $\dot{m} = 0.0058\ kg/s, \sigma = 0.03\ N/m, \theta = 170°$

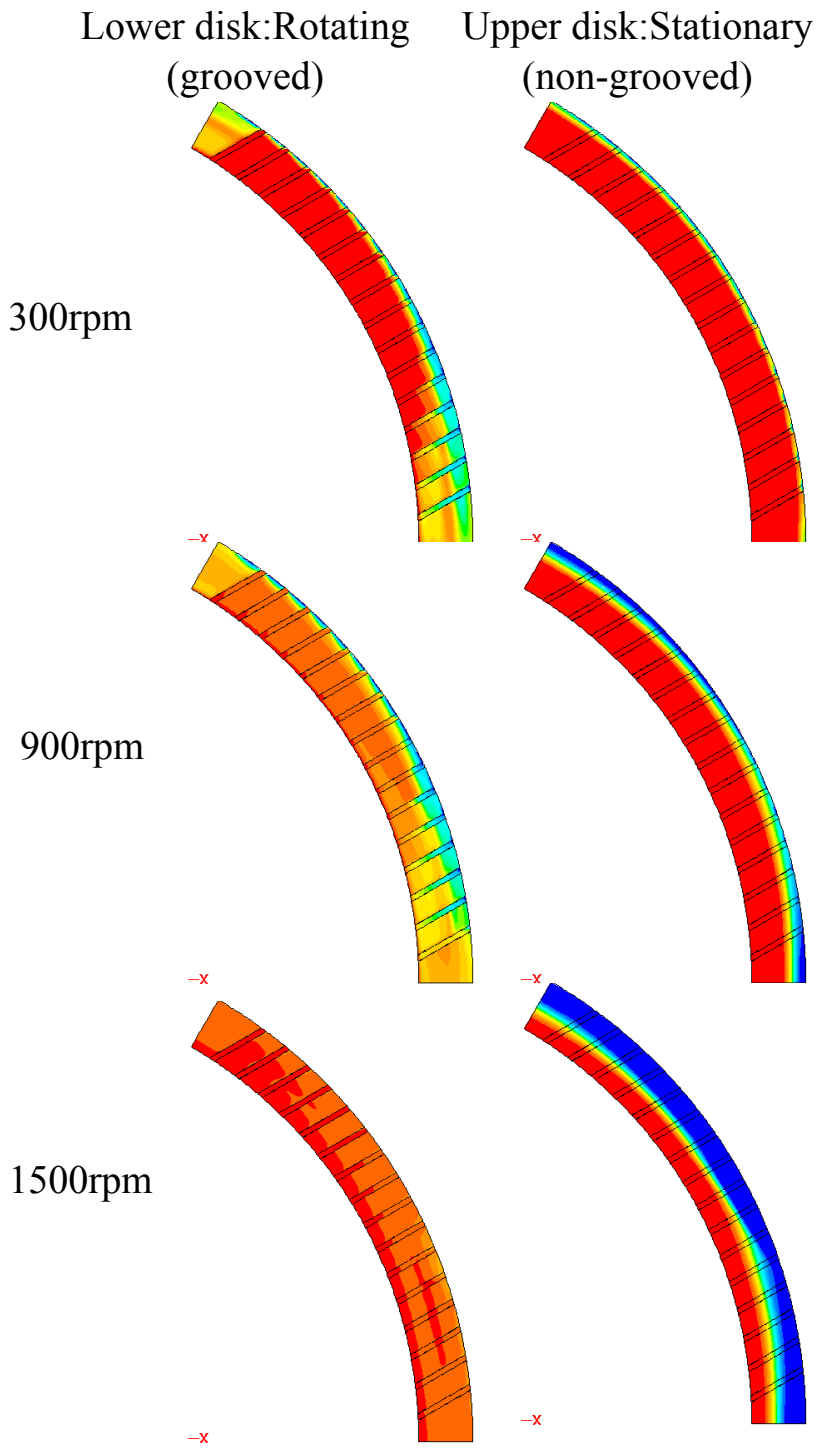

Figure 5.29: TGC oil volume contour: $\dot{m} = 0.0058\ kg/s, \theta = 0, \sigma = 0$

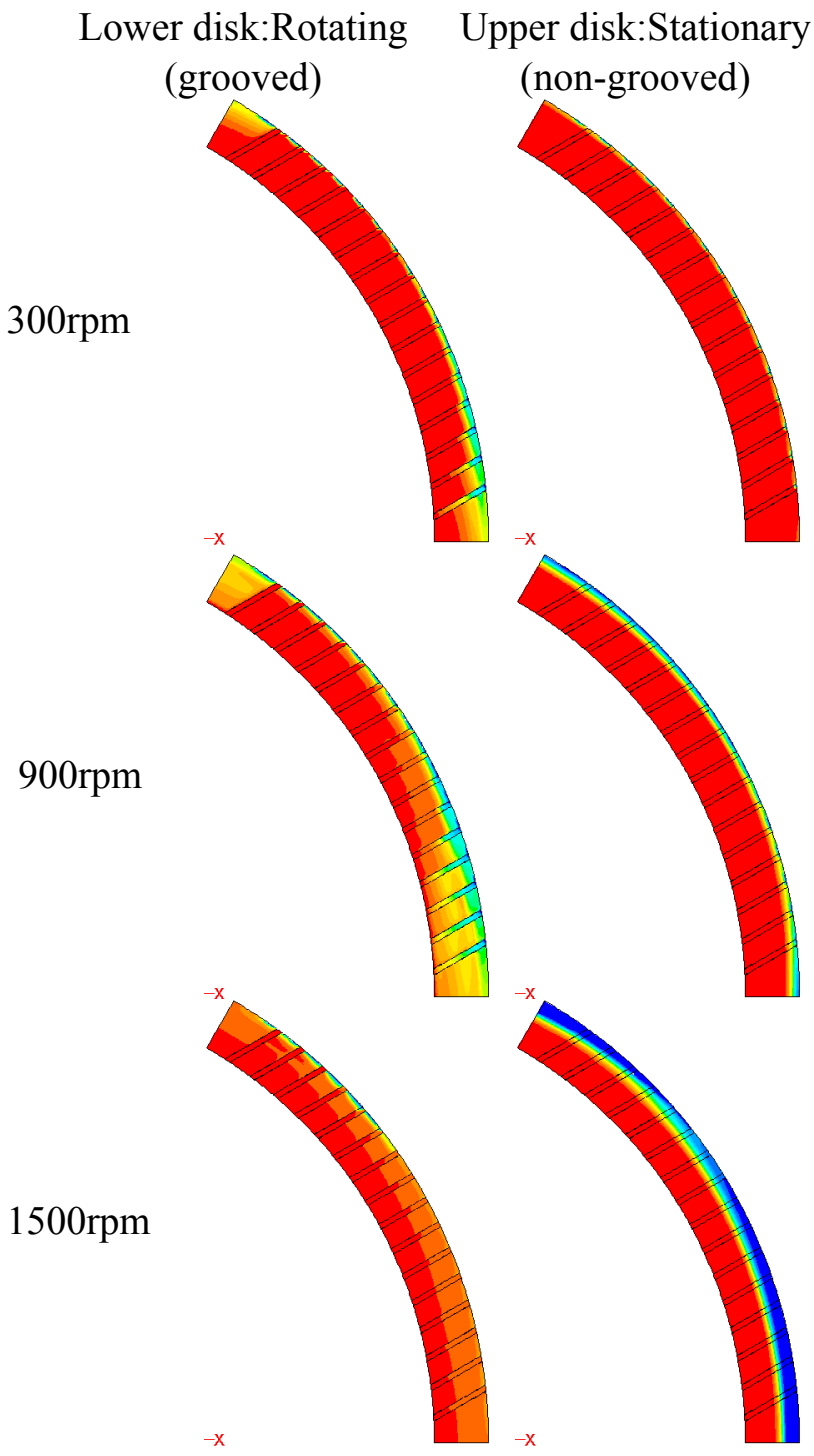

Figure 5.30: TGC oil volume contour: $\dot{m} = 0.0116\ kg/s, \theta = 0, \sigma = 0$

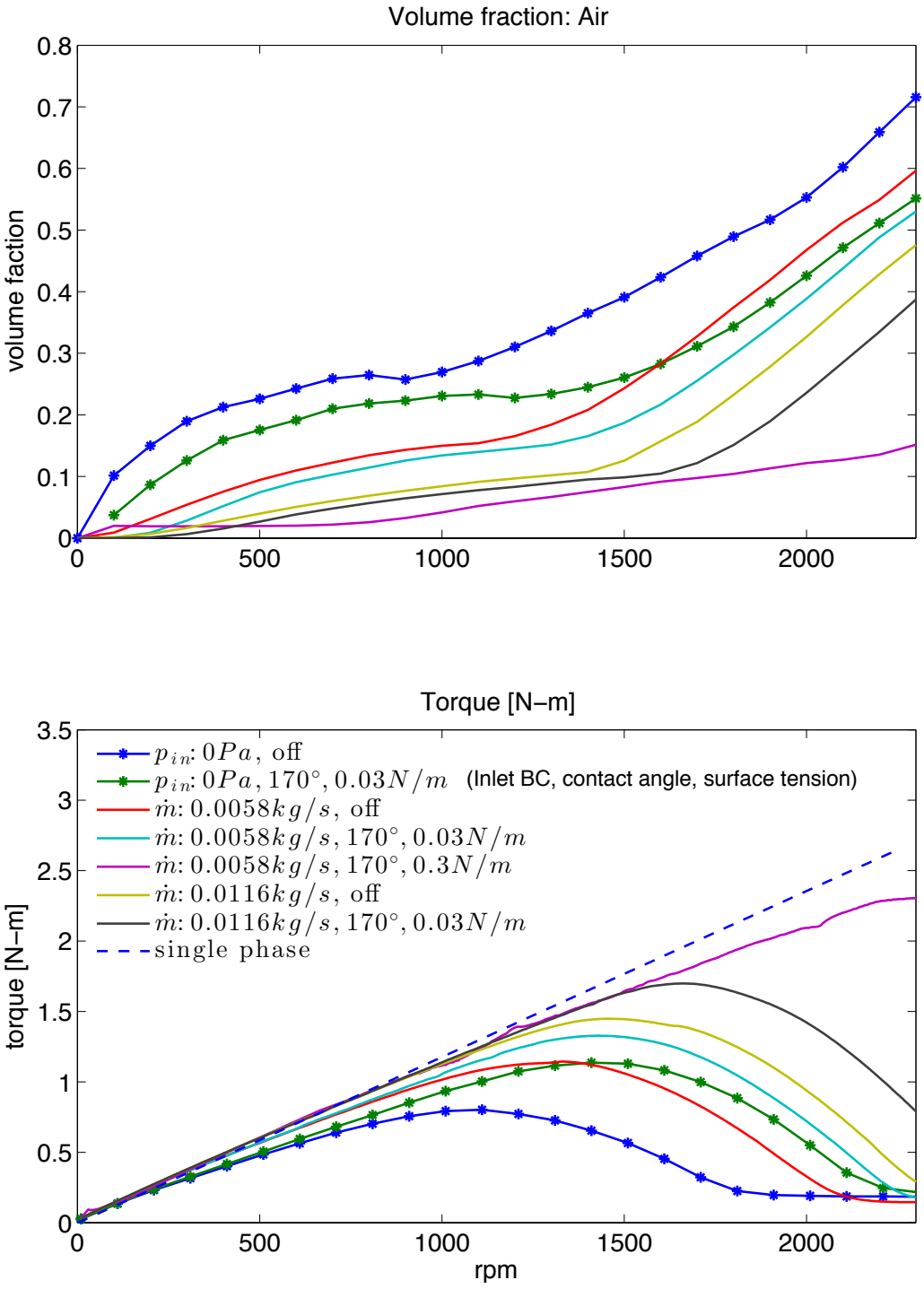

Figure 5.31: Volume fraction and torque: TGC model

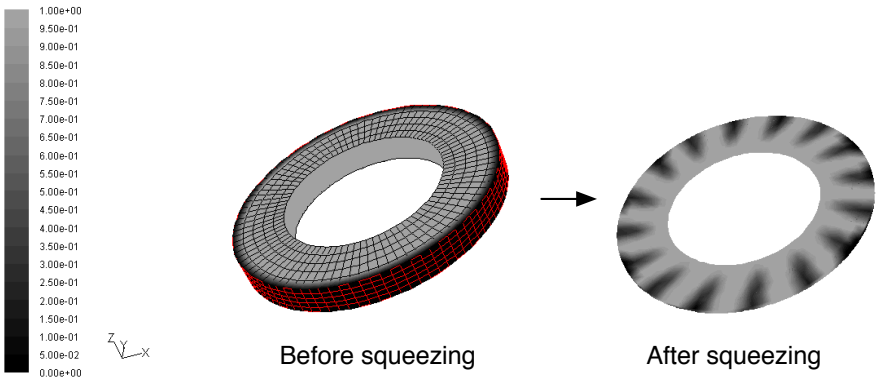

Figure 5.32: Volume fraction contour: 3D non-grooved model during squeezing

proportional to the mass flow rate, as shown in Figures 5.23 - 5.30. An increase in mass flow rate increases both the peak torque and the *rpm* of the peak torque. The numerical results also show that physical characteristics of the interface between oil and air also affect the drag torque. The same is true for surface tension and wall adhesion angle.

5.3 Clutch Engagement Process

As described in Chapter IV, the proposed iterative scheme and the CFD model were combined in order to simulate the squeeze film process in a wet clutch. To include surface roughness effect on squeeze flow, pressure flow factors were used in a separate subroutine. The heat transfer module, including frictional heat generation and asperity contact pressure were also included. As a first step, to configure the moving mesh for squeeze motion, a constant squeeze velocity was applied to a non-grooved model as shown in Figure 5.32. The decrease in oil film thickness can be easily verified.

Next, to test the effectiveness of the iterative scheme, the CFD simulations for a rectangular plate and an annular plate were compared with analytical solutions that were previously described in Chapter III. Zero-pressure boundary conditions or

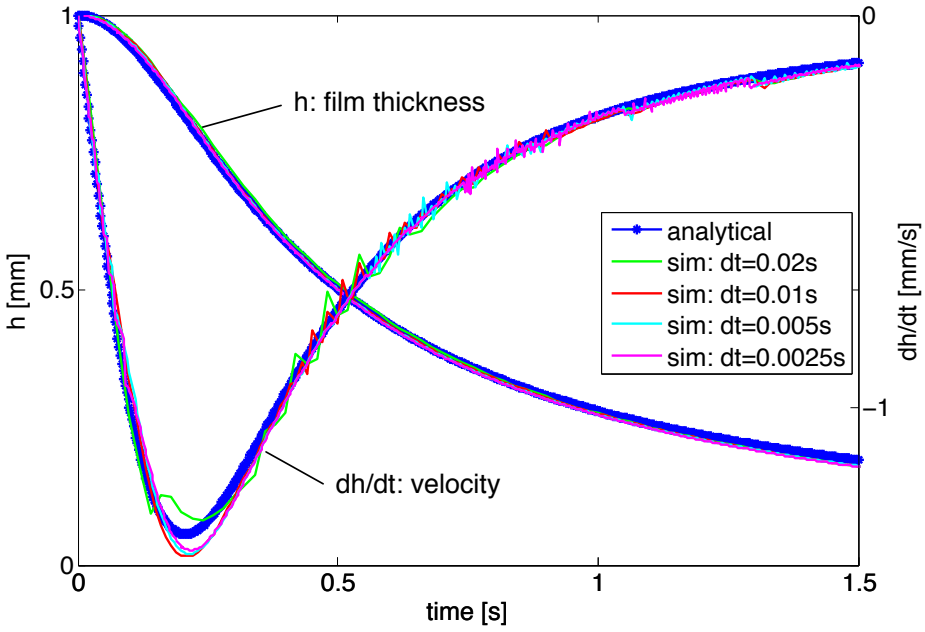

Figure 5.33: Validation: Rectangular plate model

Neumann boundary conditions were used at the inlet and outlet of the CFD model according to the boundary conditions derived for the analytical solutions.

Figure 5.33 shows a comparison of the results for a 2-D rectangular plate. With small time steps, such as 0.005 s or 0.0025 s, the simulation results for the oil film thickness show good agreement with the analytical solution.

Focusing next on Figure 5.34 corresponding to squeeze flow in the annular plate model without an inlet boundary, it was found that as the error criterion e_{crit} decreases, the step patterns in the solution profiles of the film thickness and the squeeze velocity increase. Then, a validation test with an annular disk was performed. The annular disks had were stationary and the oil viscosity and density of the validation model were 0.0344 kg/ms and 834 kg/m^3, respectively. The results in Figures 5.35 and 5.36 demonstrate that as the simulation time step is reduced, the simulation converges to the analytical solutions.

Early computational experiments using a large value for e_{crit} have also shown excellent agreement with the analytical solution. However, as shown in Figure 5.34,

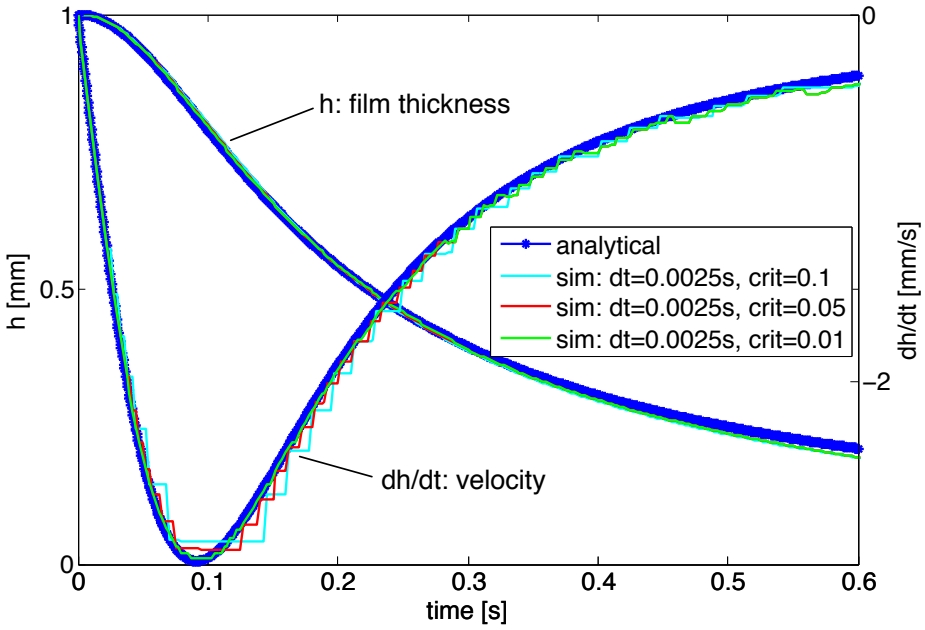

Figure 5.34: Validation: Annular plate model without inlet boundary

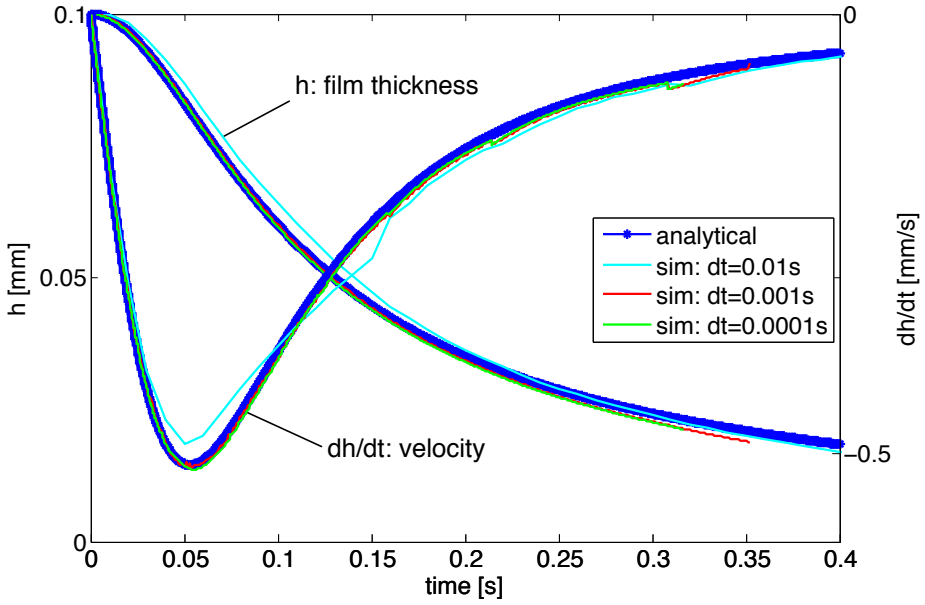

Figure 5.35: Validation: Annular plate model with zero pressure boundary

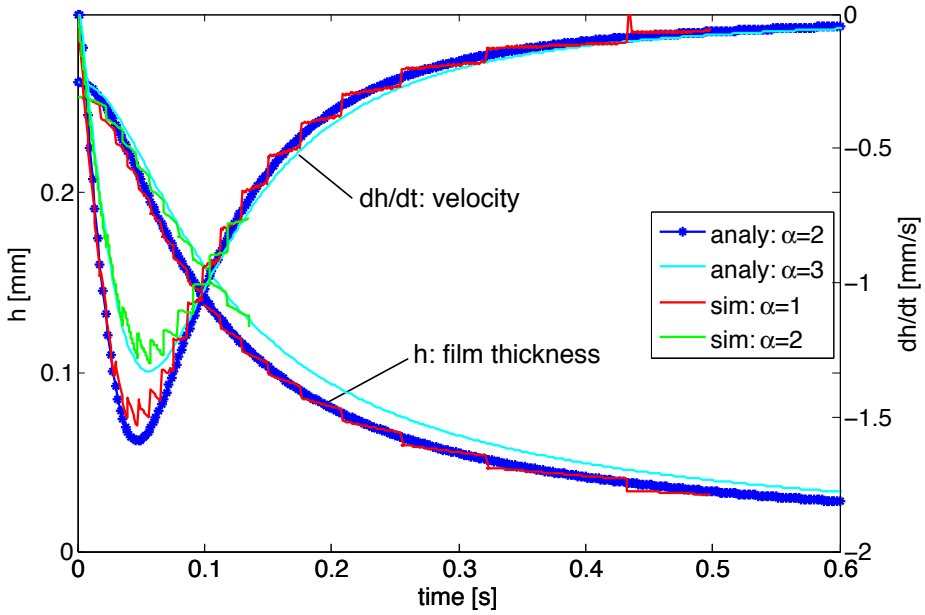

Figure 5.36: Validation: Annular plate model with inlet pressure profile

a large e_{crit} causes step patterns in the solution profiles of the film thickness and the squeeze velocity. The convergence criterion was further reduced to improve the smoothness of the solution. With $e_{crit} = 0.01$, the simulation profiles became smooth. The film thickness and squeeze velocity profiles of Figure 5.35 show the simulation results when e_{crit} is 0.01 and the time step is equal to 0.01 s, 0.001 s and 0.0001 s. The profiles are smooth and agree well with the analytical solutions. It is concluded that with sufficiently small time steps and a small e_{crit}, the squeeze film simulation using the proposed iterative method can provide accurate numerical solutions.

Finally, Figure 5.36 shows the simulation results for the annular plate model when the inlet pressure profile corresponding to a mixed boundary condition is applied. Again, the simulation results agree well with the analytical solution.

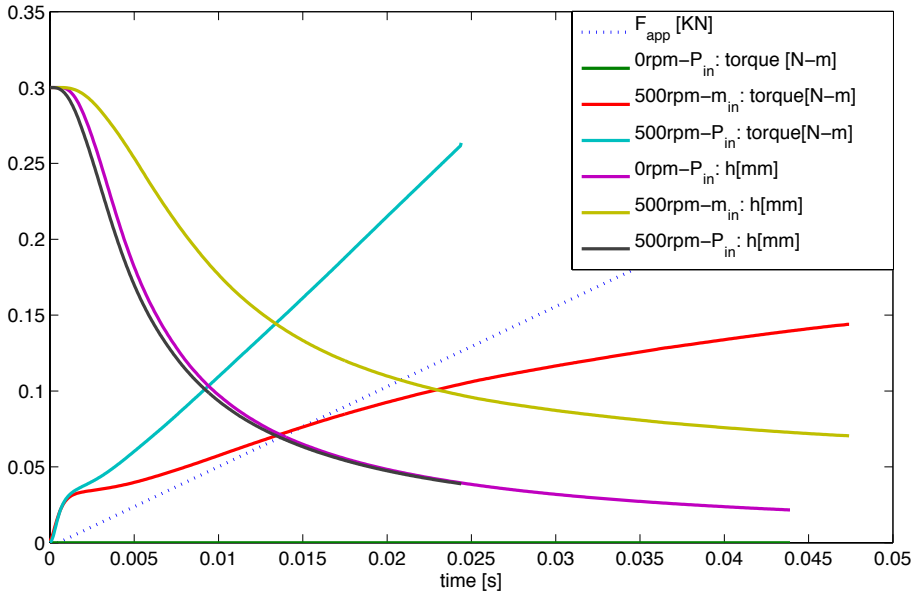

Figure 5.37: Squeeze film characteristics with p_{in} model or $\dot{m}_{in}$ model

5.4 Viscous Torque Transfer

The clutch engagement model, without considering asperity contact and permeability of the friction material, was run to validate the iterative scheme for squeeze-flow motion. Figure 5.37 shows the oil film thickness and viscous torque profiles with $p_{in} = 0$ or $\dot{m}_{in} = 0.003\ kg/s$ boundary condition for $\omega = 0$ or 500 rpm. The initial film thickness is 0.3 mm. The results show that the squeeze motion is affected by the different inlet boundary conditions while the rotating speed has a small effect on the squeeze velocity for single phase flow without a permeable friction disk. However, the viscous torque depends strongly on the rotational speed since the shear stress in a Newtonian fluid is proportional to the velocity gradient.

The effects of permeability of the friction material is shown in Figure 5.38. The simulation results for large values ($D = 0\ m^{-2}$ and $C = 2000\ m^{-1}$) and small values of permeability ($D = 3e{+}10\ m^{-2}$ and $C = 2000\ m^{-1}$) are compared for $\omega = 500\ rpm$. As expected, for large permeability values the oil film is squeezed faster. Also, the torque for large permeability increases faster because of the difference in oil film

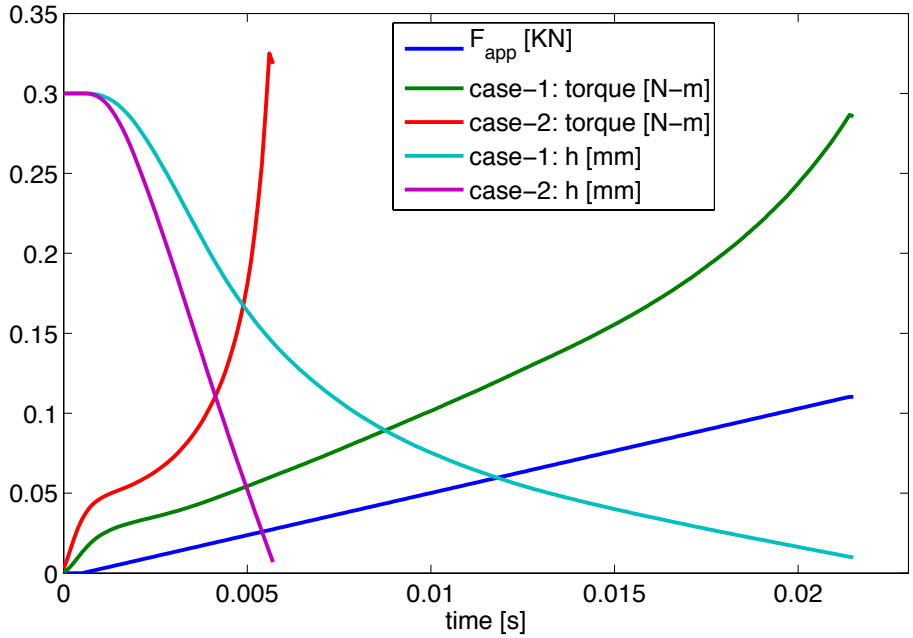

Figure 5.38: Squeeze film simulation with porous media without heat transfer model: case-1)$D = 0\ m^{-2}$ and $C = 2000\ m^{-1}$; case-2)$D = 3e + 10\ m^{-2}$ and $C = 2000\ m^{-1}$

Table 5.4: Simulation conditions of Figure 5.39

Surrounding temp.	300 K	Initial ω	500 rpm
Initial separator temp.	300 K	Initial h	0.3 mm
Friction plate	adiabatic at center core	Inlet/outlet B.C	zero pressure

thickness. According to *Wu* (1971), as the oil film thickness becomes thinner, the effect of permeability on the squeeze film velocity becomes more pronounced.

Computational results for heat generation by viscous shear are shown in Figure 5.39. The results are compared to those corresponding to a case without considering heat transfer. There are no grooves on the surface of the friction plate in either case. The initial and boundary conditions are shown in Table. 5.4. As shown in Figure 5.39(a), viscous heat generation barely affects the squeeze-film simulation. The temperature contours on the separator and friction plates show a slight variation in the radial direction. Since the separator has a larger thermal conductivity coefficient than the friction plate and the center core of the friction plate is assumed to be an

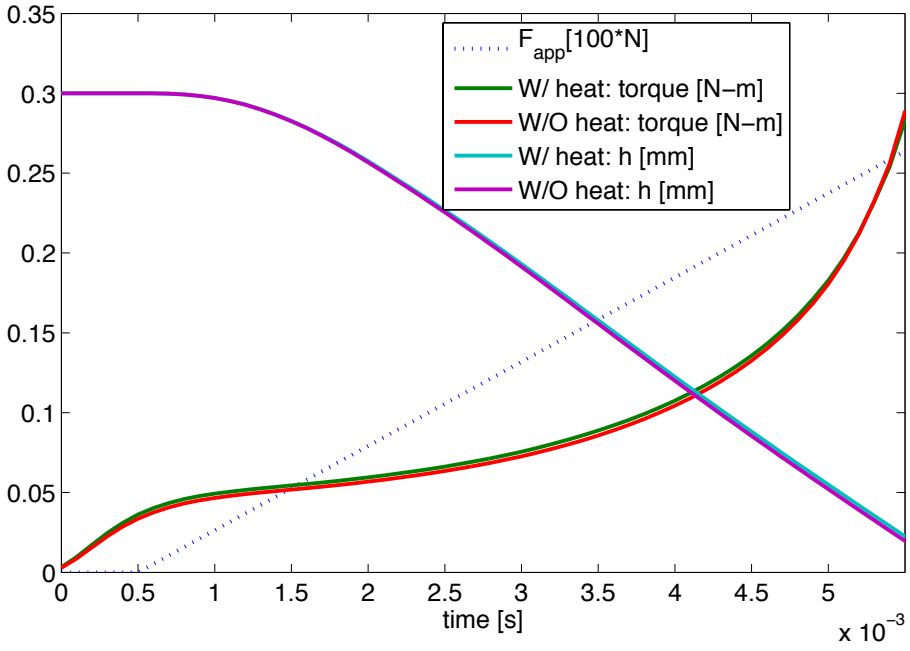

(a) Torque and oil film thickness plot

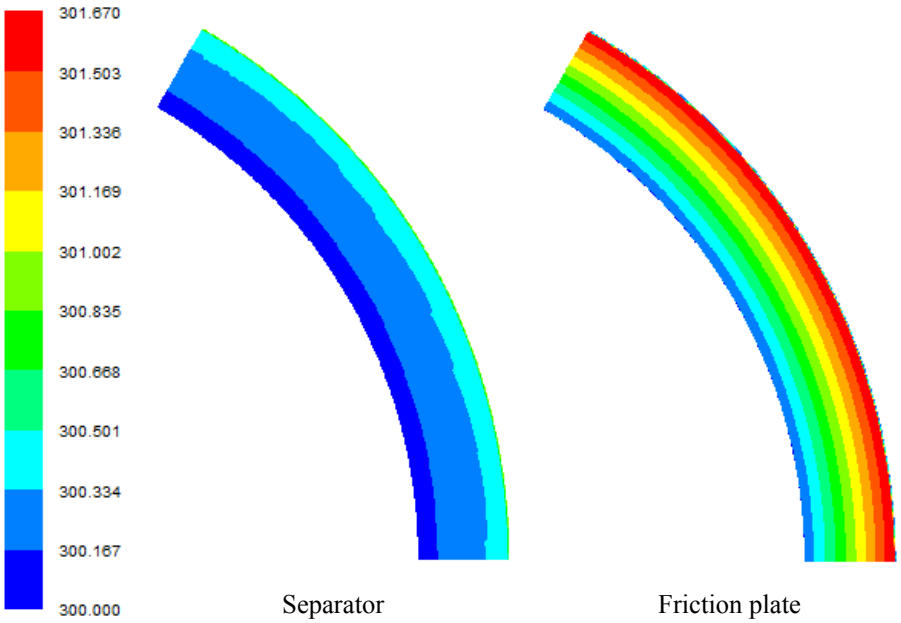

(b) Temperature contour

Figure 5.39: Squeeze film simulation with porous media and heat transfer model at $\omega = 500\ rpm$

Table 5.5: Numerical model properties for Figure 5.40

Asperity density	$3.0e+07\ m^{-2}$
Asperity tip radius	$0.0005\ m$
Roughness (RMS)	$6.0e-06\ m$
Young's modulus	$31.0e+06\ Pa$
Elastic modulus for contact	$27.0e+06\ Pa$
Friction material thickness	$5.652e-04\ m$
Friction material permeability	$1.0e-13\ m^2$
Outer radius	$0.05874\ m$
Inner radius	$0.04683\ m$
Moment of Inertia	$0.165\ kgm^2$
Initial oil film thickness	$0.0001254\ m$
Initial rpm	$1500\ rpm$

adiabatic wall, the temperature on the friction plate shows a larger variation than that of the separator. However, when solid contact is considered, frictional heat can be much larger than viscous heat. The former is considered in Chapter VI.

5.4.1 Mechanical Torque Transfer

The effects of asperity contact without frictional heat generation is now considered. As the oil film thickness decreases, the asperity contact becomes very significant to the engagement process. A transient engagement model was developed and tested to shed light on the associated mechanical torque transfer. The conditions correspond to a 30-degree periodic model. The numerical model properties are summarized in Table 5.5. The model has no grooves on the friction plate. Figure 5.40 shows the differences in oil film thickness between a model that includes asperity contact and a model that does not. The torque and rotational speed profiles between the two models begin to show different values when $h = 0.2e-04\ m$, which is approximately three times the roughness RMS ($6.0e-06\ m$). As the oil film thickness approaches at $h = 0.2e-04\ m$, T_{con} begins to increase rapidly, but the rate of increase of T_{fluid} is reduced.

With the next test, the compressibility of the friction material is included. The

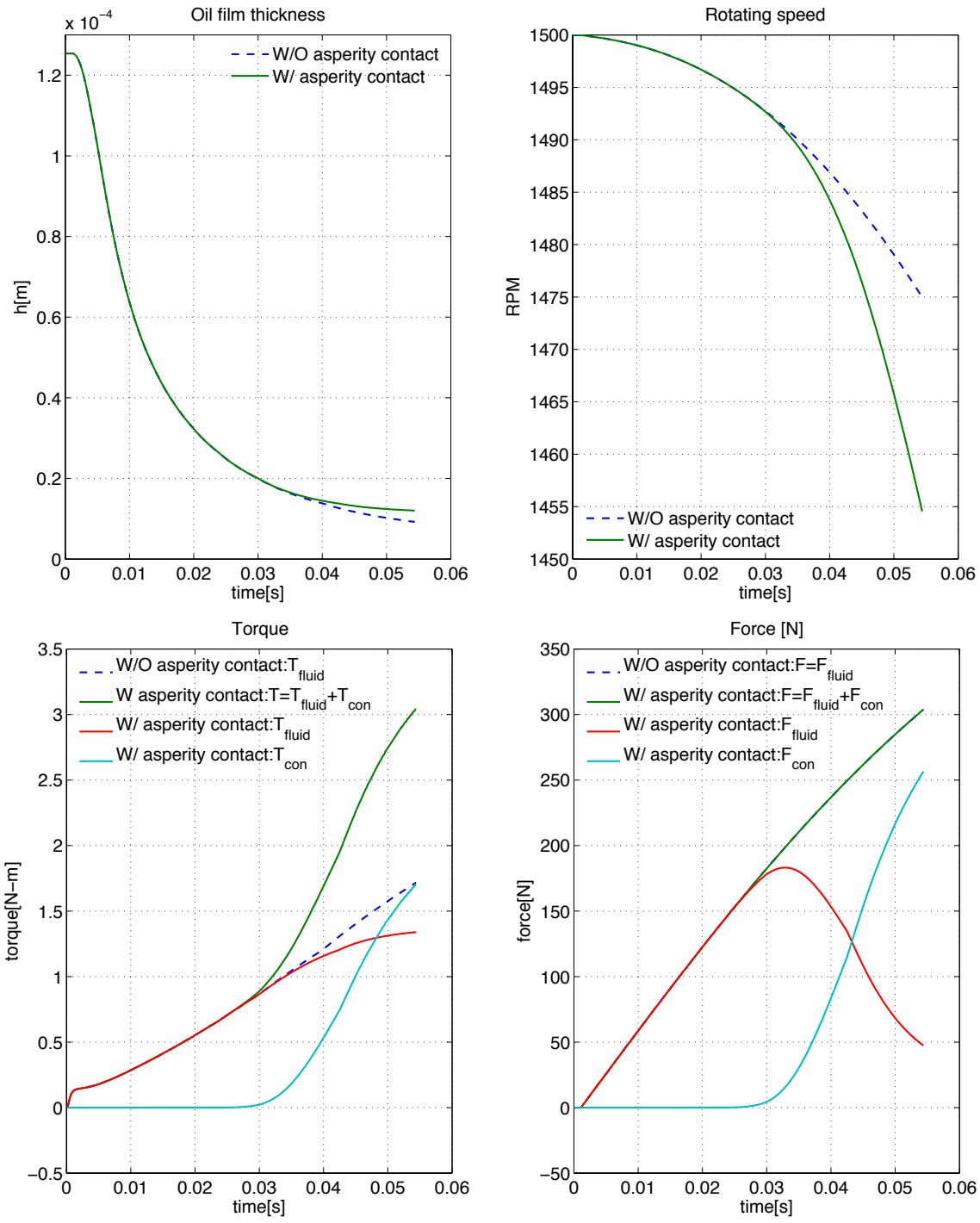

Figure 5.40: Engagement process simulation for non-grooved friction plate: The effect of asperity contact

thickness of friction material d is $5.652e-04\ m$ and the initial film thickness h is $2.54e-04\ m$. The simulation results are shown in Figure 5.41. The relevant equations and definitions (h and h_ϵ) are explained in Appendix B.1. A compressible friction material does not seem to affect F_{fluid}, F_{con} and h, but the values of torque and rpm differ slightly from those when the friction material compressibility is not considered. To include compression of the friction material in the model, an additional fitting curve was used for the relation between h and h_ϵ. h_ϵ is used to compute p_{con}. T_{con} is a function of p_{con} and μ_{fric}. Notice that a small error of h_ϵ can cause a large change in p_{con} and T_{con}. In turn, the altered value of T_{con} affects μ_{fric} because μ_{fric} is a function of the rotational speed. If the fitting curve of h_ϵ has a small error, T_{con} will be continuously changed. Therefore, it was assumed that the effect of friction material compression on h is negligible. However, the friction material compressibility can be included in the measured stroke data. In the actual wet clutch test stand (SAE No. 2), film thickness cannot be measured, but the displacement of the piston pushing the separator plate can be measured. In Figure 5.42, the difference between h and stroke $S(=h_\epsilon)$ is highlighted. For an initial value of $h = 0.0254\ mm$, Δh is 0.0215mm and $\Delta S = 0.0323\ mm$.

5.4.2 Periodic Model Limitation for Heat Transfer

Thermal influence on the engagement process model is more critical than in the open clutch model because sliding of the asperity contact interface generates not only viscous but also frictional heat during the engagement process. The high temperature of the interface can affect not only the viscous torque, but also the durability of the friction material. To include the frictional heat generation on the interface between a friction plate and a separator, the virtual thickness concept in Section 4.5 is used. Also, to consider the heat conduction in the separator, its volume is added to the engagement process model. However, when the heat conduction in the sep-

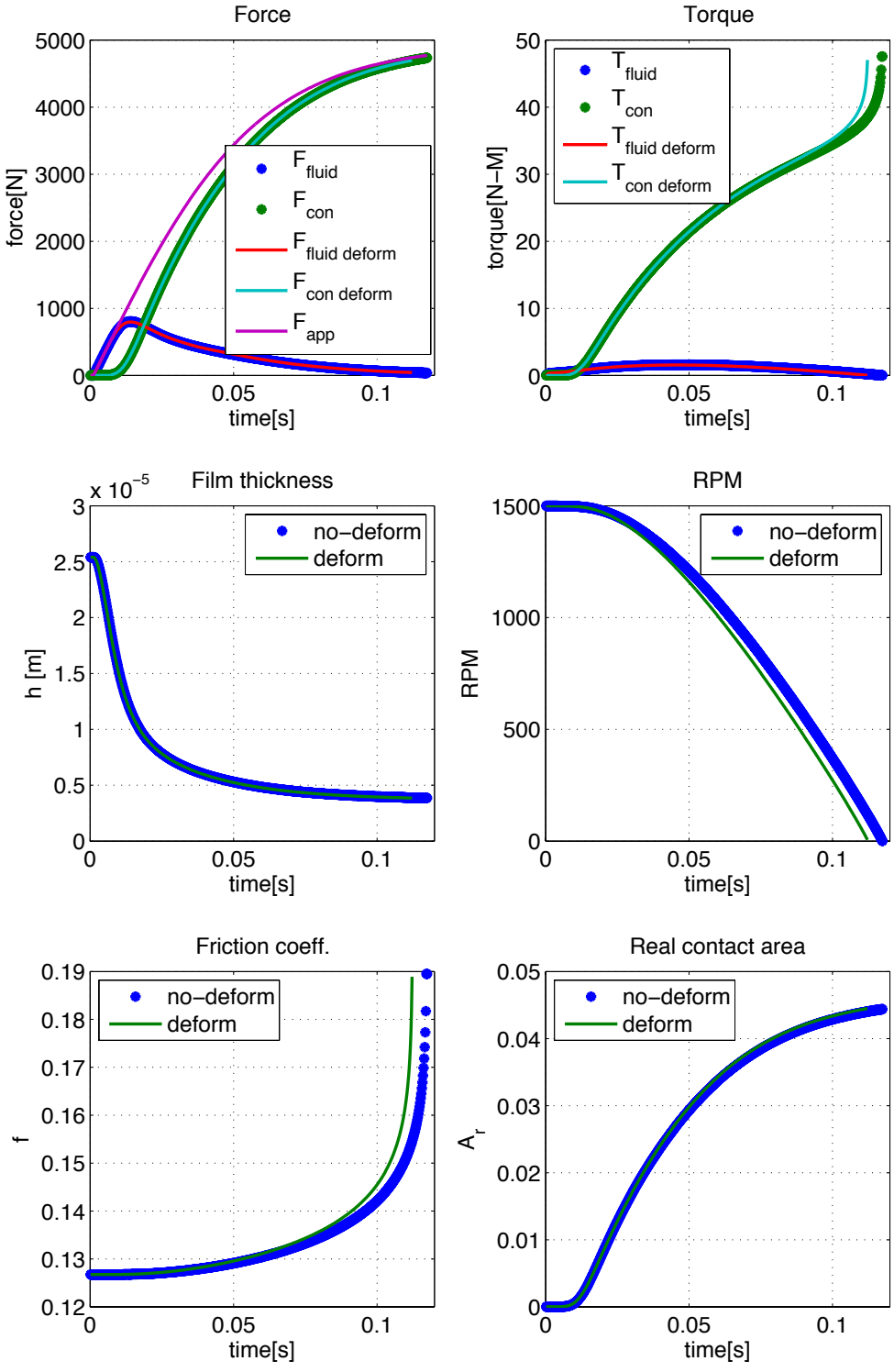

Figure 5.41: Engagement process simulation for non-grooved friction plate: The effect of asperity contact including friction material compression

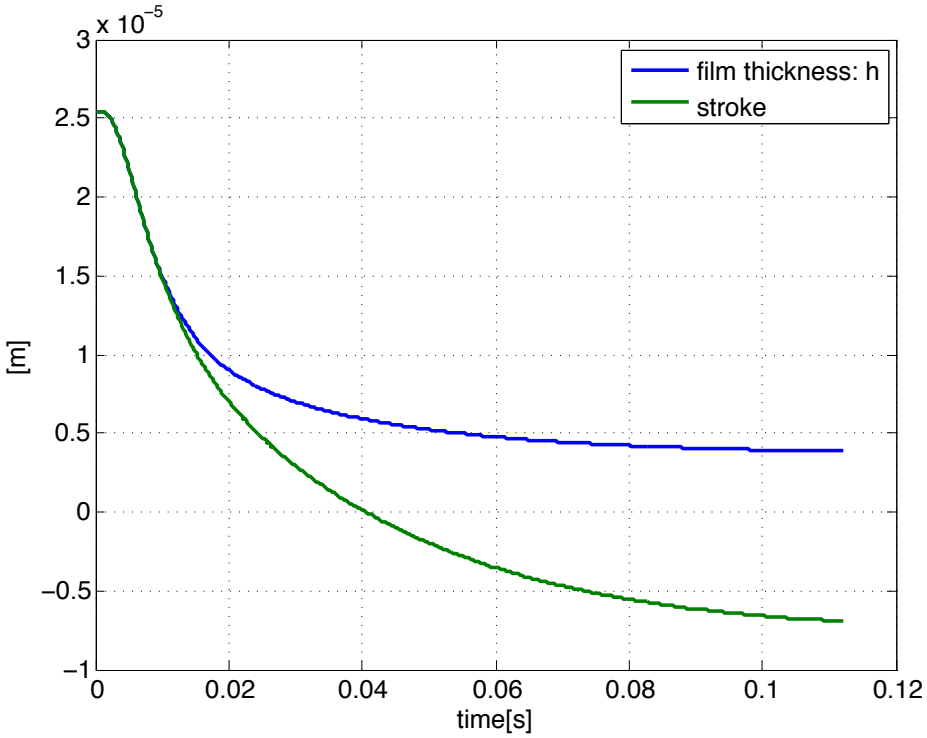

Figure 5.42: Oil film thickness h vs Stroke

arator was not considered, a moving surface wall was used in place of the moving volume of the separator. Hence, the moving separator volume was tested with the non-grooved model. Unfortunately, when both a periodic boundary condition and a moving separator volume are used together, the model fails to converge. There is double compromise in the integrity of the model, which cannot be tolerated by the underlying code limitations. Computational tests indicated that whole disk models need to be used in order to include the moving separator volume. This is disappointing, but it does not affect the reliability of the model, as it only increases the computational time of the numerical tests. Recall also that the periodic model did not represent a prefect reduction of the full disk model, so its failure in this case is not a major loss.

CHAPTER VI

Experimental Results and Model Validation

6.1 Experimental Setup

The clutch operation experiments described in this thesis were performed at the Livonia laboratory of the Ford Motor Company. All tests were set up and executed by Ford personnel; however, the writer provided input for experimental design and participated in all the experiments. Figure 6.1 shows the SAE No. 2 test stand which has been widely used as an automotive industry standard for testing friction component durability and clutch engagement characteristics.

As shown in Figure 6.2, the applied piston force and angular velocity of the clutch plate can be controlled by a feedback controller. The initial oil flow and inlet oil temperature are also maintained at a desirable level using an oil chiller and heater with a flow control valve. The vector drive controls the target slip speed and can electrically adjust the engagement time. Only one pair of steel and friction plates were used in the wet clutch experiments because the proposed simulation model consists of one steel and one friction plate. This in fact increases the probability of successful validation with the experiment as compared to a multi-disk system. One steel plate is mounted on the test housing and the other is allowed to follow the translational motion of the piston. The friction plate is rotated by the vector drive. As the piston pushes the steel plate following a given force profile, the engagement

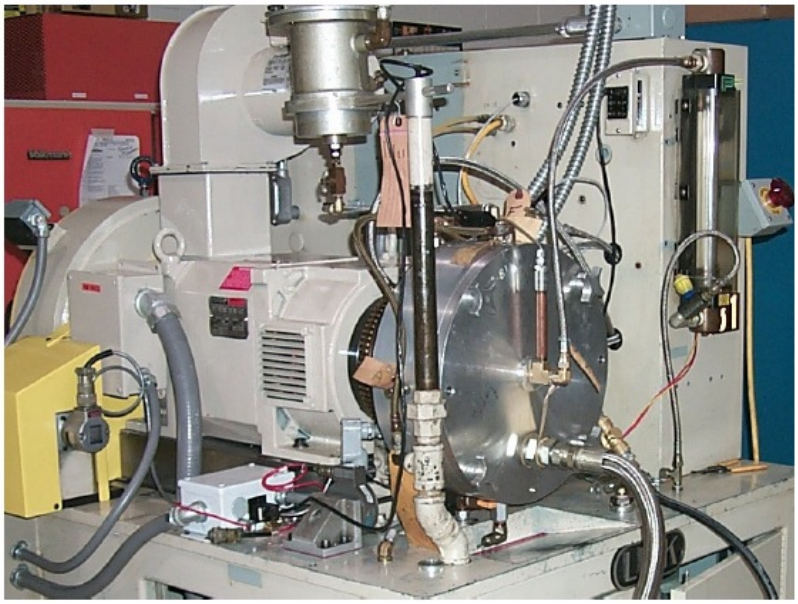

Figure 6.1: Friction component test system (*Fujii et al.*, 2006)

operation is performed while the vector drive controls the rotating speed. The air in the oil is filtered and the oil is fed through the rotating center shaft into the clutch housing, then spreads out between the clutch plates and finally drains out. One of the main performance parameters for a wet clutch, i.e. torque, is measured by a torque sensor while the programmable hydraulic actuator is operating, following a reference command pressure profile over time. The pressure in the piston chamber is controlled and measured by the difference between the two sides of the piston. A position sensor measures the piston displacement, also indicating oil film thickness and the deflection of other hardware components during clutch engagement. During the tests, stroke, temperature at several points of the steel plates, torque, *rpm*, and the flow rate are measured. The measurement errors of the sensors are listed in Table 6.1. In addition, the TGC friction plate is used in the experiments. The friction plate consists of a paper based porous lining material attached to both sides of the core steel plate. The dimensions and properties of the friction plates are listed in Table 5.1. Measurements of permeability indicate that the lining material's porosity in the radial direction is

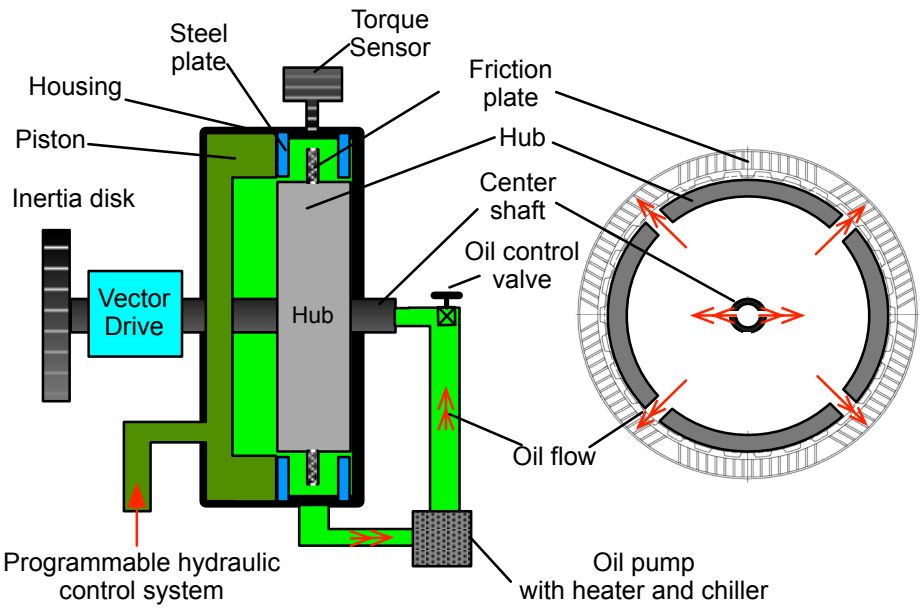

Figure 6.2: Schematic of test system

approximately 100 times larger than that in the axial direction. The porous lining material has 16 grooves over a 60 degree segment.

Table 6.1: Sensor type and accuracy for SAE No. 2

Sensor type	Range	% error for full range
Speed [rpm]	0 $\sim$ 4000	0.14
Pressure [psi]	-150 $\sim$ 150	1.00
Torque [lb-ft]	0 $\sim$ 667	0.6
Piston stroke [in]	0 $\sim$ 0.3	0.6
Temperature [F]	-50 $\sim$ 50	0.83

6.2 Experiment Results

Each test was repeated five to ten times to establish repeatability. In order to check the repeatability, the reference parameters from REF-1 to REF-9 were defined as shown in Figure 6.3. All reference parameters showed acceptable repeatability. For example, Figure 6.4 shows the STD error bars for the normalized reference parameters of the experimental results used in the engagement model validation. Overall the

Table 6.2: Wet clutch test conditions

Oil temperature $[°C]$	$5.6 \sim 82.2$
Oil density $[kg/m^3]$	$800 \sim 860$
Oil viscosity $[kg/m \cdot s]$	$0.007 \sim 0.2$
Oil initial flow rate $[kg/s]$	$0 \sim 0.016$
Target force $[N]$	1041, 2083, 3125
Force ramp $[N/s]$	10417, 104166
Initial rpm	$0 \sim 4500$

normalized reference parameters had small STDs except the normalized REF-2 in the case of 100 rpm. However, the temperature of the separator was rarely changed during the engagement process and the non-normalized REF-2 values essentially had very small difference between the repeated experiments. Therefore, the normalized REF-2 could be ignored. In addition, since a high level of noise appeared in the measured torque signal, as shown in Figure 6.5, the torque signal needed to be filtered. The noise frequency depends on the rotation speed and a low pass filter was used with the cutoff frequency of the rotation speed. Zero-phase digital filtering can preserve features in the filtered time waveform exactly where those features occur in the unfiltered waveform. Therefore, since the timing comparison with the applied force profile and rotating speed is very important for the analysis of clutch engagement data, zero-phase digital filtering was used.

6.2.1 Experimental Engagement Test

The test conditions of the experiments are listed in Table 6.2. During squeeze film model validation, various uncontrolled noise factors in the experiments were identified, such as piston seal friction force, deformation of both test samples and test stand components, and sensor uncertainties. Since the squeeze simulation model reflects only the pure squeeze motion without including any of the aforementioned effects, the experimental results were processed to exclude these noise factors.

Figure 6.6 represents a squeeze-film experimental data of non-grooved plates with

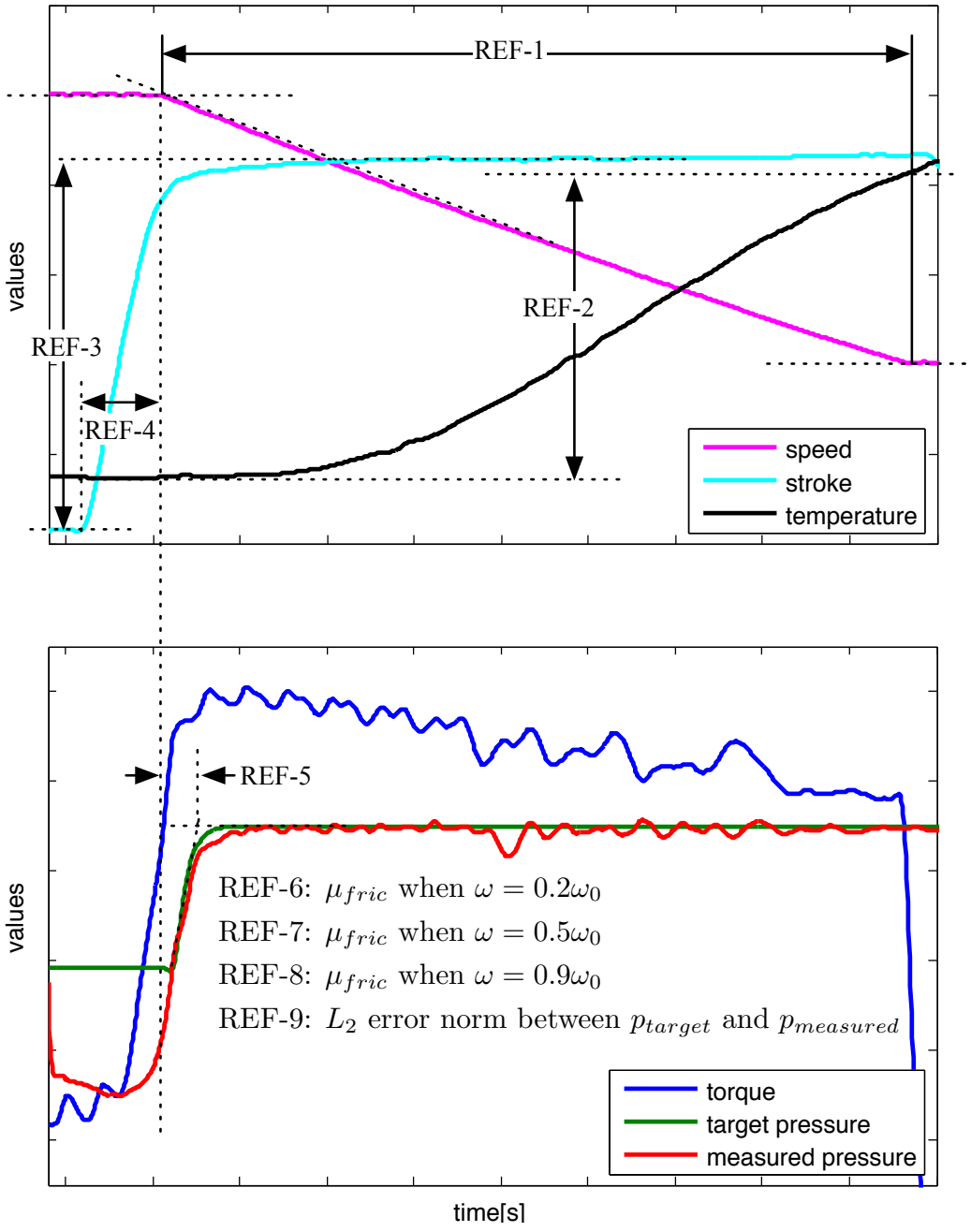

Figure 6.3: Reference parameters to check the repeatability of experiments

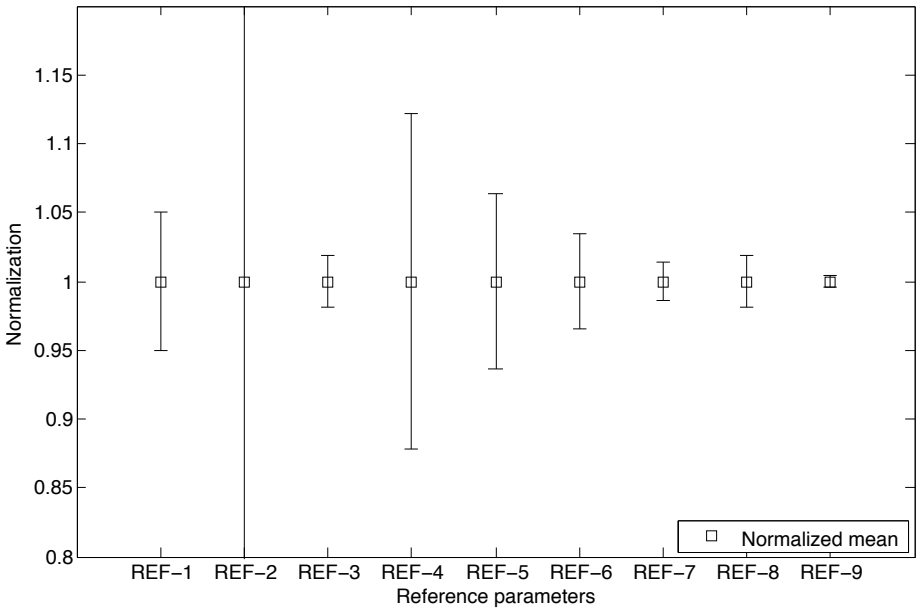

(a) Test condition: 100 rpm

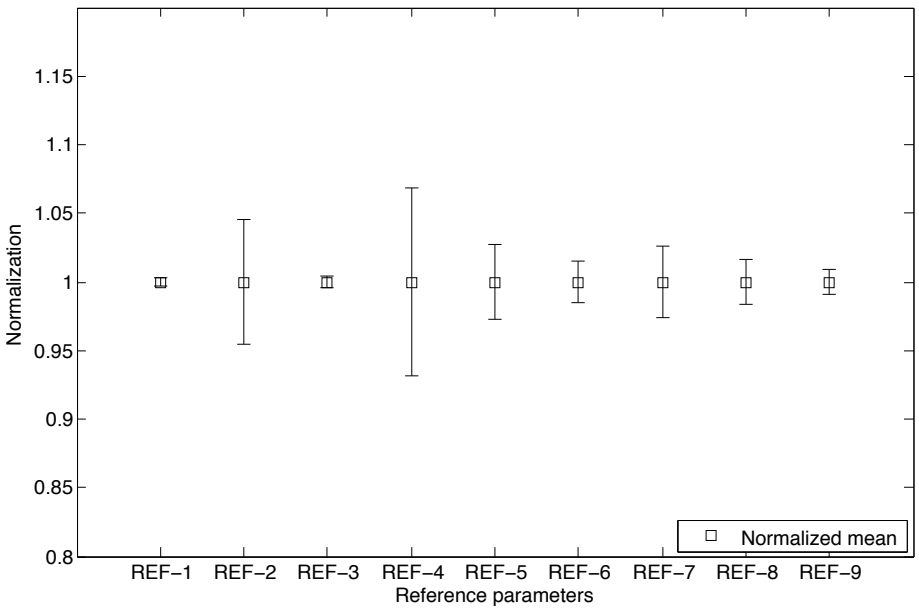

(b) Test condition: 1500 rpm

Figure 6.4: STD error bars for the repeatability of experiments

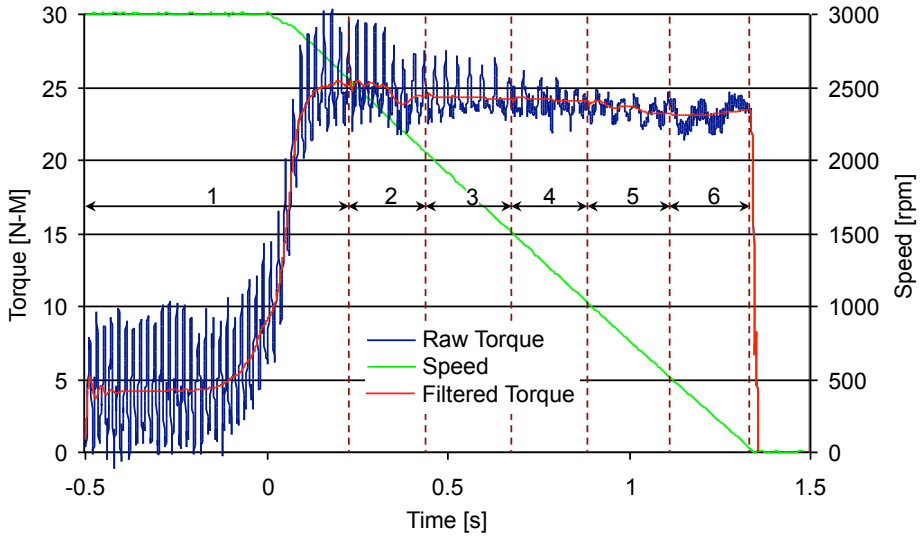

Figure 6.5: Torque signal filtering

$T = 39.4\ ^{\circ}C$, $\omega = 0\ rpm$ and $\dot{m} = 0.0079\ kg/s$ to $0.016\ kg/s$. The friction plate between the two separators was removed to establish pure squeeze flow. At t=0s to 0.8s, a constant initial pressure is applied and the stroke does not increase. However, from t=0.8s forward, while the same constant initial pressure is applied, the stroke does increase. At about $t = 3.3s$, the pressure begins to increase. The stroke also continues to increase until it reaches its final value. Since the operating condition between $t = 0\ s \sim 3.3\ s$ is not well defined, only the experimental data after $t = 3.3\ s$ were considered for comparison with the corresponding simulation results. Figure 6.7(a) shows the experimental data after $t = 3.3s$. The applied force F_{app} was input to the simulation model as shown in Figure 6.7(b). The cross sectional dimensions of the simulation model are identical to those of the real clutch.

Figure 6.8(a) shows a comparison between the experimental data and the simulation results. Both pressure and free outflow boundary conditions were used at the inlet and outlet sections. The inlet/outlet pressure value was determined by the initial $F_{app}/A = 23,491\ Pa$ because the initial F_{app} has a non-zero value in the experiment data. The film thickness with $p_{in} = p_{out} = 23,491\ Pa$ is changed more slowly

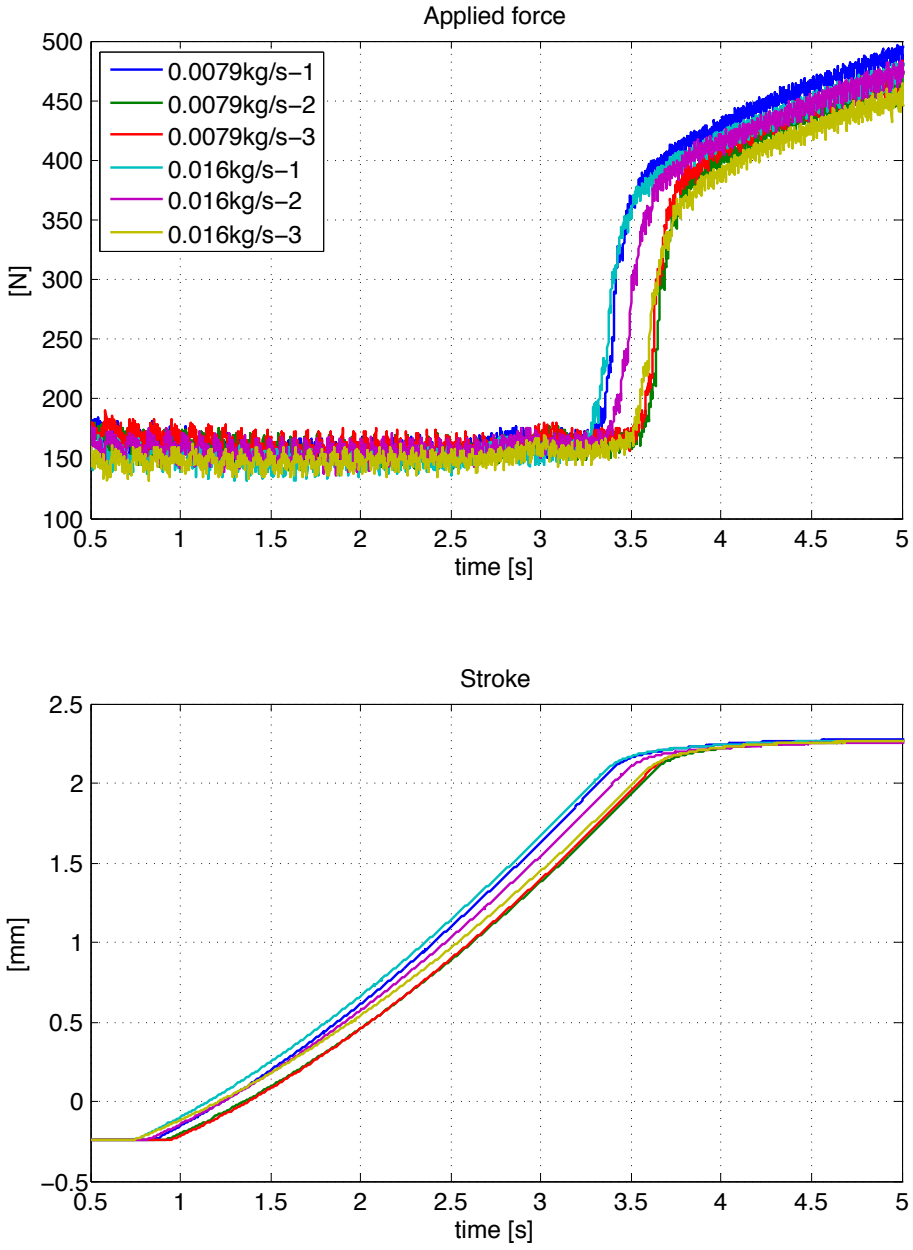

Figure 6.6: Squeeze-film experiment: $T = 39.4\ ^{\circ}C$, $\omega = 0\ rpm$; $\dot{m} = 0.0079\ kg/s$ or $0.016\ kg/s$

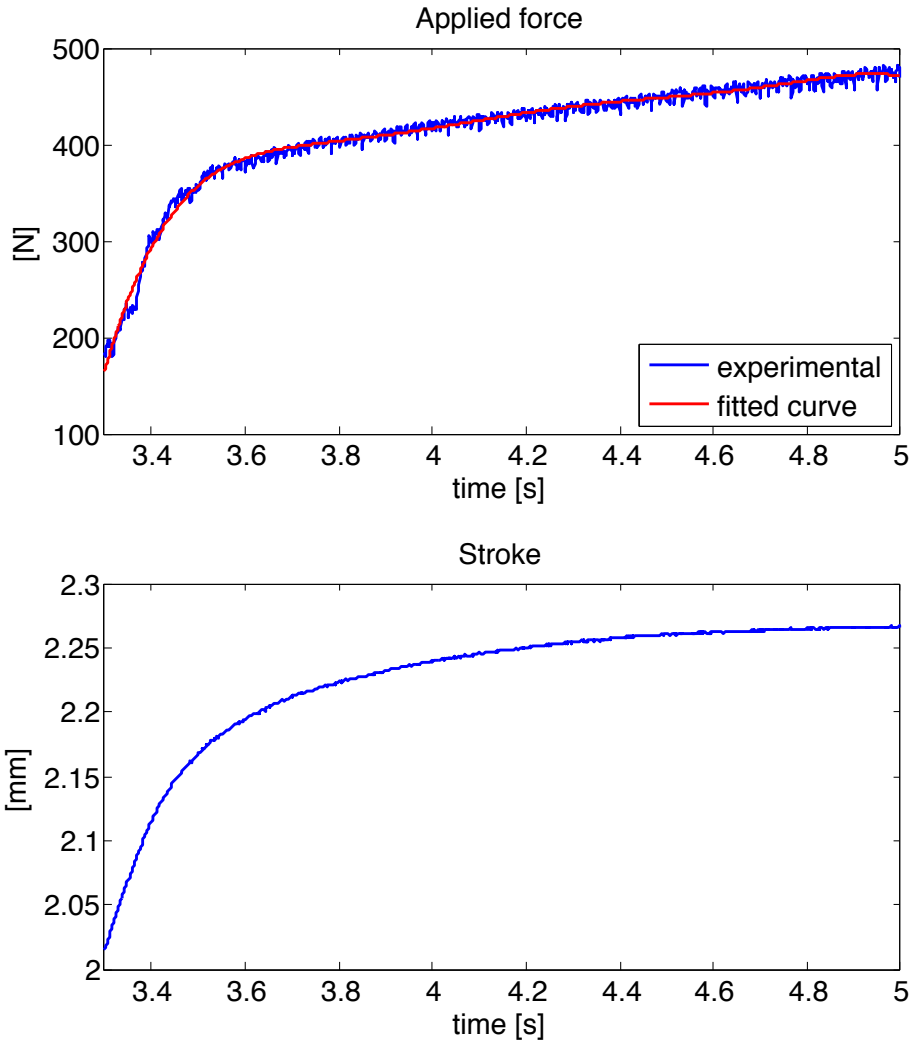

(a) F_{app} and h Magnification of Figure 6.6

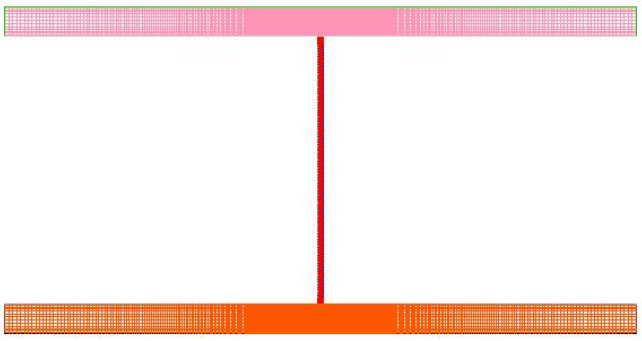

(b) Extended boundary model

Figure 6.7: Squeeze simulation model for Figure 6.6: 34 $mmx1.6$ mm, initial $h = 0.25$ mm

than that with a free outflow boundary. Figure 6.8(b) shows the pressure profiles at $t = 0.018s$ and $t = 0.0385s$ for the location corresponding to the inlet/outlet area of the conventional (Type-0) model. The results indicate that the pressure profile at the inlet and outlet may be time dependent for models that do not have extended boundary areas.

Furthermore, for the used flow rates, i.e. 0.0079 kg/s and 0.0158 kg/s, the measured stroke curves do not show a clear difference. This means that the flow rate may not be sufficient to continuously fill the gap between the test clutch plates during the experiment, as the simulation model assumes. Nevertheless, the measured stroke decreases more slowly than that of the simulation results. There are two possibilities for the difference. First, the assumed inlet and outlet boundary conditions do not reflect the actual boundary conditions. Second, there may be unknown factors in the experimental data that were not recognized. These will be associated in the following with so-called noise factors.

6.2.1.1 The effects of the inlet and outlet boundary conditions

Figure 6.9 shows the simulation results and the experimental data for non-grooved squeeze-film simulation as the extended area geometry changes. As the extended area is narrow and long, the film thickness decreases slowly. This indicates that the flow resistance at the inlet and outlet areas of the real test hardware can affect the oil film thickness.

Another type of boundary condition, i. e. a vent boundary was also considered. In this case, the boundary consists of an infinitely thin vent that introduces a loss coefficient K_L for pressure drop, i.e. $\Delta p = \frac{1}{2} K_L \rho v^2$. The results are shown in Figure 6.10 for various values of K_L. When an unrealistic loss coefficient K_L equal to 5000 is used, the simulated film thickness is closer to the experiment results. This is done only to show the sensitivity of the solution to the assumed boundary conditions. Since

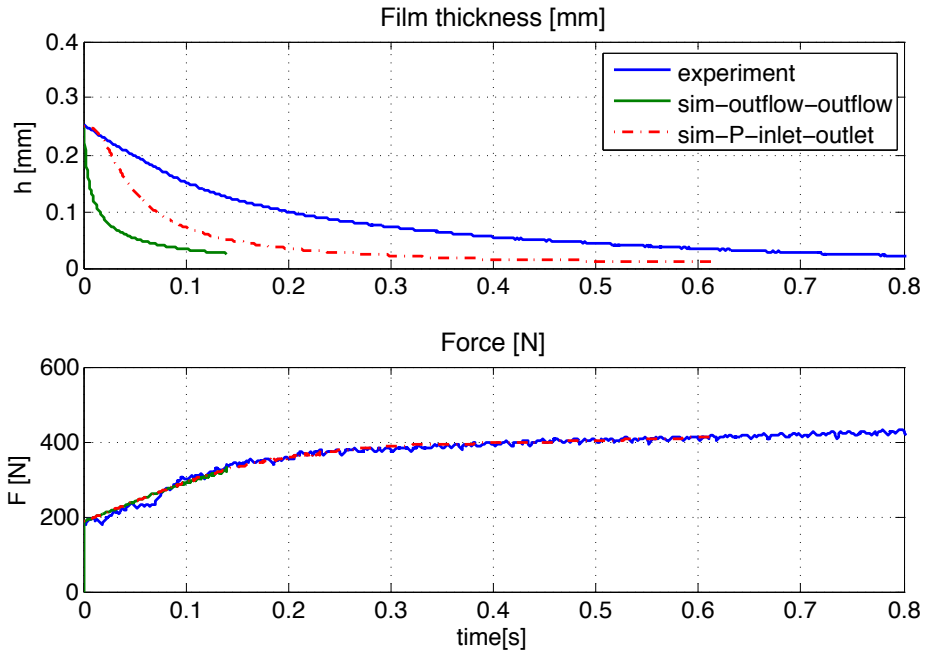

(a) Squeeze simulation results: $p_{in} = p_{out} = 23,491\ Pa$

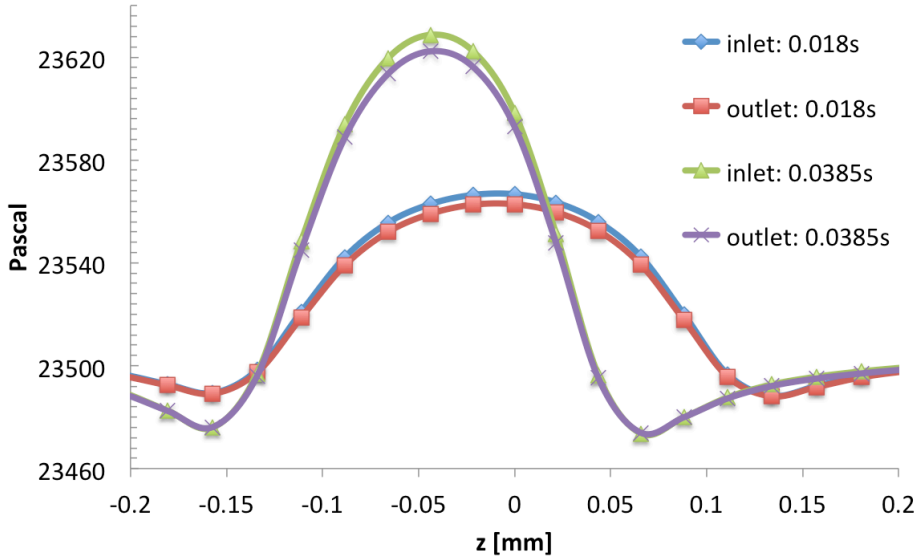

(b) Pressure profiles at inlet and outlet location of conventional model

Figure 6.8: Squeeze simulation results for Figure 6.7 : $p_{in} = p_{out} = 23,491\ Pa$

	a[mm]	b[mm]
Case-1	0.4	5
Case-2	1.6	5
Case-3	0.4	20
Case-4	1.6	20

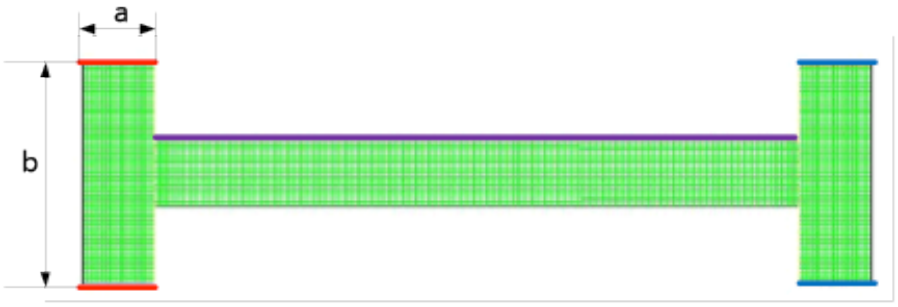

(a) Extended area sizes

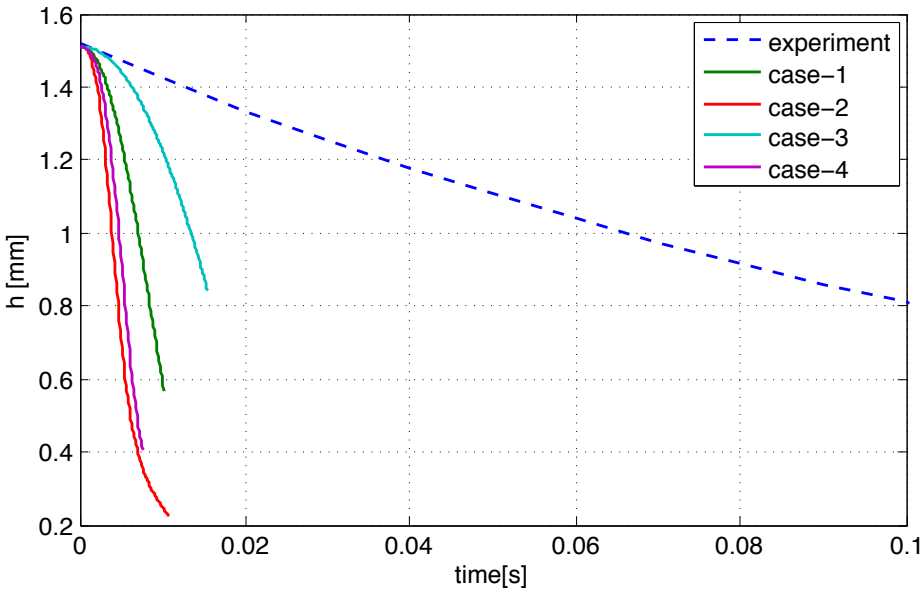

(b) Squeeze simulation results

Figure 6.9: Squeeze simulation for different extended areas

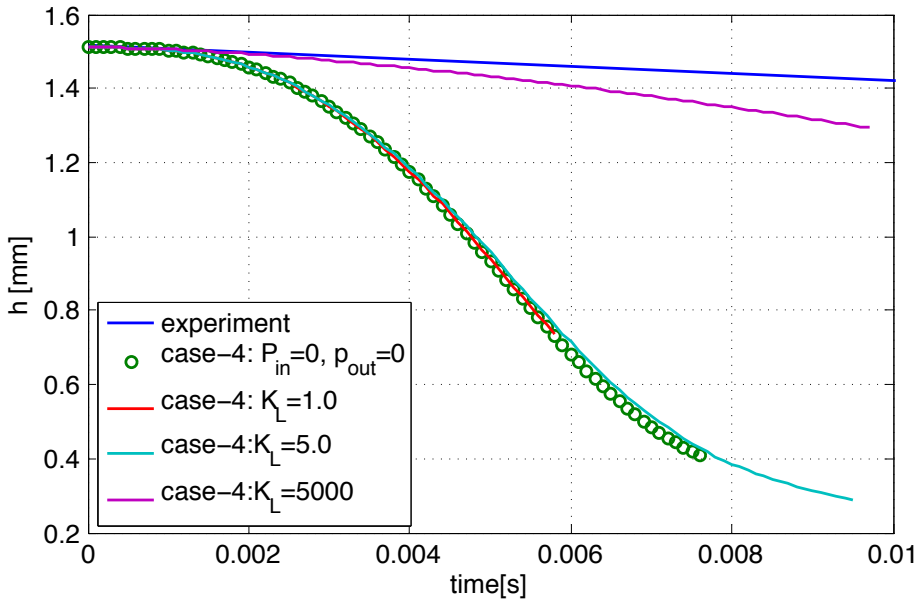

Figure 6.10: Squeeze simulation with vent boundary condition at inlet and outlet

the real boundary conditions escape a simple explanation, this experiment suggests that additional experimentation with boundary types and values is necessary.

6.3 Noise Factors

During wet clutch model validation, various uncontrolled noise factors in the experiments were identified, such as piston rubber seal friction, deformation of test samples and test stand components, and sensor uncertainties. Since the simulation model reflects only the pure squeeze motion without including any of the aforementioned effects, the experimental results were processed to exclude these noise factors. To identify the noise factors, an experimental data analysis and a FEM simulation for the piston components were performed. Also, the method of removing unknown noise factors from experimental data in *Cho et al.* (2011) was consulted.

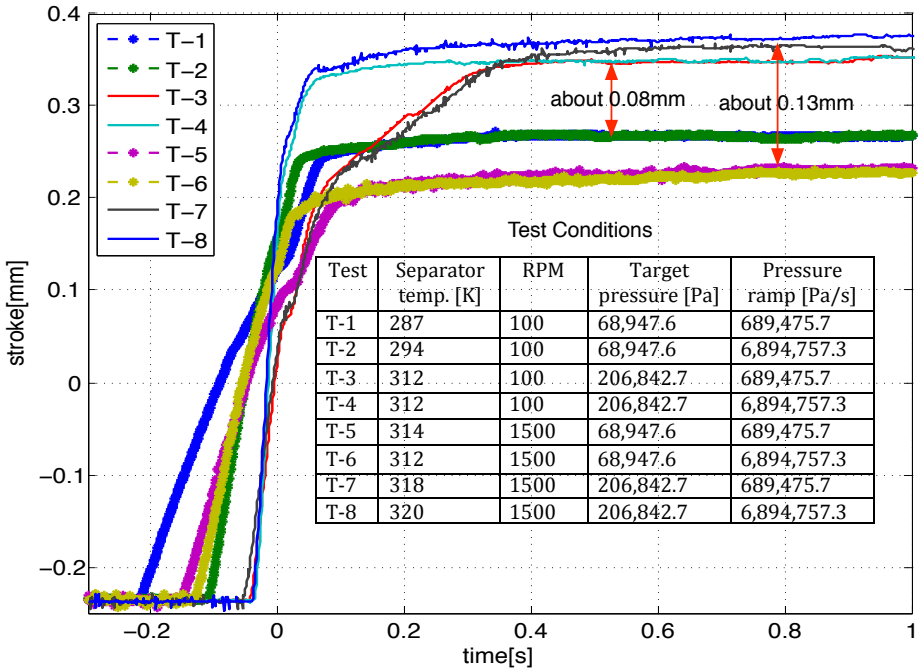

Test	Separator temp. [K]	RPM	Target pressure [Pa]	Pressure ramp [Pa/s]
T-1	287	100	68,947.6	689,475.7
T-2	294	100	68,947.6	6,894,757.3
T-3	312	100	206,842.7	689,475.7
T-4	312	100	206,842.7	6,894,757.3
T-5	314	1500	68,947.6	689,475.7
T-6	312	1500	68,947.6	6,894,757.3
T-7	318	1500	206,842.7	689,475.7
T-8	320	1500	206,842.7	6,894,757.3

Figure 6.11: Stroke curves for engagement test when initial flow rate is 0.00527 kg/s.

6.3.1 Thermal Expansion and Solid Deflection

In Figure 6.11, the stroke curves under 8 test conditions (from T-1 to T-8) are compared. These tests have a common initial flow rate of 0.00527 kg/s. Due to the differences in target pressure (68,947.6 Pa vs 206,842.7 Pa), the final stroke values are different. A higher target pressure seems to cause a larger stroke value. However, for the same target pressure, the final strokes of T-1 and T-2 differ from those of T-5 and T-6. The reason can be explained by the temperature difference of the separator. The separator temperature of T-5 and T-6 is higher than that of T-1 and T-2 because a sufficient time interval between each test was not provided. Since the temperature rise causes the thermal expansion of the test hardware including the separator, the stroke decreases at high temperature. Therefore, the thermal expansion of the test hardware can be expected to affect the experimental data. To remove the effect of thermal expansion, sufficient time needs to elapse between tests, so the hardware temperature can return to the inlet oil temperature.

To investigate the possibility of test hardware deflection, a piston deflection module was constructed. For the piston deflection module, a connector between the piston actuator and the separator was considered. When the piston pushes the separator, the piston module is deflected, so its deformation can be included in the stroke data. To find the displacement, FEM analysis was performed using ANSYS. Figure 6.12 shows the simulation results comparing different grid resolutions. The numerical solution converges as the grid resolution increases. From the finest grid solution, at $p_{app} = 275,760\ N/m^2$, the deflection is $0.03\ mm$ and the stiffness coefficient k is calculated to be $1.3889e+08\ N/m$ since the piston area is $15,109.65\ mm^2$. Also, the deformation of the friction material was investigated. The deformation of the friction material is discussed in Appendix B.1.

6.3.2 Piston Friction Force

As shown in Figure 6.13, among the many test conditions investigated, the stroke and applied force curves for the TGC engagement test data were selected for three specific test conditions: 1) 0 rpm and 0 kg/s 2) 1500 rpm and 0.0079 kg/s 3) 100 rpm and 0.0079 kg/s. These sets of data were used in the validation of the wet clutch model. Approximately at $t = 0.3\ s$, the initial applied forces have non-zero values as the stroke profiles begin to rise. This indicates that potentially noise factors act on the stroke motion. It was assumed that the non-zero applied force may be caused by the friction of the rubber seal between the piston and the chamber. To validate this assumption, attempts were made to measure the piston friction force. However, this effort was met with difficulty in accessing the piston module. Instead of measuring the piston friction force, analytical results for a circular clutch including the piston friction were compared to confirm its effect. The piston seal friction and piston connector module deflection were included in the analytical solution for a non-grooved, wet clutch model from Figure 6.14. The piston friction model was adopted from the one

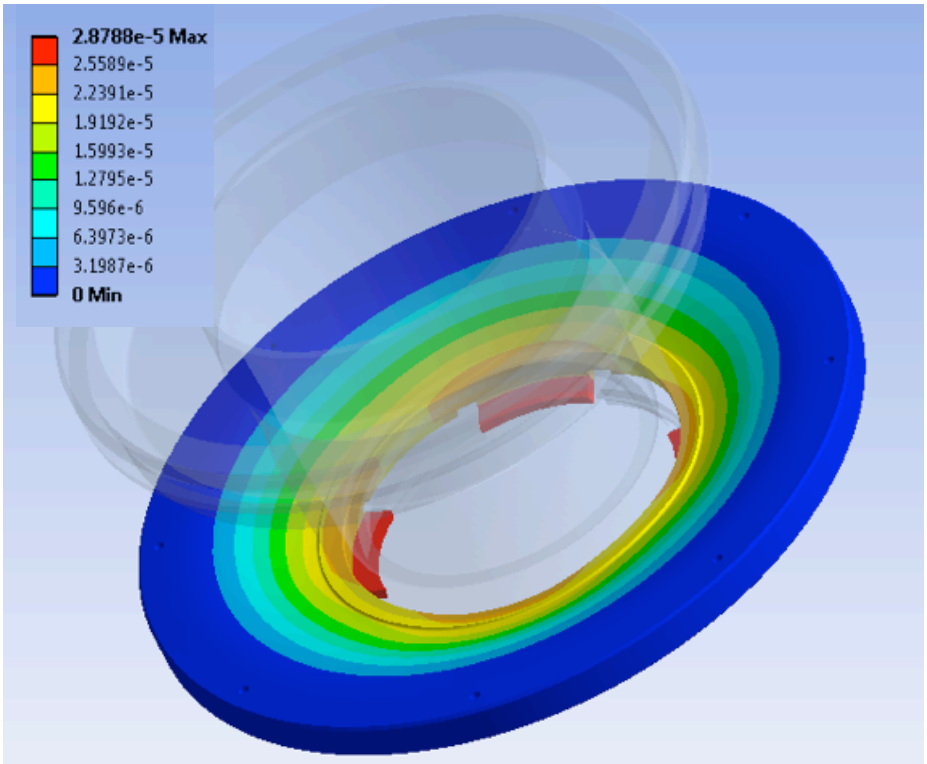

(a) Piston module deflection contour

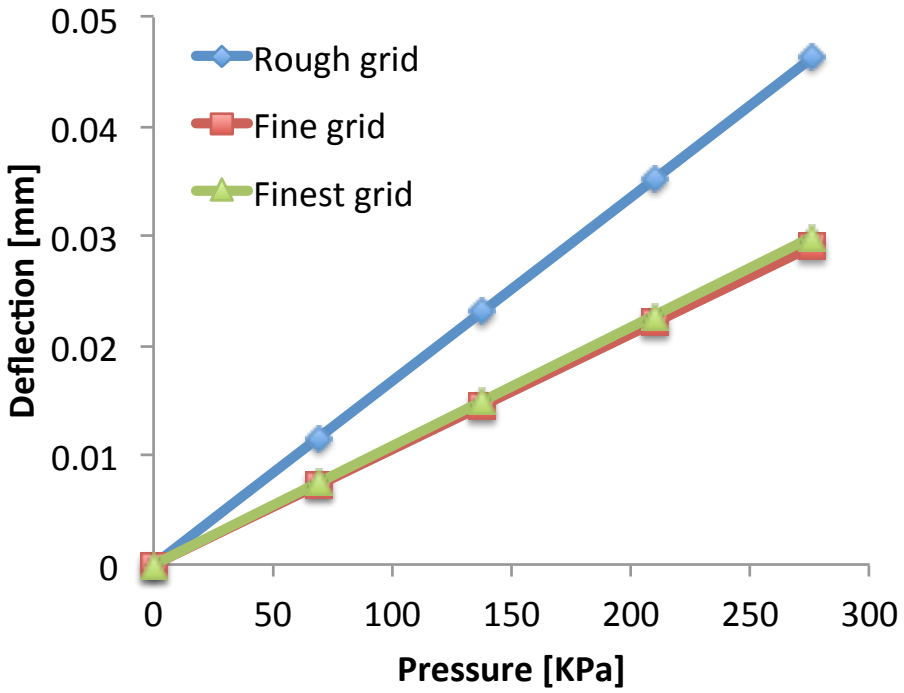

(b) Deflection vs p_{app}: Ansys

Figure 6.12: Piston module deflection simulation

of *Dahl* (1977), which is used in control engineering and reads as follows

$$\frac{dF_f}{dt} = \sigma \frac{dx_1}{dt} - \frac{F_f}{F_{max}} \left| \frac{dx_1}{dt} \right| \tag{6.1}$$
$$F_f = F_{max} \left(1 - e^{\frac{-x_1 \sigma}{F_{max}}} \right) \text{ when } F_f = 0 \; at \; x_1 = 0$$

where F_f is friction force, F_{max} is a Coulomb friction level parameter and σ is a constant coefficient. The deflection of the piston connector module was modeled as a linear spring having a stiffness coefficient in Figure 6.12. As shown in Figure 6.15, the results show that including the noise factors, the decay of squeeze film thickness is much slower than without considering any noise factors. The numerical results show that the noise factors can significantly affect the squeeze motion of a wet clutch. However, even though the aforementioned noise factors were considered, for the measured data at 0 rpm and 0 kg/s in Figure 6.13, the corresponding force profile, i.e. exp-1, could still not be explained. Indeed, there seems to exist an unexplained force even after removing the extra force attributed to the noise factors.

Since the experiment under 0 rpm and 0 kg/s allows no flow in the clutch, no force should be required to complete the stroke motion, if noise factors do not exist. Therefore, the force profile of exp-1 was used to indirectly compute the remaining unknown noise factors.

In addition, The film thickness of exp-3 is changing slightly slower than the film thickness of exp-2 although a larger force is applied in exp-3 until 0.35 s. This may be related to the influence of the rotational speed. According to *Wu* (1971), as the rotational speed of the disk increases, the load capacity and fluid film pressure decrease. Also, from the analytical solution results for an open clutch in Section 3.1, a high rotating speed and a low flow rate can cause negative pressure values in a wet clutch.

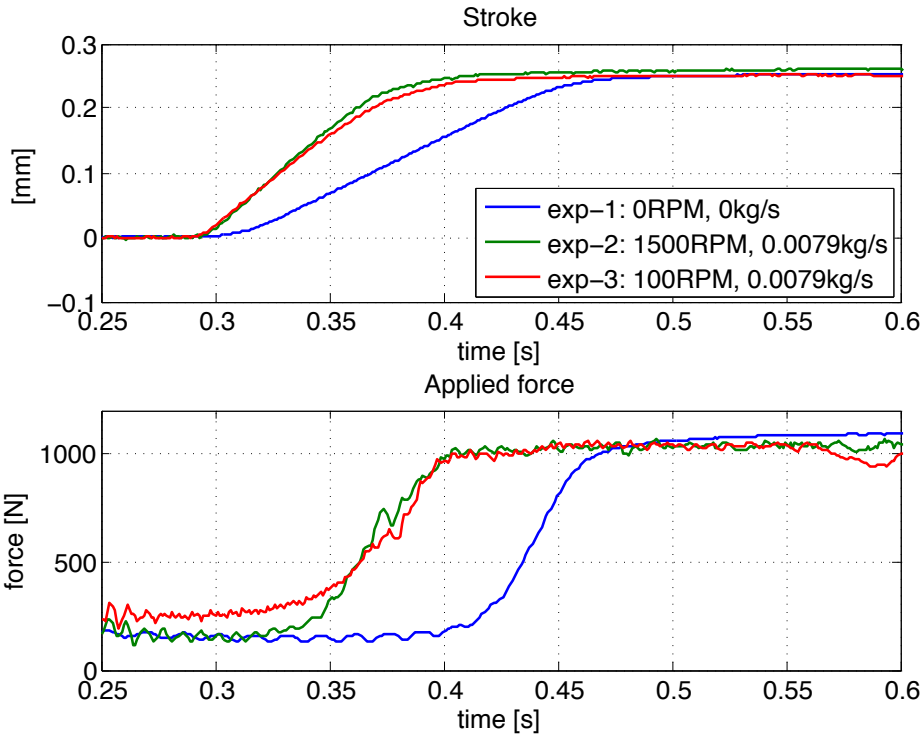

Figure 6.13: Measured data: stroke and force

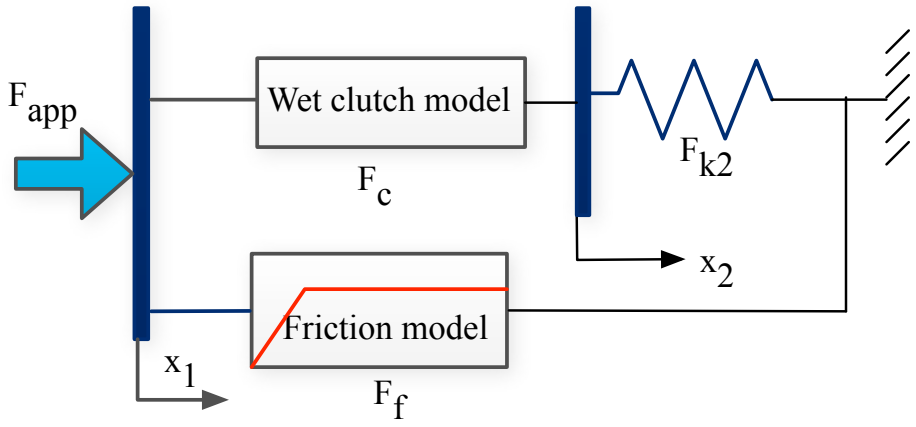

Figure 6.14: Noise factor model: piston friction model and piston module deflection

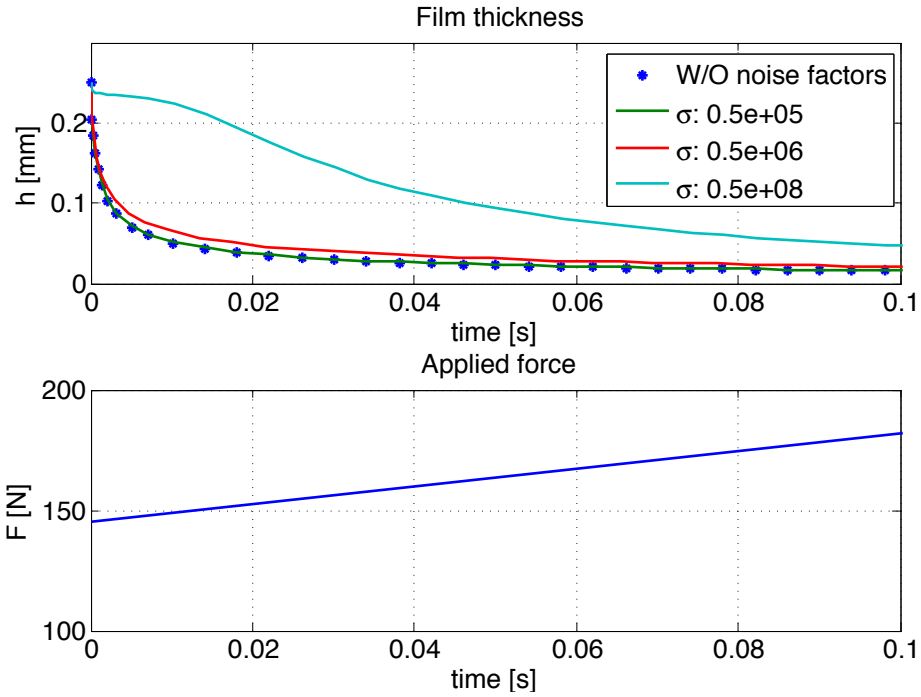

Figure 6.15: Squeeze film thickness including piston friction model and piston module deflection

6.3.3 Unknown Noise Factors

As mentioned in Section 6.3.2, to calculate the level of the unknown noise factors, the experimental force profile of 0 rpm and 0 kg/s was used in Figure 6.13. First, it is assumed that the unknown noise factors are related to the film thickness h. F and h can be plotted against each other, as shown in Figure 6.16. Then, the force profile for 0 rpm and 0 kg/s is subtracted from the measured force profile. After the elimination of unknown noise factors, the computed force profiles consists of pure F_{app} curves that are devoted only to the motion of the wet clutch. However, these F_{app} profiles should be valid only when asperity contact effects are negligible. Since the force profile of 0 rpm and 0 kg/s includes the asperity load, subtracting the force profile of exp-1 from the other profiles, i.e. exp-2 or exp-3, leads to exclusion of the asperity load, which is necessary for engagement process. Therefore, pro-1 and pro-2 in Figure 6.16 should be used in the validation of squeeze-film flow in a wet clutch,

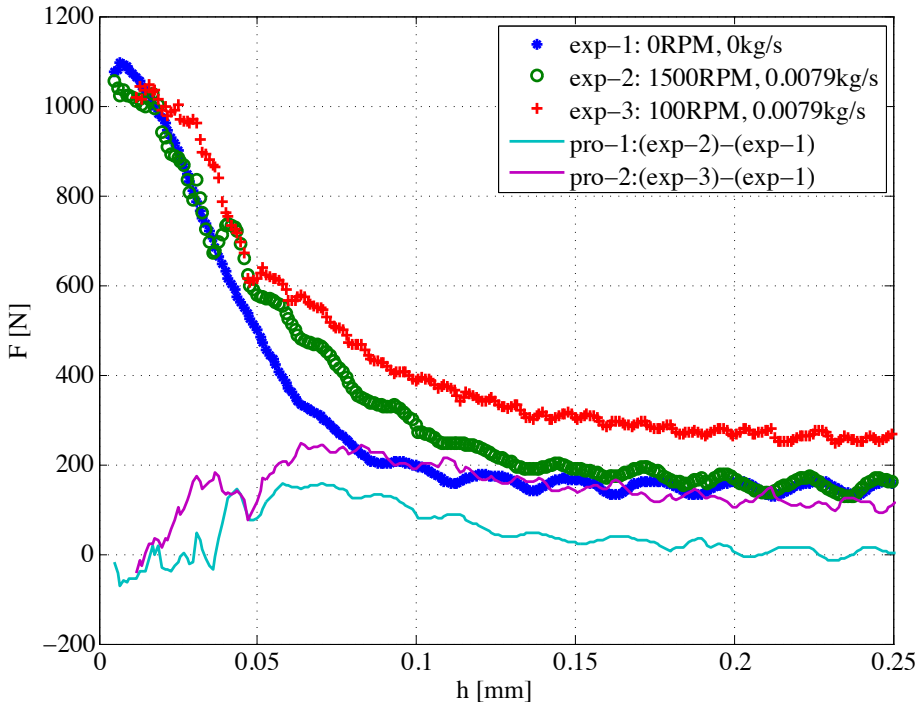

Figure 6.16: h vs F: Elimination of unknown noise factors

but are not appropriate for the whole engagement process when the latter includes asperity contact.

To validate the complete engagement process, the asperity load should be included in the F_{app} profiles. To compensate for the removed of the asperity load, the analytical solutions for real contact area and asperity load of Chapter IV are used. As shown in Figure 6.17, after removing the piston friction force and the deflection of the piston module from the measured raw data, the force profiles include only the force components of the simplified wet clutch model and the unknown noise factors. The stroke curves were modified near the final stroke level because the applied forces at the final strokes are much larger than those at early times. The modified force profiles have similar shapes to force profiles offset by the Coulomb friction factor. Therefore, to compute the asperity contact load F_{con} with respect to h and h_ϵ, Eq. (B.3) of Section B.1 and Eq. (4.34) of Section 4.6 were used in Figure 6.18.

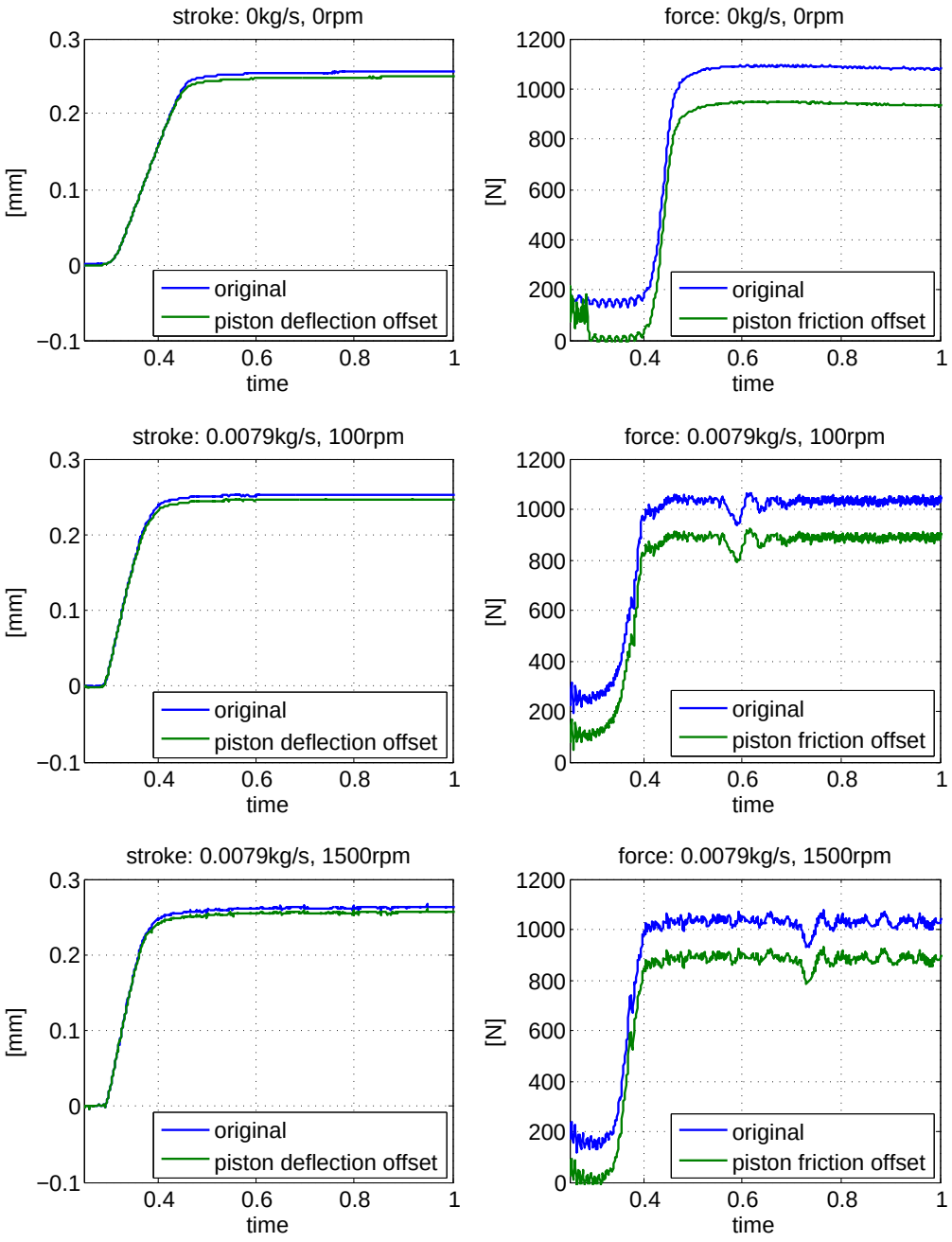

Figure 6.17: h and F vs time: Elimination of piston friction force and deflection of piston module from the measured force data

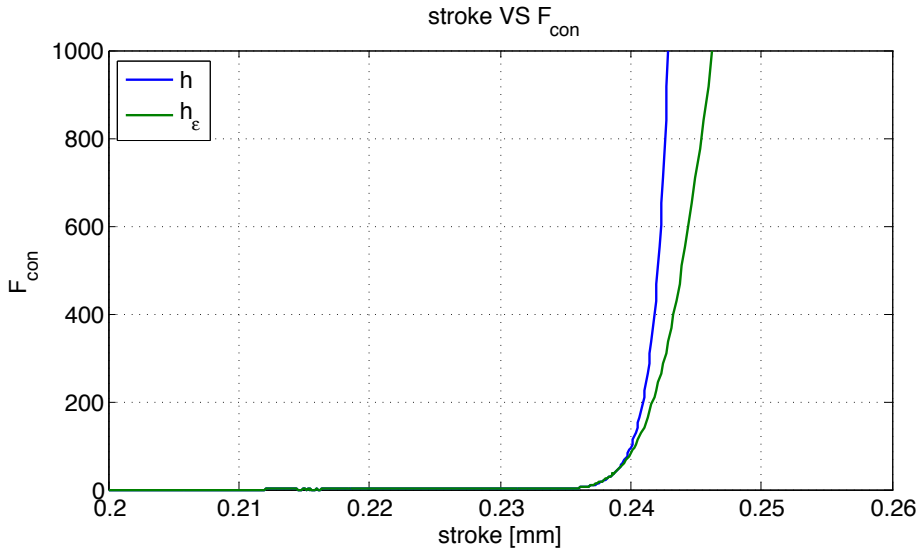

Figure 6.18: F_{con} vs stroke for h and h_ϵ

In Figure 6.19, the N-curves of 0 rpm and 0 kg/s are computed by subtracting F_{con} of Figure 6.17 from F of Figure 6.17. For 1500 rpm and 100 rpm, $F-N$ profiles not including unknown noise forces are finally computed. Figure 6.20 shows the $F-N$ profiles arranged by interpolation in the time direction.

6.4 Model Validation

6.4.1 Squeeze-Film Flow in Wet Clutch

To validate the squeeze-film model with experimental data, two approaches were used in the motion profile. First, the applied force acting on the moving clutch plate, i.e. the upper wall, is specified as an input profile to the simulation model. The output of the model consists of the resulting film thickness curve as a function of time. The second approach has the input specified in terms of the moving wall velocity as a function of time, and the reaction force from the fluid pressure within the wet clutch is obtained as the output of the model.

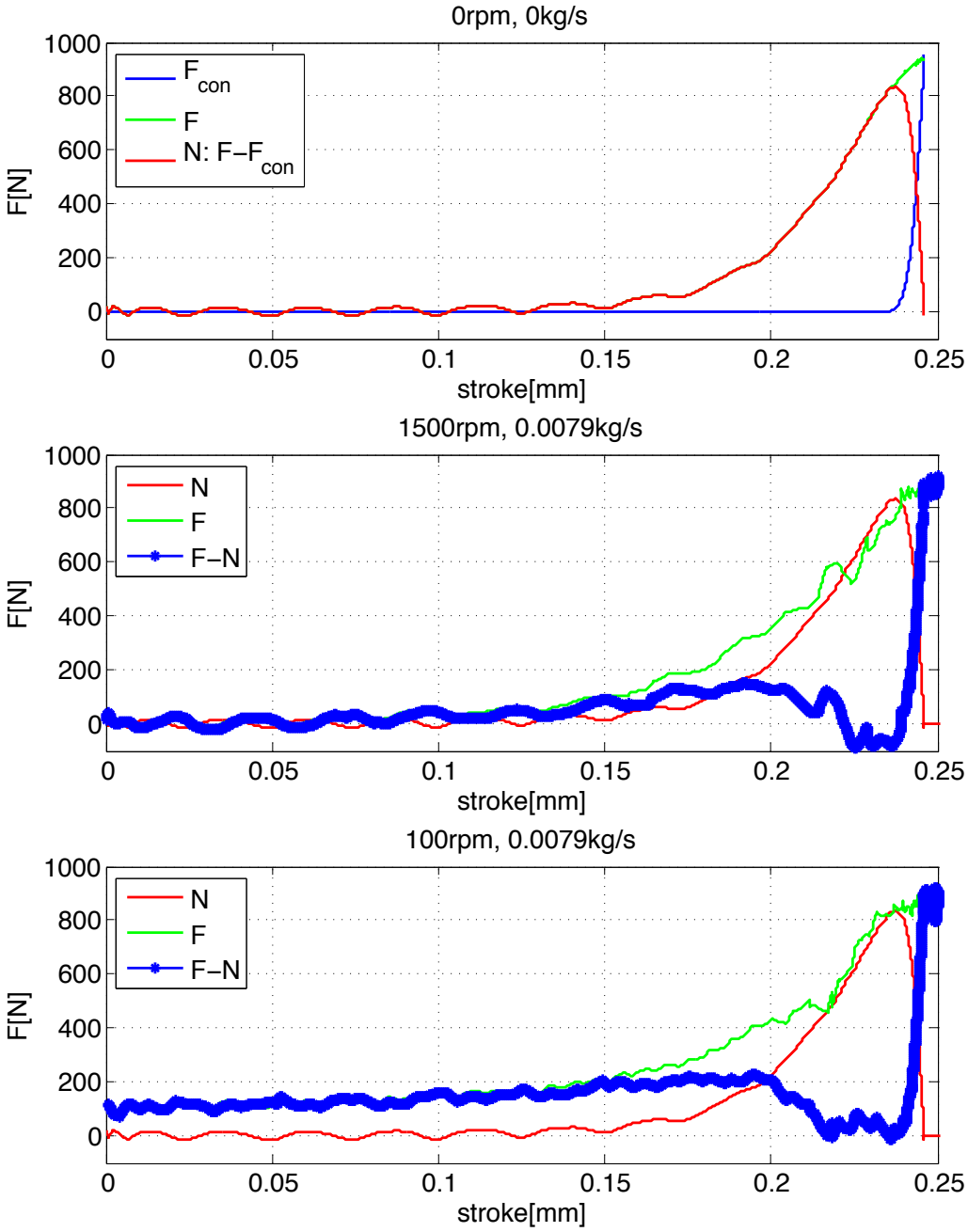

Figure 6.19: $F - N$ vs stroke after removing unknown noise force profile N at 0 rpm and 0 kg/s

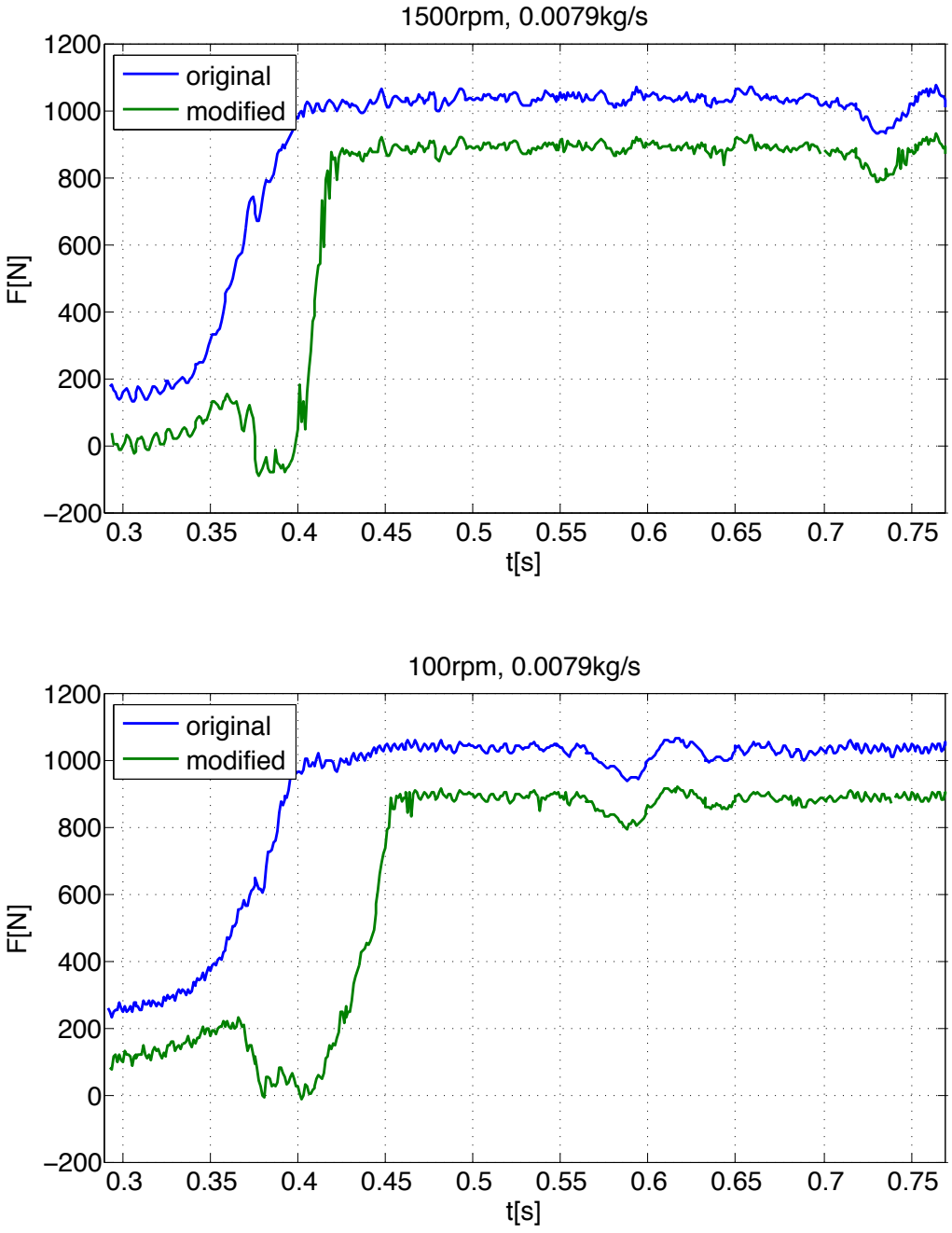

Figure 6.20: Pure F_{app} vs stroke during total engagement process

6.4.1.1 Applied force input

Table 6.3: Force profile types for squeeze simulation

Types	Permeability	Force profile feature
FP-1	Yes	Fitted curve for exp-2 in Figure 6.13
FP-2	Yes	Force offset of FP-1 (zero initial force)
FP-3	Yes	Eq. (6.2)
FP-4	No	Eq. (6.2)

Squeeze-film flow was simulated with several force profiles and was compared with the experimental results without removing the noise factors in order to measure the effect of noise factors on squeeze-film flow. The model used in the validation with the experiment includes the permeability and groove dimensions of the TGC. Zero-pressure boundary conditions was applied at both inlet and outlet boundaries. The lower wall rotates at $1,500$ rpm and 100 rpm, respectively, and the upper wall undergoes a translational motion. The applied force inputs of the simulation are listed in Table 6.3 and the comparison between simulation results and experimental data is shown in Figure 6.21. The experimental data correspond to an initial slip speed of 1500 rpm and an oil flow rate of 0.0079 kg/s.

In FP-1, a fitted curve based on the experimental force data was applied to the simulation model. The film thickness did not agree well with the experimental data. Since the non-zero initial force value of the fitted force profile may include noise factors, an offset was applied to the force profile of FP-1 in order to achieve a zero initial force in FP-2. In this case, the computed film thickness curve moves closer to the experimental data, but it still shows a significant difference.

In order to find a force profile resulting in a good match with the measured film thickness, a new force profile given by Eq. (6.2) was derived using Eq. (3.27) and the linearized film thickness curve illustrated in Figure 6.21. After $t = t_2$, a modified FP-2 profile was used. The force profile shifted the FP-2 profile down to fit the h_2 value at $t = t_2$. Although Eq. (3.27) did not include the effects of grooves and

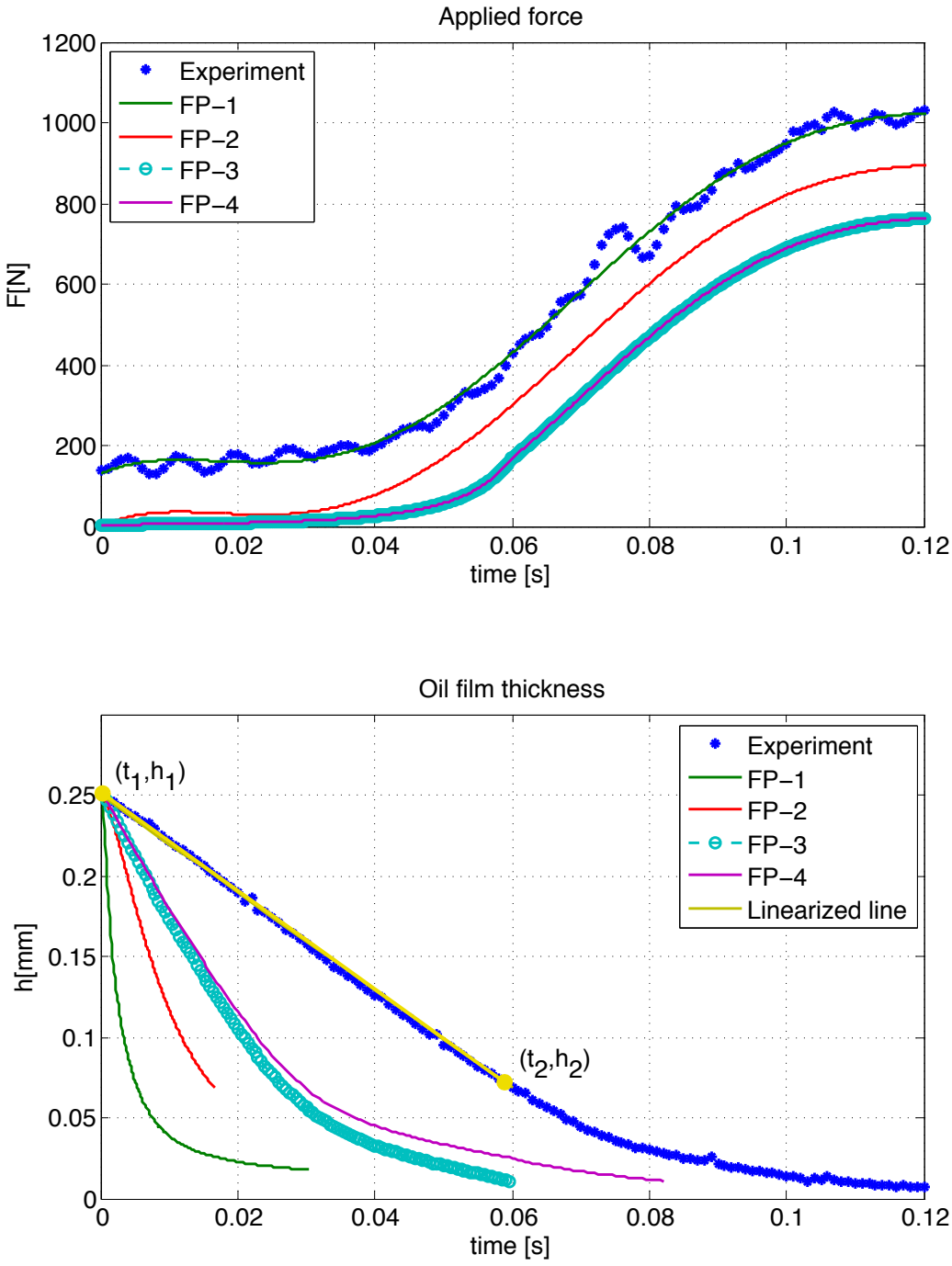

Figure 6.21: Squeeze simulation results with various force input profiles

centrifugal force, this equation was used to derive a force profile Eq. (6.2) because this may provide a basis for the comparison of the CFD model with experiments. Thus

$$F(t) = 6\Delta s\pi\mu M(h_0 + \Delta s * t)^{-3},\ when\ t_1 \leq t \leq t_2 \tag{6.2}$$

where

$$\Delta s = \frac{y_2 - y_1}{t_2 - t_1} = \frac{y_2 - h_0}{t_2},\ h(t) = \Delta s * t + h_0$$

Eq. (6.2) was used in the squeeze-film simulation including a grooved porous media zone. The film thickness of FP-3 still shows large differences as compared to the experimental data. In addition, in order to test the effect of the porous material on the squeeze-film flow, FP-3 (with porous feature) and FP-4 (without porous feature) were compared. FP-3 had a slower film thickness decay than FP-4, as expected from the findings of (*Berger et al.*, 1997; *Gethin et al.*, 1998). In conclusion, under the described computational conditions, the CFD models from FP-1 to FP-4 showed a large difference with the experimental data, so additional considerations need to be made to achieve closer agreement with the experimental data.

6.4.1.2 Velocity input

To investigate the reasons of the observed differences between the experimental and simulated film thickness results, it was decided to use the velocity of the moving clutch plate as input instead of the applied force. Using the velocity input no longer requires an iterative solution, so the simulation time is reduced. In this case, the force profile is obtained as an output of the simulation. All noise factors were included, and a sensitivity analysis of boundary conditions was conducted.

The test case pro-1, previously shown in Figure 6.16 for removing noise factors, was repeated and the results are shown in Figure 6.22(a). The first simulation,

sim-1, shows the model results using velocity input and zero pressure applied at the inlet/outlet boundaries. It can be seen that the agreement with the experimental data is not satisfactory at this stage yet. Simulations sim-2, sim-3 and sim-4 show the computed results for various non-zero inlet boundary pressures. The pressure levels specified at the boundaries were determined by trial and error because measuring the pressure at the inlet and outlet was not possible to measure during the experiments. In the case of sim-2, constant pressure values were applied at the inlet boundary. For sim-3, the inlet pressure is linearly changed from 6000 Pa to 20000 Pa. The inlet pressure in the case of sim-4 is changed from 6000 Pa to 60000 Pa following a parabolic pressure profile. The analytical force curve of FP-3 (or FP-4) for non-grooved and non-rotating disks was expected to predict larger force values than pro-1 from the grooved, rotating disk experiment. The results agree well with case pro-1 of the experimental data. This may indicate that the zero-pressure boundary condition of Eq. 6.2 is not valid for a real wet clutch test. This may also explain the difference between case pro-1 of the real clutch test and case sim-1 with zero-pressure boundary conditions. As observed in Figure 6.22(a), a parabolic inlet pressure profile leads to good agreement with the experimental results (pro-1). Finally, for low rotating speeds, case pro-2 is repeated and the simulation results are compared in Figure 6.22(b).

6.4.2 Validation of Integrated Engagement Model

In this section, all components of the engagement process are combined in a wet clutch model that includes heat transfer, rough surface flow, asperity contact, squeeze-film flow, grooved plates and flow through the porous friction material. The properties of oil, steel plate, friction plate and operating conditions used in the simulation are listed in Table 6.4. The schematic of the simulation model is shown in Figure 6.23 to identify the various components of the model.

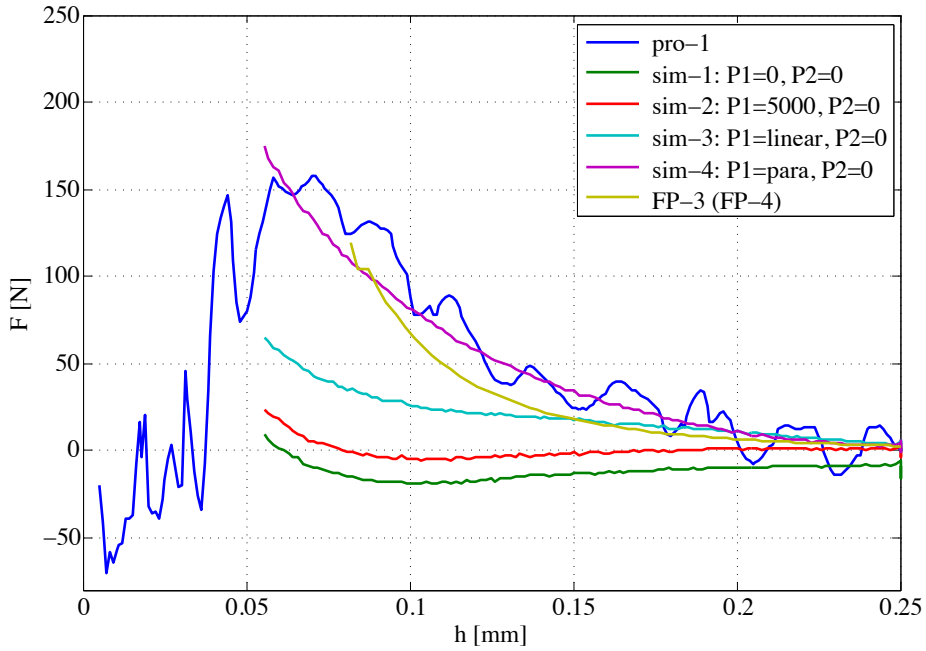

(a) 1500 rpm, 0.0079 kg/s

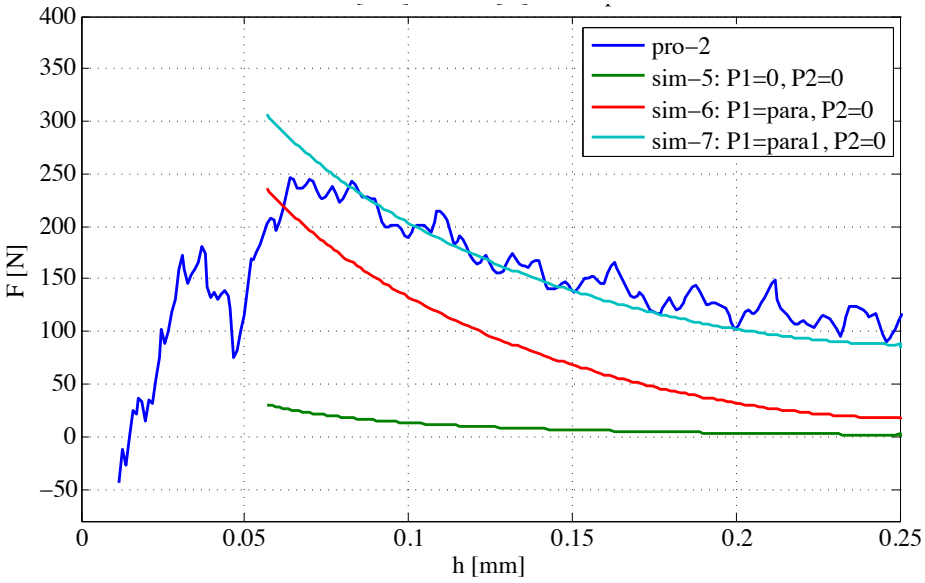

(b) 100 rpm, 0.0079 kg/s

Figure 6.22: Sensitivity test of pressure inlet boundary for squeeze flow

Table 6.4: Simulation model parameters for engagement process

Operating conditions and geometry	
Initial temperature	305.37 $[K]$
Ambient temperature	305.37 $[K]$
Convection coefficient	100 $[W/m^2\ K]$
Initial rotating speed	1500 or 100 $[rpm]$
Inner radius	82.8 $[mm]$
Outer radius	92.65 $[mm]$
Initial film thickness	0.25 $[mm]$
Moment of inertial	0.165 or 2.0 $[kg\ m^2]$
Friction plate	
Thickness (ons side)	0.66 $[mm]$
Groove width	1.0 $[mm]$
Groove depth	0.17 $[mm]$
Total groove number (one side)	96
Axial permeability	0.072 $[darcy]$
Radial permeability	7.2 $[darcy]$
Asperity density	1.3568e+09 $[1/m^2]$
Asperity tip radius	3.33680e-05 $[m]$
Roughness, rms	4.84e-06 $[m]$
Young's modulus, E	41.3 $[MPa]$
Elastic coefficient for contact area, E_R	35.97 $[MPa]$
Thermal conductivity	0.14 $[W/m\ K]$
Specific heat	1845 $[J/kg\ K]$
Separator (Steel plate)	
Thickness	3.0 $[mm]$
Thermal conductivity	46.04 $[W/m\ K]$
Specific heat	502.48 $[J/kg\ K]$
Density	8030 $[kg/m^3]$
Oil properties	
Viscosity	Eq. (4.17) $[kg/ms]$
Density	Eq. (4.19) $[kg/m^3]$
Thermal conductivity	0.126 $[W/m\ K]$
Specific heat	1845 $[J/kg\ K]$

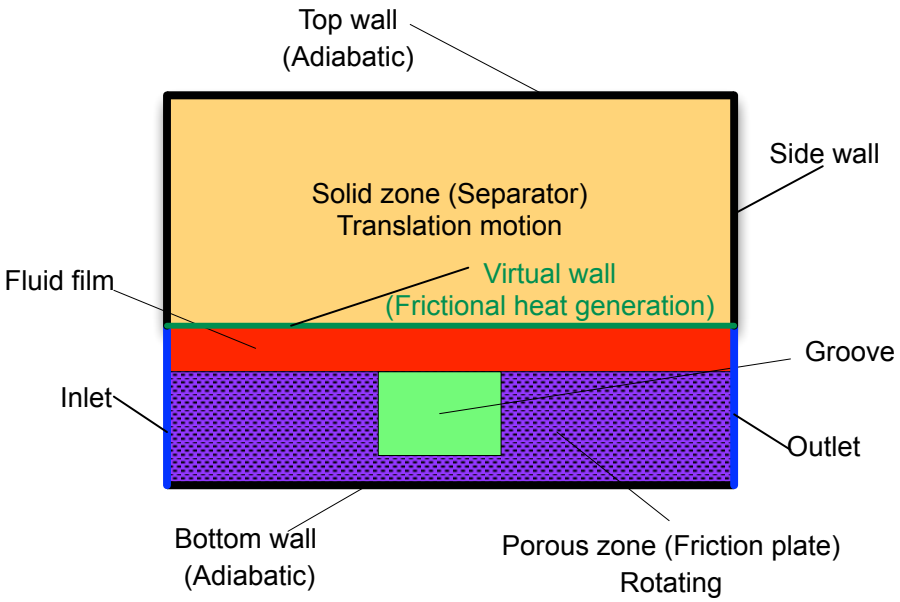

Figure 6.23: Schematic of wet clutch model for total engagement process

Since the piston pressure controls the engagement process in real clutch test, the iterative method is valuable in predicting the behavior of real wet clutch. However, for the purpose of wet clutch model validation, velocity input can be efficiently utilized in place of force input. As described in Section 5.4.2, when the heat transfer component with a solid zone (separator) is enabled in a periodic model, the model fails to converge. To overcome the moving mesh error, a 360 ° full disk model was used instead of the 60 ° periodic model. It inevitably caused the number of cells to become too large. To reduce the simulation time, velocity input was selected to avoid using the iterative method with applied force input. The velocity input profiles were obtained by fitting a smooth curve to the experimental data. The force profile now becomes an output of the model that can be used to assess the accuracy of the simulation results.

Figure 6.24 shows a velocity profile computed from the measured stroke data under flow rate 0.0079 kg/s for 100 rpm and 1500 rpm. A smooth curve fitted to the measured velocity profiles was applied as input to the model. For consistency with the

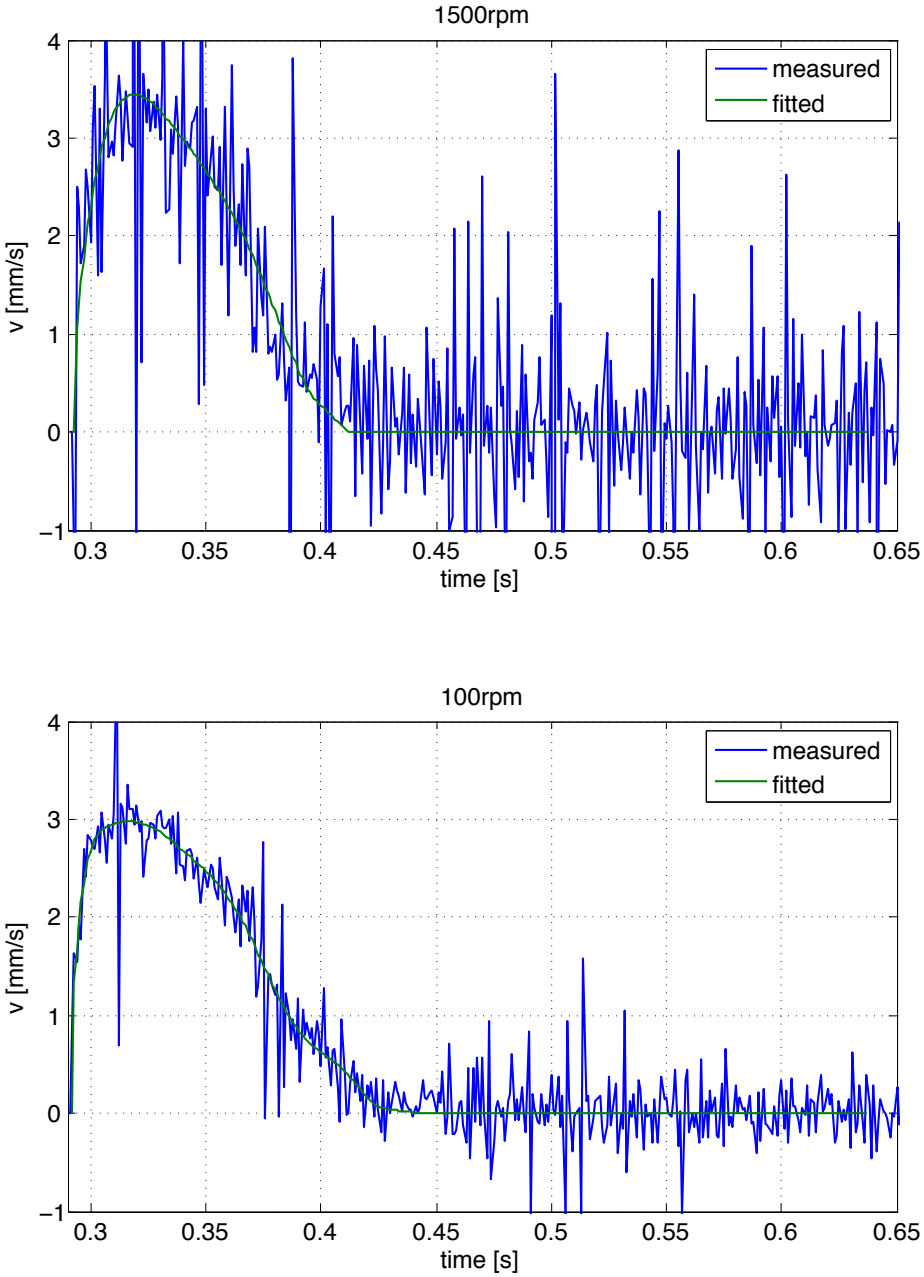

Figure 6.24: Velocity input profiles and fitted curves: 1500rpm and 100rpm, flow rate 0.0079 kg/s

computations, the start time was shifted from $t = 0.292\ s$ to $t = 0.0\ s$. The time step in the simulation was 0.001s and the total engagement time was about 1 second. A pressure boundary condition of Section 6.4.1.2 was used at the inlet boundary of the fluid film and porous zone. Both outlet boundaries were defined by zero pressure. For the solid zone (separator), the upper wall was defined as an adiabatic boundary and the side walls were defined as either a constant temperature or adiabatic boundaries. The bottom wall, i.e. the friction plate was defined as an adiabatic wall because it is made of a thin steel core plate.

For friction coefficient, Eq. (4.22) from *Berger et al.* (1996) is a function of the sliding speed. At zero rotational speed, μ_{fric} becomes infinite and the torque is undefined at the end of the engagement process. Hence, for 1500 rpm, either Eq. (4.22) or a constant value of $\mu_{fric} = 0.138$ was used in the simulation and the results were compared. The constant values of the friction coefficient was determined by adjusting its value to satisfy the real engagement time. Also, for the low initial rotating speed (100 rpm), a constant value of $\mu_{fric} = 0.186$ was again chosen to satisfy the engagement time of the experimental data.

Figure 6.25 and Figure 6.26 show the simulation results for 1500 rpm. In Figure 6.25, the rotating speed, total force F_{total} ($=F_{fluid} + F_{con}$) and total torque T_{total}($=T_{fluid}+T_{con}$) results are shown for two different inlet pressure boundary conditions and the results are compared with the corresppponding experimental data. The rotating speed curves of the model show a good agreement with the experimental data. For the force profile, the simulation results show a dependency on inlet boundary condition. In the hydrodynamic lubrication region, where rough surface effects are negligible, the force curve with the polynomial p_{in} boundary condition agree well with the experimental profile. Recall that the polynomial pressure function was derived by trial and error in Section 6.4.1.2 to match the simulated force results with the modified experimental data. However, as the asperity contact begins to affect the

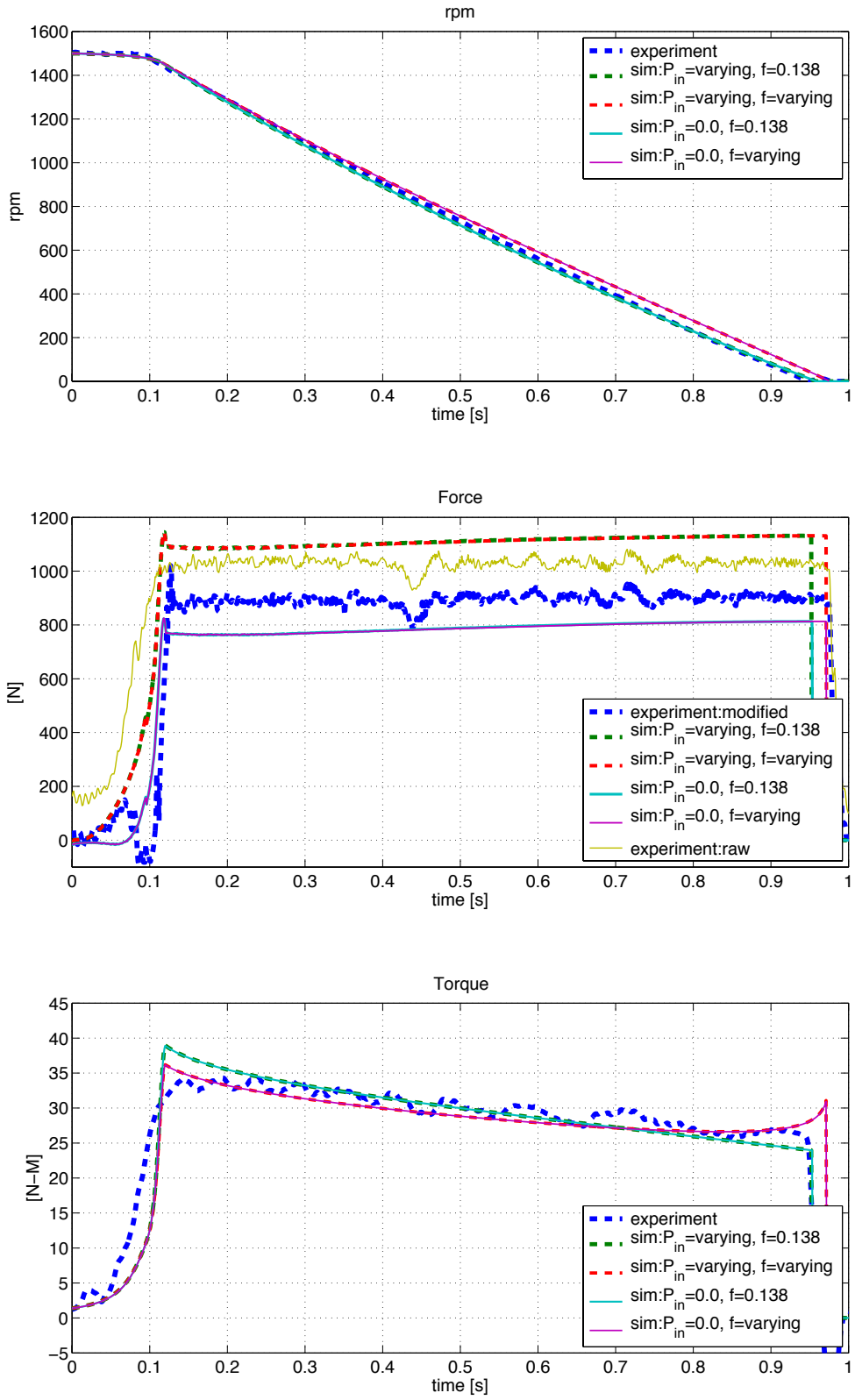

Figure 6.25: Torque and force profile comparison between simulation results and experimental data : 1500 rpm and 0.0079 kg/s

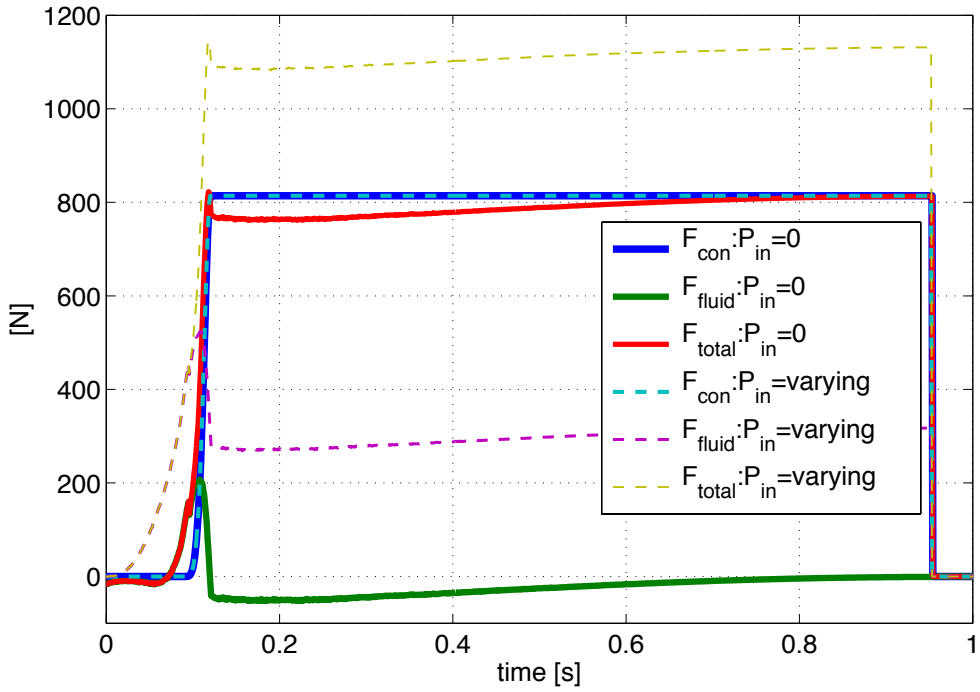

(a) Force: $p_{in} = 0$ vs $p_{in} = varying$

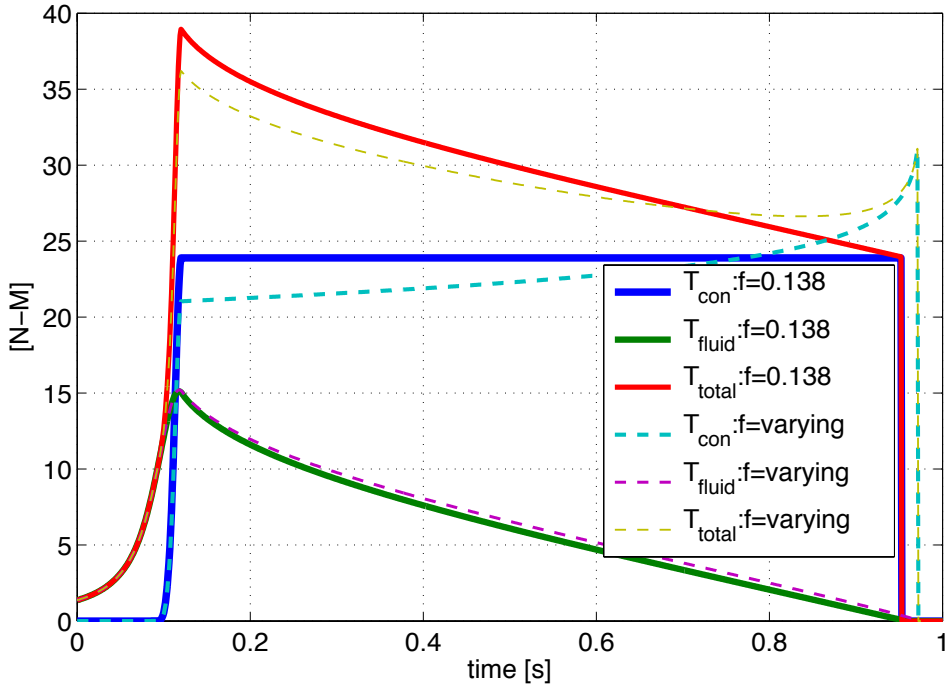

(b) Torque: $\mu_{fric} = 0.138$ vs $\mu_{fric} = varying$

Figure 6.26: The effect of μ_{fric} and p_{in} boundary condition on F and T profiles: 1500 rpm and 0.0079 kg/s

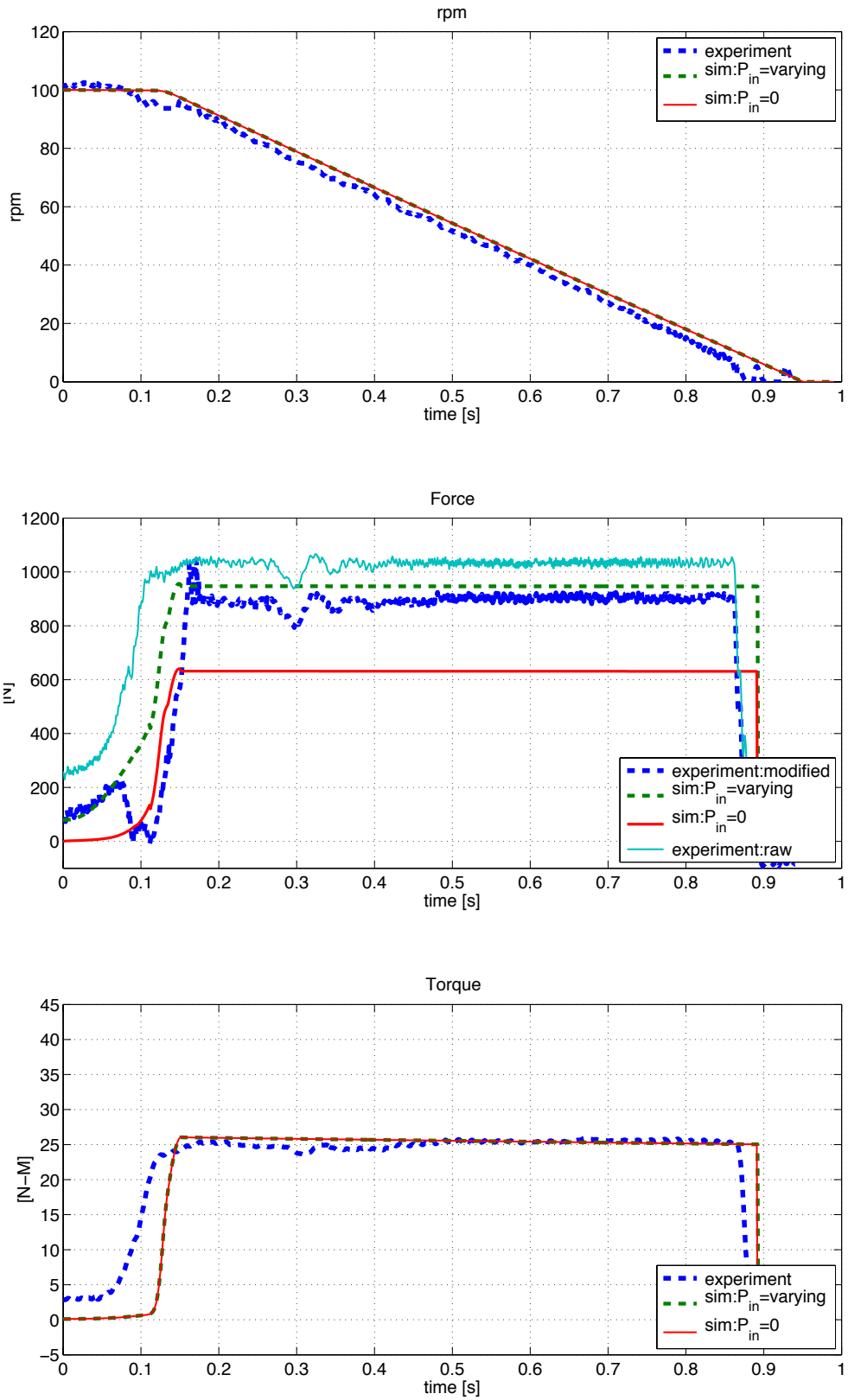

Figure 6.27: Torque and force profile comparison between simulation results and experimental data : 100 rpm, 0.0079 kg/s and $\mu_{fric} = 0.186$

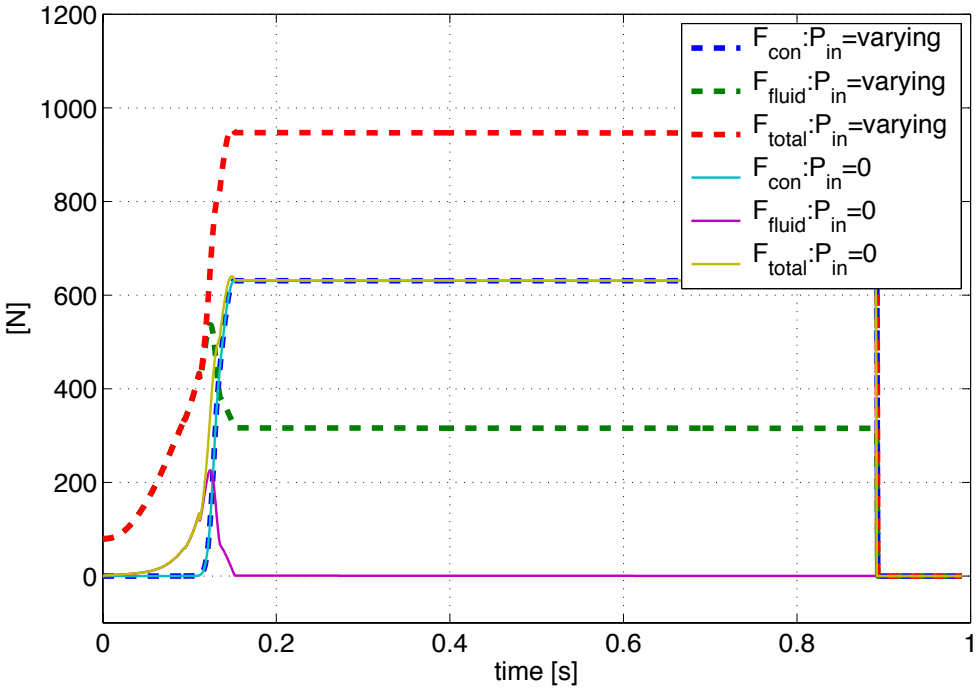

(a) Force: $p_{in} = 0$ vs $p_{in} = varying$

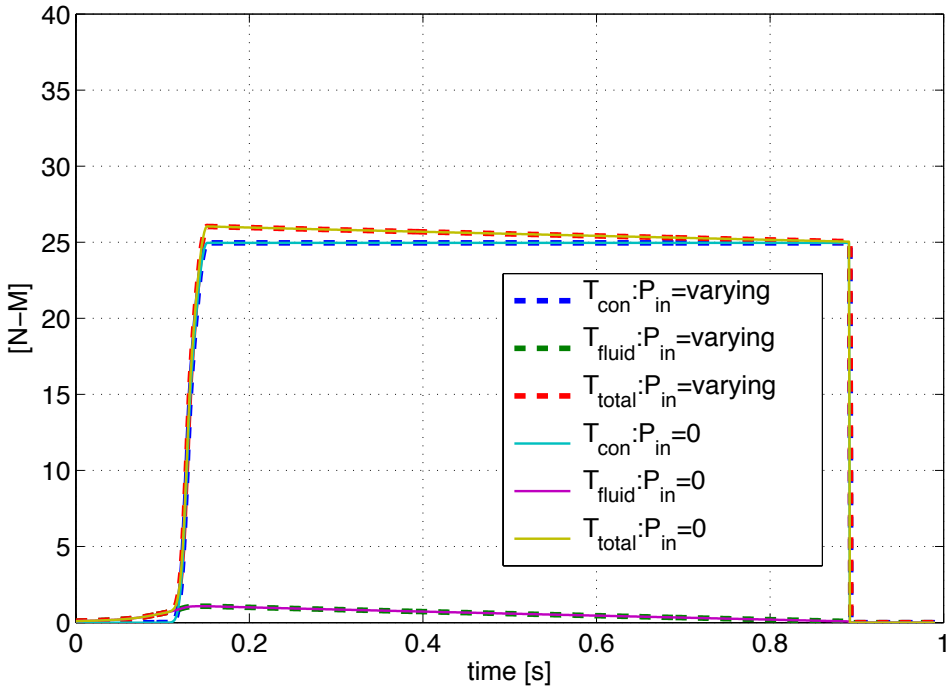

(b) Torque: $p_{in} = 0$ vs $p_{in} = varying$

Figure 6.28: The effect of μ_{fric} and p_{in} boundary condition on F and T profiles: 100 rpm, 0.0079 kg/s and $\mu_{fric} = 0.186$

engagement process, the modified experimental force profile shows better agreement with the simulation results when a zero-pressure boundary condition is used rather than the polynomial p_{in} boundary condition.

Regarding the torque, the computed results increase slower than the experimental data during hydrodynamic lubrication. However, the steady torque level of values are in good agreement with the experiment data. The steady torque level is related to the asperity contact area and the good agreement means that the theoretical asperity area equations for the non-gaussian rough height distribution, i.e. Eq. (4.32) and (4.33) are realistic models. Notice that the simulated torque with a friction coefficient given by Eq. (4.22) becomes divergent as the rotating speed approaches zero. On the other hand, the torque with a constant friction coefficient results in a higher peak torque value at $t = 0.12$ as compared to the model with a friction coefficient given by Eq. (4.22) although the torque value converges toward zero, at the end of engagement process. Fine tuning of the friction coefficient seems to be necessary. Finally, the in-depth investigations for noise factors and inlet boundary condition sensitivity require more accurate and additional experimental data. This could not be performed in the present work because it requires modification of the test stand.

In Figure 6.26(a), F_{fluid} and F_{con} are compared with regard to the inlet pressure boundary condition. The polynomial function boundary leads to higher F_{fluid} than that of the zero-pressure boundary. It can be seen that a change in the inlet boundary causes a change in F_{fluid}. The negative F_{fluid} values for $p_{in} = 0$ can be explained by examining the analytical solutions of Section 3.1. With zero inlet and outlet pressure boundaries and a high rotating speed , F_{fluid} can have negative values when $h >> 0$. Figure 6.26(b) shows T_{fluid} and T_{con} profiles. According to the definition of the friction coefficient, the T_{con} profile is changed and this change is reflected in the total torque profile.

Figures 6.27 and 6.28 show the simulation results for 100 rpm. In Figure 6.27, the

computed F_{total} has a similar trend with F_{total} at 1500 rpm. From $t = 0$ s to $t = 0.07$ s, the simulated force for P_{in} = varying is closer to the modified experimental curve. Between $t = 0.1$ s and $t = 0.14$ s, the simulated force with zero P_{in} approaches the modified experimental curve. Then, as the force attain steady values, the modified experimental force is located between the force results from the two pressure inlet boundary conditions. For T_{total} between $t = 0$ s and $t = 0.15$ s, the discrepancy between the experimental data and the simulation results is larger than those at 1500 rpm. This may be caused by noise factors not considered in the simulation model. Also, the larger torque discrepancy at low rotational speeds indicates that the noise factor may be related to the rotating speed. The rotating speed is related to the friction coefficient and the latter is a typical parameter affecting torque. It is speculated that the measured torque may include some friction torque from the test stand.

In Figure 6.28(a), the trend of the force curves for $p_{in} = 0$ is shown to be similar to the computed force curves at 1500 rpm. However, F_{fluid} for $p_{in} = 0$ has no negative values since F_{fluid} can remain positive at low rotating speeds and small flow rates. In Figure 6.28(b), the torque curves for $p_{in} = 0$ are identical to those for p_{in} = varying because the simulation model uses the same friction coefficient and velocity input.

Figure 6.29 shows the average temperature variation at the middle surface of the solid zone (separator), where the experimental temperature was measured by a thermocouple temperature sensor. The figure also shows the average interface temperature between the separator and friction plates. As expected, during the engagement process, the interface temperature is higher than the separator temperature because frictional heat is generated at the interface. However, as the transient process of engagement is completed with a zero rotating speed, the interface and separator temperatures become identical. Depending on the thermal condition of the side walls of the separator, large temperature changes are observed. The temperature with the

convection condition was higher than that with a constant temperature condition, where the constant temperature was equal to the ambient temperature.

In Figure 6.30, the simulation results of the separator temperature are compared with the corresponding measured temperature. The results agree better when using the convection thermal condition than when using a constant ambient temperature. However, the simulation results are not satisfactory except for the final temperature value. There are two possible reasons for the difference between the simulation results and the measured data. First, one separator plate is in contact with the cover plate of the test stand housing and the other is connected with the piston module. However, the connection hardware was not considered in the simulation model. In the current research, a single fluid film layer has been considered in order to simplify the model. Second, the response time of the temperature sensor may have affected the measured data. If there exists a lag in the response time of the temperature sensor, the actual temperature difference between the experimental data and the simulation will have been smaller than that in Figure 6.30. At the final engagement time, regardless of sensor lag time, the simulation solution and the measured predict approximately the same temperature value.

Figure 6.31 shows the interface temperature variation based on the simulation results with a convection boundary condition at the separator's side walls. Also, Figure 6.32 shows side view of the temperature variation at $r = 87.72\ mm$. The interface temperature continuously increases until $t = 0.6\ s$. Then, the interface temperature slightly drops at $t = 0.9\ s$ and $t = 1.0\ s$. The grooves seem to play a role in cooling down the temperature because the temperature near grooves is lower than in other areas. Also, the temperature at the outer area is slightly higher that that at the inner area. The temperature at the separator is almost uniform at $t = 0.9\ s$ and $t = 1.0\ s$ while it shows a relatively large temperature gradient at $t = 0.3\ s$ and $t = 0.6\ s$.

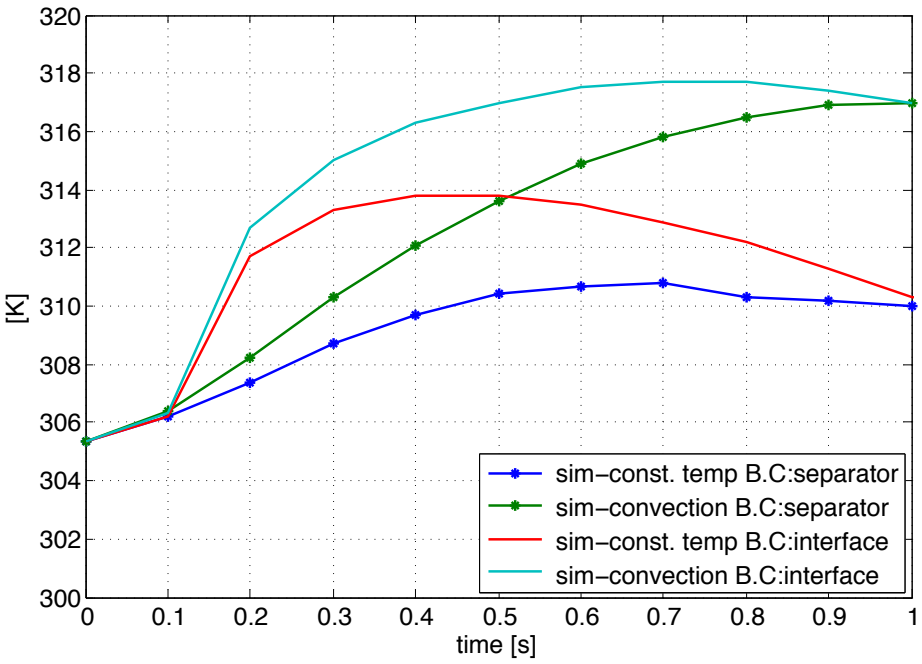

Figure 6.29: Convection B.C vs constant temperature for separator's side walls: 1500 rpm and 0.0079 kg/s

In Figure 6.33, the pressure distribution is shown. At $t = 0.3\ s$ and $t = 0.6\ s$, large pressure differences are present. This is due to the rotation of the friction plate. Since the rotational speed approaches zero at $t = 0.9\ s$ and $t = 1.0\ s$, the pressure distribution at that time becomes uniform. During the engagement process, the highest pressure and the lowest pressure points are located at the end of the periodic area, where the widest non-grooved area exists. As the grooved friction plate is rotating counterclockwise on the figure, the pressure along the circumference increases clockwise.

For the simulation results with the initial speed of 100 rpm, the temperature and pressure distribution show a smaller variation than those with initial speed of 1500 rpm because both the friction heat on the interface and the static pressure are proportional to the rotating speed.

In summary, the simulation results for the entire engagement process were validated with the experimental data for two different initial rotating speeds. The simu-

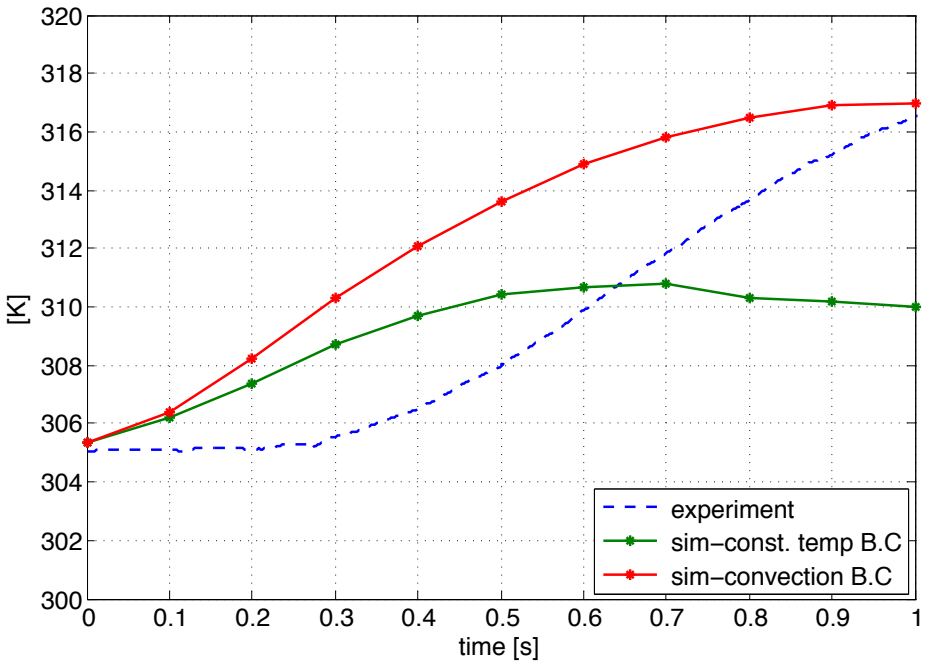

Figure 6.30: Simulation and experiment results of separator temperature for convection and constant temperature conditions: 1500 rpm and 0.0079 kg/s

lation results and the experiment data qualitatively show a similar trend for torque, force and rpm. Also, the simulation predicts satisfactorily the torque value at mixed lubrication, the engagement time, as well as the temperature at the end of engagement process. However, the predicted values of the transient temperature, and force and torque profiles during the engagement process need to be improved. Finally, an in-depth analysis of noise factors for experimental test system is required to validate and improve the simulation model.

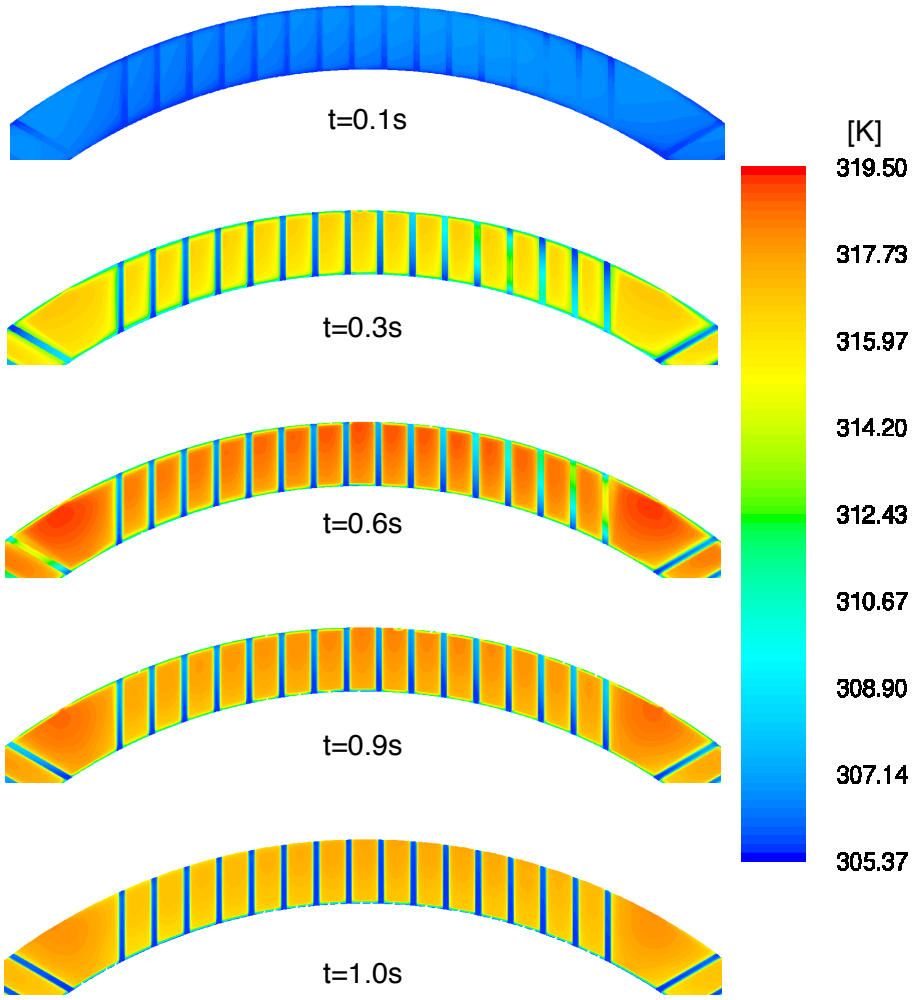

Figure 6.31: Interface temperature contour of a model with convection B.C at separator's side walls : 1500 rpm and 0.0079 kg/s

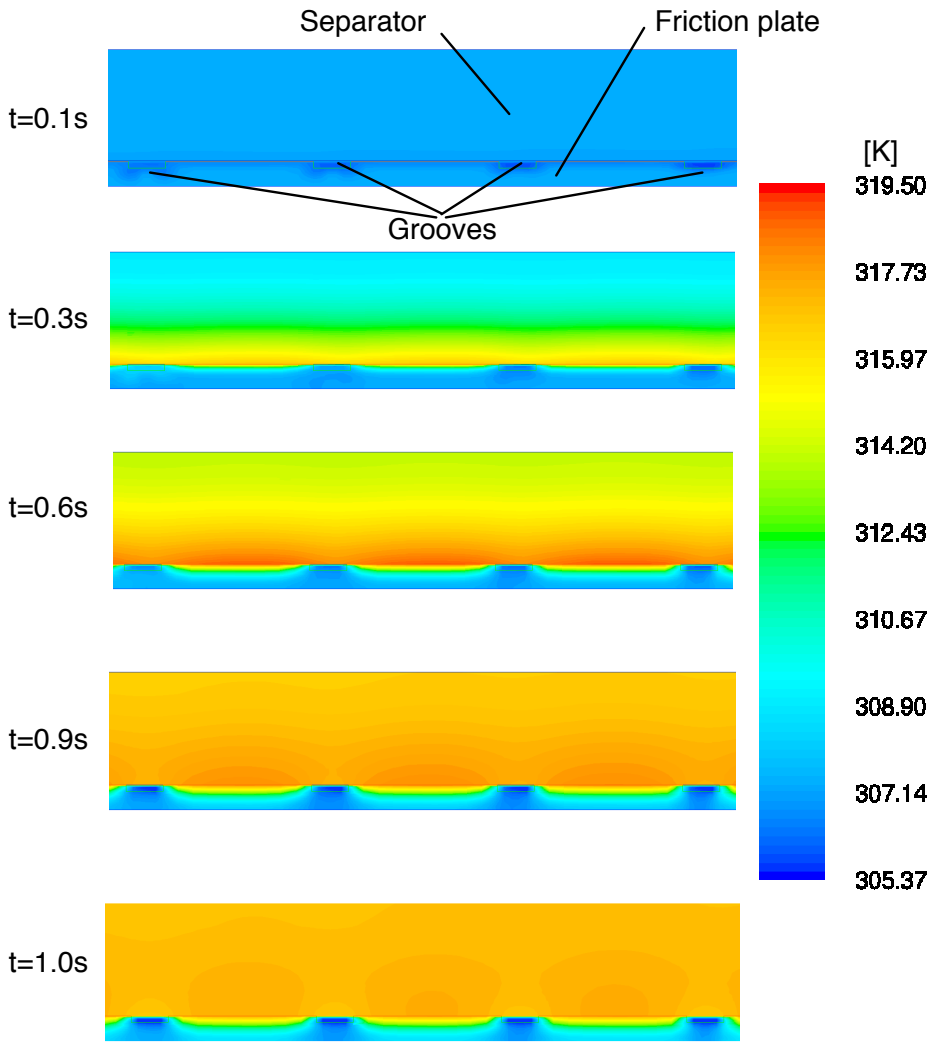

Figure 6.32: Temperature contour side view of model using convection B.C at separator's side walls : 1500 rpm and 0.0079 kg/s

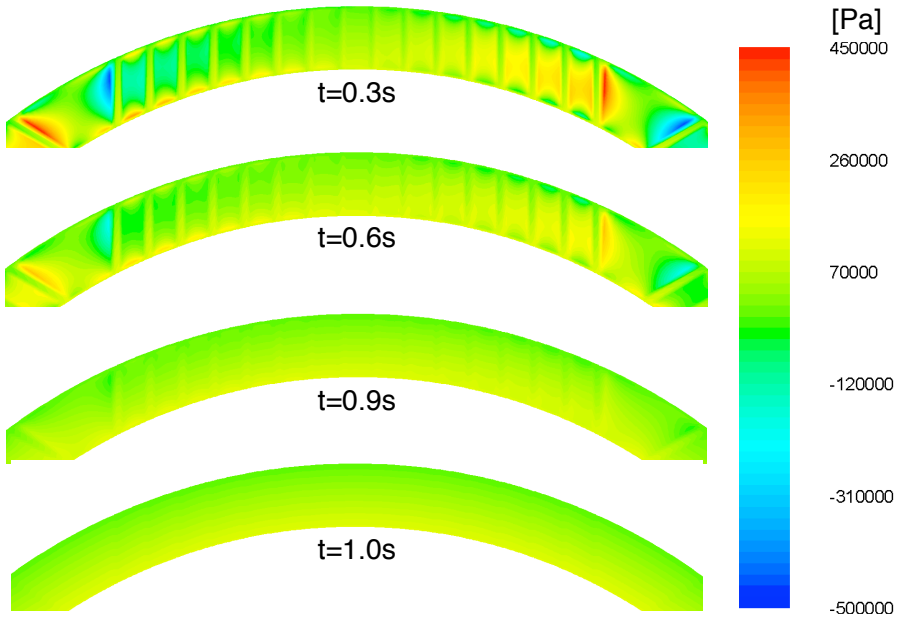

(a) Inlet pressure boundary: polynomial function

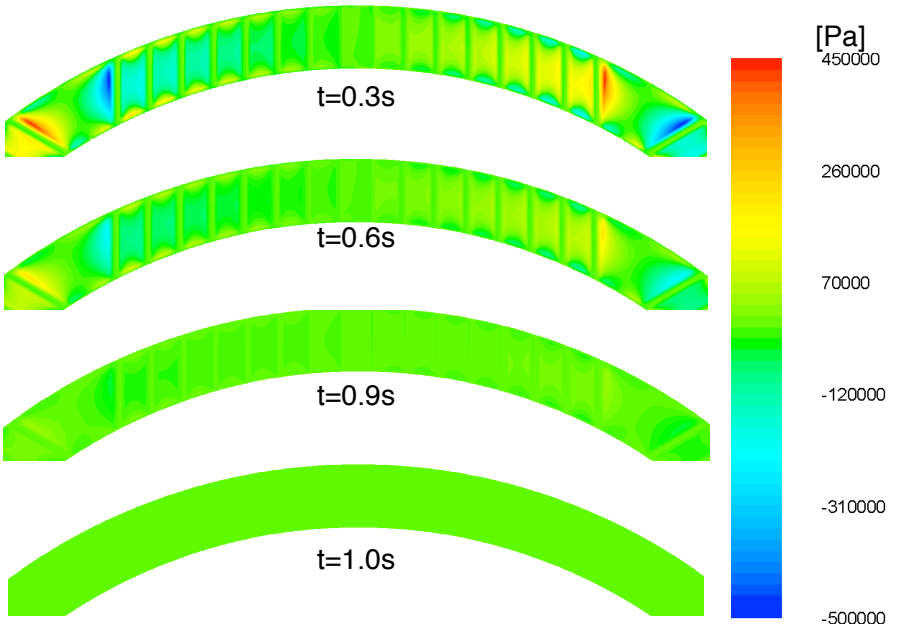

(b) Zero inlet pressure boundary

Figure 6.33: Pressure contour of oil film: 1500 rpm and 0.0079 kg/s

CHAPTER VII

Conclusions

7.1 Summary and Conclusions

In this research, a predictive wet clutch model was developed to simulate the engagement of a wet clutch of an automatic transmission. The model was validated with analytical solutions and experimental measurements. The research was motivated by the need to understand better the physical phenomena occurring in a wet clutch system, and was made possible by recent advances in computational fluid dynamics and computer hardware. The results of this study are essential for the improvement of controllability and design of automatic transmissions. The integration of the various physical components was a real challenge, and the validation of the model proved to be a formidable task. The physics of wet clutch engagement involves multi-phase flow of air and oil, squeeze-film dynamics, flow over a rough surface, asperity contact, heat transfer, flow in through the porous media of the friction material, compression of the friction material, and flow through micro-channels, e.g. friction material grooves.

The research effort in this thesis focused on the following topics:

1. Modeling work began with the simulation of open clutch flow. Although simpler to visualize than the engagement process, the characteristics of an open clutch represent a very complicated problem that is not easily explained. The results of

single-phase flow model show large pressure differences between the two sides of grooves. It was found that a computational domain limited to the flow between the disks led to numerical errors near the inlet and outlet boundary areas, especially when backflow is present. To reduce the numerical error, extended boundary models were constructed that led to significant reduction of numerical errors. The optimal size of the computational domain was a close replica of the real test hardware, including the clutch enclosure area. Drag torque results for multi-phase flow showed a typical torque trend. At low rotating speeds, the drag torque increases as the rotational speed increases. After passing the peak torque rpm, the drag torque is reduced until a constant value is reached. As the flow rate increases, both the peak torque and the rpm at the peak torque increase. The surface tension of oil and wall adhesion angle both were found to affect the drag torque.

2. The research proceeded with the modeling of squeeze-film flow during engagement of a wet clutch. A new iterative method was developed. This approach produced stable and accurate results when compared to analytical solutions of the Reynolds equation for annular and square plates under various boundary conditions. The sensitivity of model results to pressure boundary conditions was studied and guidelines were provided for the proper selection of the boundary conditions.

3. Contact torque and force were included in the model using the theoretical framework of real contact area. The non-Gaussian asperity height distribution of the TGC friction material was fitted using a polynomial PDF curve and a Gaussian Mixture model was proposed. The computed real contact area curves were compared with the measured data and showed good agreement.

4. The effects of flow next to a rough surface were introduced to the model using the

pressure flow factor. This is an empirical pressure factor for lubricant flow. A new method for computing flow factors for non-Gaussian height distribution was proposed that does not require repetitive simulations. The flow factors based on the proposed method show good agreement with the numerically generated flow factor results. The flow factor was introduced to the CFD model by a novel approach in which the fluid viscosity is dynamically adjusted.

5. A heat transfer model was coupled with the CFD model. A virtual volume concept was used to model the contact interface. Thus, the computed frictional heat flux is converted into a volumetric heat generation rate for the virtual volume. The virtual volume concept was validated by comparison with analytical solutions for a simple geometric set up.

6. The permeability of the friction material was considered using a flow through porous module. The permeability of the friction material results in faster reduction of the squeeze-film thickness. Results show that as the film thickness becomes smaller, the permeability impact on the film thickness increases. Moreover, since the change in film thickness has an influence on the clutch torque and force, the permeability of the friction material is an important parameter for wet clutch engagement.

7. The compressibility of the friction material was considered in the computation of the film thickness. It was shown that compression of the friction material can also affect the variation of a measured stroke.

8. Using experimental data a systematic effort was made to validate the proposed computer model. Since the experimental data contains noise factors, several attempts were made to de-noise the data. It was found that the deflection and friction of the piston module can be included in the engagement experiment. Other unknown noise factors were removed by considering a stroke test without

oil flow. As eliminating noise issues in the data, the model was run using velocity as input and validated using a measured force profile. The simulated rotational speed profile agreed perfectly with the measured data. The torque and force results showed qualitative agreement with the data. The torque profile showed good agreement with the data during mixed lubrication. During hydrodynamic lubrication, the torque showed a little discrepancy at high rotational speed, but the difference became significant at low rotational speeds. The computed temperature results for the separator were compared with the measured data and good agreement was obtained at the final engagement state. However, the transient profile of the temperature was unsatisfactory.

The integration of a multi-physics model for wet-clutch engagement required complex procedures and repeated a trial and error approach, as no such approach had been previously attempted. During the development of model, the influence of each component of the model on wet-clutch operation was studied independently. The general performance of the multi-physics model shows the possibility for a successful expansion to a model that includes the actual housing geometry of a multi-disk clutch system. The model developed in this research will potentially form the framework for a complete clutch model in future research.

7.2 Contributions

The main contribution of this research is the development of a baseline model for the wet clutch engagement process that is capable of including real hardware geometry. The majority of previous studies of wet-clutch systems have used some form of the averaged Reynolds equation, which limits the solution to small Reynolds numbers, i.e. lubrication flow in a very thin clearance. Although the proposed iterative technique is a part of the wet-clutch multi-physics model, the method can be used

for other applications involving squeeze flow, such as printing and thrust bearing systems.

This research also led to the construction of several novel, extended-boundary formulations. The true boundary conditions of the clutch system are unknown or difficult to measure. Furthermore, the location of the appropriate boundary has been difficult to determine. The extended boundary models that were developed in this study can reduce the numerical errors at the inlet/outlet boundaries and improve the solution accuracy, especially in the presence of recirculating flow.

A methodology for calculating pressure flow factors for flow next to rough surfaces was proposed. The approach requires a mixture model in case of a non-Gaussian PDF of the measured asperity height profile. The pressure flow factor of the measured height profile can be calculated using the pressure flow factor equation for a Gaussian PDF. This method can reduce the numerical effort required by the conventional approach of computing the flow factor by generating the rough surface and solving numerically the associated partial differential equation.

The validation of the CFD model required the collection of a valuable set of experimental data. The validation was limited by the presence of noise factors. Several new techniques for data de-nosing were proposed and implemented. The analysis has shown the necessity for upgrading the SAE No. 2 test stand.

Last but not least, the integration of all the physical processes involved in wet-clutch engagement was for the first time accomplished in a robust, multi-physics model. This was an ambitious undertaking since it has been difficult in the past to even validate the individual components of the model. The overall validation of the model is fair although some components agree very well with the measured data. The results are certainly encouraging and a number of possibilities exist for future research.

7.3 Future Research

In this research, several features of a wet-clutch system have been studied. In addition, the model was validated with experimental data and analytical solutions. However, several components of the system have not been treated with equal rigorousness in this research, so additional analytical, computational and experimental work is needed to complete the development of a reliable wet-clutch model.

First, the present simplified, two-disk model should be extended to include the complete test hardware geometry. The present model is very sensitive to the boundary conditions imposed at artificial inlet/outlet boundaries. The complete model will require an increased computational effort, but it will eliminate ambiguities at the boundary and will allow a comprehensive validation process.

Second, the SAE No. 2 test stand should be upgraded. The observation of oil and air flow within a clutch system is necessary to thoroughly understand the multi-phase phenomena occurring in a wet clutch system. Moreover, to isolate the unknown noise factors associated with the test stand, more accurate stroke and gap data between the separators should be measured. Flow rate and pressure level at the inlet and outlet need to be measured in real time. Finally, although the torque signal is filtered to remove signal noise, a hardware modification to reduce signal noise seems necessary.

Third, the open clutch model presented here needs to be validated with experimental data. In this research, the numerical solutions for an open clutch have been adopted without experimental validation. To build a more reliable open clutch model, validation with experimental data is strongly recommended.

Fourth, the effect of waviness of the clutch disks and the thermal expansion of the separator should be included in the model. The present wet-clutch model has assumed that squeeze flow and mechanical contact occurs between two parallel plates. However, the TGC plate and many other friction plates have a waviness characteristic on the surface. The waviness may cause the local contact on the top areas of waviness

profile. The local contact and the waviness shape may affect both load and torque, and are significant parameters in wet-clutch operation. Finally, thermal expansion of the separator and housing can change the film thickness and may have a significant effect on the load and torque of a wet clutch.

Fifth, the parametric study of wet clutch design factors presents an unlimited horizon for future work. The search for optimal dimensions and pattern of grooves and waviness, the permeability of the friction material, oil properties and roughness of the friction plate can be analyzed quickly and efficiently with the proposed model.

Finally, the proposed wet-clutch model has used empirical models for asperity contact and rough surface characteristics. To include the elastic deformation of real asperities and the detailed interaction between fluid and solid, a multi-scale model for a Fluid- Structure-Interaction would an ideal topic for future work.

APPENDICES

APPENDIX A

Rough Surface Generation and Flow Factor Simulation Procedure

A.1 Rough Surface Generation

To compute flow factors in the current study and to simulate real contact area, the generation of a rough surface is important. A three-dimensional scanned image of a rough surface can be used in the simulation, but due to the limitation of available test instruments, a profilometer with a contact stylus was used to measure the roughness of the friction material of the TGC. Since the measured data represent a one-dimensional profile, statistical methods were utilized to generate three-dimensional rough surface structures.

Figure A.1 shows the overall procedure for the generation of a rough surface. First, height distribution profiles of the target surface are measured. The height distribution profile has several statistical properties such as mean, standard deviation (STD), auto correlation function (ACF), skewness and kurtosis.

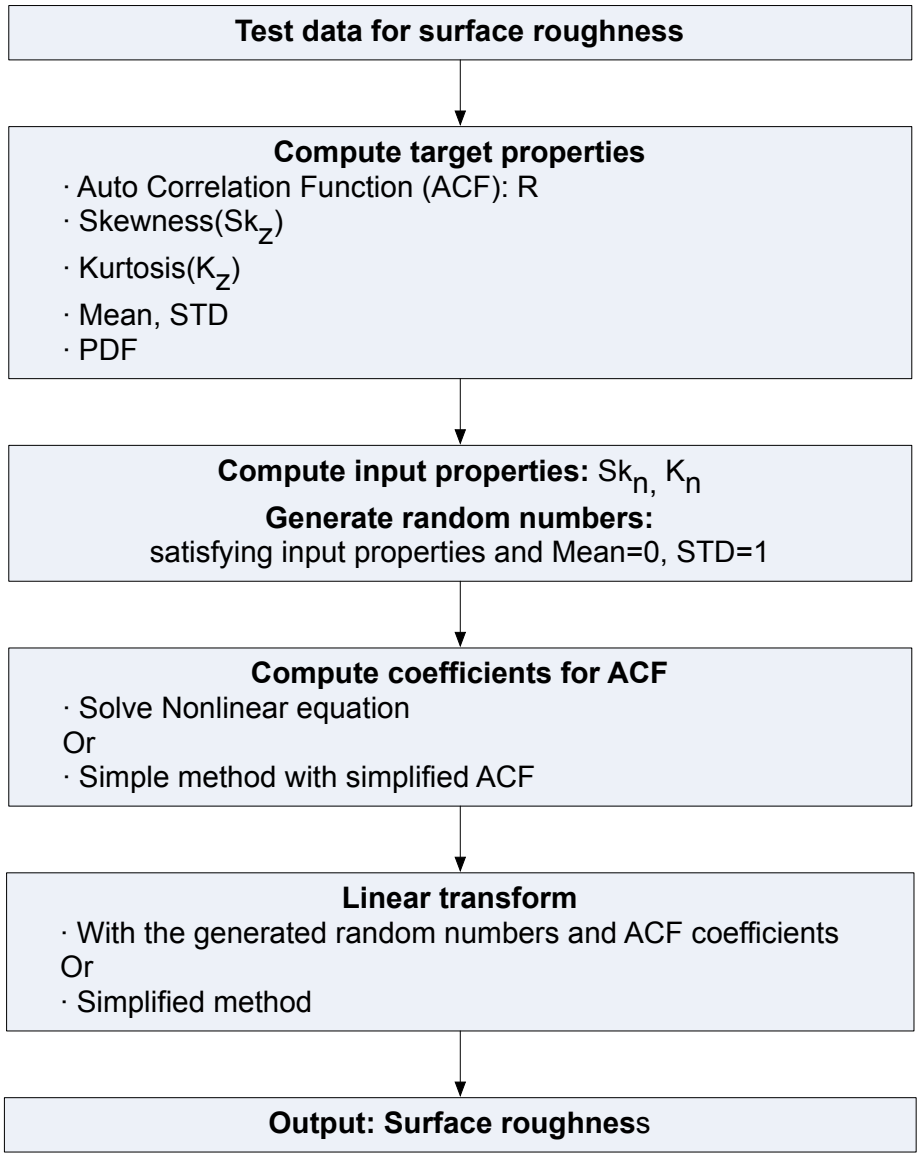

Figure A.1: Rough surface generation procedure with ACF

The skewness (SK) and kurtosis (K) are defined as follows

$$Skeness:\ Sk_z = \frac{\frac{1}{N}\sum_{i=1}^{N}(z_i - \overline{z_i})^3}{(\frac{1}{N}\sum_{i=1}^{N}(z_i - \overline{z_i})^2)^{3/2}} \tag{A.1}$$

$$Kurtosis:\ K_z = \frac{\frac{1}{N}\sum_{i=1}^{N}(z_i - \overline{z_i})^4}{(\frac{1}{N}\sum_{i=1}^{N}(z_i - \overline{z_i})^2)^{2}} \tag{A.2}$$

From *Bakolas* (2003), the discrete form of ACF can be written as

$$R(p,q) = \frac{1}{(N-p)(M-q)}\sum_{i=1}^{N-p}\sum_{j=1}^{M-q} z_{i,j}z_{i+p,j+q} \tag{A.3}$$

where $p = 0, 1, 2, ..., n-1,\ q = 0, 1, 2, ..., m-1$ and z is roughness amplitudes of an $N \times M$ matrix. In this study, instead of Eq. (A.3), an exponential ACF form was used as follows

$$R(p,q) = a_1 \exp(a_2\sqrt{p-1)^2 + (q-1)^2} \tag{A.4}$$

Second, the output rough height distribution is created by a linear transformation, as follows

$$z_{ij} = \sum_{k=1}^{n}\sum_{l=1}^{m} a_{k,l}\eta_{k+i,l+j}\ ,\ i = 1, 2, ..., N,\ j = 1, 2, ..., M \tag{A.5}$$

where η is a random number and $a_{k,l}$ are the coefficients of the nonlinear equation for ACF, i.e.

$$R(p,q) = \sum_{i=1}^{n-p}\sum_{j=1}^{m-q} a_{i,j}a_{i+p,j+q} \tag{A.6}$$

Equation (A.6) can be solved for $a_{i,j}$ using the preconditioned nonlinear gradient method from *Shewchuk* (1994).

Third, the input skewness Sk_η and kurtosis K_η are needed to generate input

random numbers $\eta_{k+i,l+j}$. The relationship between input and output for Sk and K can be written as follows

$$Sk_z = \frac{\sum_{i=1}^{q} {\theta_i}^3}{\left(\sum_{i=1}^{q} {\theta_i}^2\right)^{3/2}} Sk_\eta \tag{A.7}$$

$$K_z = \frac{\sum_{i=1}^{q} {\theta_i}^4}{\left(\sum_{i=1}^{q} {\theta_i}^2\right)^{2}} (K_\eta - 3) + 3 \tag{A.8}$$

where $\theta_i = a_{k,l}$, $i = (k-1)m$, $k = 1, .., n$, and $l = 1, ..., m$.

By satisfying Eqs. (A.8) and (A.8), the input random numbers can be generated with the Johnson translator system or the Pearson system (*Johnson*, 1949; *Elderton and Johnson*, 1969). The two systems transform the normally distributed random numbers into random numbers with the specific skewness and kurtosis using their translator curves. Finally, multiplication of Eq. (A.5) by STD leads to a rough surface having the required statistical properties such as μ, σ, Sk_η and K_η, as follows

$$z_{ij} = STD \times \sum_{k=1}^{n} \sum_{l=1}^{m} a_{k,l} \eta_{k+i,l+j} \ , \ i = 1, 2, ..., N, \ j = 1, 2, ..., M \tag{A.9}$$

Figure A.2 shows the height profile and generated rough surface for the TGC. Because of the large negative skewness, deep valleys of height are formed. The generated rough surface satisfies the statistical roughness properties of the TGC such as mean, standard deviation, skewness and kurtosis. In Figure A.3, the ACF's and histograms of generated surface roughness are compared with the measured roughness data of the TGC. The comparison shows that the main statistical properties of roughness height are satisfied by the generated rough surface.

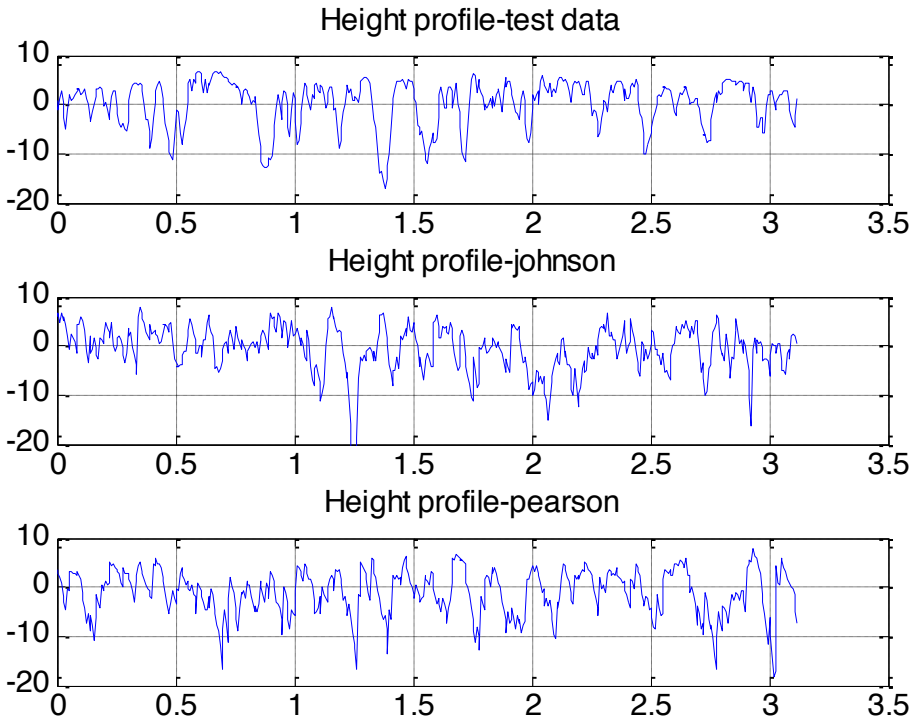

(a) Generated height profile comparison

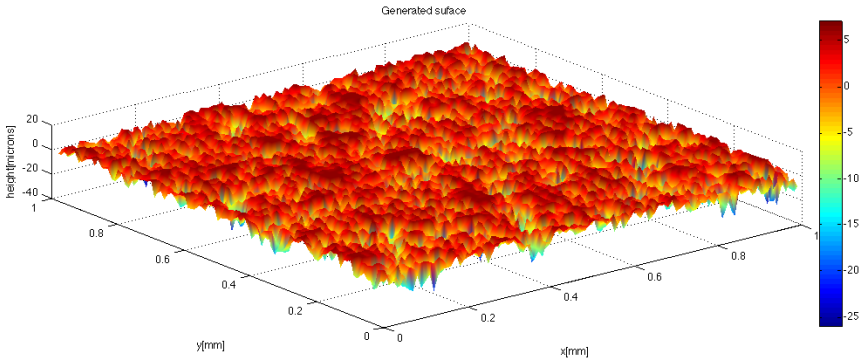

(b) Generated 3D rough surface

Figure A.2: Generated rough surface for TGC

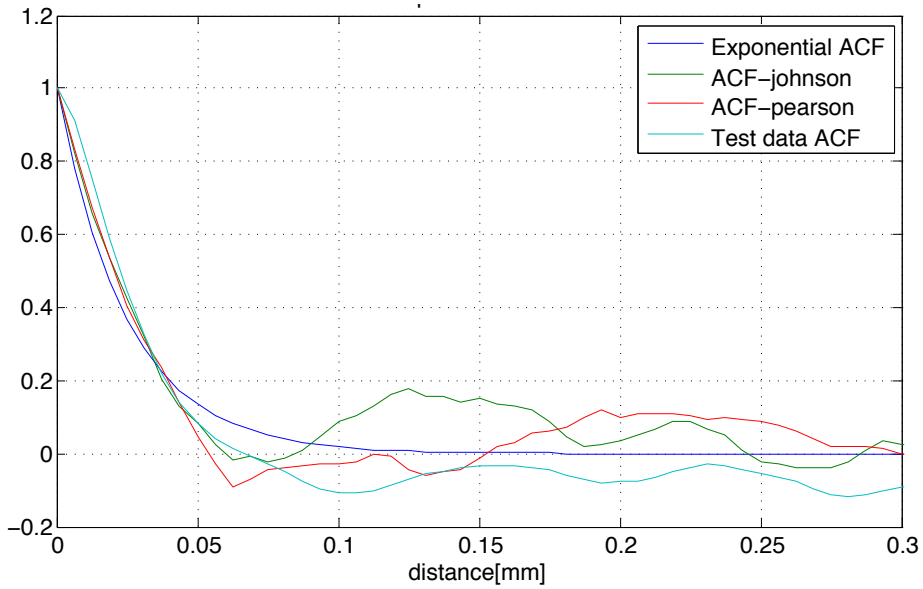

(a) Comparison of ACFs

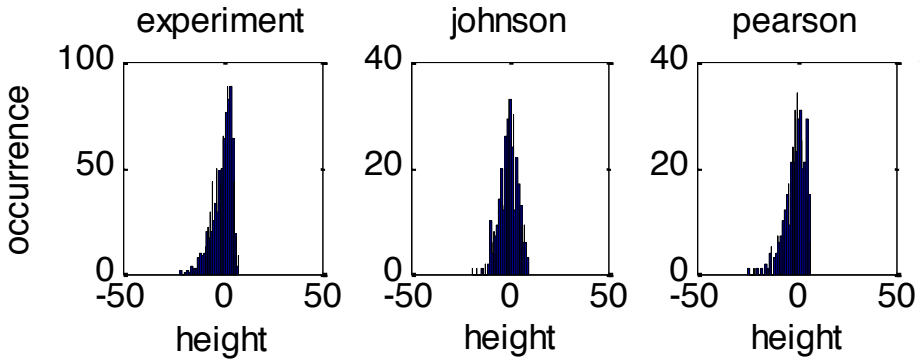

(b) Comparison of histograms

Figure A.3: ACF and histogram comparison for generated rough surface and TGC

A.2 Flow Factor Computation

In this study, only the pressure flow factor ϕ_x was considered. The numerical computation followed the procedure of *Patir* (1978a,b) with the generated rough surface data from Appendix A.1. The detailed procedure and discrete equation for computing flow factor are summarized below.

To compute the pressure flow factor, a pure rolling case is assumed and the dimensionless form of the Reynolds equation, Eq. (A.10) is solved for pressure under the boundary conditions (A.12). Since there is no flow at contact points, the pressure at contact points is assumed to be zero.

$$\frac{\partial}{\partial \bar{x}}({H_T}^3 \frac{\partial \bar{p}}{\partial \bar{x}}) + \left(\frac{L_x}{L_y}\right)^2 \frac{\partial}{\partial \bar{y}}({H_T}^3 \frac{\partial \bar{p}}{\partial \bar{y}}) = 0 \tag{A.10}$$

where

$$\bar{p} = \frac{p - p_B}{p_A - p_B},\ H_T = \frac{h_T}{\sigma},\ \bar{x} = \frac{x}{L_x},\ \bar{y} = \frac{y}{L_y} \tag{A.11}$$

with the boundary conditions

$$\begin{aligned} &p(x = 0) = p_A \text{ and } p(x = L_x) = p_B \\ &\frac{\partial p}{\partial y} = 0 \ at\ y = 0,\ y = L_y \\ &\text{No flow at contact points: } p = 0 \text{ at } h_T = 0 \end{aligned} \tag{A.12}$$

Using a central finite-difference scheme, we obtain the following approximations

$$\left(\frac{\partial \bar{p}}{\partial \bar{x}}\right)_{i,j} = \frac{\bar{p}_{i+1,j} - \bar{p}_{i-1,j}}{2\Delta\bar{x}} \tag{A.13}$$

$$\left(\frac{\partial \bar{p}}{\partial \bar{y}}\right)_{i,j} = \frac{\bar{p}_{i,j+1} - \bar{p}_{i,j-1}}{2\Delta\bar{y}} \tag{A.14}$$

$$\left(\frac{\partial^2 \bar{p}}{\partial \bar{x}^2}\right)_{i,j} = \frac{\bar{p}_{i+1,j} - 2\bar{p}_{i,j} + \bar{p}_{i-1,j}}{\Delta\bar{x}^2} \tag{A.15}$$

$$\left(\frac{\partial^2 \bar{p}}{\partial \bar{y}^2}\right)_{i,j} = \frac{\bar{p}_{i,j+1} - 2\bar{p}_{i,j} + \bar{p}_{i,j-1}}{\Delta\bar{y}^2} \tag{A.16}$$

$$\Delta x = \Delta y, \ \frac{\Delta\bar{x}L_x}{\Delta\bar{y}L_y} = 1 \tag{A.17}$$

$$H_T{}^3_{i,j} = \frac{H_T{}^3_{i+\frac{1}{2},j} + H_T{}^3_{i-\frac{1}{2},j}}{2} \text{ to x-direction} \tag{A.18}$$

$$H_T{}^3_{i,j} = \frac{H_T{}^3_{i,j+\frac{1}{2}} + H_T{}^3_{i,j-\frac{1}{2}}}{2} \text{ to y-direction} \tag{A.19}$$

Equation (A.10) can now be written as follows

$$G_{i+1,j}p_{i+1,j} + G_{i,j}p_{i-1,j} + D_{i,j}p_{i,j} + E_{i,j+1}p_{i,j+1} + E_{i,j}p_{i,j-1} = F_{i,j} \tag{A.20}$$

$$\text{for } i = 1, 2..., N \text{ and } j = 1, 2..., M$$

where

$$G_{i,j} = -H_T{}^3{}_{i-\frac{1}{2},j} \tag{A.21}$$

$$E_{i,j} = -H_T{}^3{}_{i,j-\frac{1}{2}} \tag{A.22}$$

$$D_{i,j} = -(G_{i,j} + E_{i,j} + G_{i+1,j} + E_{i,j+1}) \tag{A.23}$$

Equation (A.20) should satisfy the boundary conditions, i.e.

$$E_{i,1} = E_{i,M+1} = 0 \text{ for } i = 1, 2, ..., N \tag{A.24}$$

$$F_{i,j} = \begin{cases} -G_{i,j} & \text{for } i = 1, j = 1, 2, ..., M \\ x = 0 & \text{otherwise} \end{cases} \tag{A.25}$$

Notice that some precautions need to be taken to avoid an ill-conditioned matrix. In addition, the values at the half grid points should not be obtained by an average of the neighboring points because averaging may change the statistical properties. Therefore, the random numbers at both grid and half grid points need to be generated independently.

APPENDIX B

Engagement Simulation with Compression of Friction Material

B.1 Compression of Friction Material

In order to consider the compressive deformation of the TGC during the engagement process, h and h_ϵ are defined as shown in Figure B.1. h_ϵ is film thickness from a fixed reference line at $z = 0$ and h is defined as $h_\epsilon + \epsilon d$ where ϵ is the compressive strain of the friction material and d is the thickness of the friction plate. As the friction material is compressed, the fixed reference line (black) and the moving reference line (blue) attached on the friction material have a distance ϵd between them. As h_ϵ passes through the fixed reference line at $z = 0$, it assumes negative values. However, because ϵd increases, h maintains positive values although h_ϵ may be negative.

From *Jang and Khonsari* (2011), the compressive strain can be pre-computed from the relation between the real contact area and h_ϵ. From Eq. (4.25), the compressive strain ϵ and the real contact area A_R are related as follows

$$E\epsilon = E_R \frac{A_R(h_\epsilon + \epsilon d)}{A_N} = E_R A_r (h_\epsilon + \epsilon d) \tag{B.1}$$

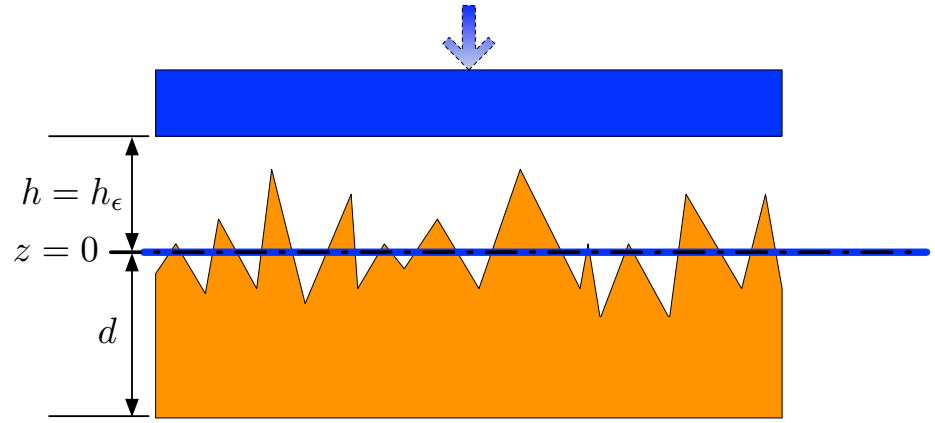

(a) Before friction material is compressed

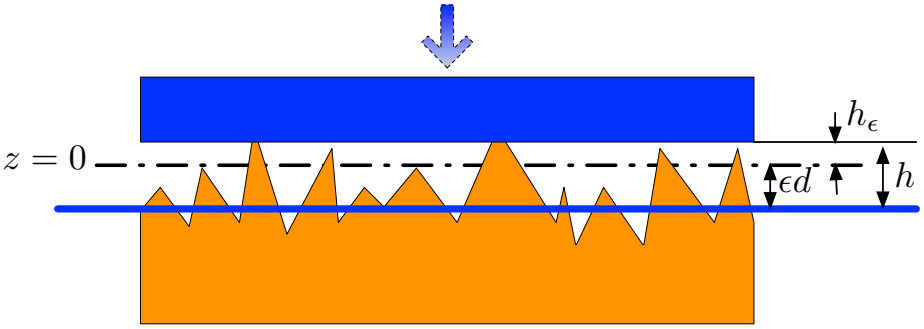

(b) During friction material is compressed

Figure B.1: Definition of h and h_ϵ

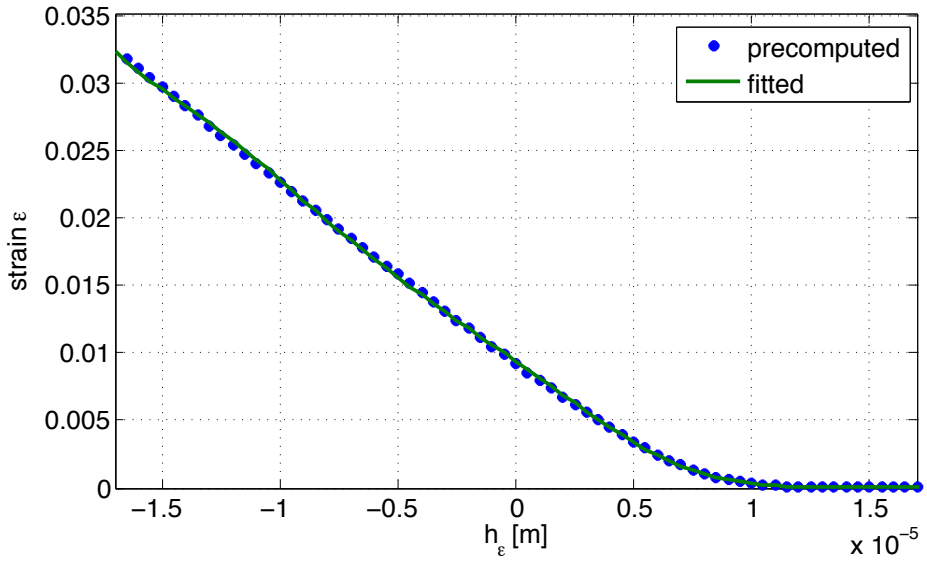

Figure B.2: TGC: Compressive strain ϵ according to oil film thickness h_ϵ

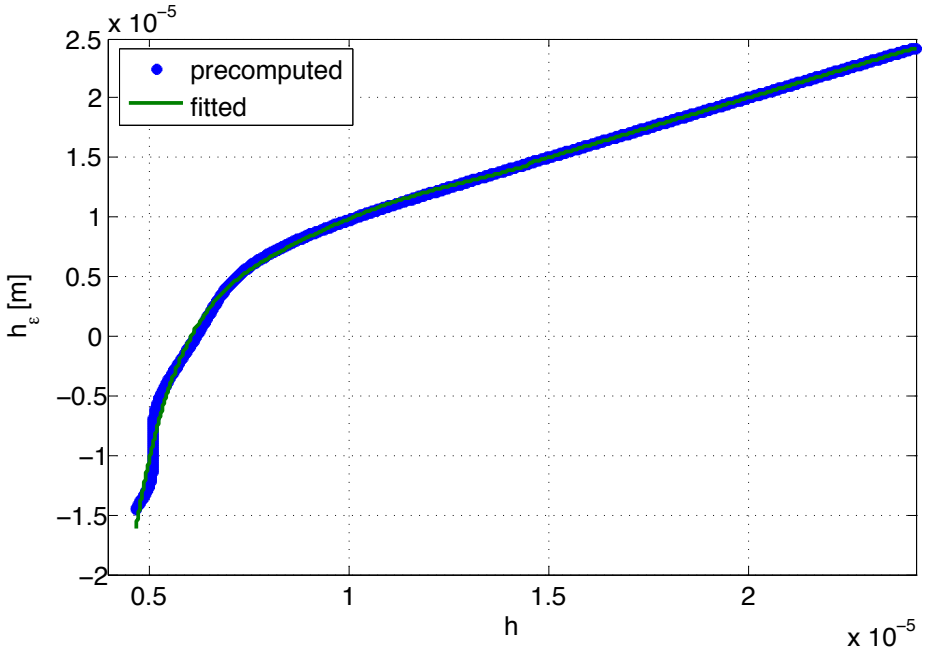

Figure B.3: TGC: The relation between h and h_ϵ

where A_R is the real contact area and A_r is real contact area per unit area.

As h_ϵ varies, Eq. (B.1) can be solved for ϵ using a root finding method. Figure B.2 shows the relation between ϵ and h_ϵ that was obtained using Newton's method.

The fitted curve in Figure B.2 can be written as follows

$$\epsilon = \begin{cases} \sum_{i=1}^{n} \exp(e_i h^{n-i}) & \text{when } h \leq 3 * rms \\ 0 & \text{otherwise} \end{cases} \tag{B.2}$$

where $e_i = (5.7510e+28, 8.8095e+23, -3.2878e+19, -8.9255e+14, -9.6106e+09, -1.3162e+05, -4.6702)$ for $n = 7$.

Using the fitted curve profile of Eq. (B.2), the relation between h and h_ϵ for the TGC can be plotted as shown in Figure B.1. The fitted polynomial curve can be written as follows

$$h_\epsilon = \begin{cases} \sum_{i=1}^{n} p_i h^{n-i} & \text{when } h \leq 3 * rms \\ h & \text{otherwise} \end{cases} \tag{B.3}$$

where $p_i = (-3.6124104e+35, 4.3576778e+31, -2.2481422e+27, 6.4754131e+22, -1.1392936e+18, 1.2558431e+13, -8.5005915e+07, 3.2612557e+02, -5.4324955e-04)$ for $n = 9$.

Following the same procedure as that given for Eq. (B.2) and (B.3) for another sample having a Gaussian roughness density function, the coefficients of Eq. (B.2)and (B.3) were calculated for two different friction material thicknesses, i.e. $d = 5.652e-04\ m$ and $d = 2.824e-04\ m$. The properties of the sample are listed in Table 5.5 and the fitted curves are plotted in Figure B.4. The computed coefficients are as follows

Case 1) when $d = 5.652e-04m$, $e_i = (9.1940e+27, -5.6720e+22, -1.0957e+19, -2.0812e+14, -3.4041e+09, -9.5411e+04, -4.3429)$ and $p_i = (1.7187e+34, -2.4051e+30, 1.4170e+26, -4.5559e+21, 8.6289e+16, -9.5954e+11, 5.6836e+06, -1.0675e+01, -2.1484e-05)$.

Case 2) when $d = 2.824e-04m$, $e_i = (1.3111e+28, 5.7782e+22, -1.1308e+19, -2.5509e+14, -4.2397e+09, -1.0786e+05, -3.8657)$ and $p_i = (3.7643e+33, -5.0032e+29, 2.7686e+25, -8.2016e+20, 1.3737e+16, -1.1962e+11, 2.5213e+05, 5.0235e+00, -2.5632e-05)$.

The overall procedure for engagement simulation including the compression of friction material is shown in Figure B.1. Equation (B.2) and (B.3) are used to compute h_ϵ and F_{con} after h is determined by the squeeze velocity v_h. Then, the total force of F_{fluid} and F_{con} are compared with the applied force F_{app}. The procedure is repeated until the force balance is satisfied.

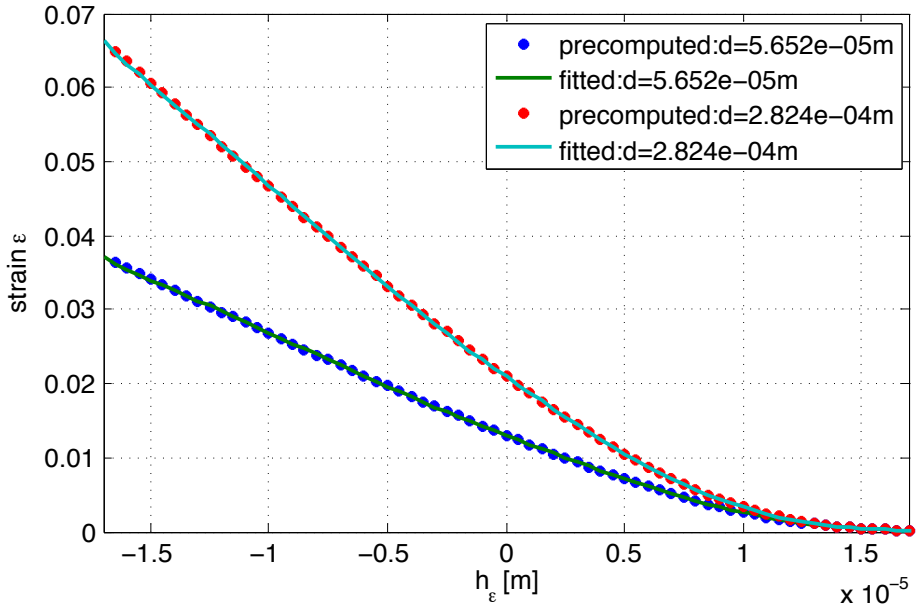

(a) Compressive strain ϵ according to oil film thickness h_ϵ

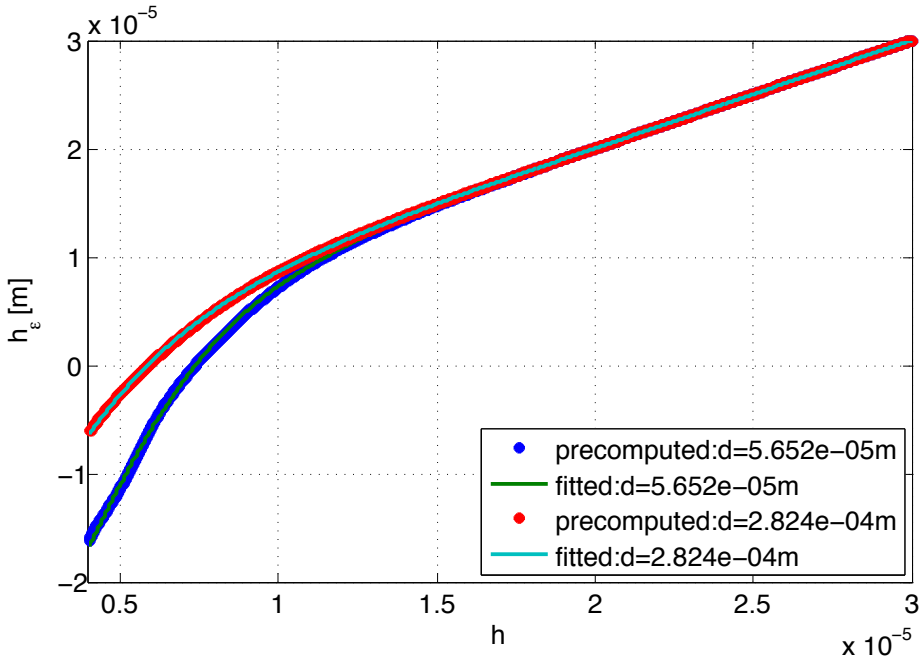

(b) The relation between h and h_ϵ

Figure B.4: Sample clutch friction material: Precomputed compressive strain ϵ and h_ϵ

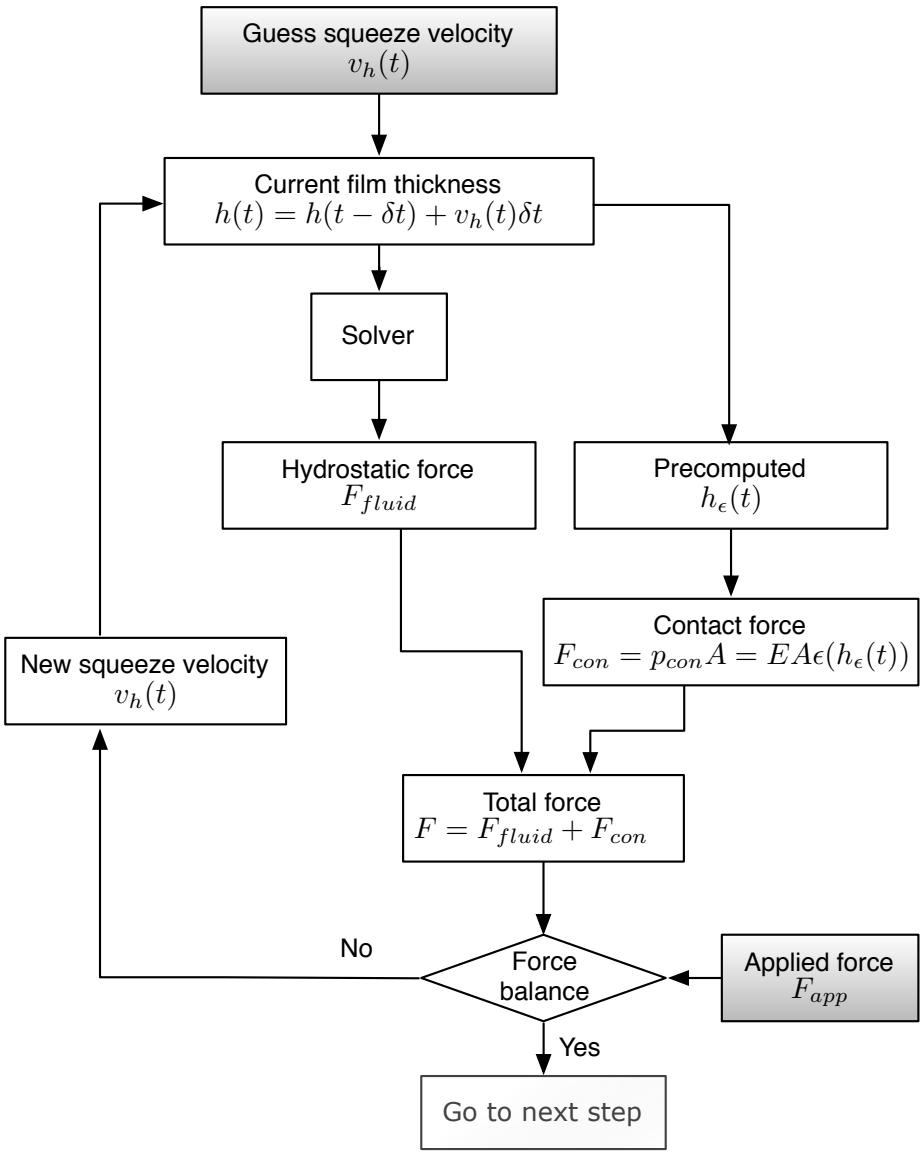

Figure B.5: Engagement process flow chart with the compression of friction material

BIBLIOGRAPHY

BIBLIOGRAPHY

A. Z. Szeri, F. L., S. J. Schneider, and H. N. Kaufman (1983), Flow between rotating disks. part 1. basic flow, *Journal of Fluid Mechanics*, *134*, 103–131, doi: 10.1017/S0022112083003250.

Aphale, C. R., J. Cho, and W. W. Schultz (2006), Modeling and parametric study of torque in open clutch plates, *Transactions of the ASME*, *122*(422–430).

Bakolas, V. (2003), Numerical generation of arbitrarily oriented non-gaussian three-dimensional rough surfaces, *Wear*, *254*(5-6), 546 – 554, doi:DOI: 10.1016/S0043-1648(03)00133-9.

Benson, D. J. (2002), Volume of fluid interface reconstruction methods for multi-material problems, *American Society of Mechanical Engineers*, *55*, 151–165.

Berger, E. J., F. Sadeghi, and C. M. Krousgrill (1996), Finite element modeling of engagement of rough and grooved wet clutches, *Journal of Tribology*, *118*, 137–146.

Berger, E. J., F. Sadeghi, and C. M. Krousgrill (1997), Analytical and numerical modeling of engagement of rough permeable grooved wet clutches, *Journal of Tribology*, *119*, 143–148.

Brennen, C. E. (2009), *Fundamentals of Multiphase Flows*, 19–26 pp., Cambridge University Press.

Bujurke, N. M., and N. B. Naduvinamani (1998), A note on squeeze film between rough anisotropic porous rectangular plates, *Wear*, *217*, 225–230.

Cho, J., N. Katopodes, N. Kapas, and Y. Fujii (2011), CFD modeling of squeeze film flow in wet clutch, *SAE International*, (2011-01-1236).

Christensen, H. (1969), Stochastic models for hydrodynamic lubrication of rough surfaces, *Proc Instn Mech Engrs*, *184*, 1013–1026.

Dahl, P. R. (1977), Measurement of solid friction parameters of ball bearings, *Distribution*.

Davis, C. L., F. Sadeghi, and C. M. Krousgrill (2000), A simplified approach to modeling thermal effects in wet clutch engagement: Analytical and experimental comparison, *Journal of Tribology*, *122*, 110–118.

Deur, J., J. Petric, J. Asgari, and D. Hrovat (2005), Modeling of wet clutch engagement including a through experimental validation, *SAE International*.

Elderton, W., and N. Johnson (1969), *Systems of Frequency Curves*, Cambridge University Press, London.

FLUENT (2009), *Ansys 12 Theory guide and User guide*, Ansys.Inc.

Fujii, Y., W. E. Tobler, and T. D. Snyder (2001a), Prediction of wet band brake dynamic engagement behaviour part 1:mathematical model development, *Proc Instn Mech Engrs*, *215*, 479–492.

Fujii, Y., W. E. Tobler, and T. D. Snyder (2001b), Prediction of wet band brake dynamic engagement behaviour part 2:experimental model validation, *Proc Instn Mech Engrs*, *215*, 603–611.

Fujii, Y., T. Snyder, R. Waldecker, and W. Tobler (2006), Dynamic characterization of wet friction component under realistic transmission shift conditions, *SAE International*, doi:10.4271/2006-01-0151.

Gethin, D. T., M. M. H. M. Ahmad, T. C. Claypole, and B. J. Roylance (1998), Numerical and experimental investigation into porous squeeze films, *Tribology International*, *31*, 189–199.

Gnoevoi, A. V., D. M. Klimov, A. G. Petrov, and V. N. Chesnokov (1996), Viscoplastic flow between two approaching or parallel circular plates, *Fluid Dynamics*, *31*, 6–13.

Gorin, A. V., and M. I. Shilyaev (1976), Laminar flow between rotating disks, *Izvestiya Akademii Nauk SSSR*, *2*, 60–66.

Greenwood, J. A., and J. B. P. Williamson (1966), Contact of nominally flat surfaces, *Proceedings of the Royal Society of London. Series A*, *295*, 300–319.

Gupta, J. L., K. H. Vora, and M. V. Bhat (1982), The effect of rotational inertia on the squeeze film load between porous annular curved plates, *Wear*, *79*, 235–240.

Hamrock, B. J., S. R. Schmid, and B. O. Jacobson (2004), *Fundamentals of fluid film lubrication 2nd*, 305–309 pp., Marcel Dekker, New York, U.S.A.

Hays, M. F. (1963), Squeeze films for rectangular plates, *Journal of Basic Engineering*, pp. 243–246.

Hirt, C. W., and B. D. Nichols (1981), Volume of fluid (vof) method for the dynamics of free boundaries, *Journal of computational physics*, *39*, 201–225.

Hoffner, B., and S. Verlag (2001), Squeezing flow of a highly viscous incompressible liquid pressed between slightly inclined lubricated wide plates, *Rheolocica Acta*, *40*(3), 289–295, doi:10.1007/s003970000123.

Holgerson, M. (1997), Apparatus for measurement of engagement characteristics of a wet clutch, *Wear*, *213*(1-2), 140 – 147, doi:DOI: 10.1016/S0043-1648(97)00202-0.

Hori, Y. (2006), *Hydrodynamic Lubrication*, Springer.

Jackson, J. D. (1964), A study of squeezing flow, *Sci. Res.*, *11*, 148–152.

Jang, J. Y., and M. M. Khonsari (1999), Thermal characteristics of a wet clutch, *Transactions of the ASME*, *121*, 610–617.

Jang, J. Y., and M. M. Khonsari (2002), On the formation of hot spots in wet clutch systems, *Transactions of the ASME*, *124*, 336–345.

Jang, J. Y., and M. M. Khonsari (2011), Three-dimensional thermohydrodynamic analysis of a wet clutch with consideration of grooved friction surfaces, *Journal of Tribology*, *133*.

Johnson, N. L. (1949), Systems of frequency curves generated by methods of translation, *Biometrika*, *36*, 149–176.

Li, P. W., and W. Q. Tao (1994), Effects of outflow boundary condition on convective heat transfer with strong recirculating flow, *Heat and Mass Transfer*, *29*, 463–470, 10.1007/BF01539498.

Mansouri, M., M. Holgerson, M. M. Khonsari, and W. Aung (2001), Thermal and dynamic characterization of wet clutch engagement with provision for drive torque, *Journal of Tribology*, *123*, 313–323.

Matveev, Y. Y., and V. N. Pustovalov (1982), Calculation of laminar flow of a viscous fluid between rotating disks, *Izvestiya Akademii Nauk SSSR*, *1*, 76–81.

Moore, D. F. (1965), A review of squeeze films, *Wear*, *8*, 245–263.

Natsumeda, S., and T. Miyoshi (1994), Numerical simulation of engagement of paper based wet clutch facing, *Journal of Tribology*, *116*(2), 232–237, doi: 10.1115/1.2927201.

Olsson, H., K. J. Astrom, C. C. de Wit, M. Gafvert, and P. Lischinsky (1998), Friction models and friction compensation, *Eur. J. Control*, *4*(3), 176–195.

Patir, N. (1978a), A numerical procedure for random generation of rough surfaces, *Wear*, *47*, 263–277.

Patir, N. (1978b), Effects of surface roughness on partial film lubrication using an average flow model based on numerical simulation, Ph.D. thesis, Northwestern University.

Patir, N., and H. S. Cheng (1978), An average flow model for determining effects of 3-d roughenss on partial hydordynamic lubrication, *Transactions of the ASME*, *100*, 1–6.

Patir, N., and H. S. Cheng (1979), Application of average flow model to lubrication between rough sliding surfaces, *Transactions of the ASME*, *101*, 220–229.

Robbe-Valloire, F. (2001), Statistical analysis of asperities on a rough surface, *Wear*, *249*(5-6), 401 – 408, doi:DOI: 10.1016/S0043-1648(01)00548-8.

Sanda, S., Y. Nagasawa, A. Suzuki, K. Ilayasin, and Hiroshi (1995), Mechanism of friction of wet clutch with paper based facings observation and modeling of facing surface during engagement , *proceedings of the International Tribology Conference*.

Sanni, S. A. (1997), Unsteady squeeze film between rectangular plates, *Wear*, pp. 98–102.

Shewchuk, J. R. (1994), *An introduction to the conjugate gradient method without the agonizing pain*, Carnegie Mellon University.

Singh, P., V. Radhakrishnan, K. A. Narayan, and Kanur (1990), Squeezing flow between parallel plates, *Ingenieur-Archiv*, pp. 274–281.

Suzzi, D., S. Radl, and J. Khinast (2009), Validation of euler-euler and euler-lagrange approaches in the simulation of bubble columns, in *ICheaP-9 The Ninth International Conference on Chemical and Process Engineering*, *Chemical engineering transactions*, vol. 17, edited by S. Pierucci, pp. 585–590.

Tatara, R. A., and P. Payvar (2002), Multiple engagement wet clutch heat transfer model, *Numerical Heat Transfer, Part A: Applications*, *42*(3), 215–231, doi: 10.1080/10407780290059512.

Ting, L. L. (1975), Engagement behavior of lubricated porous annular disk part 1: Squeeze film phase - surface roughness and elastic deformation effects, part 2: Consolidating contact phase - poroelastic effect, *Wear*, *34*, 159–182.

Vora, K. H., and M. V. Bhat (1980), The load capacity of a squeeze film between curved porous rotating circular plates, *Wear*, *65*, 39–46.

Wu, H. (1971), The squeeze film between rotating porous annular disks, *Wear*, *18*, 461–470.

Wu, H. (1978), A review of porous squeeze films, *Wear*, *47*, 371–385.

Yuan, Y., P. Attibele, and Y. Dong (2003), CFD simulation of the flows within disengaged wet clutches of an automatic transmission, *SAE International*.

Yuan, Y., E. A.Liu, and J. Hill (2007), An improved hydrodynamic model for open wet transmission clutches, *Journal of Fluids Engineering*, *129*, 333–337.

Yun, B. I. (2008), A non-iterative method for solving non-linear equations, *Applied Mathematics and Computation*, *198*(2), 691 – 699, doi:DOI: 10.1016/j.amc.2007.09.006.